Phosphoranimide-supported Nickel Clusters for Hydrotreatment

by

Ting Zhao

A thesis submitted in partial fulfillment of the requirements for the degree of

Doctor of Philosophy

Department of Chemistry
University of Alberta

Abstract

Fortuitous characterization of the cationic nickel cluster $[Ni_4(NP^tBu_3)_4][Li_3Br_4(Et_2O)_3]$ led to the rational syntheses and characterization of the mixed-valence low-coordinate cationic nickel cluster: $[Ni_4(NP^tBu_3)_4]BPh_4$ and $[Ni_4(NP^tBu_3)_4]PF_6$, and subsequently the preparation of the anionic cluster $Na[Ni_4(NP^tBu_3)_4]$. The redox chemistry of the nickel series, $[Ni_4(NP^tBu_3)_4]BPh_4$, $[Ni(NP^tBu_3)]_4$, and $Na[Ni_4(NP^tBu_3)_4]$ was investigated, with and without the presence of alkali metal cation. Oxidation of the cobalt analog $[Co(NP^tBu_3)]_4$ results in the formation of dimetallic mixed-valence cluster $[Co_2(NP^tBu_3)_4]PF_6$, which is likely due to the Na^+ contamination in the starting material. Synthesis and characterization of the pure tetrametallic $[Co(NP^tBu_3)]_4$ remains a challenge.

A new preparation of the neutral cluster $[Ni(NP^tBu_3)]_4$ was developed and turned out to be a key to address the reproducibility issue previously observed. The anionic cluster $Na[Ni_4(NP^tBu_3)_4]$, an impurity present from the previous procedure, is the actual catalyst for the hydrogenation of diphenylacetylene. The hydrogenation investigation of the nickel series, $[Ni_4(NP^tBu_3)_4]BPh_4$, $[Ni(NP^tBu_3)]_4$, and $Na[Ni_4(NP^tBu_3)_4]$ suggests that anionic cluster is a more active catalyst than the neutral cluster, which is more active than the cationic cluster. As the temperature increases, higher activities were observed for all three in the series, although much of that must be attributed to the catalysts transforming from homogeneous to heterogeneous.

The hydrosilylation and hydrogenolysis of carbonyl compounds with the tetranickel series were investigated. A preliminary study of the hydrosilylation with impure precatalyst is mainly reproducible using the purified neutral catalyst, delivering good to excellent yields of hydrosilylation product using diphenylsilane as a selective reductant. Complete silylative deoxygenation of carbonyl compound was also investigated, using a more reactive silane and higher reaction temperatures to drive the conversion. In general, aldehydes show higher reactivity than ketones, and aromatic substrates show higher reactivity than aliphatic substrates, at elevated temperature (60–80 °C). A high conversion (~ 90%) to deoxygenation products was achieved for cyclohexenone at 160 °C, albeit at long reaction time and with the catalyst in uncharacterized heterogeneous form.

In addition, several allyl-capped nickel clusters, $[Ni(\eta^3\text{-allyl})(NPEt_3)]_2$, $[Ni(\eta^3\text{-allyl})(NPPh_3)]_2$, and $[Ni(\eta^3\text{-allyl})(NP^tBu_3)]_2$, were synthesized and characterized, as the second-generation of phosphoranimide-bridged first-row transition metal clusters. This new set of compounds is important for developing new hydrotreatment catalysts because they are diamagnetic, coordinatively saturated, thermally stable, and electronically tunable. The redox investigation of $[Ni(\eta^3\text{-allyl})(NPEt_3)]_2$ led to the discovery of the allyl-capped trimetallic nickel cluster, $[Ni_3(\eta^3\text{-allyl})_3(\mu^3\text{-}NPEt_3)_2]PF_6$, and the heterotrimetallic cluster, $[(\eta^3\text{-allyl})Ni]_2CoCl_2(\mu^3\text{-}NPEt_3)_2$. These clusters provide a general method for preparing heteropolymetallic clusters in the future, which could potentially be powerful precatalysts for hydrotreatment.

Finally, the hydrodesulfurization (HDS) activity of $[Ni(NP^tBu_3)]_4$ and $[Ni(\eta^3\text{-allyl})(NPEt_3)]_2$ is discussed, together with the non-innocent role of potassium hydride and the specific promoting effect of potassium cation. The promising results obtained in these studies validate the proposal that structurally-engineered first-row transition metal compounds are capable of catalytic HDS under relatively mild conditions and warrant further investigation for the rational design of new phosphoranimide-bridged first-row transition metal clusters and the development of heterogeneous catalysts.

Preface

There are large deposits of bitumen, extremely heavy crude oil, located in northeastern Alberta, comparable in magnitude to the world's total proven reserves of conventional petroleum. The bitumen crude oil has high content of heteroatoms (S, N, and O) and metals (Ni, V). Thus, it is imperative to develop new technology to meet the increasingly stringent regulatory limitations on toxic gas emission, especially for hydrodesulfurization (HDS) and hydrodenitrogenation (HDN).

The Stryker group has been focused on the fundamental research of building first-row transition metal clusters to mimic and replace the commercial Co-MoS_2 catalyst. The exploration has been very fruitful, highlighted by two successful phosphoranimide-bridged HDS precatalysts, $[Ni(NP^tBu_3)]_4$ and $[Co_4(NPEt_3)_4]PF_6$.

In this thesis, further exploration of tetranickel cluster $[Ni(NP^tBu_3)]_4$ will be discussed first, introducing the cationic and anionic analog, $[Ni_4(NP^tBu_3)_4]BPh_4$ and $Na[Ni_4(NP^tBu_3)_4]$, followed by the activity investigation of hydrogenation, hydrosilylation and deoxygenation. In addition, the design, syntheses, and characterization of allyl-capped phosphoranimide-bridged nickel cluster will be discussed. At last, the HDS activity exploration of these nickel clusters will be included.

It should be mentioned in the beginning that Orain Brown is the main contributor of the HDS study of neutral cluster $[Ni(NP^tBu_3)]_4$ and the grafting process for heterogeneous catalyst, and Fiona Nkala is responsible for the HDS activity of allyl-capped dimer $[Ni(\eta^3\text{-allyl})(NPEt_3)]_2$.

Acknowledgements

I would like to express my deepest appreciation to my supervisor, Professor Jeffrey M. Stryker, who offered me a challenging project then guided me with wisdom, patience and enthusiasm. It is my privilege to have him as a mentor, and this dissertation would not have been possible without his persistent help.

In addition, I would like to thank all the past and present members of Stryker Research Group for all their help, advice, and support through all these many years, especially Dr. Robin Hamilton, Dr. Shaohui Yu, and Dr. Kseniya Revunova.

I would also like to acknowledge the chemistry support staffs, who are integral part of research conducted in the department, particular Wayne Moffat, Dr. Mike Ferguson, and Dr. Bob McDonald.

Most of all, I want to thank my wife Yan Liu and my parents for their persistent support and trust in me.

At last, as Bruce Lee said: Don’t pray for an easy life, pray for the strength to endure a difficult one.

Table of Content

Chapter 3. Phosphoranimide-bridged Nickel Clusters for Hydrosilylation and Deoxygenation of Carbonyl Compounds

Chapter 4 Allyl-capped First-row Transition Metal Phosphoranimide Clusters – 2nd Generation Low-valent Clusters for Catalytic Hydrotreatment

Chapter 5 Phosphoranimide-bridged Nickel Clusters for Catalytic Hydrodesulfurization (HDS)

Chapter 6 Experimental Section

List of Tables

List of Figures

Chapter 1

Chapter 2

Chapter 3

Chapter 4

Chapter 5

List of Schemes

Chapter 1

List of Abbreviations

Å	angstroms
atm	atmosphere
Bu	butyl
cm^{-1}	wavenumbers
COD	cyclooctadiene
Cp	cyclopentadienyl
Cp*	pentamethylcyclopentadienyl
CV	cyclic voltammetry
D	days
DBT	dibenzothiophene
DFT	Density Functional Theory
e	electron
eq.	equivalents
Et	ethyl
g	grams
h	hours
HMDS	bis(trimethylsilyl)smide
HOMO	Highest Occupied Molecular Orbital
Hz	hertz
IR	Infrared
kcal	kilocalories
KDA	potassium diisopropyl amide
LDA	lithium diisopropyl amide
L_n	ligand
LUMO	Lowest Unoccupied Molecular Orbitals
M	metal
Me	methyl
mg	milligrams
MHz	megahertz

min	minutes
mL	milliliter
mmol	millimole
mol	mole
^{n}Bu	*n*-butyl
NMR	Nuclear Magnetic Resonance Spectroscopy
Ph	phenyl
pm	picometers
ppm	part per million
R	generic alkyl/aryl substituent
rt	room temperature
SOMO	Singly Occupied Molecular Orbital
^{t}Bu	*tert*-butyl
TMP	tetramethylpeperidide
TOF	turnover frequency
TON	turnover number
°C	degrees Celsius
ν	Nu (frequency)
η	Eta (hapticity)

Chapter 1. Tri-*tert*-butylphosphoranimide-bridged Late First-row Transition Metal Clusters

1.1 Introduction

Homogeneous catalysis is historically an area dominated by precious metals, and this is highlighted by the Nobel prizes awarded in 2001, 2005, and 2010 for asymmetric hydrogenation,[1] olefin metathesis,[2] and palladium catalyzed C–C bond formation reactions,[3] respectively. However, catalysis with precious metal such as Pd, Ir, Rh, and Ru has obvious disadvantages, such as cost, abundance, sustainability, and toxicity, not only for the catalyst itself but also for the whole process from production to waste treatment.[4] In the last decade, catalysis with earth-abundant metals, especially first-row transition metals has become one of the most active research fields in organometallic chemistry[4] and tremendous advances have been made in many areas, including cross coupling and cycloaddition,[5-12] hydrofunctionalization,[13] hydrogenation of unsaturated species,[14-17] oxidation,[18] C-H functionalization[5,19,20] and alkene polymerization.[13,21,22]

The anionic phosphoranimide ligand, also known as phosphinimide, phosphorane-iminato or phosphorane imide, was discovered by Staudinger and Meyer[23] at the beginning of the last century and has the molecular formula [NPR_3^-]. Early exploration of phosphoranimide chemistry dates back to the 1960's by Schmidbaur et al.[24,25] A large number of main group and transition metal complexes have been characterized and reviewed since then.[26-30] Phosphoranimide complexes of the late first-row transition metal (Mn, Fe, Co, Ni, Cu and Zn) have been explored previously. For divalent metals, the core structure, an [$M_4N_4X_4$] heterocubane, prevails in most cases when the substituents on [NPR_3^-] are small, such as Me or Et.[26] In contrast, examples of metal complexes with sterically larger group such as Ph and ^{t}Bu are rare for late first-row transition metals.[31] This chapter will mainly focus on the synthesis, structure, and redox behavior of nickel clusters bearing the sterically large, strong electron donating [$NP^tBu_3^-$] ligand from the inorganic perspective.

1.1.1 Trialkylphosphoranimide ligands: versatile bonding modes, remote steric bulk, and adjustable steric and electronic character

The phosphoranimide ligand is monoanionic and isoelectronic to [OCR_3^-], [$OSiR_3^-$], and cyclopentadienyl.[32] The alkali metal salt exists as either hexamer or tetramer depending on the steric sizes of the substituents, meanwhile the discrete anion is still unknown.[28,33-38] A qualitative description of its electronic structure was obtained in the framework of Extended Hückel Theory (EHT).[39] It indicates that the highest occupied molecular orbitals of the free ligand are best described an *sp*-hybridized *lone-pair* (a_1 symmetry) and a degenerate set of orthogonal *p*-orbitals (e symmetry). The nitrogen-phosphorus bond is best described as a double bond by the NBO partitioning scheme (resonance A, Fig. **1.1**). On the other hand, when the ligand coordinates to transition metals, the negative charge on nitrogen increases and the nitrogen-phosphorus bond order decreases. As a result, the bond is best described as a polar single bond and the ligand is best interpreted as resonance structure B (Fig. **1.1**).

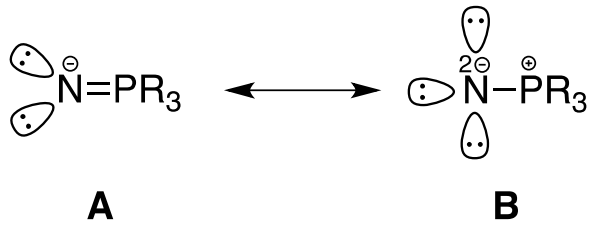

Figure **1.1**: Resonance structure of [NPR_3^-].

The bonding modes of phosphoranimide ligand are versatile, depending on the metal incorporated, the oxidation state of the metal, and the steric and electronic character of the substituents.[26] The five main bonding modes are illustrated below (Fig. **1.2**). In bonding mode A, the phosphoranimide ligand is considered a 6-electron donor by forming M≡N bonds. This terminal coordination is generally observed for metals in high oxidation states with empty d-orbitals, such as observed in [$ReO_3(NPPh_3)$] **1**,[40] [$WCl_5(NPCl_3)$] **2**,[27] $[Mo(NPPh_3)_4]^{2+}$ **3**, and $[MoNCl_3(NPPh_3)]_2^- \bullet C_7H_8$ **4**.[41] In bonding mode B, the ligand

donates 4 electrons to the metal by forming a double bond (σ + π). The M–N–P angle in this case, as in $[WCl_4(NPCl_3)_2]$ **5** (160°),[42] is more acuter than in mode A. In bonding mode C and D, phosphoranimide ligand coordinates to two metal atoms by nitrogen, acting as a μ^2-bridging ligand. In mode C, the bonding is asymmetric, resulting two different metal nitrogen bond lengths, as observed dimeric $[TiCl_3(NPMe_3)]_2$ **6**.[26] In mode D, the bonding is symmetric, and the two metal nitrogen bonds are at the same length, as in $[FeCl_2(NPEt_3)]_2$ **7**.[31] At last, in mode E the ligand coordinates to three metal atoms by nitrogen, acting as a μ^3-bridging ligand. It is often observed for metals in low oxidation states, especially late first-row transition metals, as observed in the heterocubane structures such as $[NiCl(NPMe_3)]_4$ **8**[43] and $[CoI(NPMe_3)]_4$ **9**.[44]

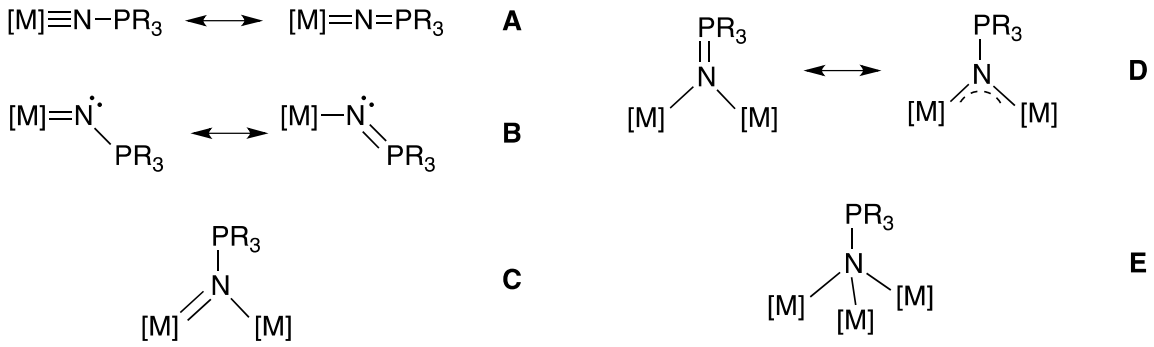

Figure **1.2**: Bonding modes for phosphoranimide ligand.

As mentioned, in most heterocubane clusters the phosphoranimide ligands bear small alkyl groups, and the oxidation state of the metal is generally +2. For metals of moderate oxidation state, the mixed bondding modes A/B or A/D were observed. In addition to oxidation state, the size of the phosphorus substituent also affects the bonding mode. For example, $[CoCl(NPR_3)]_4$ **10** has a heterocubane structure when R is small group such as methyl or ethyl,[44] while $[CoCl(NP^tBu_3)]_2$ **11** exists as a dimeric cluster with two bridging phosphoranimide categorized as mode D due to the steric demand of the ^{t}Bu group.[45] A similar influence is also found for complexes of main group metals: $[Mg_2(\mu\text{-}NP^tBu_3)_2(NP^tBu_3)_2]$ **12** exists as a dimer with two bridging and two terminal phosphoranimide while the $[Mg_3(\mu\text{-}NP^iPr_3)_4(NP^iPr_3)_2]$ **13** exists as a trimer,[46] as shown

below (Fig. **1.3**). Last but not least, the bonding mode is also significantly affected by the chemical environment at the metal center, the electronic and steric character of other coordinated ligands.

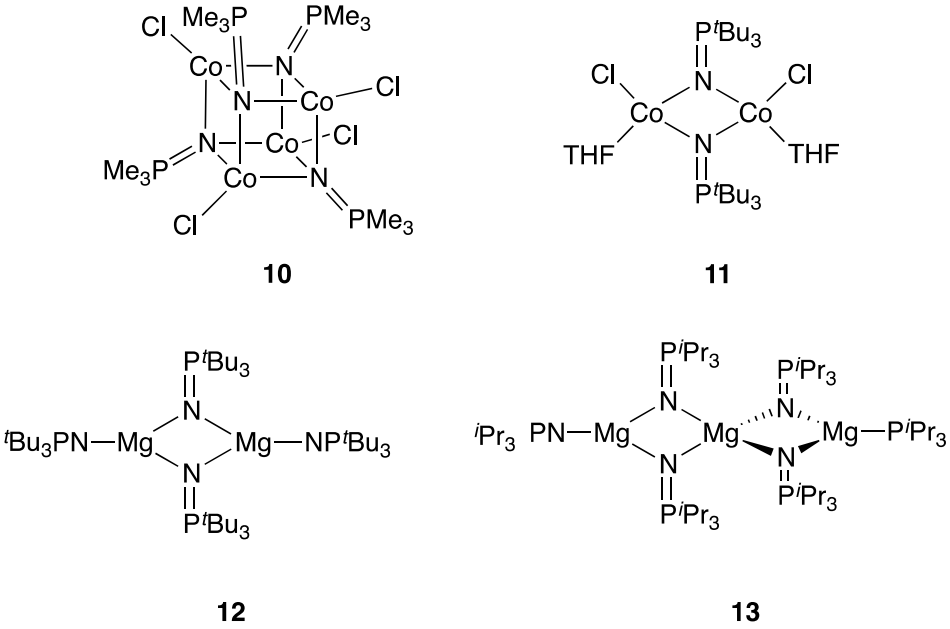

Figure **1.3**: Structures of selected phosphoranimide clusters: $[CoCl(NPMe_3)]_4$ **10**; $[CoCl(NP^tBu_3)]_2$ **11** ; $[Mg_2(\mu\text{-}NP^tBu_3)_2(NP^tBu_3)_2]$ **12** ; $[Mg_3(\mu\text{-}NP^iPr_3)_4(NP^iPr_3)_2]$ **13**.

The $TiCp(NPR_3)X_2$ (X = Cl or Me; R = ^{t}Bu) system was well studied by Stephan, et al., for ethylene polymerization as an alternative to the popular metallocene system.[47,48] In this series of compounds, the phosphoranimide ligand not only mimics the Cp anion electronically by donating as many as six electrons to the metal, but also occupies considerable steric space due to the similarity of cone angles using Tolman's model,[49] when the R = ^{t}Bu. In contrast, the Ti–P distance is much longer than the Ti–Cp-centroid distance, 3.4Å vs 2.2Å,[48] due to an extra atom in between. This suggests that even though $[NP^tBu_3^-]$ occupies relative large space, the actually steric bulk is displaced far from the metal center. Combining this character with the versatile bondding modes at nitrogen, it is proposed that the activity of low-coordinate first-row transition metal clusters should be a potentially valuable area for exploration.

Besides the versatile bondding mode and "remote steric effect",[32] the phosphoranimide ligand also offers tunable electronic and steric character. By changing the electron-donating ability of the substituents, it is possible to investigate electronic and steric influences of the substituent both on the aggregation and catalytic behavior of the metal clusters.

1.1.2 Catalyst design using trialkylphosphoranimide ligands

Phosphoranimide metal compounds and their catalytic activity have been well studied since the 1980's and a number of reviews were published since then, either about main group[28] or transition metals.[26,27,50] However, the chemistry of phosphoranimide complexes of late first-row transition metals has not been explored extensively, although a number of metal clusters were synthesized, most of which have the heterocubane structure. The main factor inhibiting the development of this chemistry was that no general procedure for the synthesis of late transition metal phosphoranimide complexes had been reported when our work was initiated.

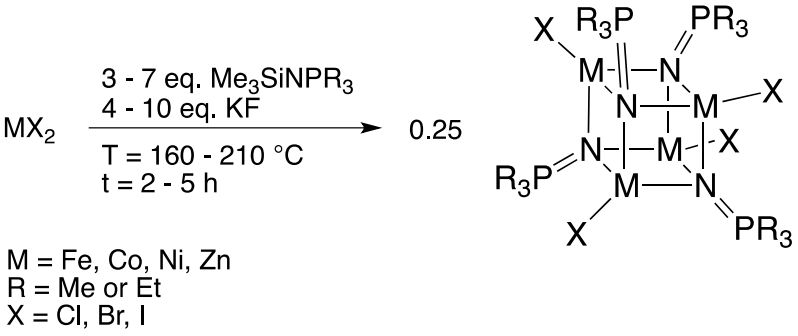

Equation **1.1**

The main strategy for synthesis, as developed by Dehnicke, et al.,[26] used the low-melting trimethylsilyl-trialkylphorphoranimide (R = Me, Et) as the solvent medium for salt exchanges with metal halides (Eqn. **1.1**). This melt-phase procedure not only limits the ligand scope to [$NPMe_3^-$] and [$NPEt_3^-$], but also inhibits scale-up of the reaction due to the

inefficiency and difficulty of purification of the product. Even the ligand salts, for example $LiNPR_3$, are made from the trimethylsilyltrialkylphosphoranimide ($TMSNPR_3$). It is also difficult to apply this preparation on a large scale because trimethylsilyl azide, which is potentially explosive at elevated temperature and acutely toxic, is not the preferred synthetic reagent.

To solve this problem, Dr. Robin Hamilton of the Stryker group adapted an older azide-free procedure to develop a new method to synthesize the ligand from the related phosphine on 10-gram scale (Scheme **1.1**). In the original procedure, a primary amine was mixed with triphenylphosphine dibromide under basic conditions to produce the N-alkyltriphenylphosphoranimide.[51] In our procedure (Scheme **1.1**), potassium amide was prepared *in situ* and mixed with trialkylphosphine dibromide, after which the excess base deprotonates the phosphoranium salt to give the phosphoranimide ligand.

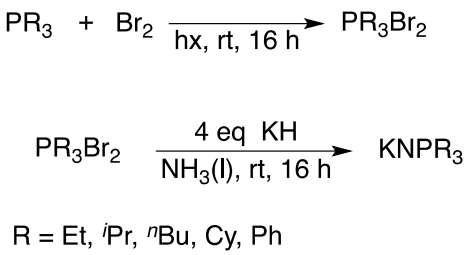

Scheme **1.1**: General procedures for the synthesis of phosphoranimide ligand.

This procedure is effective for most phosphoranimide substituents, except for [$NP^tBu_3^-$]. The synthesis of lithium tri-*tert*-butylphosphoranimide **14** begins with an interrupted Staudinger reaction to make (trimethylsilyl)tri-*tert*-butylphosphoranimide **15** (Scheme **1.2**). Then phosphoranium fluoride **16** was prepared by desilylation using potassium hydrogen difluoride. Two consecutive deprotonations by methyllithium gives the final product lithium tri-*tert*-butylphosphoranimide **14**. The stepwise deprotonation was adopted to ensure the purity of the product; otherwise residual lithium bromide proved to be inseparable from the **14**.

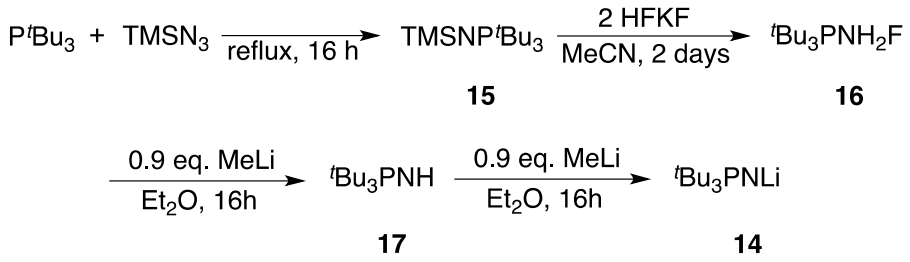

Scheme **1.2**: Synthesis of LiNP^{t}Bu$_3$ **14**.

The original motive for the Stryker group to work on this type of compound was to develop a new catalytic strategy to break the aromatic carbon-heteroatom bonds (mostly C–S and C–N) under mild condition for application to the oil sands upgrade process (Fig. **1.4**).

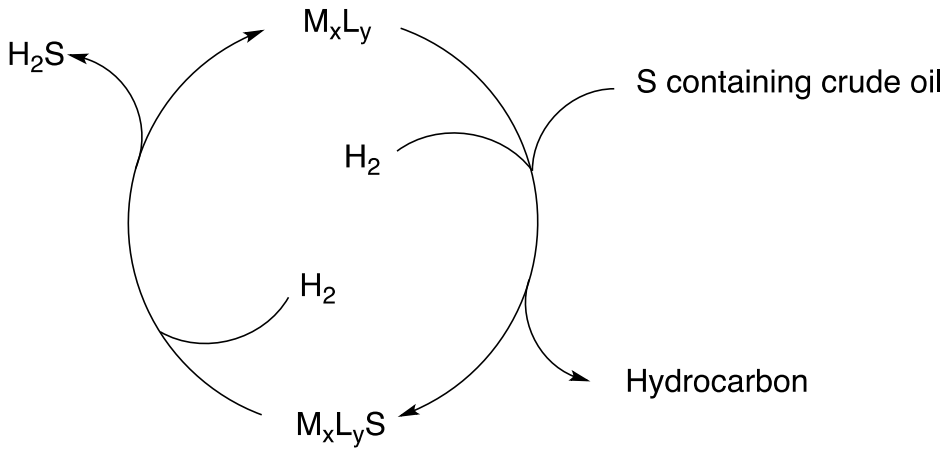

Figure **1.4**: Simplified scheme for hydrodesulfurization (HDS)

Conventionally, the first-row transition metal sulfides are believed to have much lower hydrodesulfurization (HDS) activity than the commercial Co-promoted molybdenum sulfide (Co-MoS_2) supported on alumina.[52-56] However, recent investigation brings new insights of the role of cobalt in commercial catalyst and points out the cobalt centers might be the actual active sites of the commercial catalyst.[57] This suggests the possibility of using first-row transition metal catalyst for HDS.

The phosphoranimide ligand was proposed to serve the above purpose for several reasons: (1) The electron-donating ligand could build up electron density on the metal center to facilitate the oxidative addition part of the catalytic cycle (2) Meanwhile, hydrogenation of the metal sulfide would be more favored than for early metal sulfide, due to the weaker M–S bonds (3) In addition, when sterically demanding substituents are used, the bulky phosphoranimide would promote coordinative unsaturation of the metal centers, which is critical to the HDS activity, based on the study of heterogeneous catalysts (4) Due to the versatile bondding modes of the ligand multiple metal centers would be bridged by a single nitrogen atom to form metal clusters so that the burden of mediating the full catalytic cycle is absolved for any single metal center (5) Last but not least, the relatively easy preparation of trialkylphosphoranimide with various substituents makes it easier to study the influences of the electronic and steric character of the substituents. From all the above perspectives, phosphoranimide-bridged late first-row transition metal clusters could be a new solution to the HDS and HDN process. In the last several years, many precatalysts have been synthesized and studied in the Stryker group, some of which will be mentioned later in this chapter.

Besides applications in the oil industry, it is also interesting to explore the activity of late first-row transition metal phosphoranimide clusters in other fields related to the commodity and fine chemicals industries. Low-coordinate first-row transition metal compounds have considerable potential in many chemical transformations, such as small molecule and C–H activation. In most low-coordinate complexes, bulky ligands such as multidentate phosphines or NHC's are used to block the coordination sphere of the metal to prevent further coordination and aggregation, which to some degree also inhibits the activity of the catalyst. As mentioned, the steric bulk of the phosphoranimide is located further away from the metal coordination sphere. As a result, the phosphoranimide metal cluster can form low-coordinate complexes without crowding the metal coordination sphere, leaving space for other chemistry to occur. The activity of this type of metal cluster is worth exploring due to the great potential in many fields, including catalysis and inorganic materials.

1.2 Previous work from the Stryker group

As the Stryker group has been focusing on the trialkylphosphoranimide-bridged first-row transition metal clusters for several years, it is essential here to mention some previous work briefly to bring context to this thesis. Among all the research done in the Stryker group, the work by Dr. Jeffrey Camacho-Bunquin and Dr. Houston Brown will be discussed here, due to the direct relevance to the content of this thesis.

1.2.1 Hydrocarbon soluble coplanar two-coordinate Ni and Co clusters: [Ni(NP^{t}Bu$_3$)]$_4$ 18 and [Co(NP^{t}Bu$_3$)]$_4$ 19

The discovery of tetrametallic two-coordinate nickel and cobalt clusters [Ni(NP^{t}Bu$_3$)]$_4$ **18** and [Co(NP^{t}Bu$_3$)]$_4$ **19** was made by former group member Dr. Jeffrey Camacho-Bunquin (Fig. **1.5**).[45]

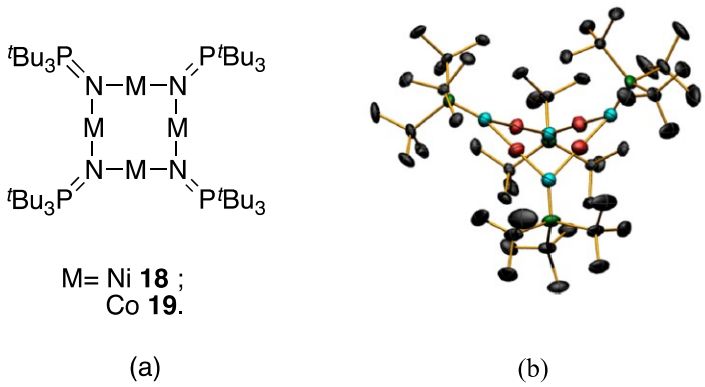

Figure **1.5**: (a) Structure of [Ni(NP^{t}Bu$_3$)]$_4$ **18** and [Co(NP^{t}Bu$_3$)]$_4$ **19**; (b) ORTEP diagram of **19**, thermal ellipsoids are shown at 30% probability and hydrogen atoms have been omitted for clarity.

The sterically bulky tri-*tert*-butylphosphoranimide is the only supporting ligand for the cluster. Each ligand bridges two metal centers through an electron rich nitrogen atom and each metal is monovalent and linearly two-coordinate. In the solid state, the four metal atoms are coplanar while the diagonal ligand alternate above and below the square plane of the metals.

The X-ray crystal refinement for $[Co(NP^tBu_3)]_4$ **19** suggested that the Co(I) centers are partially replaced by Na cations in variable amounts in different single crystals selected for structure refinement. Solution magnetic susceptibility, as measured by the Evans' method,[58] revealed that the cobalt cluster **19** is an 8-electron paramagnet, indicating two unpaired electrons per metal center and no significant amount of Co–Co bonding. On the other hand, the Ni(I) center in $[Ni(NP^tBu_3)]_4$ **18** is not replaced by Na cation even though it is prepared by the same procedure. Solution magnetic susceptibility measurement for **18** reveals close to four unpaired electrons for the cluster, suggesting one unpaired electron for each Ni(I) metal center, with d^9 configuration.

Both clusters are highly unsaturated and exhibit activity for hydrogenation of alkynes and alkenes under mild condition (room temperature, one atmosphere of hydrogen).[45] However, for the nickel cluster **18**, the hydrogenation activity of diphenylacetylene **20** was irreproducible. Even more intriguing was that when the purest available single crystal was used as the catalyst, no hydrogenation activity was observed.[59] The reproducibility issue has been addressed in the current work and will be discussed later in this thesis.

1.2.2 Heterocubane $[MeCo(NPEt_3)]_4$ 21 and $[Me_4Co_4(NPEt_3)_4]PF_6$ 22

In addition to the two-coordinate tetrametallic cluster, another synthetic accomplishment was the alkylated heterocubane cluster $[MeCo(NPEt_3)]_4$ **21** and the one-electron oxidized congener $[Me_4Co_4(NPEt_3)_4]PF_6$ **22** (Fig. **1.6**) by Dr. Houston Brown.[60] Neutral $[MeCo(NPEt_3)]_4$ adopts the typical heterocubane structure, with cobalt and nitrogen atoms positioned at alternative corners of the cube. In the cluster, each triethylphosphoranimide ligand coordinates to three cobalt atoms and each cobalt atom binds to three ligands.

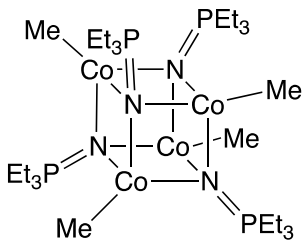

21

$[MeCo(NPEt_3)]_4$

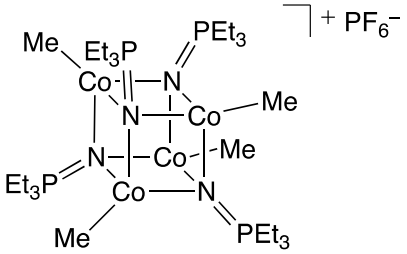

22

$[Me_4Co_4(NPEt_3)_4]PF_6$

Figure **1.6**: Structures of $[MeCo(NPEt_3)]_4$ **21** and $[Me_4Co_4(NPEt_3)_4]PF_6$ **22** characterized by X-ray crystallography.[60]

The cationic cluster $[Me_4Co_4(NPEt_3)_4]PF_6$ **22** was synthesized by one-electron oxidation of **21** using stoichiometric Cp_2FePF_6. When the electron is removed from the cluster, the average Co-N bonds length decreases from 2.87Å to 2.71Å without significantly changing the coordination environment. The four cobalt atoms stay identical to each other, which makes the cluster a type III mixed-valence compound.[61] Both the neutral and cationic clusters are active HDS catalysts in the presence of a strongly basic potassium salt (KH, KDA, KTMP) and the cationic cluster shows higher activity.[60]

1.3 Results and discussion

1.3.1 Synthesis and characterization of $[Ni_4(NP^tBu_3)_4]BPh_4$ 23

The cationic analog of neutral cluster **18** proved to be the key to the high purity synthesis of this troublesome cluster. More importantly, this discovery led directly to the identification of the putative hydrogenation catalyst first reported by Dr. Jeffrey Camacho-Bunquin.[45]

1.3.1.1 Synthesis of $[Ni_4(NP^tBu_3)_4]BPh_4$ 23

The cationic tetrameric cation $[Ni_4(NP^tBu_3)_4]^+$ was discovered serendipitously, when we targeted the dimetallic nickel cluster, $[Ni(\eta^3\text{-allyl})(NP^tBu_3)]_2$ **24**, which has bridging phosphoranimide ligands and terminal η^3-allyl groups (Scheme **1.3**). This chemistry will be detailed in a later chapter. In the reaction, $[Ni(\eta^3\text{-allyl})Br]_2$ **25** was mixed with $LiNP^tBu_3$ in diethyl ether at room temperature, giving a green pentane soluble product. Recrystallization of the assumed product **24** gave instead the unexpected cationic tetramer, $[Ni_4(NP^tBu_3)_4][Li_3Br_4(Et_2O)_3]$ **26**.

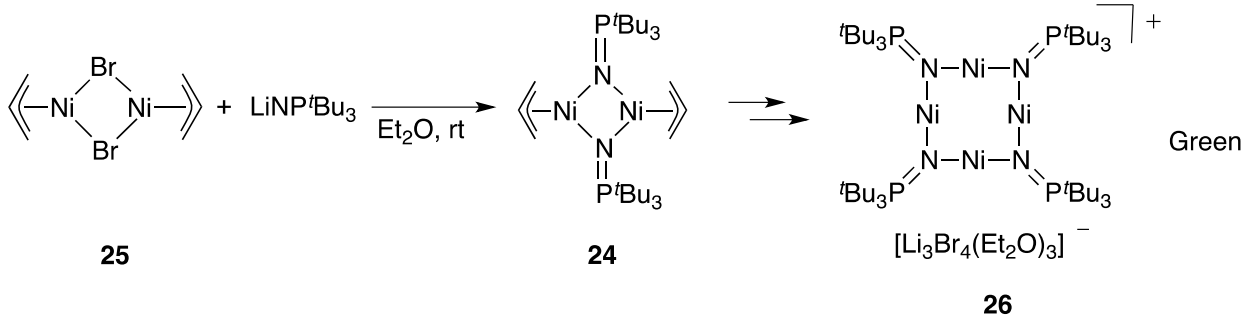

25 **24** **26**

Scheme **1.3**: Serendipitous isolation of $[Ni_4(NP^tBu_3)_4][Li_3Br_4(Et_2O)_3]$ **26**.

The unusual ether-solvated counter ion is composed of lithium and bromide ions from the starting materials and diethyl ether from the solvent. In the cluster, the oxidation state is Ni(II)/3Ni(I), while it is Ni(II) in the starting material. It is proposed that the dimetallic intermediate $[Ni(\eta^3\text{-allyl})NP^tBu_3]_2$ was formed as expected, followed by steric driven, nickel-carbon bond homolysis, reducing the metal to Ni(I). Subsequent oligomerization and partial reoxidation results in the thermodynamically favored cationic cluster **26**. It should be mentioned that the only known structurally similar tetrameric species $[Ni\{N(SiMe_3)_2\}]_4$ **27** is proposed the decomposition product of $[Ni(NSiMe_3)_2]_2$ **28**.[62] In that reaction, the authors propose a Ni–N bond cleavage pathway, reducing Ni(II) to Ni(I), and generating the nitrogen radical, $\bullet N(SiMe_3)_2$, which abstracts hydrogen from diethyl ether to give $HN(SiMe_3)_2$ **29** as a byproduct. DFT calculations suggest that the lowering of the d-electrons energy across the 3d-series might be the reason for the thermal instability of $Ni\{N(SiMe_3)_2\}_2$ **28**.[63]

From the crystal structure (Fig. **1.7**), the bondding mode of the tetrametallic cation is closely similar to the neutral tetrametallic cluster $[Ni(NP^tBu_3)]_4$ **18**, reported by Dr. Jeffrey Camacho-Bunquin.[45] The four nickel atoms locate in a square plane, and each coordinates linearly to two μ^2-phosphoranimide ligands. The counter ion $[Li_3Br_4(Et_2O)_3]^-$ was unprecedented as an anion. The only similar structure is a neutral Li_4Br_4 heterocubane with various numbers of Et_2O coordinating to the Li cations on the corners.[64] The structure of $[Li_3Br_4(Et_2O)_3]^-$ resembles the heterocubane closely, but missing a Li^+ cation on one corner.

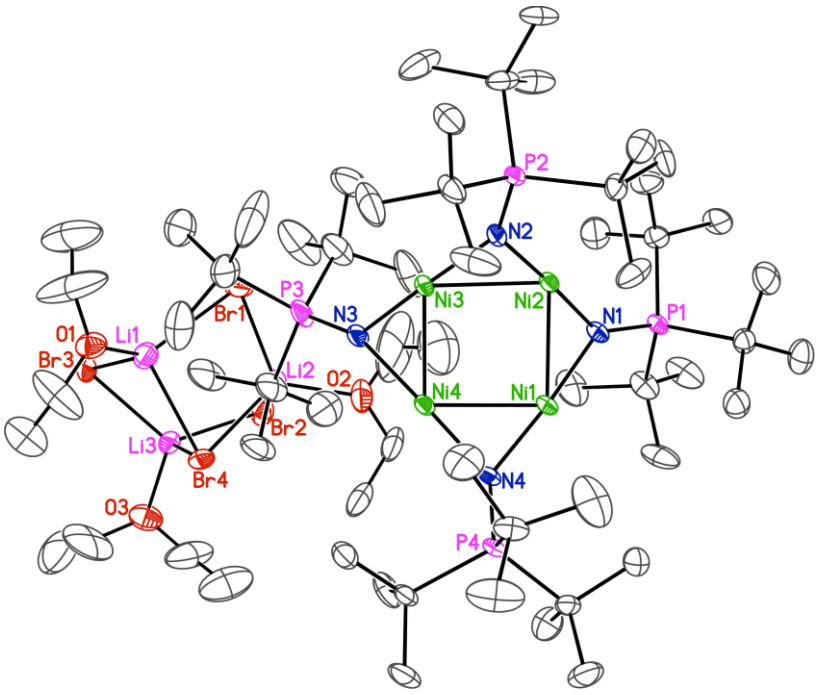

Figure **1.7**: ORTEP diagram of $[Ni_4(NP^tBu_3)_4][Li_3Br_4(Et_2O)_3]$ **26**, thermal ellipsoids are shown at 30 % probability. Hydrogen atoms have been omitted for clarity.

Based on the high-yield synthesis of $[Me_4Co_4(NPEt_3)_4]PF_6$ **22** by one-electron oxidation of neutral $[MeCoNPEt_3]_4$ **21**, accomplished by former group member Houston Brown,[60] we undertook a rational synthesis of the coplanar cation by one-electron oxidation of **18**, despite its variable purity. The oxidation is easily achieved by adding a slurry of 0.9 equivalent of Cp_2FeBPh_4 in THF to a stirred THF solution of **18** at room temperature (Eqn.

1.2). The reason for using only 0.9 equivalent of oxidant is for ease of purification. When less than one equivalent of oxidant is used, the unreacted starting material **9** could be easily extracted into pentane, together with the ferrocene. An immediate color change from green to blue was observed upon addition of the oxidant. Concentration and pentane extraction, followed by filtration removed the soluble residual starting material and ferrocene. After filtration, the remaining solid was extracted with THF; subsequence filtration and removal of the solvent gave $[Ni_4(NP^tBu_3)_4]BPh_4$ **23** as a blue powder in 83% yield. The use of Cp_2FePF_6 as an oxidant under the same conditions gave $[Ni_4(NP^tBu_3)_4]PF_6$ **30** in a slightly lower yield.

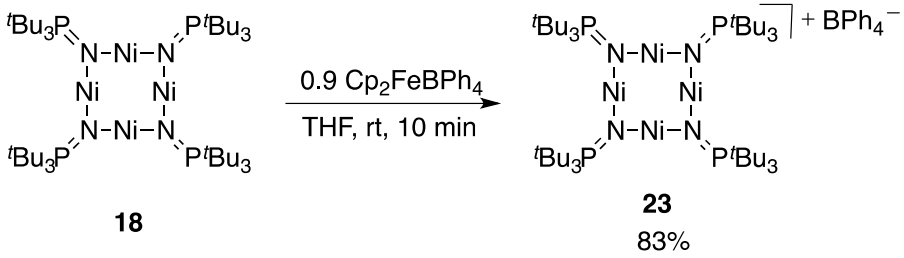

Equation **1.2**

1.3.1.2 X-ray crystallography of $[Ni_4(NP^tBu_3)_4]BPh_4$ 23 and $[Ni_4(NP^tBu_3)_4]PF_6$ 30

The cationic clusters $[Ni_4(NP^tBu_3)_4]BPh_4$ **23** and $[Ni_4(NP^tBu_3)_4]PF_6$ **30** are soluble in polar solvents such as THF and DME, but not soluble in nonpolar hexane, Et_2O and toluene. Single crystals were obtained by cooling the saturated THF solution of **23** in the -35 °C freezer in the glovebox. Crystal data collection and refinement parameters are provided in the appendix.

The average bond lengths and angles of all three cationic cluster and neutral cluster **18** crystals are listed in Table **1.1**. When comparing the data of the **23**, **30**, and **26** with **18**, it is apparent that the neutral $[Ni(NP^tBu_3)]_4$ **18** is more symmetric than the cationic compound. For example, in the neutral cluster the Ni-Ni distances are all 2.3749 Å while in the cationic cluster **23** the Ni–Ni distances vary between 2.370 Å and 2.420 Å. More

dramatic irregularity was observed in N-Ni-N bond angles: in the neutral cluster **18** all angles fall between 178.3° and 179.6°, while in the cationic cluster **23** the angles are 178.5°, 178.5°, 179.4° and 175.9°.

Table **1.1**: Selected average bond lengths and angles of **18**, **23**, **30**, and **26** (L= NP^tBu_3).

	$[NiL]_4$	$[Ni_4L_4]BPh_4$	$[Ni_4L_4]PF_6$	$[Ni_4L_4][Li_3Br_4(Et_2O)_3]$
Ni-N bond length (Å)	1.865(2)	1.840(2)	1.837(4)	1.843(3)
N-P bond length (Å)	1.566(2)	1.581(1)	1.584(7)	1.582(4)
Ni-Ni distance (Å)	2.3749(0)	2.3953(2)	2.3967(46)	2.4002(122)
Ni-N-Ni angle (°)	79.1(1)	81.2(6)	81.4(4)	81.3(6)
N-Ni-N angle (°)	178.8(3)	178.1(7)	177.6(9)	176.5(4)

As the counter ion was changed from $[Li_3Br_4(Et_2O)_3]^-$ to BPh_4^- to PF_6^-, the same irregularity in bond lengths and bond angles was also observed. Considering the large size of the clusters, crystal packing force alone could be the reason for the inconsistent bond lengths and angles.

From the bond length data, it is clear that upon oxidation the average Ni–N bond length was shortened, approximately by 22-28 pm. This is likely due to the reduced electron repulsion between nickel and nitrogen atoms when one electron is removed from the cluster. Meanwhile the average N–P bond length is 15-18 pm longer than the average length in neutral cluster, suggesting weaker N–P bond. Based on the crystal data the nitrogens in all clusters are between sp^2 and sp^3 hybridized, it is speculated that upon oxidation there is more *s* character and less *p* character in the Ni–N bonds and meanwhile more *p* character and less *s* character in the N–P bonds. This effect on Ni–N and N–P bond lengths is precedented in the case of oxidation of $[MeCoNPEt_3]_4$ **21** to $[Me_4Co_4(NPEt_3)_4]PF_6$ **22**,[60] however unlike the shortened Co–Co distances in **22** as mentioned earlier, the Ni–Ni distances in the tetrameric nickel cluster even increase by about 20 pm. The reason for this difference is the steric hindrance of the bulky $[NP^tBu_3^-]$

ligands. The space filling diagram of the neutral $[Ni(NP^tBu_3)]_4$ **18** shows the ^{t}Bu groups of the diagonal ligands lie very close in space with a distance of 2.464 Å between the closest hydrogen atoms (Fig. **1.8**). The hindrance between diagonal ligands keeps the cluster from contracting to the center. Instead, the average Ni-N-Ni angle in cationic cluster is approximately 2° more obtuse than in neutral cluster. Despite all the changes in bond lengths and angles, the average N-Ni-N angles is only slightly smaller than 180° and the nickel centers are still considered linearly two-coordinate.

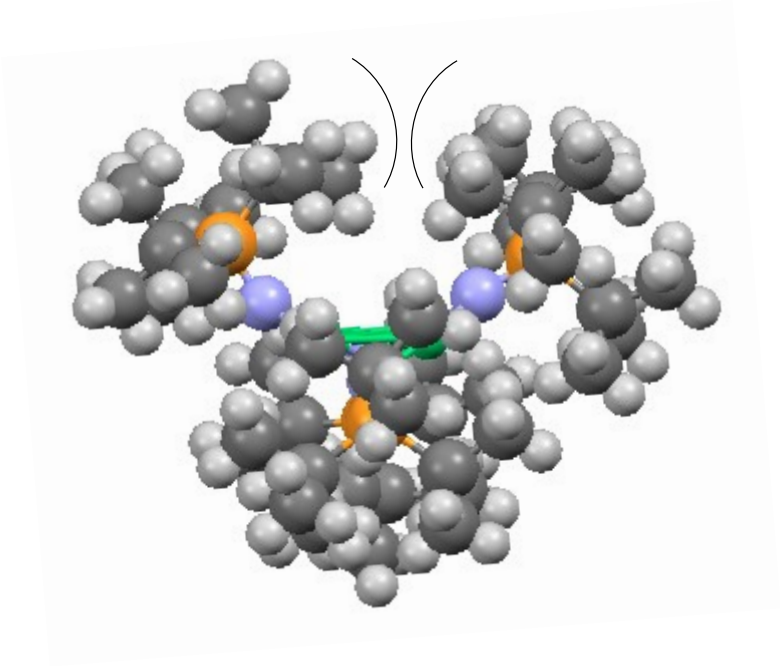

Figure **1.8**: Space filling diagram of **18**, thermal ellipsoids are shown at 30 % probability.

In the crystal structure, there is another asymmetry observed about bond angles. The angles between N-P bonds and Ni-N-Ni surfaces of a pair of diagonal ligands always fall into two categories, one of them is close to linear and the other is clearly bent (Fig. **1.9**). This asymmetry was observed in all three cationic and the neutral clusters. It is assumed that this angle irregularity is also likely the result of crystal packing force in the solid-state and should equilibrate in solution.

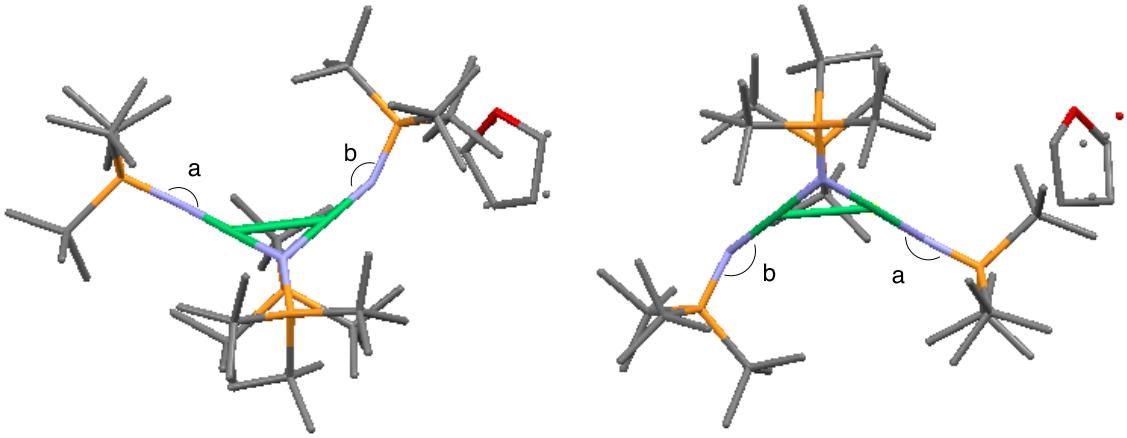

Figure **1.9**: Diagram of the unidentical angles between N–P bonds and Ni–N–Ni plane in neutral cluster **18**.

1.3.1.3 Infrared spectroscopy

Infrared spectra of both $[Ni_4(NP^tBu_3)_4]BPh_4$ **23** and $[Ni_4(NP^tBu_3)_4]PF_6$ **30** were obtained in the solid state. Solution infrared spectra were also obtained, but the main complex absorptions overlap with solvent absorptions. The P–N bond absorptions are listed below (Table **1.2**). These data are consistent with the data from X-ray crystallography. The P–N stretch for neutral cluster is 1072 cm^{-1} and the absorption for **23** and **30** are 1042 cm^{-1} and 1052 cm^{-1}, respectively, 30 cm^{-1} and 20 cm^{-1} lower than in the neutral cluster **18**, which confirms the weaker P–N bonds in the cation. The signal difference between cationic clusters with different counter ions was also about 10 cm^{-1} apart, suggesting the counter ions are not entirely independent in solid state.

Table **1.2**: P–N bonds absorptions in **18**, **23**, and **30** in solid state.

Nickel cluster	P-N bond stretch
$[Ni(NP^tBu_3)]_4$	1072 cm^{-1}
$[Ni_4(NP^tBu_3)_4]BPh_4$	1042 cm^{-1}
$[Ni_4(NP^tBu_3)_4]PF_6$	1052 cm^{-1}

1.3.1.4 Magnetic susceptibility

The magnetic measurement of the neutral cluster **18** by the Evans' method,[58] gave an effective magnetic moment of 4.40μ_B in solution at room temperature. This result suggests that there are approximately 4 unpaired electrons for the whole cluster at ground state. Using the same method, the cationic cluster **23** gives an effective magnetic moment of 5.59μ_B in THF at room temperature. This result suggests a total of 5 unpaired electrons per cluster, if the cation stays as a tetramer in THF solution. In addition, measurement of the temperature-dependent solid-state molar magnetic susceptibility of **23** has been completed by a collaborator, using the SQUID method. These results are consistent with the data from the Evans' method in solution (Fig. **1.10**).

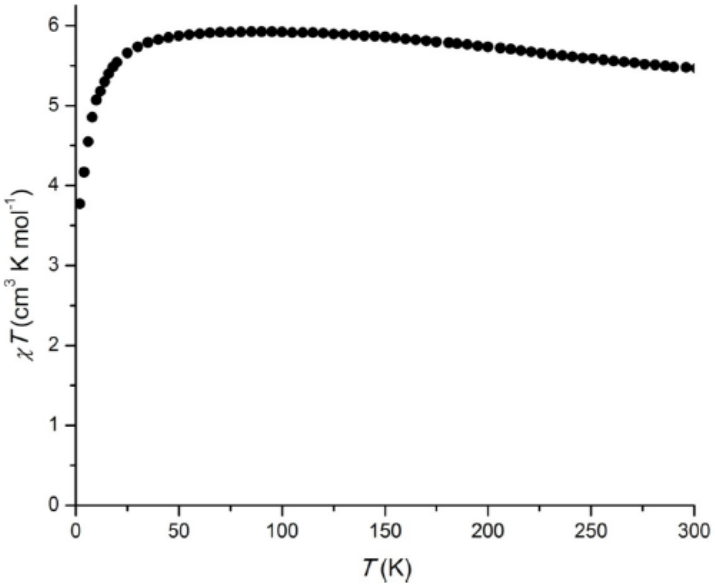

Figure **1.10**: Temperature-dependent solid-state molar magnetic susceptibility of **23** by SQUID.

These results are to some degree unexpected because based on the splitting pattern of d orbitals of linear two-coordinate metals, the single electron in the dz^2–orbital is the one that should be removed from one metal, (Fig. **1.11**) resulting in a cationic cluster bearing somewhere closer to 3 unpaired electrons. The rationalization for this experimental result is probably that the phosphoranimide ligand here behaves as a non-innocent ligand in the oxidation. Instead of the metal center, the oxidant abstracts an electron from the ligand,

likely from the nitrogen atom (or, equivalent, the N=P double bond). In other words, from the molecular orbital point of view, in the MO diagram of the cluster there is likely at least one orbital that is nearly degenerate with the four singly occupied metal-based molecular orbitals (SOMOs). This is likely to be a more nitrogen-based molecular orbital and the energy gap between this orbital and the SOMO is smaller or at least close to the pairing energy.

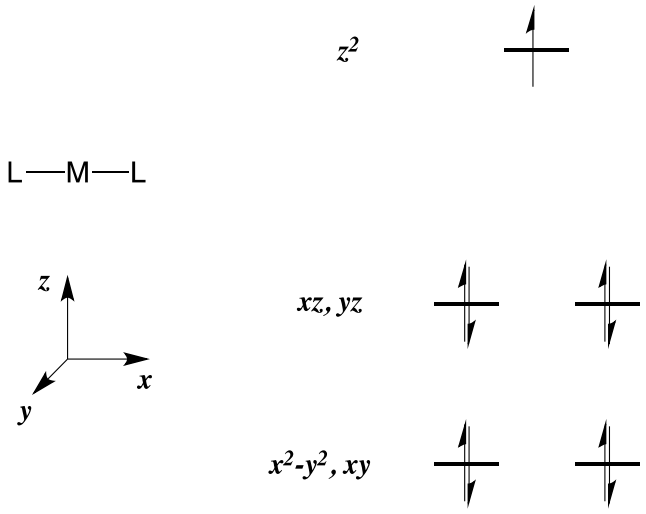

Figure **1.11**: Splitting pattern of d-orbitals for linear two-coordinate d^9 metals.

A detailed computational investigation is currently underway, again by collaborators. It is expected that results of the FMO computation will be helpful to understand the magnetic property and activity of the clusters.

1.3.1.5 Cyclic voltammetry

To study the redox behavior of the tetranickel cluster **18** and **23**, Cyclic voltammetry was carried out under one atmosphere of nitrogen or argon. The results were collected using WaveNow USB potentiostat in compact voltammetry cell (starter kit) of Pine Industry Instrumentation, using Aftermath operating software. Ceramic patterned Platinum electrodes were used as working and counter electrodes, and pseudo silver electrode was used as reference (for non-aqueous solutions). *n*-Bu_4NPF_6 was used as electrolyte with 0.1

mol/L concentration. The analyte solution is prepared in the glovebox by dissolving the analyte in *n*-Bu_4NPF_6 solution to make 0.01mol/L solution of analyte. THF was used as the solvent for all the CV. The general scan rate is 0.1V/s unless otherwise noticed. The Fc^+/Fc couple was used as the reference for all the CV.

The cationic cluster **23** rather than the neutral cluster **18** was used in these experiments, given the high purity and stability of the compound. The neutral cluster **18** decomposes slowly over a week in solution to give a precipitate that is not soluble in THF, even when stored in the -30°C freezer of the glovebox. This is likely due to the low-coordinate nature of Ni centers. The purity of the compound itself was also in question: the neutral cluster prepared by Dr. Jeffrey Camacho-Bunquin was, we believe, usually contaminated with some over-reduced component, which will be discussed later in this chapter. On the other hand, the cationic cluster $[Ni_4(NP^tBu_3)_4]BPh_4$ **23** is kinetically much more stable, both in solution and the solid state. There is no sign of decomposition after six months in solid state when stored properly in the glovebox. This has resulted in self-consistent and reproducible electrochemical measurements.

As described in the experimental section, the electrochemical cell of the CV instrument was set up in the glovebox, sealed, and then transferred out of the glovebox for the experiment. The Fc^+/Fc couple was used as internal reference in some cases. The results are shown below (Fig. **1.12**).

Two quasireversible one-electron reduction events were observed. The first reduction was attributed to the conversion of the monocationic cluster to the neutral cluster at a potential of $E_{1/2}$ = –0.613V. This is anticipated, since the neutral cluster **18** has been isolated and fully characterized. Furthermore, a second reductive event is observed at $E_{1/2}$ = –1.886V, which correlates with the reduction from the neutral cluster to monoanionic cluster $[Ni_4(NP^tBu_3)_4]^-$. Assuming that the anionic cluster remains a tetramer after the reduction, at least on the CV-timescale, the oxidation state of the cluster is mixed-valence 3Ni(I)/Ni(0). Based on the $E_{1/2}$ from CV, sodium amalgam should be a strong enough

reductant to reduce the neutral cluster,[65] however, this is not observed chemically, although this possibility was not investigated, at least carefully.

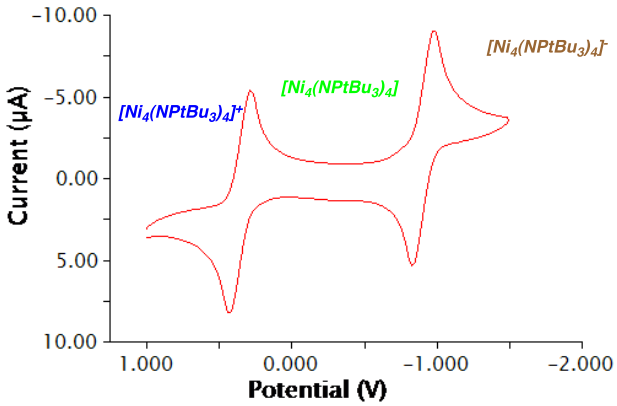

(a)

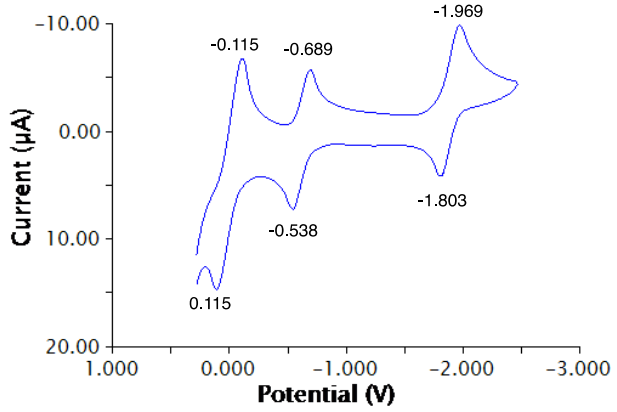

(b)

Figure **1.12**: CV of **23**. (a) CV without internal reference; (b) CV with Cp_2FePF_6 as internal reference.

The electrochemistry also confirmed that both redox reactions are one-electron events. The differences in peak potentials for each event are 0.151V and 0.165V, respectively, which is relative broadened from the ideal 0.059V difference for a reversible one-electron redox event. As a result, both events should be quasireversible. The wide peak differences are likely due to slow rate of electron transfer, resulting from the high activation barrier, but the effects of reversible cluster dissociation cannot be discounted.

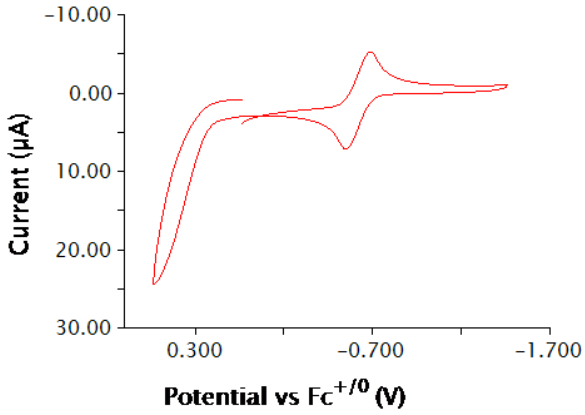

(a)

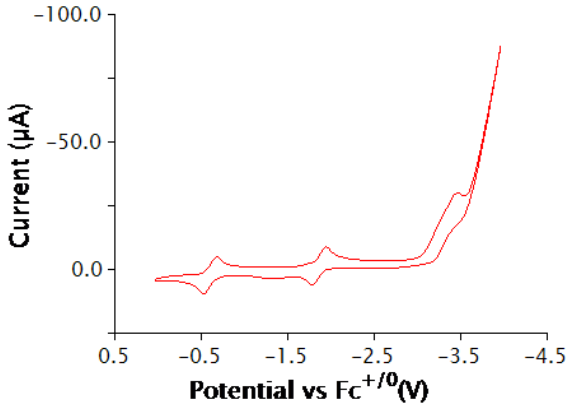

(b)

Figure **1.13**: CV of **23** under wider scan range: (a) 0.5V ~ –1.5V; (b) 0.2V ~ –4.0V.

Cyclic voltammetry covering a wider scan range suggested another irreversible redox events as shown below (Fig. **1.13**). When the potential rises to around +0.3V (relative to $Fc^{+/0}$), no further oxidation of the monocationic cluster is observed other than the oxidation of solvent. On the opposite direction, another irreversible reduction of the monoanion was observed around -3.3V, together with the reduction of THF under such highly reductive potential. This redox event is irreversible, implying the disassembling of the presumed dianionic cluster. The reduction is not chemically accessible due to the extremely strong reduction potential.

1.3.2 Synthesis and characterization of $Na[Ni_4(NP^tBu_3)_4]$ 31

The insight obtained from cyclic voltammetry suggests the possibility of clean one-electron chemical reduction of the neutral tetrameric cluster **18**. Based on the data, the reduction potential of the reducing agent has to be at least close to -2.2V, limiting us to alkali and alkali earth metals to achieve the reduction chemically.

1.3.2.1 Direct reduction of $[Ni(NP^tBu_3)]_4$ 18 with alkali and alkali earth metals

Attempted reductions of **18** with lithium metal (Eqn. **1.3**) and potassium graphite (KC_8) (Eqn. **1.4**) were unsuccessful in delivering a single product. When lithium wire was added to the solution of **18** in THF, the color of the solution changes gradually from green to brown. After stirring for one hour, the major product was brown and soluble in pentane, however there was always a variable amount of uncharacterized black precipitate as a byproduct.

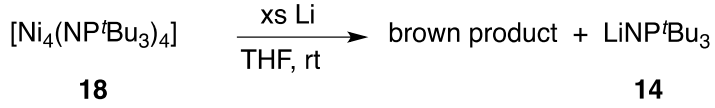

Equation **1.3**

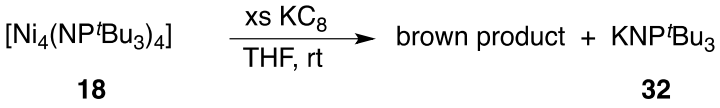

Equation **1.4**

When KC_8 was used as reductant, the color changed much faster, normally within one minutes. The major product was again brown and pentane soluble, but the amount of precipitate obtained could not be estimated due to the residual graphite in the reaction mixture. ^{31}P-NMR spectroscopy of each product showed the presence of the alkali metal salt of the ligand, $LiNP^tBu_3$ (31ppm)[36] or KNP^tBu_3 (16ppm).[66] This suggests a dissociative pathway for decomposition from the putative anionic cluster.

When sodium was used as reductant, more possibilities could be explored by using sodium amalgam consisting of various percentages of sodium (Scheme **1.4**). It is found that the concentration of sodium has a clear effect on the rate of this reaction. When liquid 0.9% Na/Hg was used, no color change was observed, and the starting material was recovered almost quantitatively after two days at room temperature. Increasing the sodium concentration to 2.4% led to a slow reduction of the neutral cluster **18**, reaching an end product in two days. When liquid 40% Na/Hg was used, the color of the solution changed to brown within 15 minutes. Similar to the reduction by Li and KC_8, ^{31}P-NMR spectroscopy detects the signal of the sodium salt of the ligand, $NaNP^tBu_3$, at 26 ppm, which was not quantified.

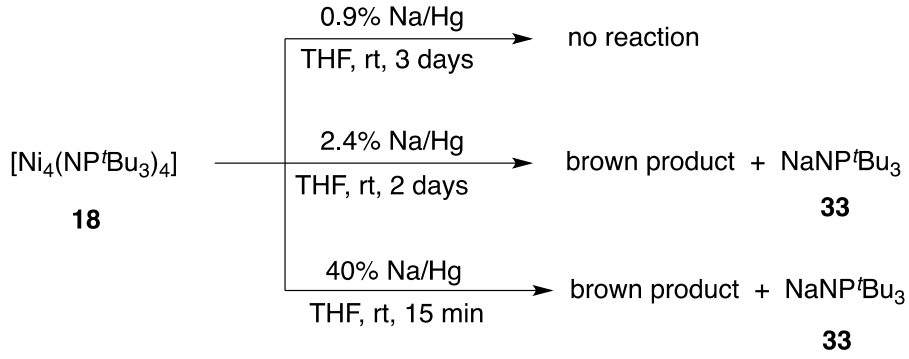

Scheme **1.4**: Reduction of **18** with sodium amalgam with different concentrations.

In all cases, recrystallization of the brown solid in the glovebox was attempted at low temperature using different solvents or solvents mixtures, including pentane, hexane, THF and DME. The only crystal that could be obtained was from the reduction using 40% Na/Hg. The crystal proved to be $NaNP^tBu_3$ **33** with a distorted heterocubane structure with sodium and nitrogen atoms occupying alternative corners of the cube. The crystal structure of $NaNP^tBu_3$ is similar to distorted cubic framework of $LiNP^tBu_3$, synthesized by the Stephan et al.[36] Details of this crystal structure are provided in the appendix.

In addition to the alkali metals, Mg powder could in principle achieve the reduction of the neutral cluster **18** (Eqn. **1.5**). However, with this reductant, transmetallation of the ligand prevailed instead. The solution became colorless upon stirring and a white product was collected and confirmed to be $[Mg(NP^tBu_3)_2]_2$ by ^{31}P-NMR spectroscopy, as previously reported by Stephan, et al.[46] Furthermore, Cp^*_2Co was also evaluated as a soluble one-electron reductant, but provided no conversion. (Eqn. **1.6**)

$$[Ni_4(NP^tBu_3)_4] \xrightarrow[THF,\ rt]{ex\ Mg} [Mg(NP^tBu_3)_2]_2$$

Equation **1.5**

$$[Ni_4(NP^tBu_3)_4] \xrightarrow[THF,\ rt]{Cp^*_2Co} \text{no reaction}$$

Equation **1.6**

1.3.2.2 Overreduction of $[Ni(NP^tBu_3)]_4$ 18

Although the direct reduction of the tetrameric nickel cluster was not successful, another group member, Orain Brown, easily accomplished the alkali metal reduction of the Cu(I) analog of the neutral cluster **18** (Scheme **1.5**).

Surprisingly, instead of the monoanionic cluster, only the dianionic cluster, $Li_2[Cu_4(NP^tBu_3)_4]$ **35**, was obtained via a one pot synthesis from the lithiated ligand. Further exploration revealed an intriguing role of lithium cation in this unexpectedly facile two-electron reduction. A dianionic cluster could only be obtained when Li^+ was present in solution. If KNP^tBu_3 **32** was used in the synthesis, the neutral cluster $[Cu(NP^tBu_3)]_4$ **36** was obtained quantitatively instead, even in the presence of excess reductant.

Cyclic voltammetry of the **36** also supports this result (Figure **1.14**): When Li^+ was absent in the solution, no reduction event was observed even under strongly reductive conditions, –2.30V, referenced to $Fc^{+/0}$. When 20 equivalents of $LiBF_4$ were added to the THF solution, two reductive events were observed. The shape of the CV curve changed at slower scan

rates, suggesting that some chemical transformation was triggered after the first reduction. It is clear that the Li^+ cation plays an essential role in modulating the redox behavior of $[Cu(NP^tBu_3)]_4$ **36**.

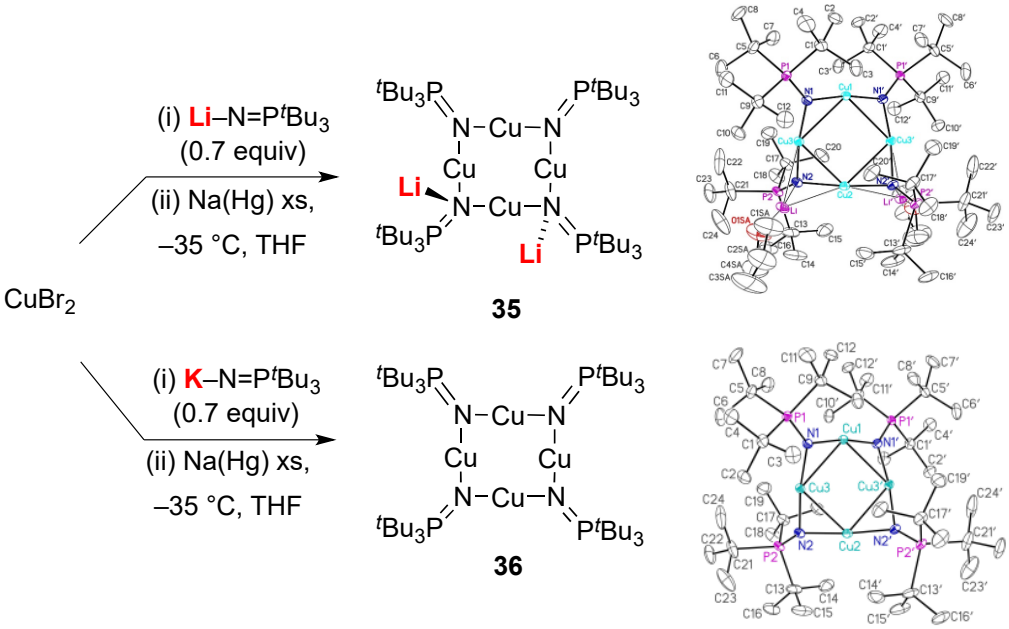

Scheme **1.5**: Syntheses and ORTEP diagrams of $Li_2[Cu_4(NP^tBu_3)_4]$ **35** and $[Cu(NP^tBu_3)]_4$ **36**.

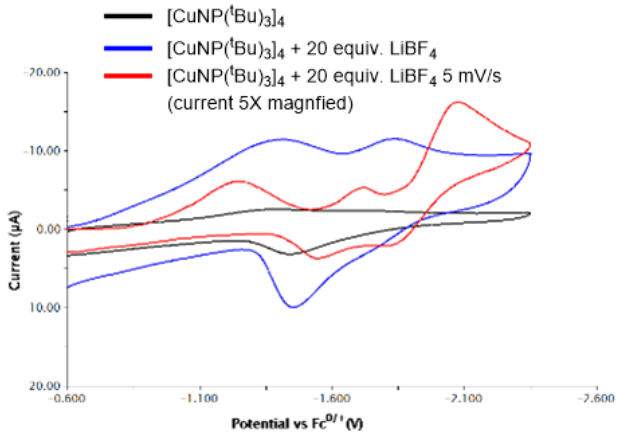

Figure **1.14**: Cyclic voltammetry of **36**, with and without Li^+ cation.

Further computational study is ongoing, and is essential to provide more insight into the unique role of the main group counter ion in this process. The details of the copper chemistry will not be discussed in this thesis.

In combination with the decomposition observed during the chemical reduction of neutral cluster **18**, we suggest that the alkali metals were not innocent outer-sphere reductants in the reaction. To further investigate the role of alkali metal cations in controlling this reduction, cyclic voltammetry of **23** in the presence of various alkali metal cations was explored.

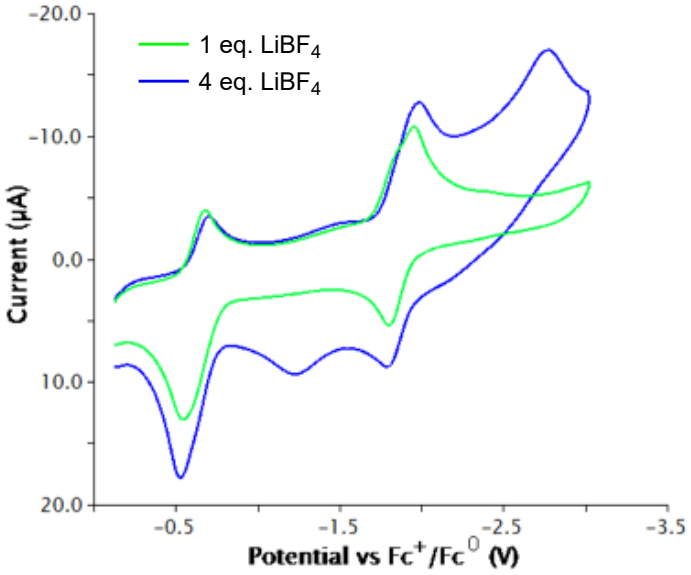

Figure **1.15**: Cyclic voltammetry of **23** with 1 equivalent (green) or 4 equivalents (blue) of $LiBF_4$ in THF, scan rate = 100 mV/s.

Initially, the cyclic voltammetry in the presence of soluble Li^+ was tested. One equivalent of $LiBF_4$ was added to the solution of cationic **23** and electrolyte (Fig. **1.15**). No significant change in the CV spectrum was observed, compared to the trace obtained in the absence of Li^+. The reduction potential of both one-electron events are the same as before and no other reductive event was observed. Interestingly, when four equivalents of $LiBF_4$ were added to the solution, another reductive event was observed after the second reductive event, around -2.771V. The oxidative counterpart of the event showed itself at -1.230V,

suggesting that this event is irreversible, and likely leads to cluster reorganization and/or decomposition.

This overreduction was only observed in the presence of 4 equivalents of Li^+. We propose that the timescale for the CV is relatively short compared to the rate of the Li^+ coordination to the already anionic cluster, thus requiring an excess to be competitive. The CV of $LiBF_4$ itself shows no such reduction peak. In summary, similar to the case of $[Cu(NP^tBu_3)]_4$ **36**, overreduction of the cluster was observed in the presence of Li^+. However, this overreduction leads to decomposition of the cluster, in contrast to the isolable $Li_2[Cu(NP^tBu_3)]_4$ **35**.

For comparison, CV spectra of **23** in the presence of various amounts of Na^+ were also obtained. In Figure **1.16** (a), the CVs of both $NaBPh_4$ and **23** are shown on the same plot. The background voltammagram of $NaBPh_4$ was not entirely flat, showing a broad signal around -2.3V. The CV of **23** in the presence of Na^+ is shown below (Fig. **1.16** (b)), from which we can conclude that the traces were basically the superimposition of the reductions shown in Fig. **1.18** (a). In contrast to the case of Li^+, no further reduction event was observed, at least at CV-timescale. As noted earlier, liberated $NaNP^tBu_3$ **33** was observed when trying to reduce the neutral cluster **18** with Na/Hg. Based on the electrochemistry, we can conclude that the decomposition is less the result of overreduction but the kinetic instability of the anionic cluster itself. There is also a chance that the overreduction in the presence of Na^+ is simply much slower than the case of Li^+, so it was not observed in the CV spectra.

The CV in the presence of K^+ was also investigated. The results were similar to the case of sodium cation. The CV obtained was the overlap of cationic cluster **23** and $KBPh_4$ (Fig. **1.17**). No further redox event was observed in the presence of potassium cation.

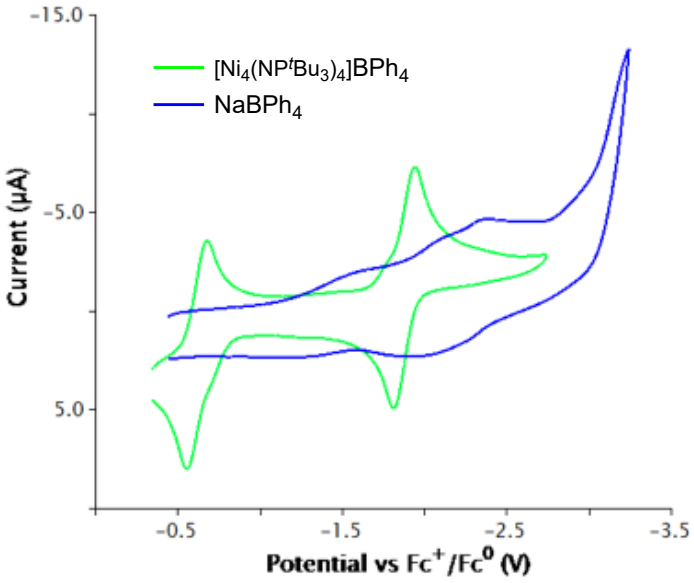

(a)

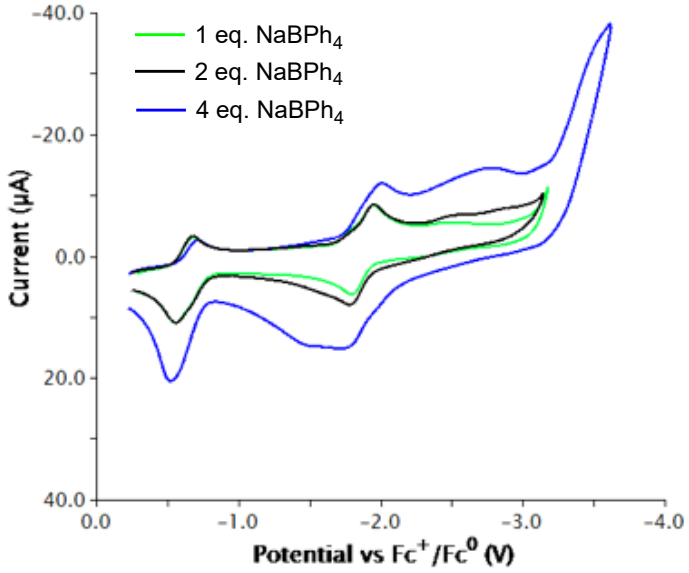

(b)

Figure **1.16**: (a) CV of **23** (green) and $NaBPh_4$ (blue)in THF; (b) CV of **23** with 1 equivalent (green), 2 equivalents (black), and 4 equivalents (blue) of $NaBPh_4$ in THF, scan rate = 100 mV/s.

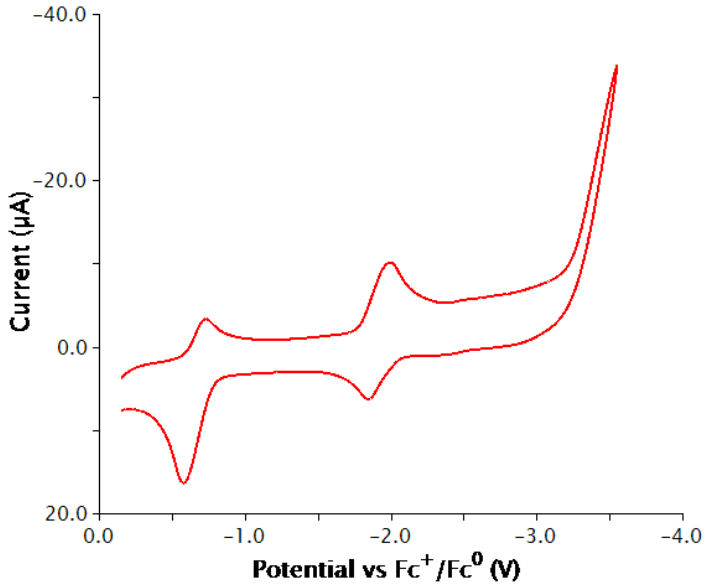

Figure **1.17**: CV of **23** with 4 equivalents of $KBPh_4$ in THF, scan rate = 100 mV/s.

1.3.2.3 Attempt to reduce $[Ni(NP^tBu_3)]_4$ 18 without overreduction

Based on the cyclic voltammetry, overreduction by alkali metals probably arises from additional reduction beyond the monoanionic cluster, triggering anionic ligand dissociation and reorganization/decomposition of the cluster. To avoid such overreduction several methods were evaluated. First, use of a stoichiometric amount of the reductant was posited. Considering the high molecular weight of the neutral cluster **18**, sodium and lithium anthracenides[67] and sodium naphthalenide[68] were prepared in THF and used as a solution, aiming to provide accurate stoichiometry of reductant. The radical anions are in principle strong reductants and presumed to reduce the neutral cluster **18** to the anionic cluster. However, this approach does not lead to substantial reduction of **18** (Eqn. **1.7**).

$$[Ni(NP^tBu_3)]_4 \quad (\mathbf{18}) \quad + \quad \begin{matrix} Na[C_{14}H_{10}] \\ \text{or} \\ Li[C_{14}H_{10}] \\ \text{or} \\ Na[C_{10}H_8] \end{matrix} \quad \xrightarrow[\text{THF, rt}]{} \quad \text{no reaction}$$

Equation **1.7**

Various crown ethers were also used as additives in the reduction, aiming to isolate the metal cation from direct interaction with the reduced cluster. We proposed that if the alkali cation does not coordinate to the reduced metal cluster, the overreduction might be prevented and the monoanionic cluster could be isolated, as observed in the initial cyclic voltammetry. Unfortunately, when crown ether was present, a great number of byproducts of various solubilities were observed for each pair of alkali metal and crown ether used. When Li^0 and 12-crown-4 were used, a minor THF-soluble product was isolated in a low yield. This product is brown and paramagnetic, but attempts to grown single crystals by slow evaporation, vapor diffusion, or liquid layer diffusion all ended up in failure (Eqn. **1.8**).

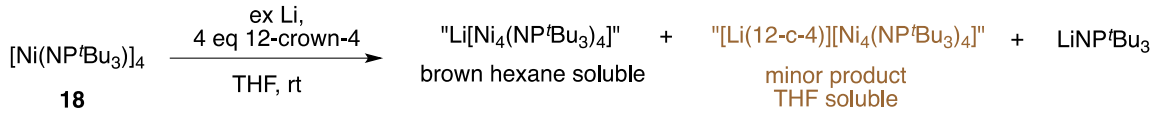

Equaiton **1.8**

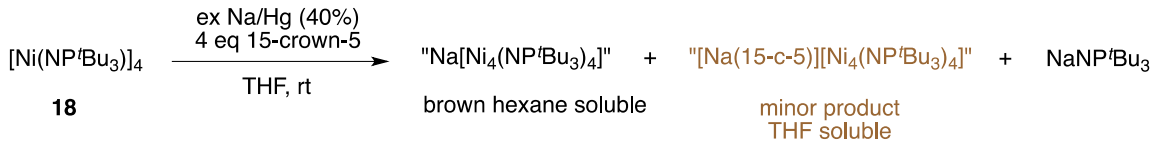

Equation **1.9**

Similar results were obtained when the combinations of Na/Hg and15-crown-5 was used (Eqn. **1.9**). Recrystallization did not provide any transition metal clusters. Occasionally, single crystals of the neutral starting material **18** were obtained from the recrystallization, implying the instability of the anionic cluster.

Eventually, when KC_8 and 18-crown-6 were used for the reduction, single crystals of one of the products were grown and partially characterized by X-ray diffraction (Eqn. **1.10**). The quality of the crystal was not adequate for full structural characterization because the two atoms coordinating to K^+ and Ni could not be identified. Based on the reaction conditions, dinitrogen was the most likely assumption, and the structure could be proposed

as [K(18-crown-6)][(κ-N_2)Ni(NP^{t}Bu$_3$)] **39** (Fig. **1.18**). The formal oxidation state of the nickel in this material is 0. This result suggests that the monoanionic nickel cluster is not kinetically stabilized by adding crown ether, but rather destabilized. The dinitrogen adduct of Ni(0) and K^+ is precedented,[69] but the linear bonding mode is unknown. However, this structure is not interpreted here due to the uncertainty of the assignment of nitrogen atoms.

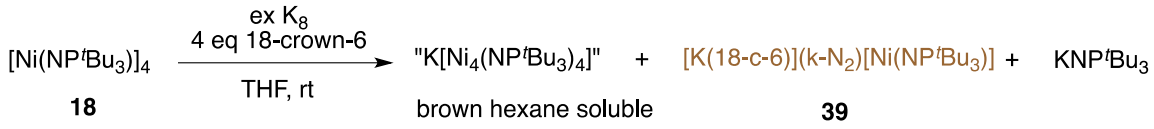

Equation **1.10**

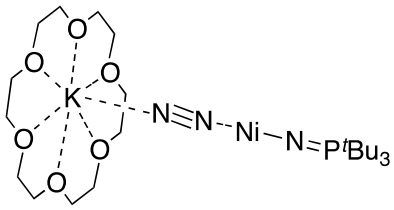

Figure **1.18**: Proposed structure of [K(18-crown-6)][(κ-N_2)Ni(NP^{t}Bu$_3$)] **39**.

Based on these results, the reduction of the neutral cluster was repeated under an argon atmosphere, either on an argon Schlenk line or in an argon-filled glovebox. However, the results were similar: no single crystals of monoanionic cluster or any other product could be obtained.

Aside from the strategies above, ion exchange was also used in another attempt to isolate a stable anionic tetramer. The neutral cluster was first reduced with 40% Na/Hg, and the solvent removed after a short reaction time (15 min). Upon extraction with pentane, a brown solution was obtained, to which anhydrous ^{n}Bu$_4$NBr was then added with the anticipation that KBr might precipitate out of the solution. Unfortunately, multiple paramagnetic products were isolated and no single crystals could be grown to characterize any of them (Eqn. **1.11**).

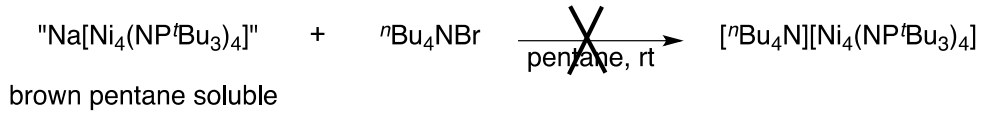

Equation **1.11**

1.3.2.4 Synthesis of $Na[Ni_4(NP^tBu_3)_4]$: a consistent procedure

Because the isolation of pure monoanionic cluster $Na[Ni_4(NP^tBu_3)_4]$ **31** was unsuccessful, it became crucial to develop a consistent, reproducible preparation for use of this compound for further exploration of its activity. The priority was to determine whether the anionic cluster is monoanionic or dianionic; either was possible and both may be present; meanwhile, rearrangement to other oligomers remains a reasonable possibility.

To confirm the molecular formula of the anionic cluster, a redox conproportionation reaction was carried out to determine the purity of the crude reduction product. An excess of 40% Na/Hg was added to the THF solution of neutral cluster **18** and the reaction mixture was stirred for 15 minutes. The solution was decanted from unreacted sodium amalgam and mixed with a nominally equimolar amount of the cationic cluster **23**. The near quantitative yield of pure, neutral tetramer **18** obtained from this experiment establishes that the brown product is the monoanionic cluster $Na[Ni_4(NP^tBu_3)_4]$ **31** (Eqn. **1.12**).

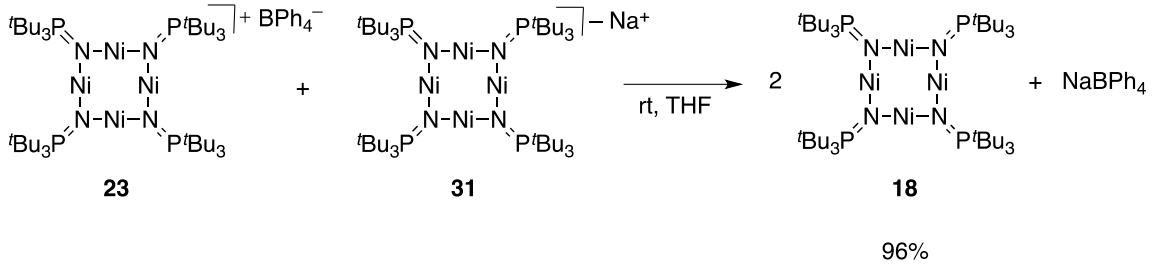

Equation **1.12**

Since quantitative synthesis and storage of the monoanionic cluster **31** is impossible, a repeatable, consistent preparation at a reasonable scale is necessary for further exploration of catalytic activity as a function of cluster charge. To fulfill this task, UV-Vis spectroscopy

was used to monitor the reduction reaction. The UV-Vis absorption spectra of the three clusters (**18**, **23**, and **31**) in THF are distinctly different, as shown (Fig. **1.19**). The reduction of **18** to **31** takes only about 10 minutes to proceed to completion upon addition of excess 40% Na/Hg. The UV spectrum of the solution did not change after ten minutes and no precipitate was formed within half one hour. Thus, for further exploration, the anionic cluster **31** would be prepared by stirring a solution of **18** with excess 40% sodium amalgam (one drop for reactions under 100 mg) for 15 minutes, filtered, and used immediately.

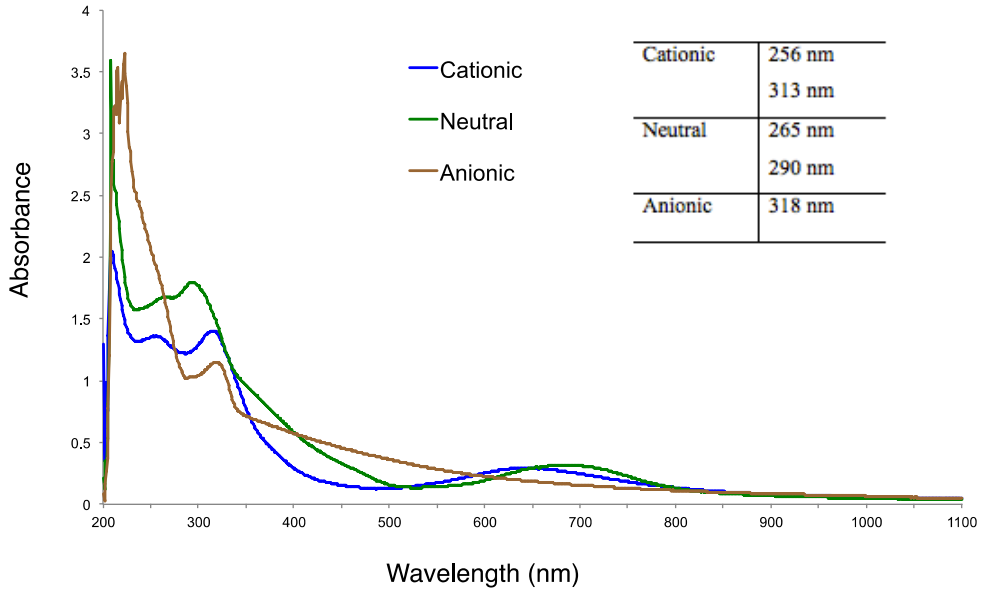

Cationic	256 nm 313 nm
Neutral	265 nm 290 nm
Anionic	318 nm

Figure **1.19**: UV-Vis spectra of **18**, **23**, and **31** in THF.

To conclude, the interconversions of the three isostructural tetrameric nickel clusters by redox chemistry are summarized in Figure **1.20**. The synthesis of cationic cluster **23** was conveniently done on multigram scale and the cluster can be stored in the glovebox for a long period. Both the neutral **18** and anionic clusters **31** were prepared *in situ* from this precursor as needed.

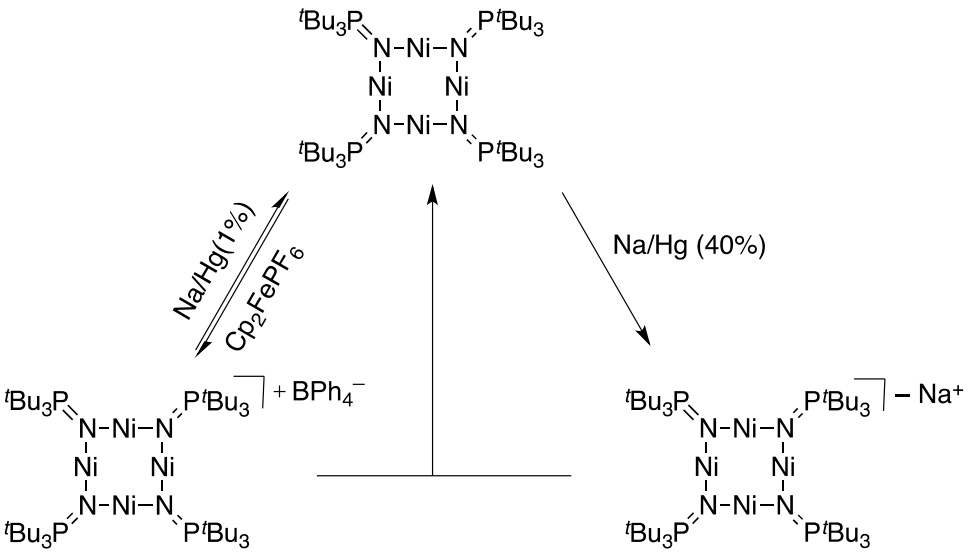

Figure **1.20**: Summary of transformations among **18**, **23**, and **31**.

1.3.3 Synthesis and characterization of $[Co_2(\mu\text{-}NP^tBu_3)_2(NP^tBu_3)_2]PF_6$ 37

The tetracobalt cluster, $[Co(NP^tBu_3)]_4$ **19,** has a very similar structure to **18**. In both clusters, each ligand bridges to two metal centers through the electron-rich nitrogen atoms, and each metal is divalent, and linearly two-coordinate. The four metal atoms in each cluster are coplanar, while the diagonal ligands point toward the same direction of the square plane. The principal difference between the two clusters is that in crystals of **19**, the cobalt atoms are partially substituted by a varying percentage of Na^+ cation. This substitution could affect the redox chemistry dramatically, something we felt was imperative to investigate.

1.3.3.1 Synthesis of $[Co_2(\mu\text{-}NP^tBu_3)_2(NP^tBu_3)_2]PF_6$ 37

The one-electron oxidation of **19** was carried out under the same conditions as for **18**. The reaction, unexpectedly, gave multiple products with different solubilities. With an increasing amount of Cp_2FePF_6, a greater fraction of THF-soluble product was obtained. Eventually upon addition of eight equivalents of the oxidant, the reaction proceeded to completion, giving a brown, THF-soluble product in good yield (Eqn. **1.13**). Single crystals

of the product were grown by slowly cooling a saturated THF solution to -30°C in the glovebox freezer. X-ray diffraction revealed the structure to be $[Co_2(\mu\text{-}NP^tBu_3)_2(NP^tBu_3)_2]PF_6$ **37** (Fig. **1.21**). The fate of the missing cobalt and sodium atoms and the reasons for requiring excess oxidant are not known yet.

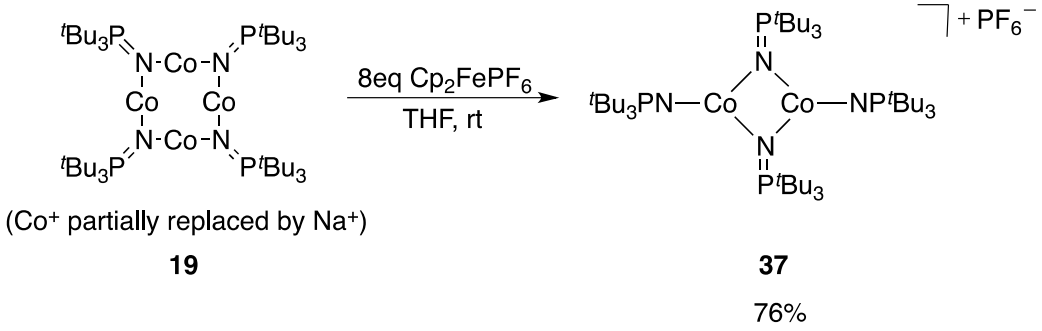

Equation **1.13**

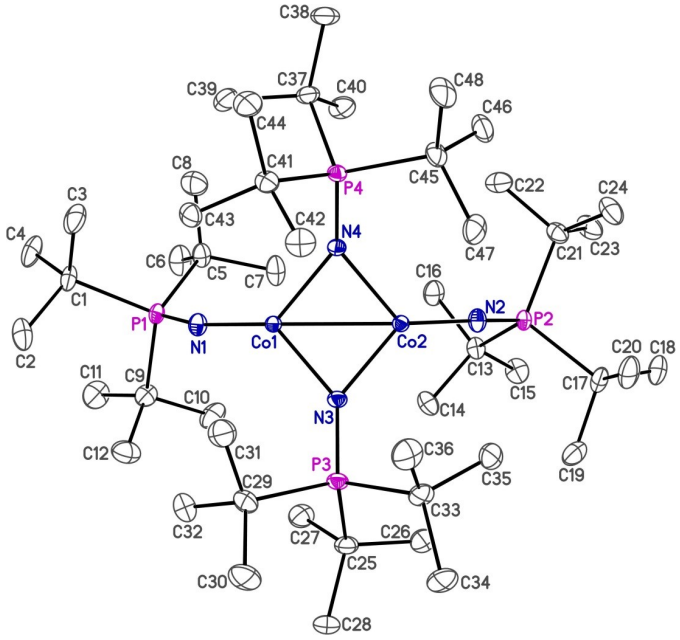

Figure **1.21**: ORTEP diagram of cationic **37**, thermal ellipsoids are shown at 30 % probability. Counter ion and hydrogen atoms have been omitted for clarity.

In the crystal structure of **37**, two cobalt atoms are bridged by two μ^2-phosphoranimide ligands, forming a four-membered ring. Additional phosphoranimide ligand coordinates

terminally to each cobalt metal. The cationic bimetallic cluster **37** can be seen as the one-electron oxidation product of the neutral dimetallic compound, $Co_2(\mu\text{-}NP^tBu_3)_2(NP^tBu_3)_2$ **38**, which was previously synthesized and characterized by Dominique Hebert in the Stryker group.

We believe that the instability of the anticipated cationic mixed-valence cluster is at least partly because of the substantial replacement of Na^+ in the neutral cluster **19**. In the case of nickel analog **18**, when the cluster is oxidized the positive charge delocalizes to all four metals to form a type III mixed-valence Ni(II)/3Ni(I) cluster. In the case of **19** some of the Co^+ is displaced by Na^+, which disrupts the symmetry and delocalization of the positive charge. As a result, the four cobalt atoms in the square are no longer identical, leading to the reorganization of the cluster. At that stage, further oxidation might become possible and the product **37** is likely the highest oxidation state that could be achieved by Cp_2FePF_6.

This could be clarified if the pure, sodium-free cluster could be synthesized by an alternative route, which is currently under study by another group member. Computational investigation of redox and magnetic phenomenon is also ongoing.

1.3.3.2 X-ray crystallography of $[Co_2(\mu\text{-}NP^tBu_3)_2(NP^tBu_3)_2]PF_6$ 37

A single crystal of the **37** was analyzed by X-ray crystallography. Crystal, data collection, and refinement parameters are provided as an appendix. In these data, a pattern of bond irregularity was found, so average data are used unless otherwise noted. In the solid-state structure (Fig. **1.22**), it is clear that the nitrogen atoms of the bridging phosphoranimide ligands are nearly sp^2-hybridized. The four Co-N(bridging) bond lengths are found in a narrow range between 1.9318(12) Å to 1.9415(12) Å, which suggests the bonding mode for the bridging phosphoranimide is best described by mode D, as shown below. In contrast, the average Co-N(terminal) bond distance is 1.7827(12) Å, much shorter than in the bridging ligands, indicating a higher Co–N(terminal) bond orders. The average Co-N(terminal)-P angle is 159.9°, which is typical for terminal bondding mode B when combined with high electronic unsaturation at the metal. The bridging phosphoranimide

ligand is considered to be a 6e$^-$ donor and the terminal phosphoranimide is considered to be a 4e$^-$ donor. As a result, electron counting ends up suggesting valence occupancy of 15 and 16 electrons for the two cobalt atoms, respectively.

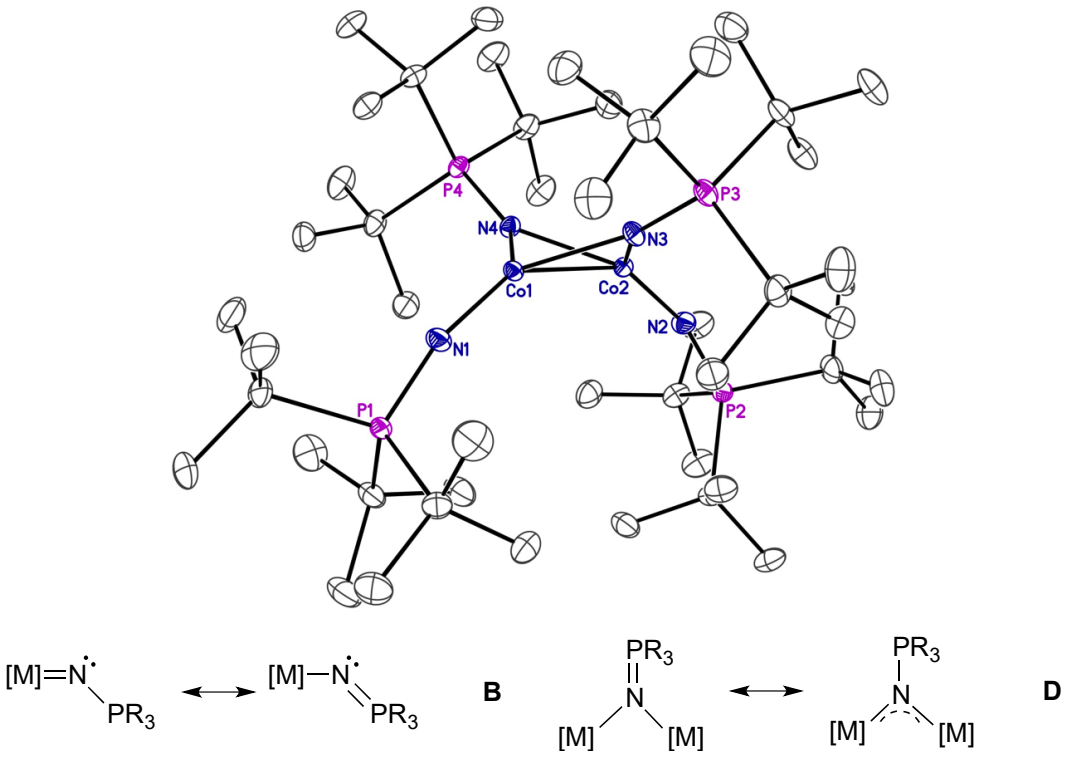

Figure **1.22**: ORTEP structure and bonding modes for **37**, the counteranion has been omitted for clarity.

A comparison of the cationic **37** with the neutral **38** provides some insight into the effects of oxidation. The Co-N(bridging) distances in the cation shorten from an average of 1.9763(12) Å in **38** to 1.935(12) Å in **37**; meanwhile the Co-N(terminal) distances shorten from an average of 1.8149(12) Å to 1.7827(12) Å. Significant Co–N contraction is anticipated, as a result of reduced electron repulsion and delocalization upon one-electron oxidation. Not surprisingly, as the M-N bonds become shorter, the N-P bonds elongate, lengthering from 1.5730(12) Å to 1.6032(12) Å for the bridging phosphoranimide and from 1.5458(12) Å to 1.5784(12) Å for the terminal phosphoranimide. The lengthening results from of the stronger Co–N bonds, as the Co–N bonds increase in *s* character, the N-P bonds

assume more *p* character in the hybridization. The same trend is also observed upon oxidation of nickel cluster **18**.

The core Co_2N_2 unit adopts a butterfly shape in both cationic **37** and neutral **38**. Upon oxidation, the N-N distance remains the same as 2.8022(12) Å, but the Co-Co distances decreases from 2.5088(12) Å to 2.3851(12) Å. The average Co-N(bridging)-Co angle contracts from 78.84(8)° to 76.00(8)°, as the average N(bridging)-Co-N(bridging) angle opens from 90.31(8)° to 92.64(8)°. The torsion angles of Co-N-N-Co stays almost identical, 133.19(12)° versus 133.20(12)°.

In summary, although the core Co_2N_2 contracts, by shortening the Co-N(bridging) and Co-Co distances, the Co-N-N-Co dihedral angles remain identical. No reaction chemistry of or catalysis using **37** has been explored because this cluster and corresponding neutral dimer **38** remain under investigation by other members in the group.

1.4 Conclusion

In this chapter, the synthesis, physical characterization and redox chemistry of the both homoleptic phosphoranimide-bridging clusters **18** and **19** have been explored. For the nickel analog, the oxidation products $[Ni_4(NP^tBu_3)_4]BPh_4$ **23** and $[Ni_4(NP^tBu_3)_4]PF_6$ **30** have been prepared and fully characterized. Upon oxidation, the shape of the cluster does not change much, presumably a consequence of the steric demand of the $[NP^tBu_3^-]$ ligand, even stronger Ni-N bonds and weaker N-P bonds were observed. Both **23** and **30** are type III mixed-valence clusters.

The monoanionic reduction product $Na[Ni_4(NP^tBu_3)_4]$ **31** has been prepared in reasonably pure form and identified, but the cluster could not be fully characterized. Attempts to grow single crystals failed due to the kinetic instability of the cluster. However, a consistent *in situ* preparation of relatively pure **21** has been developed for further synthetic and catalysis exploration.

On the other hand, one-electron oxidation of $[Co(NP^tBu_3)]_4$ **19** results in the formation of the dimetallic mix-valence cluster $[Co_2(NP^tBu_3)_4]PF_6$ **37**, which is probably the result of Na^+ replacement in the nominally neutral cluster **19**. Synthesis and characterization of pure **19** remains an ongoing challenge by other members of the group.

Chapter 2. Phosphoranimide-bridged Nickel Catalysts for Hydrogenation of Alkenes and Alkynes

2.1 Introduction

The phosphoranimide-supported late first-row transition metal clusters were originally proposed for catalytic hydrotreatment in petroleum upgrading processes, such as hydrodesulfurization (HDS) and hydrodenitrogenation (HDN). In addition to that, a range of activities were also explored, due to the low-coordinate and low-valence character of the cluster, including hydrogenation of alkyne and alkene. Based on preliminary results obtained by Dr. Jeffrey Camacho-Bunquin,[45,70] the neutral cluster **18** was an effective precatalyst for hydrogenation of alkynes and alkenes. However, later group members found the hydrogenation results irreproducible, depending on different batches of the catalyst.[71] Even more confusing was that extremely low conversion was generally observed when the purest-looking single crystals were used in the reaction. These results led to our assumption that the catalyst previously investigated had been contaminated, and quite possibly, the contaminant was most active in the catalysis. Now, since the cationic cluster **23** and anionic clusters **31** have been prepared and characterized, it became imperative to investigate the hydrogenation activity for all three clusters (Fig. **2.1**).

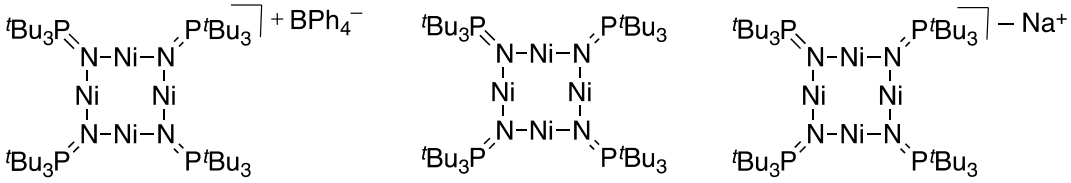

Figure **2.1**: Structures of **23**, **18**, and **31**.

In this chapter, the irreproducibility of hydrogenation of diphenyl acetylene will be discussed first, followed by the hydrogenation investigation of **23**, **18**, and **31**.

2.2 Results and discussion

2.2.1 Reproducibility issues with [Ni(NP^{t}Bu$_3$)]$_4$ 18

As discussed in the first chapter, Dr. Jeffrey Camacho-Bunquin reported the synthesis of neutral cluster **18** together with some preliminary hydrogenation results, as shown below (Fig. **2.2**).[45] In these results, the hydrogenation of both allylbenzene **40** and diphenylacetylene **20** proceeded to completion in quantitative yield at room temperature. However, these results were found to be irreproducible. Especially in the case of **20**, conversions lower than 5% were often observed. The hydrogenation of **40** was less problematic, as the average yield was above 95% across several catalyst batches. It was even more intriguing that the lowest yields were obtained when the reactions were run more carefully and when the purest single crystals were used.

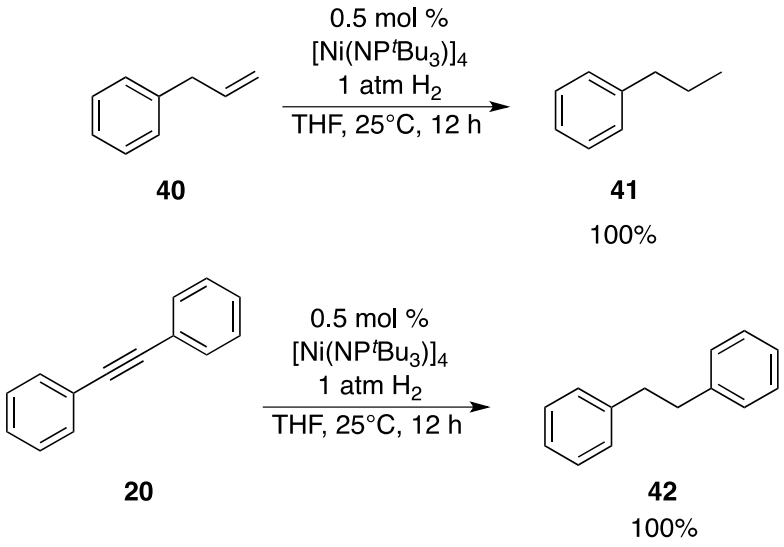

Figure **2.2**: Hydrogenation of allylbenzene **40** and diphenylacetylene **20** using **18**.

Based on these observations, we proposed that the precatalyst used by Dr. Jeffrey Camacho-Bunquin was likely impure, contaminated by variable amount of the actual catalyst. Thus, the neutral cluster **18** is possibly not an active hydrogenation precatalyst.

To determine the actual catalyst in the reaction, it is instructive here to reevaluate the preparation of the catalyst in the first place.

In the old procedure, $NiBr_2$•DME **43** was used in excess to prevent the formation of [Ni(μ-NP^tBu_3)(NP^tBu_3)]$_2$ **44**. Excess 1% Na/Hg was used to reduce the putative dimeric intermediate [NiBr(NP^tBu_3)]$_2$ **45** to the neutral cluster **18**; meanwhile the excess $NiBr_2$ would presumably be reduced to nickel metal (Eqn. **2.1**). Later, Dr. Jeffrey Camacho-Bunquin adapted this procedure to a newer version by replacing the 1% Na/Hg with 2.4% Na/Hg. The reason for the change was that the 2.4% amalgam is a solid, making it easier to handle in the glovebox and reducing the amount of Hg used.

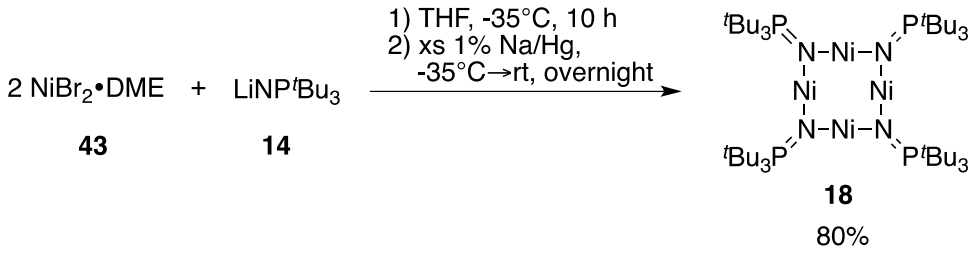

Equation **2.1**

As described in Chapter 1, neutral cluster **18** could be reduced by 2.4% Na/Hg to give the anionic cluster Na[$Ni_4(NP^tBu_3)_4$] **31**. The reaction was relatively slow, taking 2 days to observe the color change from green to brown. Consequently, we proposed that it was very likely that some amount of the anionic cluster **31** contaminated the neutral cluster, and **31** might be the actual precatalyst for hydrogenation. To confirm this assumption, we have now investigated the hydrogenation activity of both **18** and **31**, separately, in reasonable pure form.

2.2.2 Hydrogenation of alkenes and alkynes with [Ni(NP^tBu_3)]$_4$ 18

Catalyst purity is essential to obtain accurate and reproducible results. Since the neutral cluster **18** is not kinetically stable to storage over a week, the catalysts used here were prepared *in situ* by reduction of cationic **23** by 1% Na/Hg, which does not overreduce the

18. The hydrogenation reactions were set up in middle-walled glass reactors in the glove box with a 1 mol% loading of **18**. The reactions were run for six hours and then opened to air before work-up. The products were characterized by ^{1}H-NMR spectroscopy and/or gas chromatography (GC). For GC, the detector responses for all the starting materials and all possible products were calibrated so quantitative results could be obtained. The calibration process is included in chapter 6.

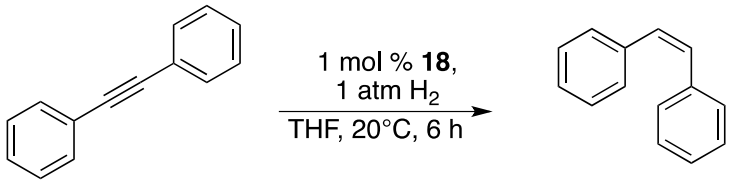

Equation **2.2**

The hydrogenation of **20** was revisited, and a very low conversion to *cis*-stilbene **46** was observed (Eqn. **2.2**). This result confirms the assumption that the pure neutral cluster **18** is not an effective precatalyst.

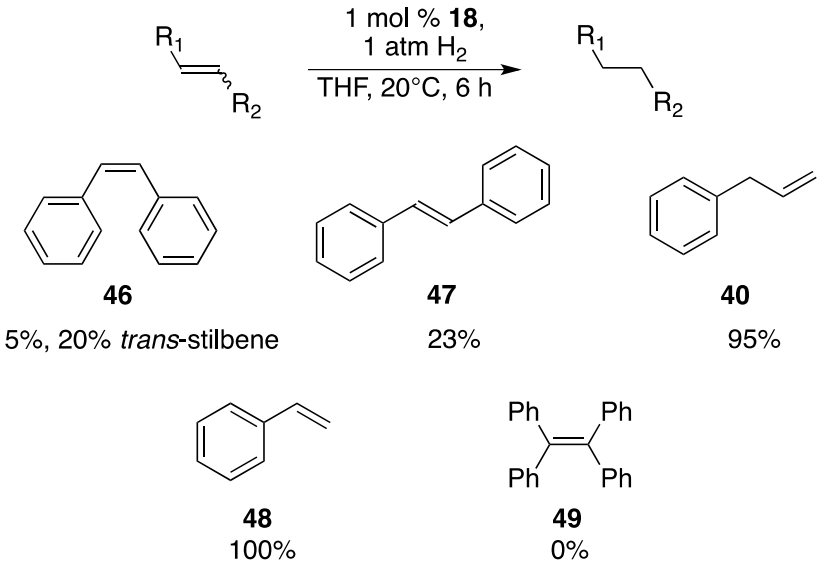

Figure **2.3**: Hydrogenation of selected alkenes with 1 mol% neutral cluster **18**.

In addition, a short list of alkenes was hydrogenated under the same conditions (Fig. **2.3**). For *cis*-stilbene **46**, the isomerization product *trans*-stilbene **47** is the major product in 20% yield, while only 3% of bibenzyl **42** was detected. The conversion of *trans*-stilbene **47** to **42** proceeded in 23% yield under these conditions. Based on these yields, it is assumed in the case of **46** that the isomerization product **47** is hydrogenated to give the **42** observed. As a sterically unhindered alkene, allyl benzene **40** gave 95% yield of hydrogenation product, without detectable alkene isomerization. Quantitative yield was obtained for styrene **48** hydrogenation, without polymerization. Finally, no conversion was observed for the hydrogenation of sterically hindered tetraphenylethylene **49**. This is not surprising because the ligands occupy substantial space around the nickel centers, undermining the accessibility of highly hindered substrates.

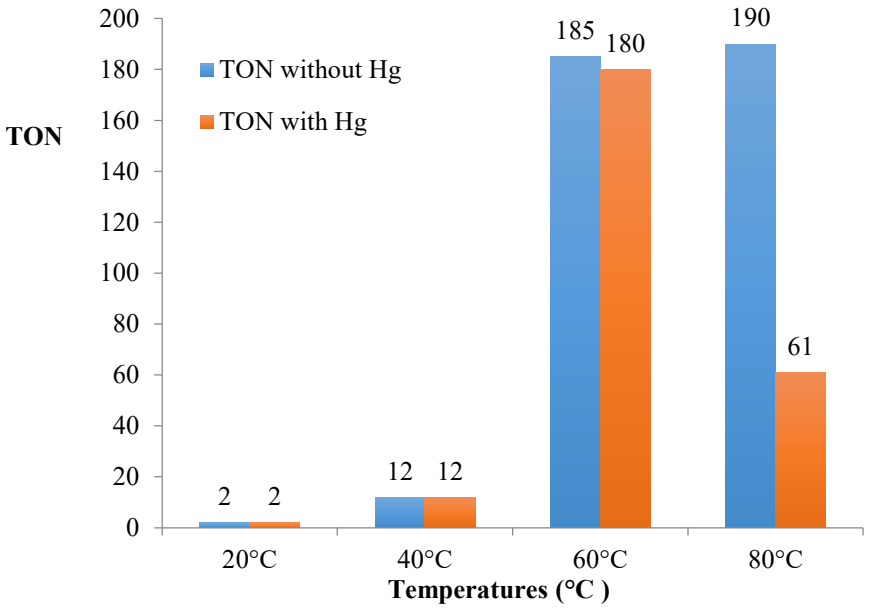

Figure **2.4**: Hydrogenation TON of **20** using **9** at different temperatures, with and without mercury poisoning.

As a typical substrate for catalytic hydrogenation of alkyne, the hydrogenation of diphenylacetylene **20** was explored further at various temperatures (Fig. **2.4**). The activity was compared based on turnover number (TON), defined by the number of π-bond being

hydrogenated per mole of precatalyst over the same period. It should be mentioned that the TON might not be accurate for two reasons: (1) The hydrogenation rate of alkyne and alkene should be different; (2) The reaction rates might change during the reaction due to changes of substrate concentration. Thus, the TON is only used here for qualitative comparison.

The results suggest increased activity as the temperature increases. The catalyst was mainly homogeneous below 60 °C. As the temperature was raised to 80 °C, however, the TON drops from 190 to 61 in the presence of Hg, suggesting that the cluster decomposed and agglomerated to heterogeneous catalyst. The homogeneity of the catalyst was also tested by the Hg test,[72] in separate experiments. It should be mentioned that the Hg test itself is not definitive, a suit of complimentary tests are necessary to confirm the homogeneity of the catalyst (TEM, quantitative ligand poisoning, kinetics, and so on).[73]

2.2.3 Hydrogenation of alkenes and alkynes with $Na[Ni_4(NP^tBu_3)_4]$ 31

It is clear then, that the neutral cluster **18** is not an active catalyst for the hydrogenation of **20** at room temperature. We next assessed the activity of the anionic cluster $Na[Ni_4(NP^tBu_3)_4]$ **31**. It is necessary to be clear that the exact structure of **31** has not been characterize. The reproducible procedure to prepare **31** *in situ* provides materials with reasonable good quality, but there is still a chance that some amounts of impurities could be generated by the procedure.

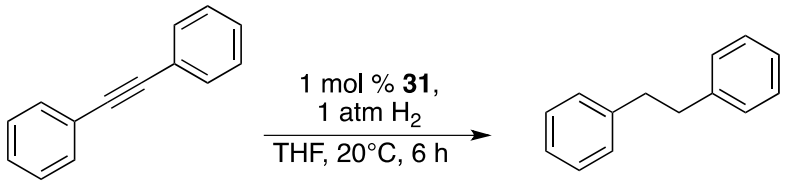

20 **42**
100%

Equation **2.3**

Again the hydrogenation of **20** was studied first. The result shows quantitative conversion to **42** over the six-hour reaction (Eqn. **2.3**). This result strongly supports our assumption that the anionic cluster **31** is the actual catalyst for the hydrogenation of **20**.

Furthermore, the same range of alkene substrates was explored under the same conditions (Fig. **2.5**). In most cases, the anionic cluster **31** exhibited higher activity than the neutral cluster **18**, as higher conversions were observed. Quantitative yield was obtained for hydrogenation of **40** to give **41**. About 45% of the **47** was converted to **42**. For **46**, the major product with this catalyst is **42** in 85% yield, with only 15% of **47** observed after full conversion of the starting material. In the case of **48**, polymerization overrides hydrogenation, likely initiated by one electron transfer. No conversion was again observed for the sterically hindered **49**, as obtained using neutral cluster **18**.

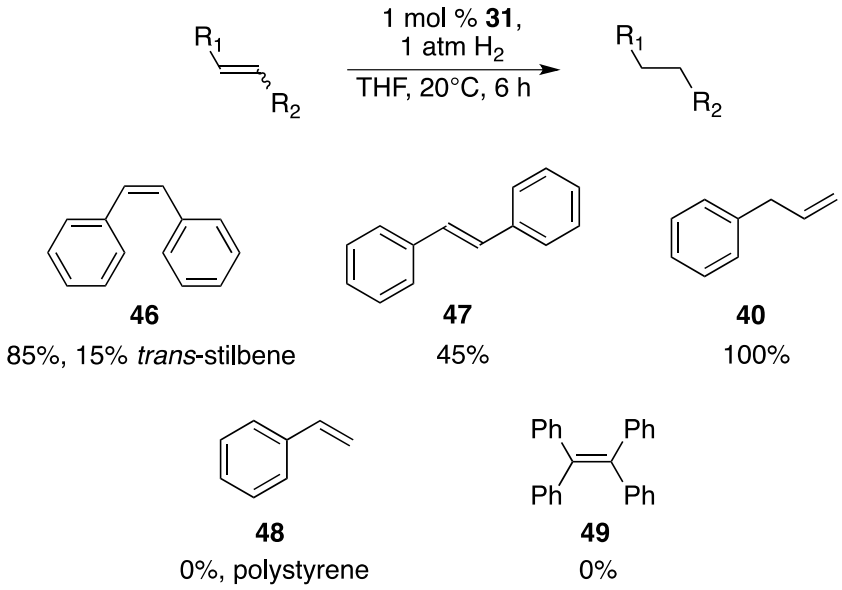

Figure **2.5**: Hydrogenation of selected alkenes with 1 mol% anionic cluster **31**.

The homogeneity of the catalyst was also tested by mercury poisoning at various temperatures. The results are shown in Figure **2.6**. The catalyst was mainly heterogeneous at room temperature, as adding excess mercury into the solution resulted in a decrease of TON from 200 to 57. A similar result was obtained at 80 °C, which gave a TON of 64 in

the presence of excess mercury. When the temperature was kept at 0 °C, however, the catalyst appears to remain homogeneous, as an almost identical TON, 100 versus 102, was obtained. In summary, for hydrogenation of **20** the anionic cluster **31** is homogeneous at 0 °C, but becomes heterogeneous when the temperature approaches 20 °C.

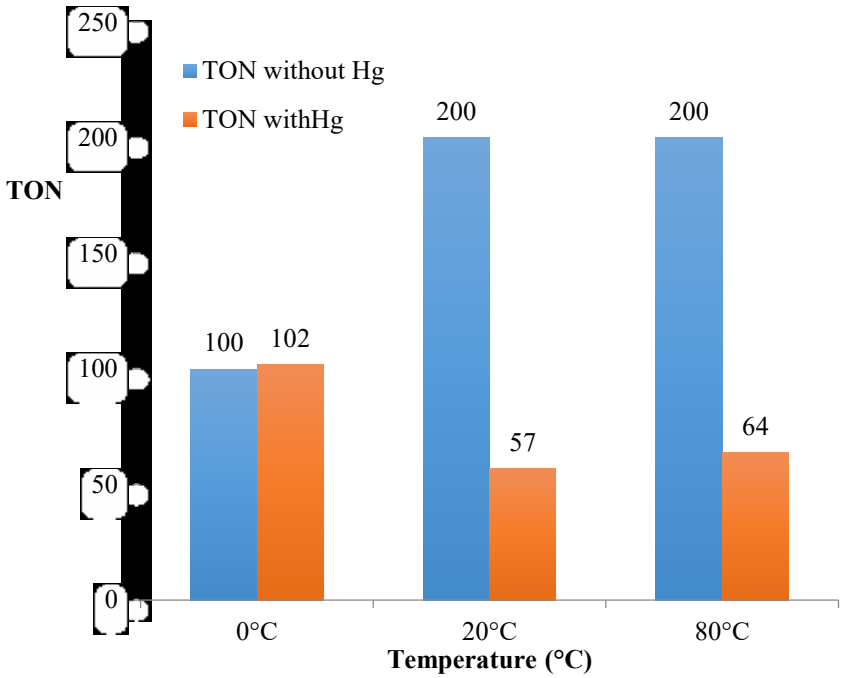

Figure **2.6**: Hydrogenation TON of **20** using **31** at different temperatures, with and without mercury.

As early results indicate, the hydrogenation rates and possible routes for *cis*-stilbene **46** and *trans*-stilbene **47** are different. **46** can either isomerize to **47** or be hydrogenated to **42**; in contrast the isomerization of **47** to **46** is not favored, and the hydrogenation rate is slow. To further investigate the transformations of these species, GC was used to monitor the progress of the hydrogenation of **20** over a three-hour period. The results are shown below in Figure **2.7**.

The same concentrations of catalyst and substrate were used. The reaction was set up in a three-neck flask charged with a dry ice condenser, which was connected to a H_2-filled Schlenk line. Aliquots were taken every 30 minutes by cannula, transferring approximately

1 mL of solution. The sealing of this set up is likely not as ideal as obtained using a middle-wall glass reactor, which explains why the reaction did not proceed to completion. Despite this, the graph clearly elucidates the reaction progress.

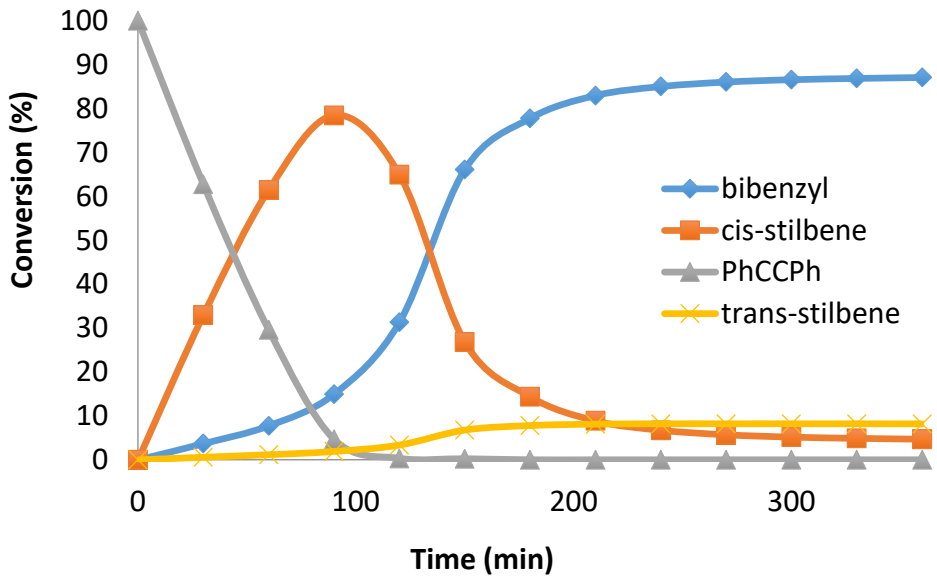

Figure **2.7**: Progress of the hydrogenation of **20** catalyzed by 1 mol% of **31** at room temperature and 1 atm H_2.

From the figure it is clear that the rate of hydrogenation of **20** stays almost constant until most all of the **20** was consumed, regardless of the decreasing concentration of substrate as the reaction progressed. **46** is the primary product of the first hydrogenation, while **47** was the minor product. After **20** was consumed, the hydrogenation of the **46** to **42** and isomerization to **47** took place competitively, although the hydrogenation is faster than isomerization. As a result, the conversion of **42** increased steadily until it was close to quantitative. The hydrogenation of **47** was very slow, leaving about trace amount **46** and **47** unconverted.

The hydrogenation reaction was carried out in THF, because better activity was observed in polar solvents from previous study. Since the anionic catalyst **31** is soluble in many organic solvents, the hydrogenation activity in different solvents was also investigated.

The results (Fig. **2.8**) indicate that optimal activity was obtained in THF. In less polar diethyl ether, the TON was about a quarter of that in THF. In nonpolar solvents such as pentane or hexane, the TONs were observed as 97 and 89, about half that in THF, but surprisingly faster than in ether. Lower activity was also observed in aromatic solvents toluene and benzene, out of which almost no conversion was obtained in benzene. Last but not least, barely any conversion is observed in DME, likely because DME is a much better ligand than THF, possibly inhibiting substrate binding by coordinating to the metal centers. From the whole series, we did not find an obvious trend for activity based on polarity or coordinating capability. The activity in specific solvent is probably based on a combination of several factors such polarity, coordinating capacity, solubility of H_2, decomposition rates and so on.

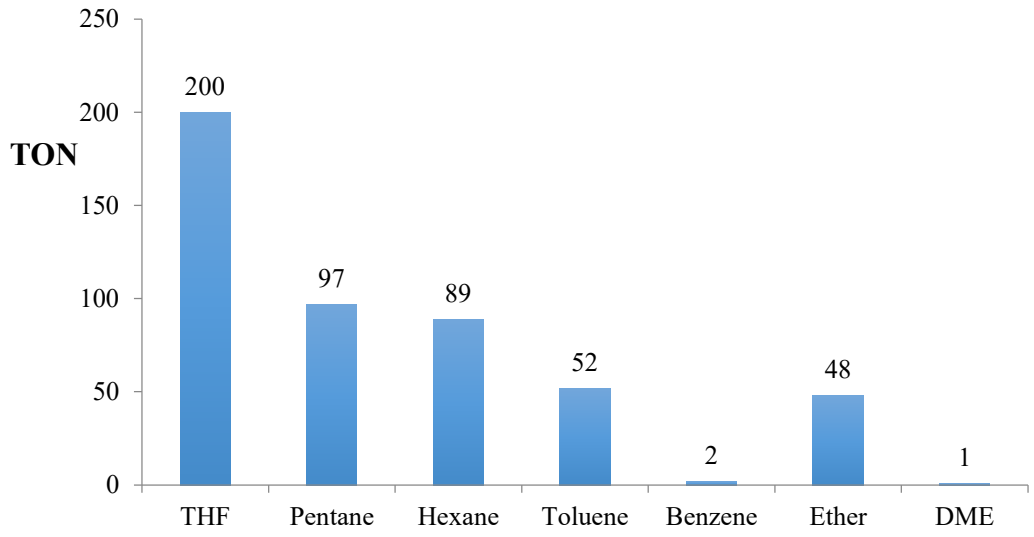

Figure **2.8**: Hydrogenation TON of **20** using **31** in various solvents, under the general condition.

2.2.4 Hydrogenation of alkenes and alkynes with $[Ni_4(NP^tBu_3)_4]BPh_4$ 23

As a further control, the hydrogenation activity of cationic cluster $[Ni_4(NP^tBu_3)_4]BPh_4$ **23** was also investigated for comparison with **18** and **31** in the series (Fig. **2.9**). For the hydrogenation of **20** no conversion was observed at room temperature. Catalytic activity improved as the temperature increased. Quantitative conversion is obtained at 80 °C; however, the mercury test suggested that the reaction was already mainly heterogeneous at this temperature.

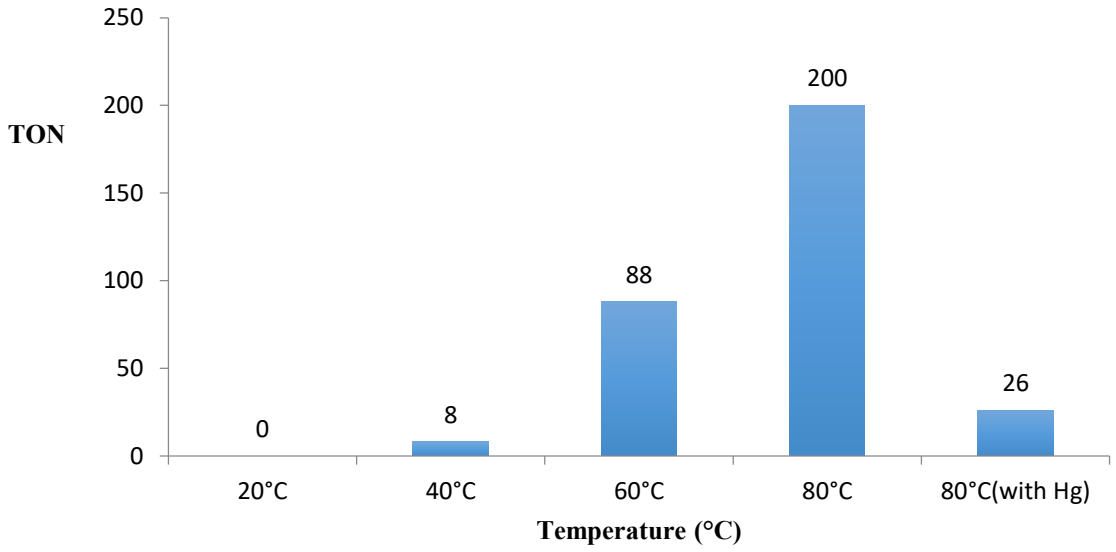

Figure **2.9**: TON of hydrogenation of **20** catalyzed by 1 mol% **23** under general conditions.

The hydrogenation of alkenes was also studied under the same conditions. As shown in Figure **2.10**. The cationic cluster **23** showed the lowest activity for hydrogenation. 2% conversion was observed for **46** isomerization to **47**, meanwhile only 1% for hydrogenation of **47** to **42**, respectively. In contrast, high conversions of hydrogenation products were observed for the more reactive and sterically accessible **40** and **48**. No conversion for **49** was observed, as anticipated.

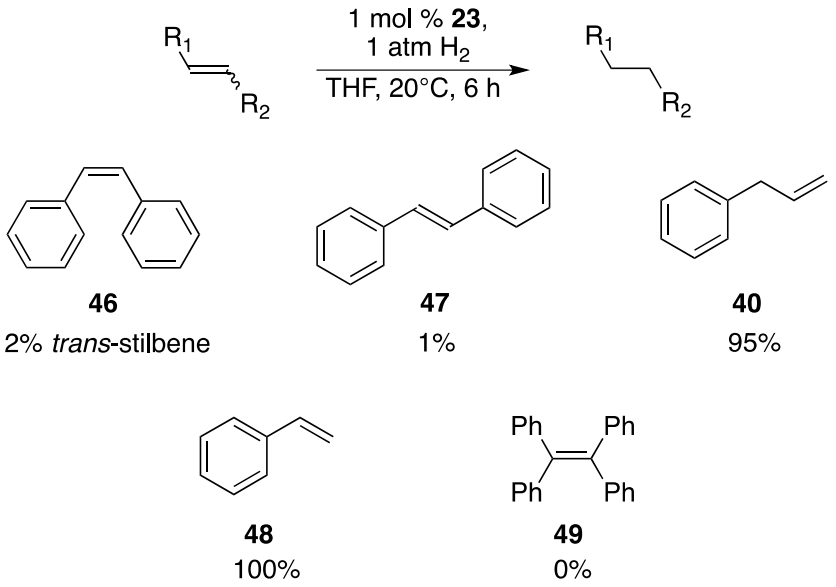

Figure **2.10**: Hydrogenation of selected alkenes with 1 mol% **23** under general conditions.

Based on the hydrogenation of **20** and selected alkenes using **18**, **23**, and **31**, we conclude that the anionic cluster **31** is a more active precatalyst for hydrogenation than neutral cluster **18**, which is a more active precatalyst than cationic cluster **23**. All of the catalysts transfer from homogeneous to heterogeneous at higher temperature. The anionic cluster **31** transforms around 20 °C, neutral cluster **18** at 80 °C. The cationic cluster **23** is already heterogeneous when it shows good activity at 80 °C. We propose the low-coordinate nature of the metals is the reason for this decomposition. The neutral and cationic precatalysts are kinetically stable, protected by the sterically demanding ligand, but at some stages along the catalytic cycle may be more prone to aggregate and precipitate, especially when there are other low-valent metals within bonding distance in the cluster. On the positive side, thermal decomposition provides one or more active heterogeneous catalysts. With further design and development, we are optimistic we can build more robust, more active soluble precatalysts and rationally-designed heterogeneous systems for hydrogenation.

2.2.5 Proposed mechanism for hydrogenation

Based on the results and observations on the hydrogenation reactions, a mechanism is proposed (Fig. **2.11**). It should be mentioned that **18**, **23**, and **31** have distinctive activities, depending on the charge of the cluster. The mechanism presented here is based on the neutral cluster **23**, even though the relevancy of other clusters will be mentioned.

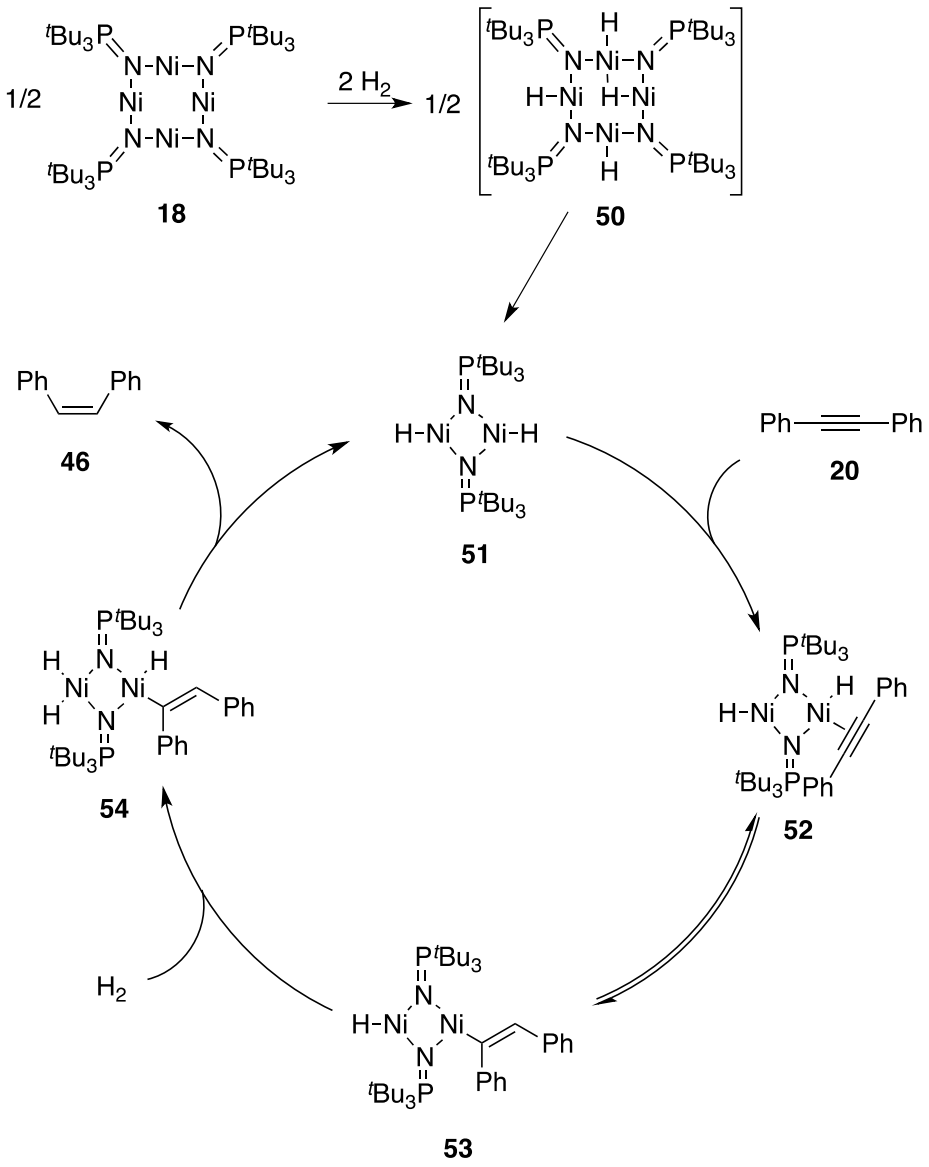

Figure **2.11**: Proposed mechanism for hydrogenation of **20** using **18**.

The mechanism is highly tentative because not much concrete information has been collected to elucidate the details along the catalytic cycle. This is mainly due to the lack of

effective methods to study these paramagnetic transition metal clusters in solution. Preliminary DFT computations suggests one equivalent of the neutral cluster reacts with two equivalents of H_2 without activation barrier, forming a mixed-valence tetrahydridonickel cluster represented by **50**. Both terminal and bridging nickel hydride is proposed because they were both detected by IR around 2000 cm^{-1} and 1600 cm^{-1}.[70]

The tetrahydridonickel cluster **50** then dissociates into two dimeric nickel species **51**. The dissociation is proposed here due to the similar pathway observed in HDS for tetrametallic $[Me_4Co_4(NPEt_3)_4]PF_6$ **22**. In the case of cationic **23** and anionic **31**, the dissociation could lead to dimetallic clusters with different charges, which may explain the activity difference.

The substrate **20** then coordinates to **51** to give **52** as an intermediate. Subsequent migratory insertion delivers the hydride from the same face of nickel center to form **53**, which determines the *cis* geometry of the double bond in the major product. In the vinylnickel complex **53**, both nickel atoms are three-coordinate and bimetallic hydrogen activation gives trihydridonickel(II) cluster **54**. Subsequent reductive elimination releases the product **46** and regenerates the active catalyst **51**. Hydrogenation of **47** is slow due to the steric bulky phosphoranimide ligand, which hinders the coordination of the substrate. When **46** is the substrate, the migratory insertion step is reversible so the isomerization to **47** is possible.

During the catalytic cycle, the low-valent nickel cluster could agglomerate to produce a heterogeneous catalyst, which is possibly even more active for hydrogenation by other related mechanisms.

In addition, the dissociation to form dimers would be entropic more favored under elevated temperature, which explains the improved hydrogenation activity of the cationic cluster **23** and neutral cluster **18** at higher temperatures. Meanwhile, increasing the reaction temperature also accelerates the agglomeration/decomposition to heterogeneous catalysts. It is also possible that several oligomers are present in the system and each has its own catalytic cycle.

2.3 Conclusions

In this chapter, the reproducibility problems revealed in our study of the hydrogenation of **20** with the neutral cluster **18** were raised, studied, and addressed. The root of this problem is the overreduced, anionic impurity present in the neutral cluster when prepared by the procedure developed by Dr. Jeffrey Camacho-Bunquin. The neutral cluster **18** was found to be ineffective as a hydrogenation catalyst at room temperature. In contrast, the impurity, anionic cluster **31**, was the highest-activity catalyst for hydrogenation.

Due to the unstable nature of the neutral and anionic clusters, a new procedure was developed to synthesize the cationic cluster **23** on gram scale and purify it rigorously. The neutral cluster **18** and anionic cluster **31** can then be prepared *in situ* before using them.

The hydrogenation activities of three nominally isostructural tetranickel clusters were investigated to determine electronic effects on catalysis. In general, the anionic cluster **31** forms a more active catalyst than neutral cluster **18**, which is more active than cationic cluster **23**. As the temperature is increased, higher activities were observed for all three compounds, although much of that must be attributed to the catalysts transforming from homogeneous to heterogeneous.

The low-valent nature of the metal and the coordinatively unsaturated framework of metal clusters are assumed to be the reason for this decomposition to heterogeneous catalyst. Further investigation will be undertaken to understand this transformation; meanwhile, a new generation of metal clusters have been designed rationally to prevent the uncontrolled aggregation of metal clusters.

Chapter 3. Phosphoranimide-bridged Nickel Clusters for Hydrosilylation and Deoxygenation of Carbonyl Compounds

3.1 Introduction

Catalytic hydrosilylation (hydrosilation) of carbonyl compounds is a widely applied transformation in both the laboratory and industry (Fig. **3.1**).[14,74-80] In addition, the hydrosilylation of carbonyl compounds is also related to the catalytic reduction of CO_2 and CO, for the purpose of energy storage and value-added commodities.[81-87] The field has been mainly dominated by precious metal catalysts, especially rhodium and ruthenium, at least until the last decade, during which numerous innovations in hydrosilylation were reported using mononuclear first-row transition metal catalysts and different ligand scaffolds.

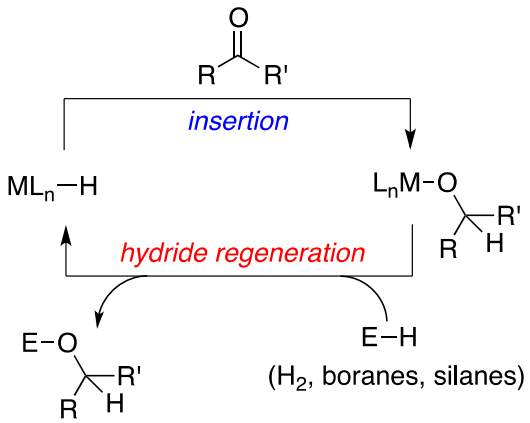

Figure **3.1**: General mechanism for carbonyl reduction catalyzed by transition metal hydride.

In 2007, Beller et al. reported $Fe(OAc)_2$ catalyzed carbonyl hydrosilylation using PCy_3 as ancillary ligand at 65 °C.[88] Later in the same year they published the enantioselective version of the reaction using a chiral ligand under the same reaction conditions.[89] Also in 2007, Nishiyama and coworkers published the $Fe(OAc)_2$ catalyzed hydrosilylation using

both nitrogen- and sulfur-based ligands under similar conditions.[90,91] In 2008, Chirik et al. demonstrated the bis(imino)pyridine iron dialkyl system for catalytic hydrosilylation at ambient temperature[92] and subsequently the enantioselective version in 2009.[78] Since then, numerous hydrosilylation systems at have been developed with a number of first-row transition metals and ligand scaffolds. Iron[76,77,80,93-98] and cobalt[77,93,99,100] are the most popular metals adopted in this field, each with several successful ligand systems which overturns at ambient temperature; meanwhile others metals, including nickel,[75,101-103] copper[104-106] and titanium[107,108] have also been used.

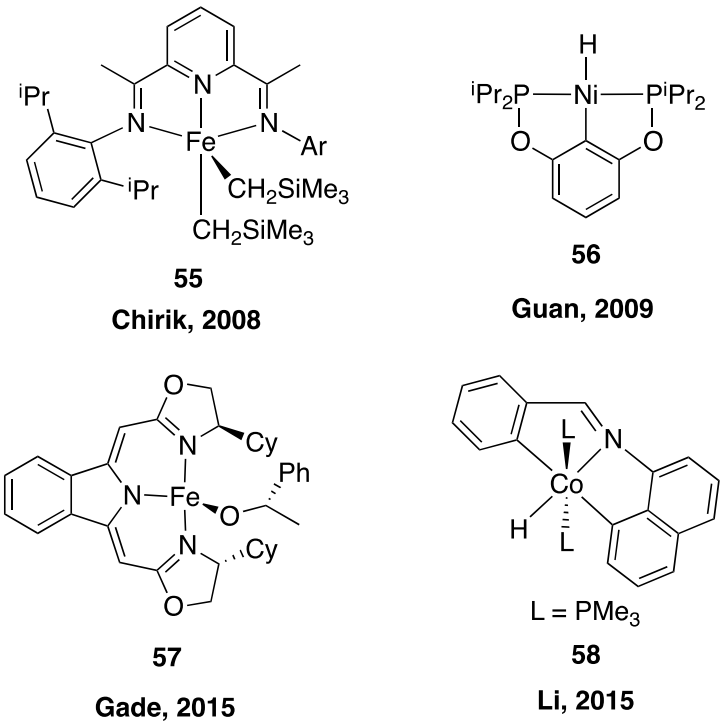

Figure **3.2**: Examples of first-row transition metal pincer catalysts for catalytic hydrosilylation of carbonyl compounds.

The pincer architecture is the most-used ligand scaffold for hydrosilylation of carbonyl compounds. The mechanisms generally involve metal hydride intermediates, which form metal alkoxides after carbonyl insertion.[14] Representative iron, cobalt, and nickel catalysts are shown above (Fig. **3.2**).

In addition to pincer complexes, several low-valent first-row transition metals catalysts have been reported. In 2010, Tilley et al. reported the hydrosilylation of carbonyls with the simple bivalent $Fe[N(SiMe_3)_2]_2$ **59** at room temperature, which remains one of the most efficient catalysts at present.[80] Peters et al. reported the hydrosilylation using chelating phosphinoborane complexes $[^{Mes}B(o\text{-}Ph_2PC_6H_4)_2]Ni$ **60**.[75] This complex can achieve H–Si σ-bond activation by a frustrated Lewis pair mechanism, in which the low-valent nickel behaves as a strong Lewis base and the labile borane behaves as the Lewis acid (Fig. **3.3**). Later they published both the cobalt and iron versions of the catalyst using similar ligands for hydrosilylation[93] and proposed the same mechanism for silane activation. Both metals showed higher activity than the nickel analog.

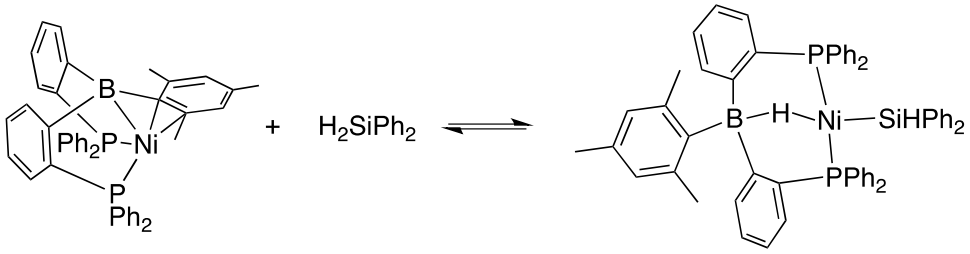

Figure **3.3**: Silane activation by $[^{Mes}B(o\text{-}Ph_2PC_6H_4)_2]Ni$ **60**.

In the tetrametallic clusters **18**,**23**, and **31**, the nickel atoms coordinate linearly to two phosphoranimide ligands regardless of the oxidation state. Herein we report the evaluation of these compounds for catalytic hydrosilylation of carbonyl compounds. Dr. Jeffrey Camacho-Bunquin accomplished some preliminary result with the nominally neutral cluster **18**.[70] However, as has been discussed, the purity of the catalyst led to irreproducible results for hydrogenation of alkenes and alkynes. Now that all three clusters can be prepared in reasonably pure form, it was time to revisit the catalytic hydrosilylation of carbonyl compounds.

3.2 Results and Discussion

First, it is important to point out that hydrosilylation using neutral cobalt cluster $[CoNP^tBu_3]_4$ **19** will not be discussed in this chapter since the partial replacement of Co(I) by Na^+ in the precatalyst is inevitable and an alternative preparation has not yet been developed successfully.

According to previous results from our group, the hydrosilylation of cyclohexanone **61** catalyzed by nominally neutral cluster **18**, in the presence of phenylsilane was not selective, giving a product mixture of (cyclohexyloxy)phenylsilane **62** and bis(cyclohexyloxy)phenylsilane **63** (Eqn. **3.1**).

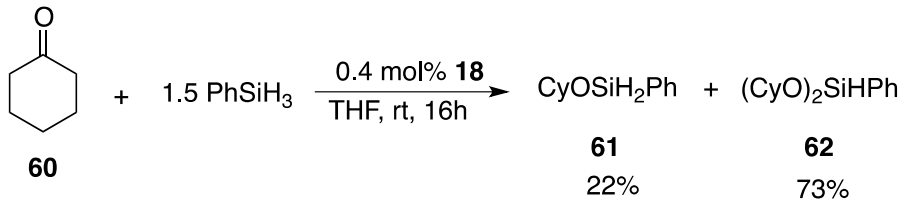

Equation **3.1**

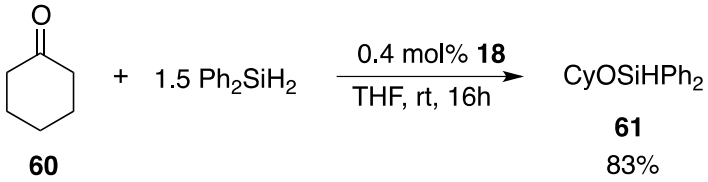

Equation **3.2**

The reaction was reproducible using catalyst **18** prepared by the new method. The mixture of products is likely due the high activity and multiple hydrogens in phenylsilane and the lack of steric hindrance to impede further reactions. When diphenylsilane was used as reducing reagent, the reaction becomes selective, giving **61** as a single product (Eqn. **3.2**). Thus only diphenylsilane was used as the reducing agent in this chapter.

3.2.1 Hydrosilylation of carbonyl compounds using $[Ni(NP^tBu_3)]_4$ 18

The hydrosilylation of carbonyl compounds was carried out using neutral cluster **18**, as prepared by the new procedure. The reactions were set up in the glovebox. The starting materials, THF, and a glass-encased stir bar were added into a 5-dram glass vial and let stir for 1 or 16 hours. Although the hydrosilylation of aldehydes was much faster than ketones and sometimes proceeded to completion in several minutes, the same reaction time was applied to all substrates. The products were characterized by ^{1}H-NMR spectroscopy and compared with known compounds in the literature. C_6Me_6 **63** was used as internal standard to determine the conversions/yields of the products by NMR integration.

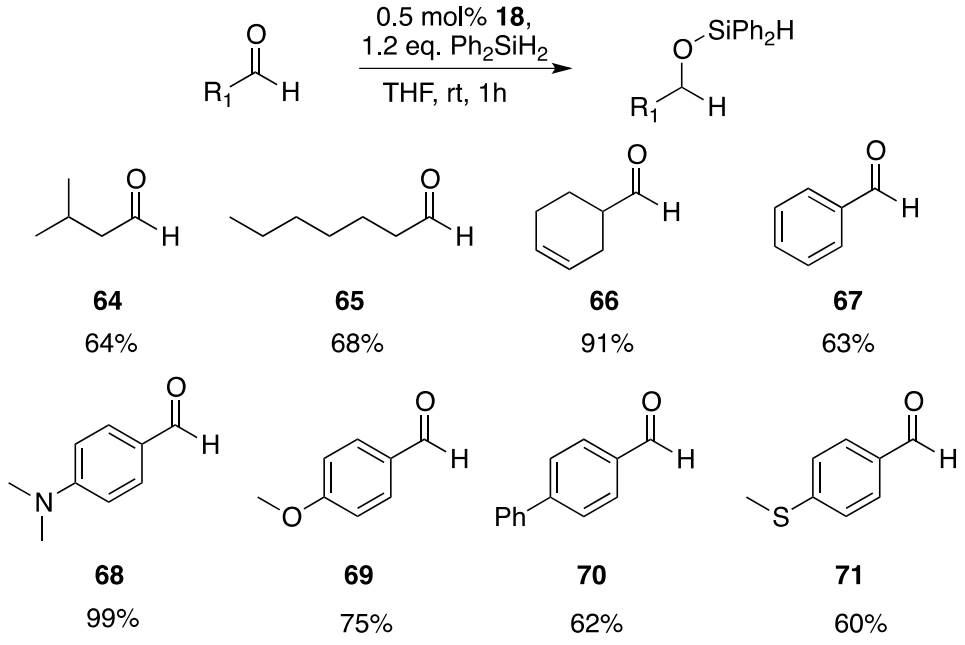

Figure **3.4**: Results for hydrosilylation of aldehydes using neutral cluster **18**.

The results of the hydrosilylation of selected aliphatic and aromatic aldehydes are shown above in Figure **3.4**. The reactions were much faster than the hydrosilylation of ketones. Immediate color changes were observed from green to yellow, and the reactions normally proceeded to completion within one hour. High conversions were observed for hydrosilylation, but the reaction was not selective for monohydrosilylation product. The main byproduct is bisalkoxydiphenylsilane (R_2SiPh_2). 64% yield was obtained for isovaleraldehyde **64** and 68% yield for heptaldehyde **65**. 1,2,3,6-Tetrahydrobenzaldehyde

66 gave 91% yield, leaving the isolated alkene unreacted, suggesting good selectivity for the reduction of aldehydes over isolated alkenes. The high yield of **66** could simply be the steric effect, which inhibits the second hydrosilylation of (RO)$SiPh_2H$. The aromatic aldehydes gave moderate to good yields of 60% to 75% for reduction of benzaldehyde **67**, *p*-anisaldehyde **69**, biphenyl-4-carboxaldehyde **70** and *p*-(methlythio)benzaldehyde **71**; a quantitative yield was observed for 4-(dimethylamino)benzaldehyde **68**. The reason for the higher yield could be that the electron-donating dimethylamino group deactivates the product (RO)$SiPh_2H$, preventing it from further hydrosilylation.

When compared with the earlier results using less pure catalyst, it is found that the hydrosilylation using pure neutral cluster **18** is consistent with early results: similar yields were obtained for almost all the substrates reported previously.[70]

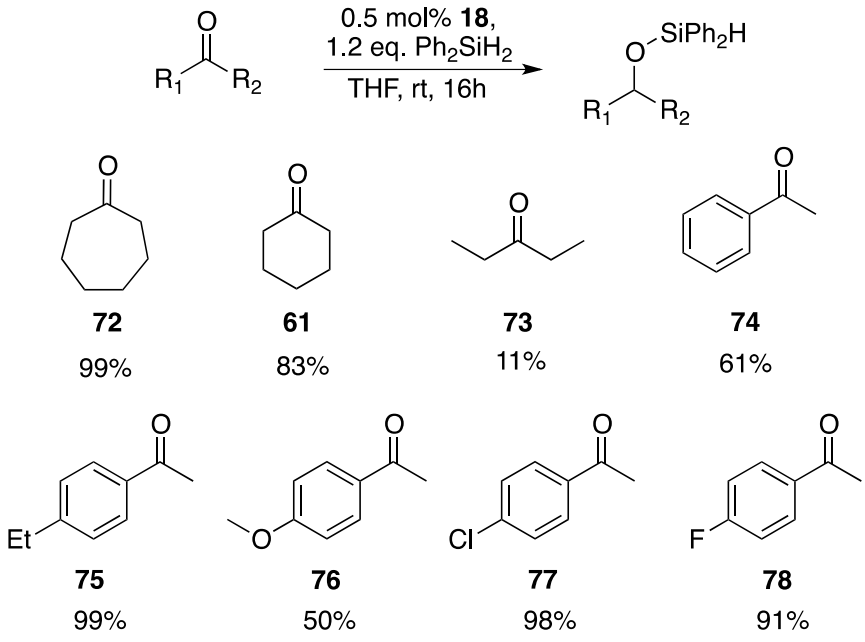

Figure **3.5**: Results for hydrosilylation of ketones with neutral cluster **18**.

The hydrosilylation of ketones was carried out under the same conditions. The reaction rates were much slower than those of aldehydes. At room temperature, one hour was normally required to detect a color change visually; the reactions were thus run for 16

hours. The results are shown above in Figure **3.5**. In general, only a single one product was observed other than the starting material, so the yields are the same as conversions unless otherwise discussed. Good to excellent yields were obtained for most substrates. For aliphatic ketones, 99% and 83% yields were obtained for cycloheptanone **72** and cyclohexanone **61**, respectively, but only 11% yield for the hydrosilylation of 3-pentanone **73**. The lower yields for aliphatic acyclic ketones have also been observed for several other catalytic systems. Aromatic ketones acetonephenone **74** and 4'-methoxyacetophenone **76** gave moderate yields of 61% and 50%. When the aromatic ring is substituted with electron withdrawing or alkyl groups, the yields are much higher, 91% to 99% for 4'-ethylacetophenone **75**, 4'-chloroacetophenone **77** and 4'-fluoroacetophenone **78**.

3.2.2 Hydrosilylation of carbonyl compounds using $Na[Ni_4(NP^tBu_3)_4]$ 31

Since we confirmed that the anionic cluster $Na[Ni_4(NP^tBu_3)_4]$ **31** is the actual catalyst for hydrogenation of alkenes and alkynes, it was also necessary to determine the hydrosilylation activity of **31**. The catalyst used in this case was prepared *in situ* by fast reduction of neutral cluster **18** with excess 40% Na/Hg. The hydrosilylation reactions were set under the same conditions as those using neutral cluster **18**.

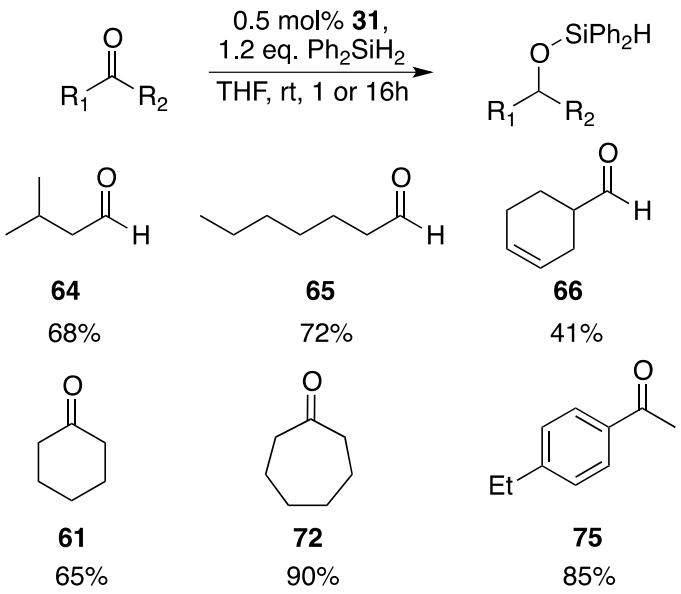

Figure **3.6**: Results of hydrosilylation of carbonyl compounds using anionic cluster **31**.

The results of several selected carbonyl compounds are shown in Figure **3.6**. The yields were generally comparable to or somewhat lower than those obtained from neutral cluster **18**. For the aliphatic aldehydes **64** and **65**, the yields after were 68% and 72%, similar to those using **18**. Only a 41% yield was obtained for the hydrosilylation of **66**, but 38% of the dialkoxydiphenylsilane (R_2SiPh_2) was also obtained as byproduct. For **61** and **72**, 65% and 90% yields were obtained, compared to 83% and 99% using **18**. A similar result was obtained for **75**, a 14% lower conversion than that catalyzed by **18** over the same time period. In addition to the lower yield, the anionic catalyst eventually precipitates out of the solution upon prolonged stirring, suggesting the cluster likely decomposes and agglomerate to heterogeneous nickel, probably still containing some phosphoranimide ligand.

In conclusion, the anionic cluster **31** is also an active hydrosilylation catalyst, but the selectivity and activity is not as good as the neutral cluster **18**.

3.2.3 Hydrosilylation of carbonyl compounds using $[Ni_4(NP^tBu_3)_4]BPh_4$ 23

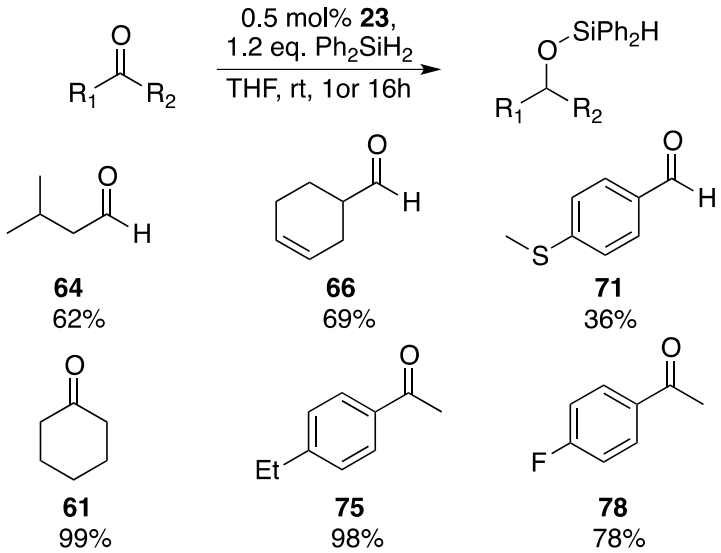

Figure **3.7**: Results of hydrosilylation of carbonyl compounds using cationic cluster **23**.

The hydrosilylation catalyzed by cationic cluster $[Ni_4(NP^tBu_3)_4]BPh_4$ **23** was also tested for comparisons to **18** and **31**. The results of the reactions of selected carbonyl compounds are shown above (Fig. **3.7**). Although a 62% yield was obtained for **64**, close to that obtained from catalyst **18**, only 69% and 36% yields were obtained for **66** and **71**, much lower than those obtained from **18**.

In contrast, the hydrosilylation of ketones was much more efficient than that of aldehydes and sometimes more efficient than either precatalyst **18** or **31**. Close to quantitative yields were obtained from **64** and **75**. The electron-withdrawing substituted substrate **78**, however, gave only 78% conversion, lower than that obtained with the neutral cluster **18**.

3.2.4 Discussion of mechanism of hydrosilylation

As in the case of catalytic hydrogenation, the mechanism is highly tentative due to the lack of concrete information about the intermediates along the catalytic cycle. Thus it will be premature to propose a detailed catalytic cycle. However, some possibilities will be discussed.

The simplest proposal is based on the neutral cluster **18**, as the best yields were generally obtained using that cluster, however the relevancy of **23** and **31** will be discussed. As we propose the active catalyst for catalytic hydrogenation is a bimetallic cluster, a similar dissociation is even more likely to happen in the case of hydrosilylation, due to the higher steric bulk of the silane. As a result, we proposed the first step is the bimetallic oxidative additions of the two equivalents of H–Si bond, likely followed by dissociation into two equivalent of dimeric clusters.

There could be two possible pathways to reduce the C=O double bond. One is hydride insertion into the carbonyl group to give the nickel alkoxy intermediate, the other is the silyl-directed migratory insertion of the carbonyl.[75] After this, the final product is reductively released and the activation of another equivalent of silane regenerates the bimetallic cluster.

In the case of anionic cluster **31**, the dissociation could give some anionic dimeric cluster. As already known from hydrogenation of alkene and alkyne, the anionic cluster is more likely to transform to heterogeneous catalyst. It explains why precipitate is observed when anionic cluster **31** was used. In addition, losing some of the reactive catalyst might lead to the lower yields than those using neutral cluster **18**.

In contrast, when cationic cluster **23** is used as the catalyst, the dissociation could result in cationic bimetallic cluster, which could be a better catalyst for electron-rich substrate, as a better hydrosilylation yield was obtained for **75**.

It is also necessary to mention that diphenylsilane, as a reducing reagent, might lose an electron to the cationic precatalyst to form some neutral species. This transformation might lead to some more complex radical mechanism(s), which might be the reason low yields were obtained for aldehydes.

To learn more about the mechanism of the hydrosilylation, more experiments need to be done, including kinetic, NMR study, IR to collect more information of the intermediates.

3.2.5 Deoxygenation of carbonyl compounds using $[Ni(NP^tBu_3)]_4$

The deoxygenation of carbonyl compounds and alcohols is an important transformation in refining highly oxygen-rich biomass-derived feedstocks.[109-115] The reduction with silane provides insightful information about carbonyl hydrodeoxygenation using our homogeneous catalysts. To assess the tendency of low-valent nickel clusters to hydrogenolyze the second C-O bonds after the hydrosilylation of carbonyl compounds, the deoxygenation of carbonyl compounds was studied under higher temperatures.

Since the neutral cluster **18** proved to be best hydrosilylation catalyst for carbonyl compounds, the deoxygenation research was mainly based on this catalyst. $PhSiH_3$ was used as the reducing reagent due to higher activity for hydrosilylation and deoxygenation,

as determined from Dr. Jeffrey Camacho-Bunquin's preliminary study. The reactions were carried out in medium-walled glass reactors fitted with glass-encased stir bars. After the reaction, acidic work-up was used to convert the silyl ether to alcohol by hydrolysis. GC-mass spectrometry was used to characterize the products. The identities of the products were assigned by comparison with the mass spectra of known compounds in an electronic database. The assignments of known compounds are reliable, but the assignments of unknown compounds are tentative, based only on the mass spectra. It is also necessary to point out that the conversions reported are unstandardized GC conversions and might not be accurate. It is impossible to calibrate all the products, given the amount of work involved and the fact that some of the compounds are even unknown. For research at this early stage, the inaccuracy of the conversions is tolerable.

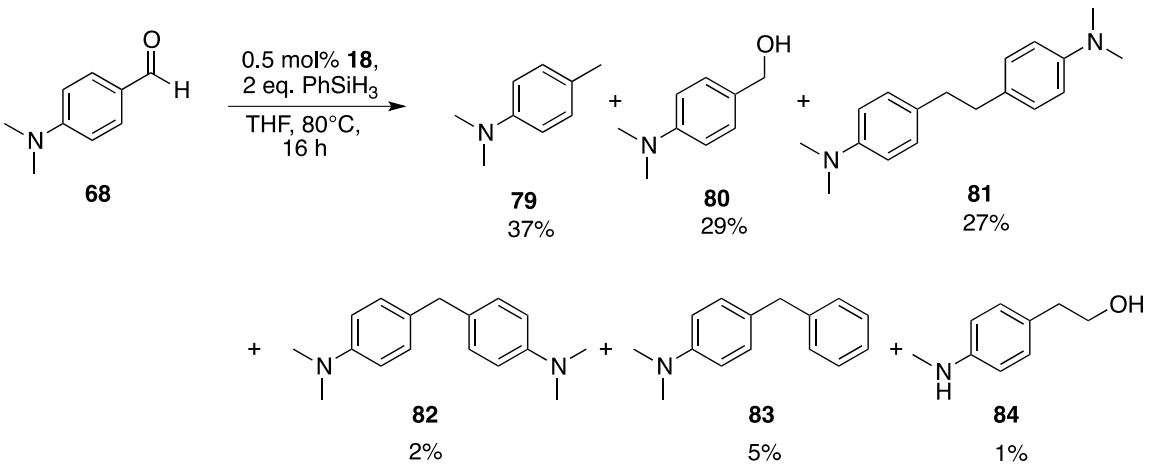

Equation **3.3**

The hydrodeoxygenation of **68** was selected for initial study, since a quantitative yield was obtained for the hydrosilylation. Based on the conversions from GC-MS, after overnight reaction at 80 °C**,** a 37% conversion was obtained to the deoxygenation product **79** and 29% conversion for **80** resulting from simple hydrosilylation (Eqn. **3.3**). In addition, 27% conversion to deoxygenated dimer **81**,[116] was also obtained. The deoxygenative dimerization is unprecedented. Aside from that, several other deoxygenation products (**82**, **83**, and **84**) were also detected, in low conversions, most arising from C–C bond scission. In all, a combined conversion of 71% to carbonyl deoxygenation product was obtained.

The deoxygenation of other substituted benzaldehydes was also investigated, including **69** (Eqn. **3.4**) and **71** (Eqn. **3.5**). For **69**, only three products were observed by GC-MS. The conversion to the deoxygenation product, 4-methylanisole **85**, was only 10%, but the deoxygenated dimer **87** accounted for 22%, leaving the initial hydrosilylation product **86** in 67% conversion. The combined conversion to deoxygenation product was a substantial 32%, but much lower than the amino-substituted substrate. For **71**, conversion to deoxygenated products was lower still; the conversion to the silyl ether accounts for 87% and is the major product. The deoxygenation product **88** and deoxygenated dimer **90** were produced in 4% and 9% conversions, respectively.

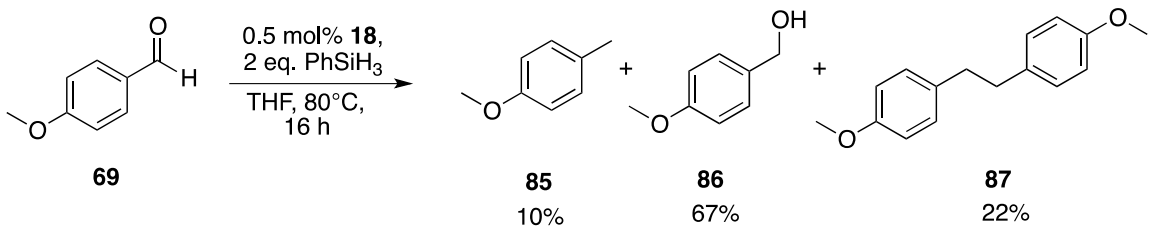

Equation **3.4**

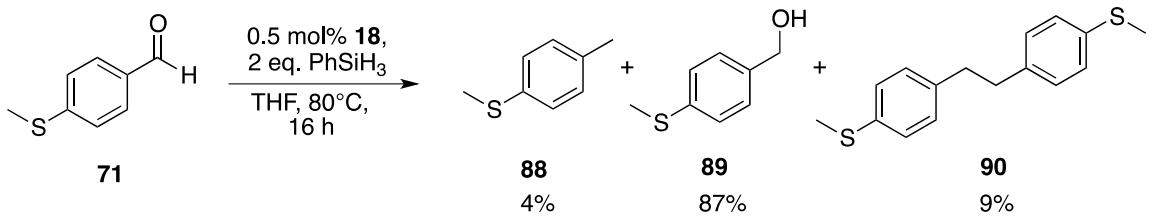

Equation **3.5**

Compared to the reaction of aromatic aldehydes, the hydrodeoxygenation of aromatic ketones was not as effective at these temperatures, very likely due to the inherently lower reactivity. It is known already that the first step of hydrosilylation event was much slower for ketones than aldehydes, which could account for markedly lower rates of deoxygenation. For 4'-ethylacetophenone **75**, **92** from hydrosilylation was obtained in 31% conversion; meanwhile, all the deoxygenation products (**91**, **93**, and **94**) combined accounted for only 6% conversion (Eqn. **3.6**). Similar results were observed for 4'-

acetanisole **76**: a 25% conversion to the simple reduction product **96** and a 7% conversion to deoxygenation products (**95**, **97**, and **98**) (Eqn. **3.7**).

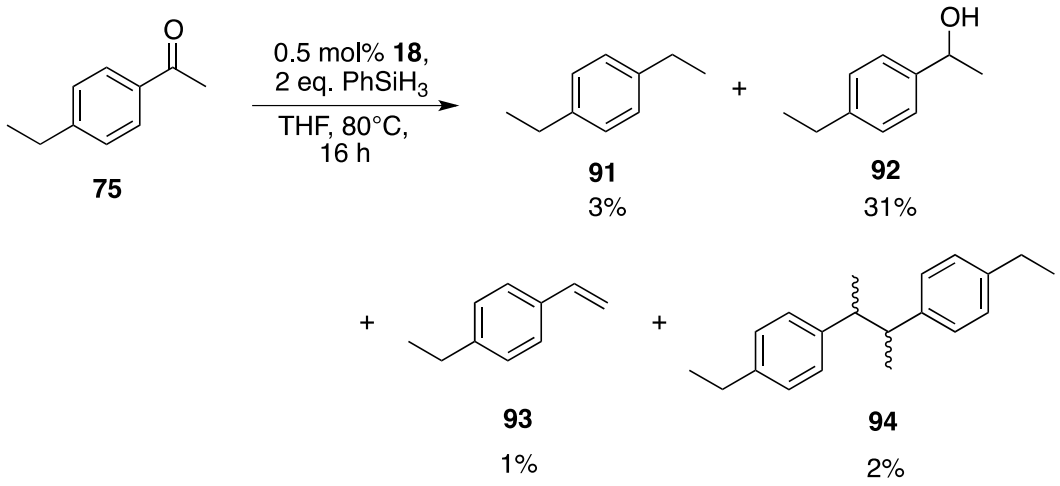

Equation **3.6**

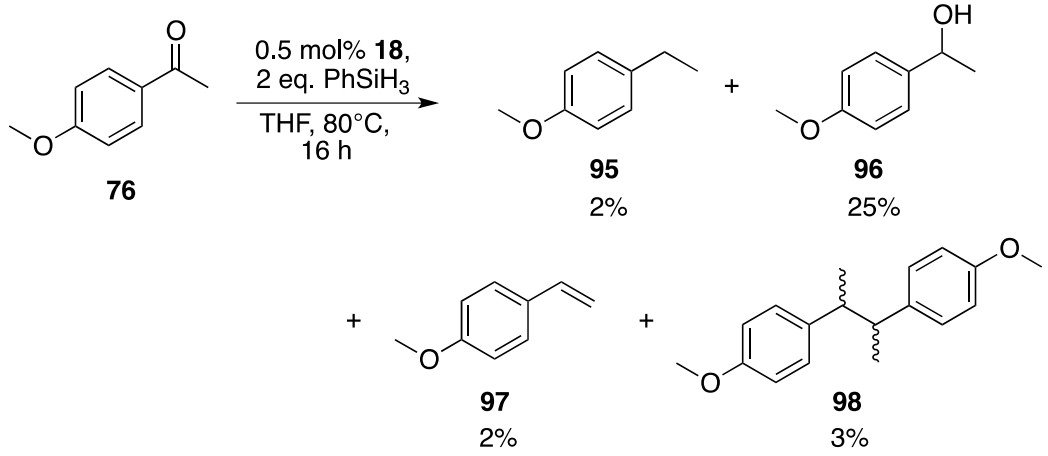

Equation **3.7**

Moreover, the reactivity of some conjugated aliphatic ketones was determined, in part to model oxygenated terpene components in biomass. The results show only a trace amount of catalytic deoxygenation at 60 ºC, giving a total of 3% hydrocarbon from carvone **99** (Eqn. **3.8**) and 2% for 3,4-diphenyl-2-cyclopentenone **102** (Eqn. **3.9**). These results suggest that aromatic carbonyl substrates are more reactive for hydrodeoxygenation than non-aromatic substrates in general.

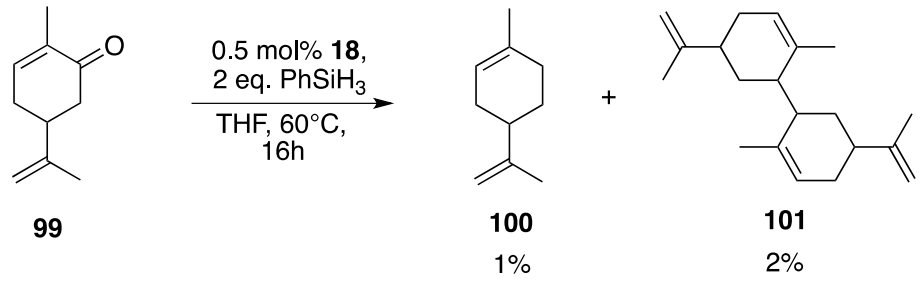

Equation **3.8**

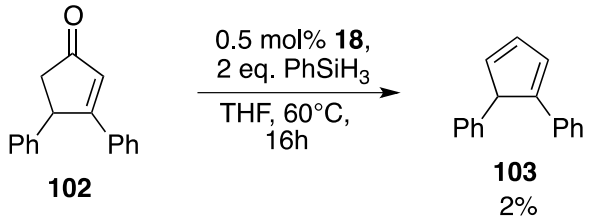

Equation **3.9**

The reaction was run at 60-80 °C because moderate conversions were obtained for the same substrates at the same temperatures from Dr. Jeffrey Camacho-Bunquin's preliminary results. These results are also irreproducible.

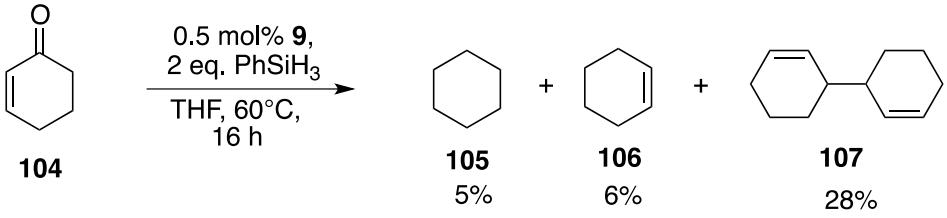

Equation **3.10**

We subsequently studied the deoxygenation under more intense conditions. Another unsaturated ketone, 2-cyclohexen-1-one **104**, was deoxygenated at 60 °C under standard conditions. Three oxygen-free products were obtained: cyclohexane **105**, cyclohexene **106** and 1,1'-bi(cyclohex-2-ene) **107** in respective conversions of 5%, 6% and 28%, a combined 39% total for deoxygenation (Eqn. **3.10**). With the temperature raised to 160 °C, the activity increases dramatically (Eqn. **3.11**). The conversions to **105**, **106**, and **107** were

21%, 12% and 51%, respectively, while 1,4-hexadiene **108** was also observed as fourth deoxygenation product in 6% conversion. In total, deoxygenation products combined for 90% conversion, comparing to 39% obtained at 60 °C.

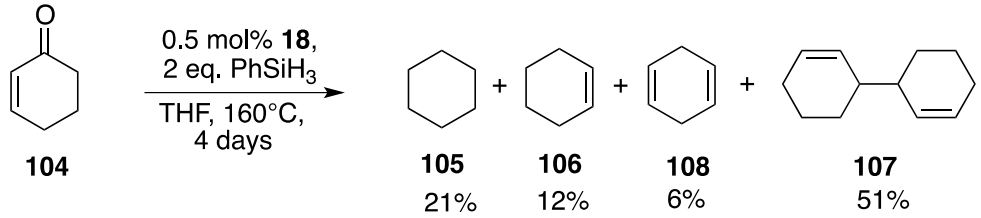

Equation **3.11**

Further study of catalytic HDO, using silanes and hydrogen is ongoing in the group. Detailed mechanistic proposal is not provided here due to the lack of concrete information. Furthermore, the fact that the deoxygenative dimerization is only achieved by heterogeneous before implies the catalyst might be heterogeneous, and the mechanism might be complicated.

3.3 Conclusions

In this chapter, the hydrosilylation and hydrogenolysis of carbonyl compounds with nickel catalysts **18**,**23**, and **31** were investigated. Our earlier study of hydrosilylation with impure precatalyst **18** is mainly reproducible, delivering good to excellent yields of hydrosilylation using diphenylsilane as a selective reductant. The cationic cluster **23** and anionic cluster **31** are both active catalysts under mild conditions for hydrosilylation of carbonyl compounds, even though lower yields were obtained than using the pure neutral cluster **18**.

Complete silylative deoxygenation of carbonyl compound was also investigated, using a more reactive silane and higher reaction temperatures to drive the conversion. In general, aldehydes show higher reactivity than ketones and aromatic substrates show higher reactivity than aliphatic substrates, at moderate temperature (60–80 °C). Cyclohexenone was selected as substrate for deoxygenation under higher temperature conditions. At 160

°C, a high conversion (~ 90%) to deoxygenation products was achieved, albeit at long reaction time.

The present investigation clarifies and resolves the reproducibility problems arising from the early use of anion-contaminated neutral cluster **18** for hydrosilylation and deoxygenation. These results provide enough potential to warrant further investigation and incentive to prepare related metal cluster catalysts with higher activity. The conversions or yields could be optimized in future. Furthermore, future development of heterogeneous catalysts is also possible.

Catalytic HDO using hydrogen as the reductant is the ultimate objective Further study will be continued by others in the group, completing the first comprehensive report of catalytic deoxygenation using this unique new catalyst system.

Chapter 4. Allyl-capped First-row Transition Metal Phosphoranimide Clusters – 2nd Generation of Low-valent Clusters for Catalytic Hydrotreatment

4.1 Introduction

In the first three chapters, the syntheses, characterization and catalytic activity of some low-coordinate first-row transition metal phosphoranimide clusters were discussed, mainly focusing on the coplanar tetranickel series: $[Ni_4(NP^tBu_3)_4]BPh_4$ **23**, $[Ni(NP^tBu_3)]_4$ **18**, and $Na[Ni_4(NP^tBu_3)_4]$ **31**. The coordinatively unsaturation and electron-richness of the metal centers promote the activation of small molecules such as hydrogen and silane, making the catalysts promising candidates for other industrial processes. This includes industrially important hydrodesulfurization (HDS) and potentially important hydrodeoxygenation (HDO) processes. Preliminary results also suggested that HDS activity was particularly effective in the presence of a strong base scavenger, KH (Eqn. **4.1**), but not NaH or LiH. However, the series of tetranickel catalysts bear some shortcomings, which inhibit further application. Specifically:

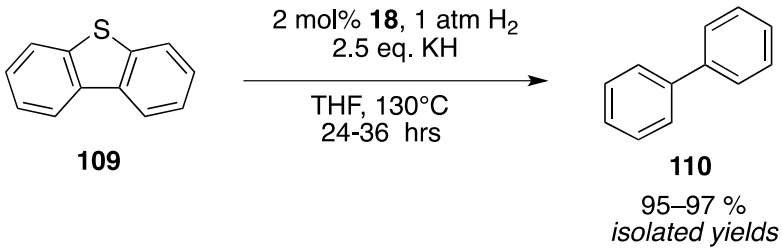

Equation **4.1**

(a) *Kinetic instability of the catalyst.* Low-coordinate metal complexes are kinetically unstable in general due to the vacant coordination sites available for potentially coordinating molecules, either ligands or solvents. Two-coordinate Ni(I) compounds, **111** for example, normally incorporate sterically hindering ligands to prevent self-association or binding of other molecules (Fig. **4.1**),[117] which undermines activity at the same time. In

the tetranickel series, the anionic cluster **31** is not a stable compound and single crystals could not be grown due to the kinetic instability in solution; the neutral cluster **18** is relatively more stable and crystalline, although it could not be stored without decomposition, even in the glovebox. Only the cationic cluster **23** is stable enough for storage without decomposition. The kinetic instability of **18** and **31** prohibits their large-scale syntheses and storage. As a result, the catalyst has to be prepared immediately before each reaction.

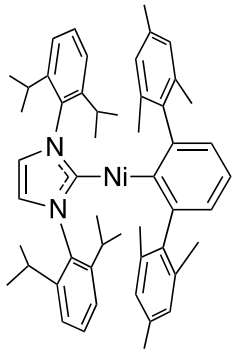

111

Figure **4.1**: Example of a two-coordinate Ni(I) complex.

(b) *The homogeneity of the catalyst*. In addition to the kinetic instability, the homogeneity of the catalyst is questionable, despite acceptable elemental analysis. Even when the catalysts are pure at the beginning of the reaction, it is not likely that the catalysts stay homogeneous and active throughout the reaction as the coordinating environment changes. Once the reaction is initiated, the stable precatalyst could form reactive intermediates, and the chance of aggregation/decomposition to heterogeneous metal black increases significantly. As a matter of fact, the results of homogeneity tests during the hydrogenation of alkynes showed that all catalysts became partially heterogeneous as the temperatures increases. In **18**, **23**, and **31**, each ligand coordinates to two nickel atoms, which means there is could be strongly basic lone pair on each nitrogen during the catalytic cycle. Considering that a metal hydride must be involved in the catalytic cycle, there is a considerable chance of reductive elimination to form an N–H bond leading the subsequent catalyst decomposition pathway.

(c) *Tunability of the substituent*. The tunability of the substituent group of the phosphoranimide ligands is a valuable feature in the rational design of their first-row transition metal clusters. However, in this series, the [NP^{t}Bu$_3^-$] ligand behaves more or less as an exception. Attempts to prepare other [Ni(NPR$_3$)]$_4$ clusters failed to yield well-defined products. The unique electronic and steric character of [NP^{t}Bu$_3^-$] allows the characterization of the coplanar tetrametallic series, but the chemistry is not applicable to other ligands, which narrows the scope.

(d) *Paramagnetism of the metal clusters*. As all of the metal clusters discussed above are paramagnetic, and hence the use of NMR spectroscopy, one of the most powerful tools in organometallic chemistry, was limited to study the structure of intermediates or mechanistic details of the chemistry. Lacking of concrete mechanistic study, further improvement of catalyst design is difficult.

To address these shortcomings, it became essential to develop new first-row transition metal clusters that are readily prepared in pure form, more thermally robust, electronically tunable, and structurally variable if we want to further understand and develop catalytic applications of first-row transition metal phosphoranimide clusters.

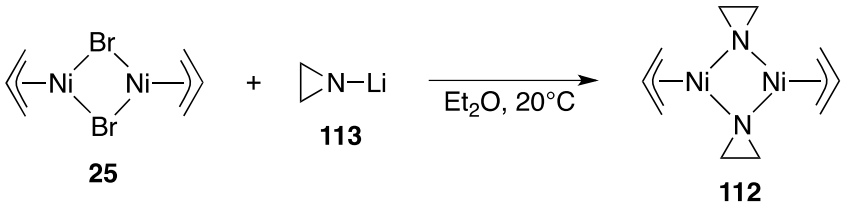

Figure **4.2**: Synthesis of [Ni(η^3–allyl)(NC$_2$H$_4$)]$_2$ **112**.

After some literature search,[118-120] we considered that one potential solution is the use of a multidentate "hydrogenolysis-ready" ancillary ligand in the precatalyst, so that each metal center is more coordinatively saturated and thus more stable. The ligands should occupy multiple coordination sites at the metal center and should be easily removed under standard reaction conditions: elevated temperatures and hydrogen. The precedent of a dimeric nickel

aziridide compound , [Ni(η^3−allyl)(NC_2H_4)]$_2$ **112**, raised the possibility of using the η^3-allyl group as the ancillary ligand (Fig. **4.2**).[121,122]

The η^3−allyl anion was expected to be a good candidate for several reasons. First, it is a 4-electrons donor that occupies two coordination sites, making each metal center more saturated. The π_2- and π_3-orbitals of allyl also allow greater interaction with the d-orbitals of the metal center (Fig. **4.3**), promoting back-donation from the metal. Second, if the nickel adopts the square planar geometry analogous to **112**, a diamagnetic electronic state is anticipated, allowing NMR spectroscopy to be used for further study. Last but not least, in the presence of hydrogen at elevated temperature, the allyl ligand is likely to react by hydrogenolysis and hydrogenation to produce the active nickel hydride cluster, in whatever oligomer it forms.[123]

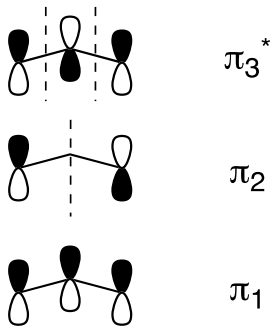

Figure **4.3**: Cartoon molecular orbitals for allyl group.

4.2 Results and Discussion

4.2.1 Synthesis and Characterization of [Ni(η^3−allyl)($NPEt_3$)]$_2$ 114

The synthesis of [Ni(η^3−allyl)($NPEt_3$)]$_2$ **114** was first attempted by salt metathesis of [Ni(η^3−allyl)Br]$_2$ **25**[122,124] (Eqn. **4.1**) and $KNPEt_3$ **115**. Two products were obtained from the reaction, the major product **114** was red and pentane-soluble, and the minor product **116** was orange and ether-soluble (Eqn. **4.2**).

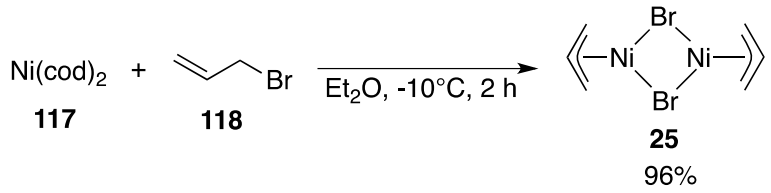

Equation **4.1**

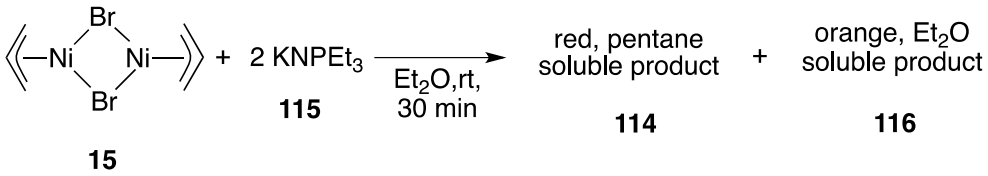

Equation **4.2**

Single crystals of the minor orange compound were grown by cooling a saturated ether solution. X-ray crystallography revealed the structure as $\{[Ni(\eta^3\text{–allyl})(NPEt_3)]_2\}_2[LiBr]_2$ **116**, the LiBr adduct of the target dimer, $[Ni(\eta^3\text{–allyl})(NPEt_3)]_2$ **114** (Fig. **4.4**). In this cluster, two equivalents of dimeric $[Ni(\eta^3\text{–allyl})(NPEt_3)]_2$ **114** are held together by two equivalents of LiBr. Each lithium cation coordinates to the lone pairs of the two nitrogen atoms in each dimer. The orientation of the allyl group are disordered, so the structure in Figure **4.4** is just one possible structure.

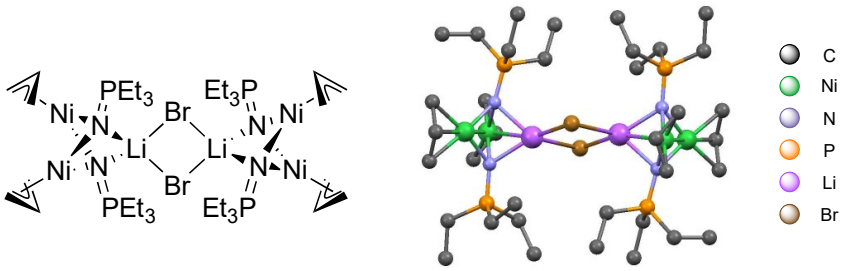

Figure **4.4**: Structure and ORTEP diagram of $\{[Ni(\eta^3\text{–allyl})(NPEt_3)]_2\}_2[LiBr]_2$ **116**, thermal ellipsoids are shown at 30% probability and hydrogen atoms are omitted for clarity.

Reexamination of the $KNPEt_3$ **115** preparation revealed that some amount of LiBr came from the reaction of $LiNH_2$ **119** and PEt_3Br_2 **120**, the first step of the ligand synthesis (Fig. **4.5**). The LiBr is soluble in Et_2O and slightly soluble in pentane; thus, it is carried through all the way to the product **115**.

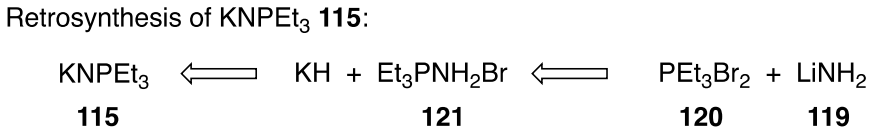

Figure **4.5**: Retrosynthesis of $KNPEt_3$ **115**.

To address this issue, Dr. Robin Hamilton in our group developed a new procedure for the synthesis of **115**, in which the **120** was mixed with excess KH in liquid ammonia. In this reaction, both the nucleophilic substitution and deprotonation happened in the one pot reaction. **115** could be synthesized on a large scale in up to 89% yield without contamination from LiBr (Eqn. **4.3**).

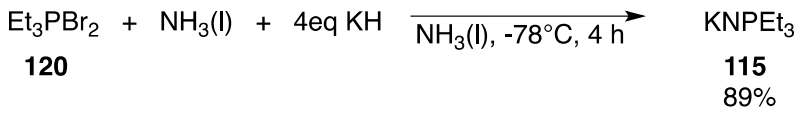

Equation **4.3**

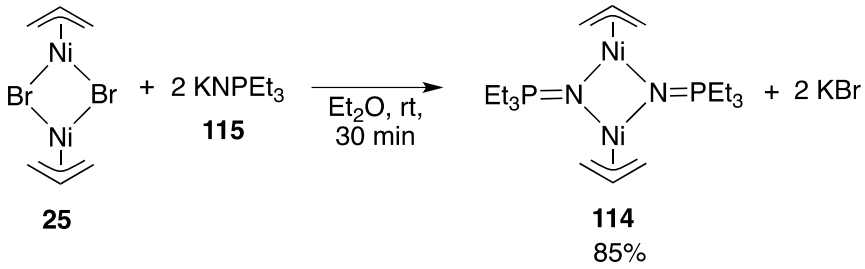

Equation **4.4**

The synthesis of $[Ni(\eta^3\text{–allyl})(NPEt_3)]_2$ **114** was successful under the same reaction conditions, but by using **115** prepared by the new procedure. The product is red and pentane

soluble, as anticipated (Eqn. **4.4**). Because both the two starting materials and the product are soluble in pentane and other organic solvents, the purification of this complex was challenging. The best way to ensure the quality of the product is using an exact 1 : 2 ratio of the starting materials, running the reaction on large scale, and subsequent careful recrystallization. Single crystals of the dimer were obtained by cooling a saturated pentane solution in the freezer of the glovebox. On occasion, the crude product was obtained as a thick oil, but solid could be obtained by recrystallization.

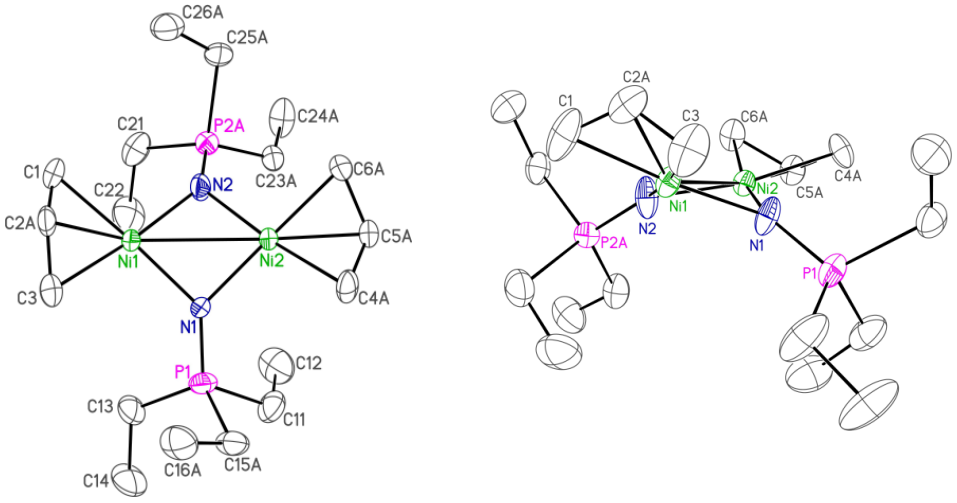

Figure **4.6**: ORTEP diagram of [Ni(η^3−allyl)(NPEt$_3$)]$_2$ **114**, thermal ellipsoids are shown at 30% probability and hydrogen atoms have been omitted for clarity.
The figure above is one possible geometry of **114**.

X-ray crystallography was used to determine the structure of the compound, which is shown in Figure **4.6**. The structure is as anticipated: each phosphoranimide ligand bridges two nickel atoms through the nitrogen atom. The η^3-allyl groups π-coordinate to nickel, each occupying two coordination sites. The nickel atoms bear the square planar geometry, thus the compound is diamagnetic. The refinement of **114** suggested the orientation of allyl group is highly disordered, the two allyl group can point to the same or opposite direction.

The ^{31}P-NMR spectrum shows two singlets at 34.61 ppm and 34.12 ppm with close to 1 : 1 ratio, representing the two inequivalent phosphoranimide ligands in the cluster. The ^{1}H-

NMR spectrum also shows two sets of allyl signals. The central protons of the allyls appear at 5.293 ppm and 5.229 ppm, respectively, as triplet of triplets. The other protons are shifted upfield in the range of 2.2–1.4ppm: the *syn*-protons show at 2.189 and 2.152 ppm as doublets and the *anti*-protons resonate at 1.475 ppm and 1.450 ppm, also as doublet. The ethyl groups resonate in the alkyl region in the same 1 : 1 ratio, appearing at 1.376 and 1.339 ppm for the methylene groups, and at 1.158 and 1.127 ppm for the methyl groups.

Combining the result of X-ray crystallography and NMR spectroscopy, it is speculated that **114** is a mixture of the *Syn*-isomer and the *Anti*-isomer, as shown below (Fig. **4.7**). For the *Syn*-isomer, due to the low energy barrier for nitrogen inversion,[125] **S1** and **S2** should be equilibrating in solution rapidly and cannot be differentiated. On the other hand, **A1** and **A2** are identical compound. The *Syn*-isomer and the *Anti*-isomer has very close to 1:1 ratio in the product, each has their own set of NMR data.

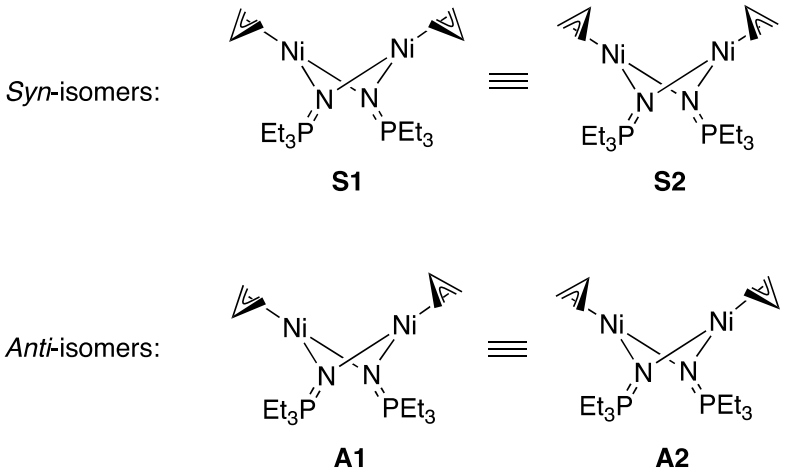

Figure **4.7**: *Syn*-isomer and the *Anti*-isomer of **114**.

In the crystal structure, the P–N bond lengths are 1.546(11) Å, shorter than the 1.578(9) Å in the neutral heterocubane $[MeCo(NPEt_3)]_4$ **21** and 1.595(6) Å in the cationic heterocubane $[Me_4Co_4(NPEt_3)_4]PF_6$ **12**, in which the $[NPEt_3^-]$ ligand coordinates to three metals. This suggests stronger P–N bonds in **114**, due to the different bonding. The total bond angles around nitrogen is 356.67(8)°, not far from 360°. Further, when **114** was mixed

with a suspension of LiBr in Et_2O, the same LiBr adduct **116** was obtained, although not quantified (Eqn. **4.5**). This result supported the basic, lone pair character on nitrogen. The nitrogen center of each phosphoranimide is between sp^2- and sp^3-hybridization, strongly favoring the sp^2 hybridization.

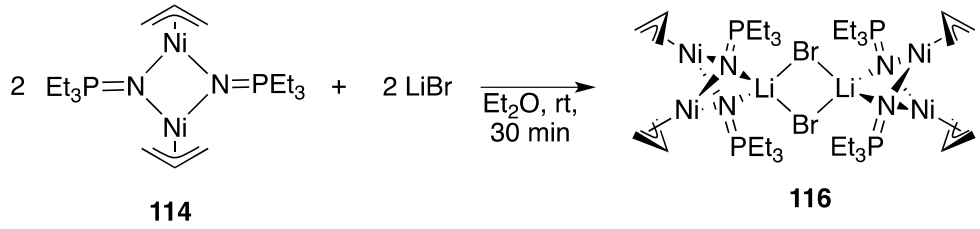

Equation **4.5**

4.2.2 Synthesis and Characterization of $[Ni(\eta^3-allyl)(NPPh_3)]_2$ and $[Ni(\eta^3-allyl)(NP^tBu_3)]_2$

To assess the electronic tunability of the allyl-capped nickel phosphoranimide clusters, phosphoranimide ligands with different substituents were also investigated. Dimeric $[Ni(\eta^3-allyl)(NPPh_3)]_2$ **122** was synthesized using potassium triphenylphosphoranimide **123** by the same procedure as for **114** (Eqn. **4.6**). The resulting allyl complex **122** is orange, soluble in Et_2O and THF, and slightly soluble in nonpolar solvents such as pentane or hexane. As for the ethyl analog of the dimer, **122** is also diamagnetic. The ^{31}P-NMR and ^{1}H-NMR spectra of **122** share the same signals and patterns as observed for dimeric **114**. Single crystals were grown successfully from mixed solution of THF and hexane. X-ray crystallography revealed that the solid state structure of **122** is analogous to that of **114**. Details of the structure are provided in the appendix.

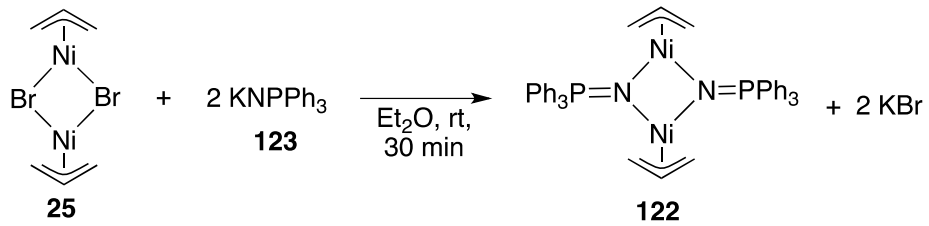

Equation **4.6**

In addition to **122**, the corresponding more electron-rich *tert*-butyl version of the complex, $[Ni(\eta^3-allyl)(NP^tBu_3)]_2$ **24,** was also pursued. Our attempt to synthesize this compound under the same conditions used previously resulted in the isolation of a green, pentane-soluble compound (Eqn. **4.7**). However, recrystallization of the product gave the mixed-valence tetramer, $[Ni_4(NP^tBu_3)_4][Li_3Br_4(Et_2O)_3]$ **26**, as discussed in the first chapter. Tetrameric **26** is proposed to the result from decomposition of the putative product **24**. When the reaction was carried out in a non-polar solvent such as hexane, the green product obtained gave an elemental analysis consistent with allyl dimer **24**. However, no single crystals could be grown to conclusively identify the structure.

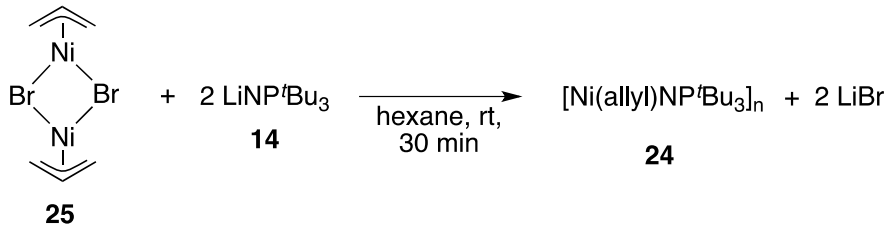

Equation **4.7**

It is also essential to mention that this green product is paramagnetic. For metals with a d^8 configuration, it is well established that in the square planar geometry, the ligands' σ-orbitals interact with the metal d_{x2-y2} orbitals to form strong bonds, at the expense of pairing eight d-electrons in the other four d-orbitals. In contrast, a near-tetrahedral geometry is favored by lower pairing energy and reduced steric crowding.[126] Thus, it is possible that the sterically bulky $[NP^tBu_3^-]$ ligand favors the tetrahedral geometry. Although paramagnetic square planar Ni(II) compounds are precedented,[127-129] they are very rare. It is also possible that the cluster **24** adopts an oligomeric structure rather than dimer or adopts a different coordination mode for the allyl groups. For example, the electron-donating $[NP^tBu_3^-]$ ligand could encourage the allyl to equilibrate between η^1- and η^3-coordination, which triggers the hemolytic scission to give allyl radicals and formation of mixed-valence byproduct **26**.

4.2.3 Trimetallic Phosphoranimide Clusters: Synthesis and Characterization of $[Ni_3(\eta^3-allyl)_3(\mu^3-NPEt_3)_2]PF_6$ 124

With the fully characterized allyl-capped dimer **114** in hand, its redox chemistry was investigated, targeting mixed-valence clusters. Oxidation with Cp_2FePF_6 was attempted, at first in THF solution. The orange product obtained from this procedure was soluble in polar solvents such as THF or DME, but not soluble in hexane, benzene or ether.

Single crystals of the product were grown successfully by cooling a saturated DME solution in the freezer of the glovebox (-35 °C). X-ray crystallography revealed the structure, an unexpected cationic *trimetallic* cluster, $[Ni_3(\eta^3-allyl)_3(\mu^3-NPEt_3)_2]PF_6$ **124** (Fig. **4.8**).

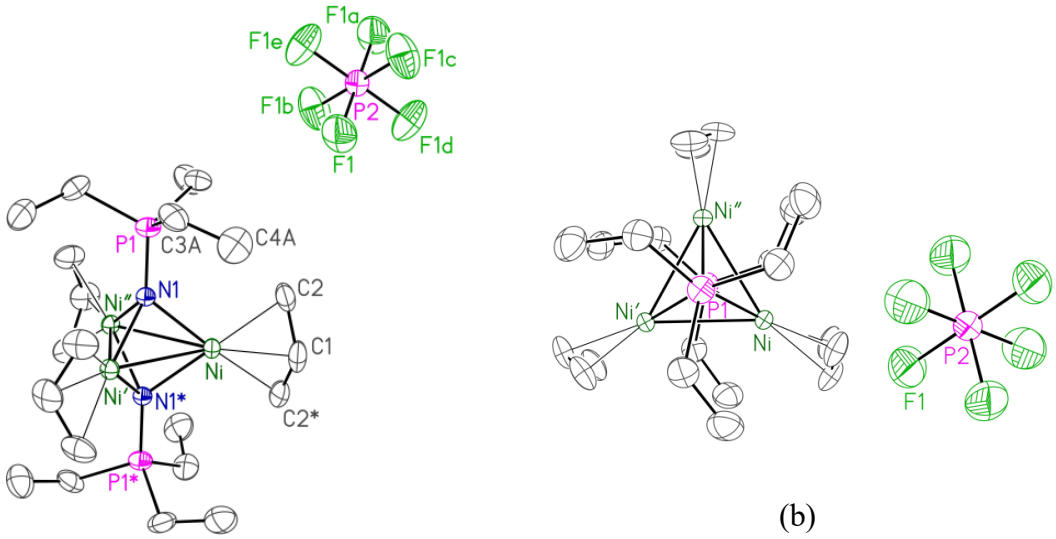

(a) (b)

Figure **4.8**: ORTEP diagram of $[Ni_3(\eta^3-allyl)_3(\mu^3-NPEt_3)_2]PF_6$ **124**, thermal ellipsoids are shown at 30% probability and hydrogen atoms have been omitted for clarity: (a) view from the side; (b) view from the top.

Based on the structure of this cluster, two equivalents of Cp_2FePF_6 are needed to provide the counter ions for three equivalents of **114**. Instead, 1.8 equivalents of Cp_2FePF_6 were

used per three equivalents of dimeric **114** so that trimetallic monocationic **124** could be separated easily from unreacted **114** due to the substantial solubility difference. Quantitative yield was obtained, considering Cp_2FePF_6 as the limiting reagent (Eqn. **4.8**).

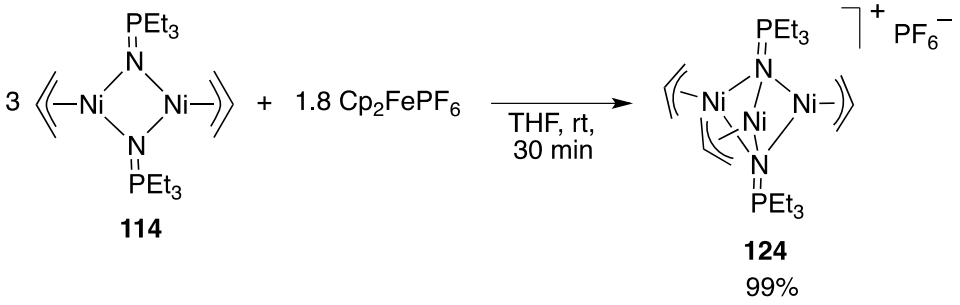

114 **124** 99%

Equation **4.8**

In the crystal structure, the three nickel atoms reside in the triangular core of the cluster, with two [$NPEt_3^-$] ligands coordinating apically on the top and bottom of the core. The nitrogen atom of each ligand coordinates symmetrically to three nickel atoms through three lone pairs. Meanwhile, each nickel atom coordinates to one allyl group through the typical η^3-bondding mode, perpendicular to the trinickel plane.

There are in total two phosphoranimide ligands, three allyl groups, and one hexafluorophosphate counter ion in each cluster, which sum to six negative charges. Thus the formal oxidation state of each nickel center is +2, surprisingly, unchanged.

This product was unexpected, considering that the oxidation state remains the same despite the oxidant that was added to the solution. Cp_2FePF_6 did not act as a catalyst because Cp_2Fe was observed among the products by NMR spectroscopy. In the product, the nickel to ligand ratio is 3 : 2, instead of 1 : 1 in the starting material. As a result, it must be the extra equivalent of ligand that was oxidized. As discussed for the LiBr adduct **116**, the nitrogen can coordinate to a Lewis acid through the basic lone pair. We propose that the observed reaction is a cluster reorganization initiated by electron transfer. First, the oxidant removed one electron from the cluster, making the nickel center electrophilic. Then the nitrogen from another dimer coordinates to the electrophilic nickel center and initiates a

reorganization process, leading ultimately to the formation of **124**. In the end, the ligand was oxidized by the oxidant. Unfortunately, an attempt to isolate the byproduct was unsuccessful.

Viewed from the top, the trinickel core constitutes an equilateral triangle, with identical nickel-nickel distances, 2.64(1) Å. The three allyl groups "point" in the same direction, clockwise in the figure. Each nickel atoms bears a twisted square planar coordination geometry with the allyl group and the two phosphoranimide residues, one above and one below. However, unlike the dimeric nickel compound $[Ni(\eta^3-allyl)(NPEt_3)]_2$ **114**, in which both Ni atoms are square planar and diamagnetic, this trimetallic cluster is paramagnetic. The reason could be the "close contacts" between the ligand ethyl group and the allyl hydrogens, which causes twisting and pseudo tetrahedral molecular orbitals. It is worth noting that in **124**, the N-Ni-N angles contract from approximately 83.3(4)° in **114** to 76.4(6)°, further away from the standard 90°.

The only similar phosphoranimide-bridged precedent for this structure is $[Ni_3(PMe_3)_3C1_3(\mu^3\text{-}NPMe_3)(\mu^3\text{-}NH)]$ **125** (Fig. **4.9**) ,[43] in which one phosphoranimide and one imido bridge the trimetallic core through an μ^3-bondding mode. The nickel centers in **125** are also all Ni(II). The Ni–Ni distances in **125** are almost the same as those found in **124**, 2.639 Å vs 2.64(1) Å. Moreover, similar bond distances are also found in Ni–N bond, 1.953 Å in **125** vs 1.94(2) Å in **124**, as well as N–P bonds, 1.609(7) Å in **125** vs 1.61(6) Å in **124**. However, the trimetallic cluster **125** is diamagnetic; each nickel center is square planar with 16 electrons in the coordination sphere.

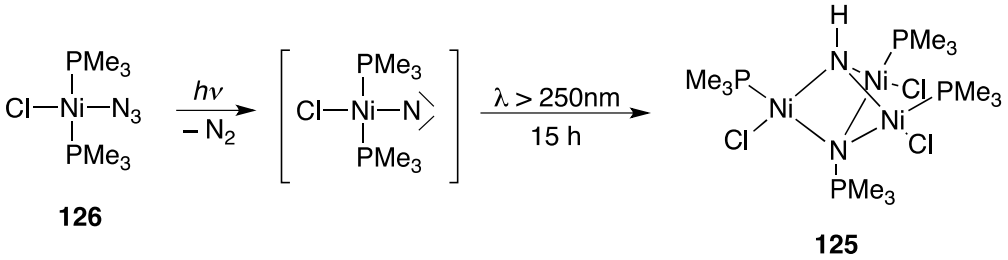

Figure **4.9**: Synthesis of $[Ni_3(PMe_3)_3C1_3(\mu^3\text{-}NPMe_3)(\mu^3\text{-}NH)]$ **125**.

Selected average bond lengths and angles for $[Ni(\eta^3\text{-allyl})(NPEt_3)]_2$ **114** and $[Ni_3(\eta^3{-}allyl)_3(\mu^3{-}NPEt_3)_2]PF_6$ **124** are listed in Table 4.1. The Ni-Ni distances are significantly shorter in trimetallic **124** than in **114**, at 2.6415(0) and 2.703(1) Å, respectively. This is likely because the three nickel atoms must bind to a single phosphoranimide nitrogen atom in **124**. The Ni-N bonds are longer in the trimetallic **124**, at 1.942(0) Å vs 1.900(2) Å, as are the P-N bonds, 1.616(0) Å vs 1.551(6) Å. This lengthening is also expected because the nitrogen atoms in **124** are prone to sp^3-hybridized, providing less s-character to both the Ni-N bonds and N-P bonds. The Ni-N-Ni angles are more acute in **124**, again due to the same change in hybridization. As discussed earlier, the N-Ni-N angles contract from approximately 83.28(7)° to 76.48(0)°, again due to the complete change in bonding mode.

Table **4.1**: Selected average bond lengths and angles in **114** and **124**.

	$[Ni(\eta^3\text{-Allyl})NPEt_3]_2$	$[Ni_3(\eta^3\text{-Allyl})_3(\mu^3\text{-}NPEt_3)_2]PF_6$
Ni–Ni (Å)	2.703(1)	2.6415(0)
Ni–N (Å)	1.900(2)	1.942(0)
P–N (Å)	1.551(6)	1.616(0)
N-Ni-N (°)	83.28(7)	76.48(0)
Ni–N–Ni (°)	90.73(2)	85.72(0)

4.2.4 Heterotrimetallic Transition Metal Clusters: Synthesis and Characterization of $[(\eta^3\text{-allyl})Ni]_2CoCl_2(\mu^3\text{-}NPEt_3)_2$ 126

The Lewis basic character of the doubly-bridged phosphoranimide nitrogen can be exploited to build heterometallic transition metal clusters by rational design. Both the LiBr adduct **116** and trimetallic cation **124** support this idea. As also demonstrated in this chapter, the three-coordinate phosphoranimide is generally more stable than the two-coordinate ligand, which includes a strongly nucleophilic lone pair on nitrogen. Thus, we next investigated the use of neutral dimer **114** as a precursor to prepare heterotrimetallic clusters triply-bridged by two phosphoranimide ligands.

In this demonstration, anhydrous $CoCl_2$ **127** was used as an unsaturated, Lewis acidic metal complex. The reaction is shown below (Eqn. **4.9**), leading to the formation of a green compound, isolated in 58% yield (once the structure was determined). The product was soluble in THF, slightly soluble in Et_2O, and insoluble in nonpolar solvents such as hexane or benzene.

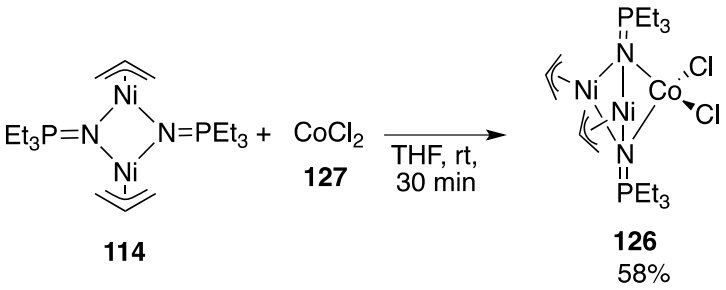

Equation **4.9**

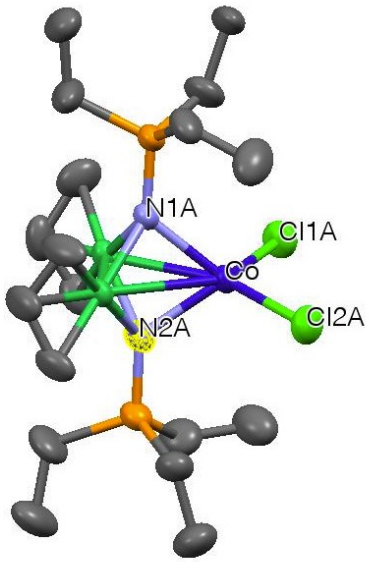

Figure **4.10**: ORTEP diagram of $[(\eta^3\text{-allyl})Ni]_2CoCl_2(\mu^3\text{-}NPEt_3)_2$ **126**, thermal ellipsoids are shown at 30% probability and hydrogen atoms have been omitted for clarity.

Rigorous characterization again required X-ray crystallography. Single crystals were obtained by cooling a saturated THF solution to -35 °C. The structure solution revealed the cluster to the $CoCl_2$ adduct of dimer **114,** with the formula $[(\eta^3\text{-allyl})Ni]_2CoCl_2(\mu^3\text{-}NPEt_3)_2$

126 (Fig. **4.10**). Both of the nitrogen atoms coordinate to the cobalt metal, forming a similar core structure to that seen in trimetallic nickel cation **124**. The phosphoranimide ligand coordinates apically to two nickels and one cobalt, and the allyl groups coordinate to the nickel in a typical η^3-bonding mode, perpendicular to the Ni_2Co plane. On the cobalt side, two chlorides reside almost in the same plane as the Ni_2Co core, making the cobalt pseudo-tetrahedral. The compound is paramagnetic, not surprisingly, due to the d^7 configuration of Co center.

In a comparison of the average bond lengths between heterotrimetallic **126,** neutral dimer **114** and trimetallic **124**, the same trends are found upon introduction of the third metal center (Table **4.2**). With the phosphoranimide ligands coordinated to three metals, the Ni-Ni distance contracts from 2.703(1) Å in **114** to 2.5827(5) Å in **126**. The Ni-N bonds become longer and weaker, stretching from 1.900(2) Å to 1.948(7) Å, close to the 1.942(0) Å observed in cationic **124**. Similar changes in bond distances were observed for the P–N bond, elongating from 1.551(6) Å to 1.606(1) Å, again very close to the distance in **124**. In contrast, the Co-N distances are longer than the Ni-N distances, averaging 2.031(4) Å versus 1.948(7) Å. This is likely because the nickel and cobalt centers are in very different electronic environments and coordination spheres. In a word, when the third metal is introduced, the metals are brought closer to each other, and the Ni–N and P–N bonds become weaker and longer.

Table **4.2**: Selected average bond lengths for **114**, **124**, and **126**.

	114	**124**	**126**
Ni–Ni (Å)	2.703(1)	2.6415(0)	2.5827(5)
Ni–N (Å)	1.900(2)	1.942(0)	1.948(7)
P–N (Å)	1.551(6)	1.616(0)	1.606(1)

Synthetically, attempts to convert heterotrimetallic **126** into hydrotreatment precatalyst by double methylation at cobalt using Me_2Mg in dioxane were unsuccessful, as no product could be characterized (Eqn. **4.10**). It is possible that the Co is reduced instead of alkylated. In future development, it is worth attempting to convert **126** to a cationic heterotrimetallic

cluster with an outer-sphere counter anion first, followed by allylation to form a compound isostructural to **124**.

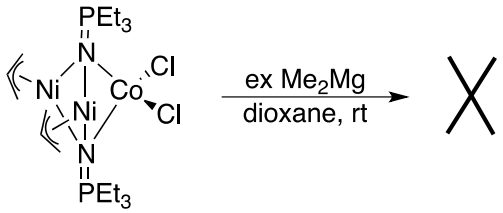

126

Equation **4.10**

The assembly of a heterotrimetallic cluster proves the rationality and provides a potentially general strategy to expand this chemistry to other Lewis acidic metals, preparing a series of heteropolymetallic precatalyst clusters. Further study on syntheses of heteropolymetallic clusters and investigation of their potential as hydrotreatment precatalysts is continuing.

4.2.5 Generalizing allyl precatalyst Synthesis: Preparation of $[Co(\eta^3\text{-allyl})(NPEt_3)]_n$ 128

To expand the scope of allylated phosphoranimide precatalysts, we targeted the synthesis of analogous allyl-capped cobalt complexes. The synthesis of this cluster and its use in catalysis is now under investigation by Ms. Fiona Nkala and Dr. Kseniya Revunova in our group. Thus the details of this chemistry will be presented in Ms. Fiona Nkala's thesis. Herein, the syntheses are discussed briefly.

The synthesis of the dimeric cobalt cluster $[Co(\eta^3\text{-allyl})Cl]_n$ **129** was demonstrated, simply by adding equimolar allyl Grignard reagent to a suspension of $CoCl_2$ (Eqn. **4.11**). The green product passes elemental analysis for $[Co(\eta^3\text{-allyl})Cl]_n$, however no single crystals have been obtained to date. The reason could be a highly disordered allyl group, a mixture of different oligomers, or disproportion or the putative product. Either will make the recrystallization difficult.

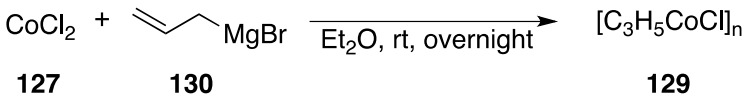

Equation **4.11**

A range of phosphoranimide anions were added to this precursor. The use of $KNPEt_3$ **115** provided impure product(s) that could not be isolated or characterized (Eqn. **4.12**). In contrast, the addition of KNP^tBu_3 **132** led to the isolation of an orange-brown compound **133**, which passed combustion analysis for this formula (Eqn. **4.13**). Unfortunately, no crystals of this material have been obtained.

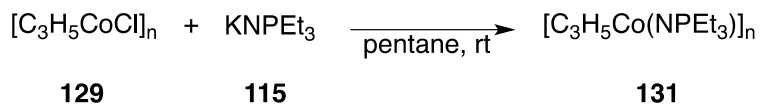

Equation **4.12**

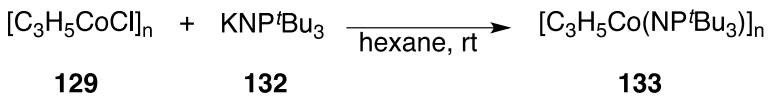

Equation **4.13**

4.3 Conclusion

In this chapter, the syntheses and characterization of allyl-capped phosphoranimide-bridged nickel dimers are reported (**114**, **122**, and **24).** $[Ni(\eta^3\text{-allyl})(NPEt_3)]_2$ **114** and $[Ni(\eta^3\text{-allyl})(NPPh_3)]_2$ **122** were synthesized and fully characterized using infrared spectroscopy, NMR spectroscopy, X-ray crystallography, and elemental analysis. The synthesis of $[Ni(\eta^3\text{-allyl})(NP^tBu_3)]_2$ **24** was unsuccessful due to the thermal instability of the dimer.

This new set of compounds is important for developing new hydrotreatment catalysts. **114** and **122** are the first two diamagnetic compounds of their kind, providing opportunity for more mechanistic study by NMR spectroscopy. In addition, the allyl-capped dimers are

thermally more stable and tunable than the early tetrametallic series, which allows for further substituent exploration.

The trimetallic cationic cluster, $[Ni_3(\eta^3\text{-Allyl})_3(\mu^3\text{-NPEt}_3)_2]PF_6$ **124**, was synthesized fortuitously when the mixed-valent dimer was targeted. Based on **124** and the LiBr adduct **116**, a rational design for the preparation of heterotrimetallic clusters was demonstrated by the successful synthesis of $[(\eta^3\text{-allyl})Ni]_2CoCl_2(\mu^3\text{-NPEt}_3)_2$ **126**.

The syntheses and characterization of the new trimetallic clusters **124** and **126** is of great potential for preparing heteropolymetallic clusters by rational design. By exploiting the basicity of the nitrogen in double-bridged precursors, it should be possible to develop a general strategy for accessing a large number of heteropolymetallic clusters.

Chapter 5. Phosphoranimide-bridged Nickel Clusters for Catalytic Hydrodesulfurization (HDS)

5.1 Introduction

In recent years, the increasing demand for cleaner transportation fuel with lower toxic gas emissions (SO_x and NO_x) brings new challenges to the petroleum upgrading industry.[130] New upgrading technology is imperative, especially for the oil sands industries, to meet the increasingly stringent regulatory limitations, as the crude oil from the oil sands has high content of sulfur, nitrogen, and metals. The current methods used in the industry are based on delayed-coking to remove the bulk of the nitrogen, metals, and asphaltene fractions of bitumen, followed by catalytic HDS, mostly using sulfided second- and/or third-row transition metals, primarily molybdenum or tungsten, promoted by cobalt, nickel.[131] The HDS process requires intensive heating (300–650°C) and high pressure of hydrogen (10–120 atm) to extrude the sulfide from the precatalyst and generate coordination vacancies on the surface.

Industrial research into heterogeneous HDS catalysis has spanned more than half a century, yet the study of heterogeneous catalysts remains mainly focused on molybdenum sulfides.[52,56] Research suggests that first-row transition metal sulfides suffer low activity compared to the second- and third-rows metals. The activity of metal sulfides is known and can be depicted as a "volcano plot" (Fig. **5.1**).[53,54]

However, recent studies on the role of the cobalt and nickel promoters in commercial Co-MoS_2 catalysts have revealed a possible alternative interpretation of activity.[57] The HDS activity of first-row transition metal sulfide is greatly affected by the catalyst support. Improved activity has been observed for cobalt sulfide when supported on carbon and for nickel sulfide supported on silica. In addition, Raney nickel[132-134] itself is capable of stoichiometric desulfurization of dibenzothiophene (DBT) under mild conditions, a common model compound for deep HDS. Thus, we believe that soluble *molecular*

catalysts derived from cobalt, nickel, or other first-row transition metals could show competitive activity, with appropriate "engineering".

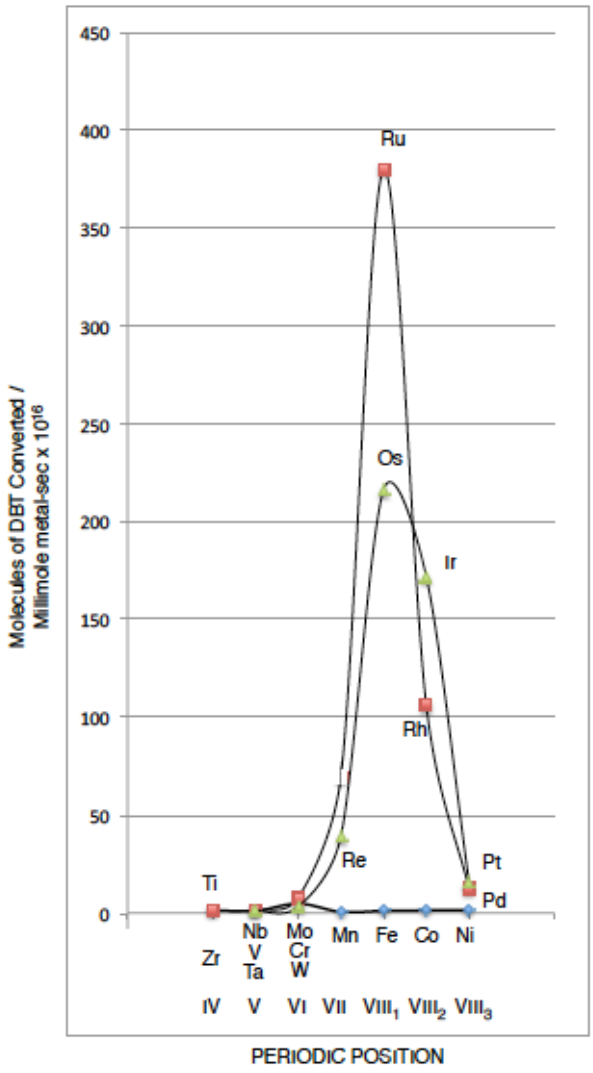

Figure **5.1**: HDS activity of transition metal sulfides as a function of their periodic position.

In contrast, research into homogeneous catalysts for HDS was not limited to metal sulfides; however, this field has not been very fruitful. Several HDS systems have been developed, among which most provide only stoichiometric HDS or hydrogenative C–S bond scission.[135-140]

In general, several philosophies have been adapted in the design of HDS catalysts: (1) low-coordinate, low-valent metal centers commonly infiltrate the design of HDS model catalysts, and are proposed to facilitate substrate coordination and the oxidative addition of the C–S bond; (2) transition metal hydrides were also believed to be important intermediates in heterogeneous HDS, so many metal hydrides were prepared; and (3) catalysts incorporating multiple metal atoms in clusters were designed, aiming to represent the metal-metal cooperation assumed for heterogeneous catalysts. Most of the homogeneous catalysts were designed to have one, some, or all of these characteristics.

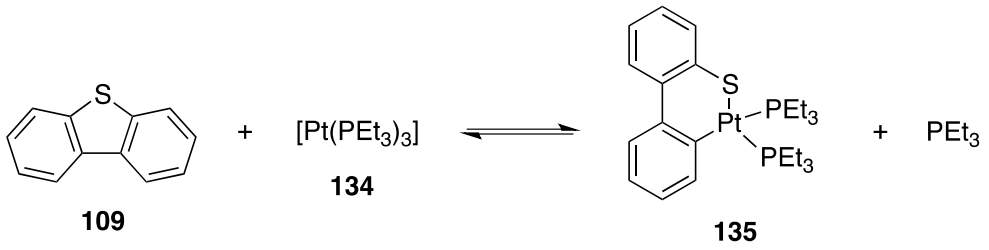

Figure **5.2**: C–S bond scission using **134**.

For example, the low-valent Pt(0) compound $[Pt(PEt_3)_3]$ **134** is capable of undergoing oxidative addition of the C–S bond of **109**, reversibly (Fig. **5.2**).[135,137] As for first-row transition metals, the low-valent unsaturated Co intermediate formed upon heating **136** was also reactive toward C–S bond scission, in this case of thiophene **137** (Fig. **5.3**).[138]

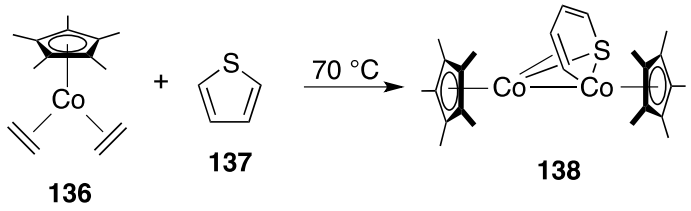

Figure **5.3**: C–S bond scission of **137** using Co complex **136**.

Tripodal phosphine-stabilized iridium hydride **139,** developed by Bianchini, Sanchez-Delgado, et al.[136] is an active catalyst for DBT HDS. Although the TOF is only about 0.4/h, it is the only homogeneous compound that turns over under hydrogen pressure (Fig. **5.4**).

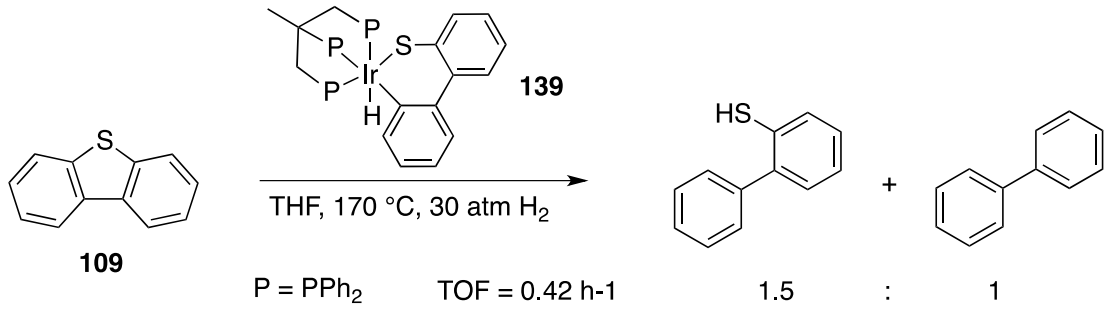

Figure **5.4**: HDS using Ir complex **139**.

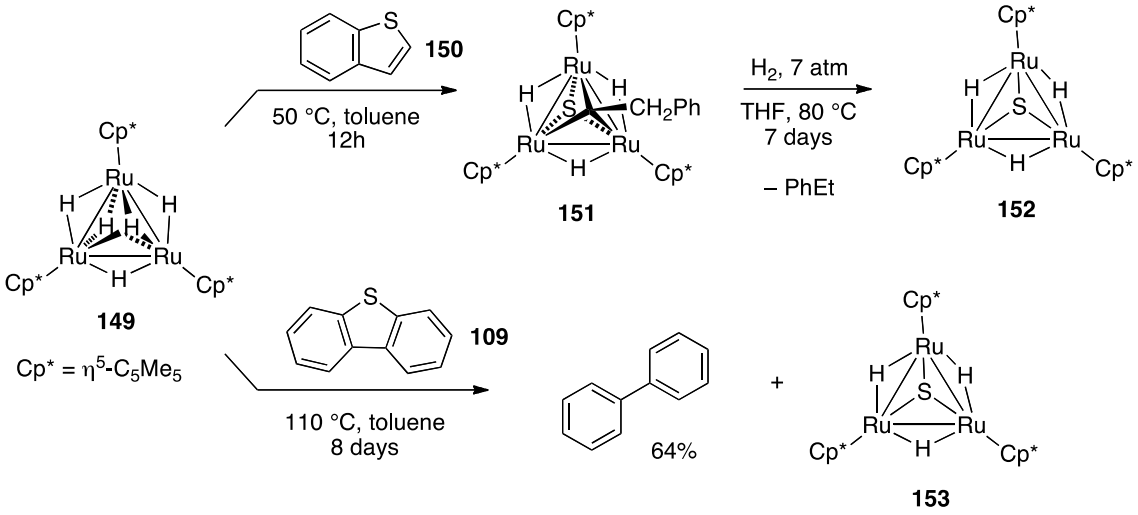

Figure **5.5**: Stepwise HDS using trimetallic ruthenium hydride cluster **149**.

Furthermore, several multimetallic clusters have been developed that perform stoichiometric HDS. Two of the most representative and relevant are the trimetallic ruthenium hydride cluster **149**[139] (Fig. **5.5**) and the Ni(I) hydride dimer **154**[140] (Fig. **5.6**). Both accomplish stoichiometric HDS under relatively mild conditions (rt to 110°C), but only slowly.

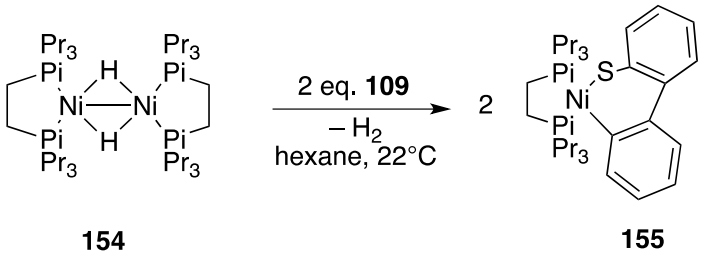

Figure **5.6**: HDS using Ni(I) hydride dimer **154**.

M. David Curtis, et al., reported the tetrametallic mixed Co/Mo sulfide cluster **156**,[141] which is a mimic of the commercial heterogeneous catalysts (Fig. **5.7**). Research into this complex has provided valuable insight into the binding of substrate, C–S bond scission, and metal-metal cooperation.

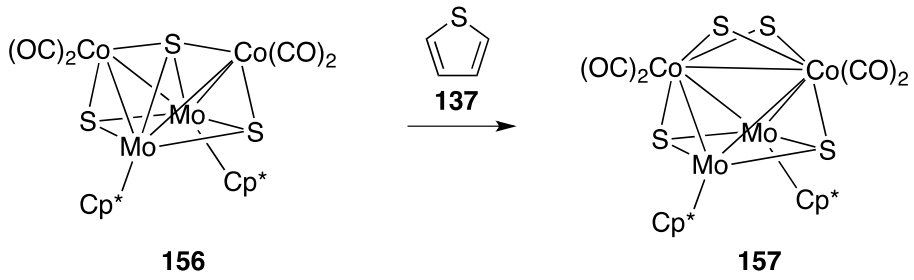

Figure **5.7**: Desulfurization of **137** using Co/Mo sulfide cluster **156**.

Our group has synthesized the phosphoranimide-bridged first-row transition metal clusters for catalytic HDS under mild conditions, as they are coordinatively unsaturated multimetallic clusters that could form metal hydride intermediates with appropriate activation. According to a preliminary HDS study by Dr. Jeffrey Camacho-Bunquin, the putative neutral nickel cluster **18** is an active HDS catalyst when using stoichiometric KH as an irreversible scavenger for H_2S (Eqn. **5.2**). As the pure neutral cluster **18** is now available, it became imperative to reinvestigate this putative HDS activity. Furthermore, the unusually specific role of KH as a promoter for HDS will also be discussed.

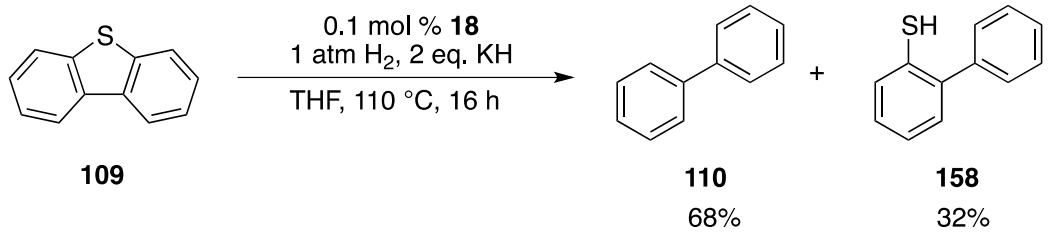

Equation **5.2**

Finally, the catalytic HDS activity of two allyl-capped precatalysts, $[Ni(\eta^3\text{-allyl})(NPEt_3)]_2$ **114** and $[Ni_3(\eta^3\text{-allyl})_3(\mu^3\text{-}NPEt_3)_2]PF_6$ **124** for hydrogenation and HDS were also studied,

together with a preliminary exploration of a simple heterogeneous nickel catalyst for hydrogenation.

5.2 Result and discussion

5.2.1 The non-innocent role of strong base scavengers in catalytic HDS

In the preliminary results obtained by Dr. Jeffrey Camacho-Bunquin (Eqn. **5.2**), the role of the strongly basic scavenger, potassium hydride (KH), is suspicious. KH was introduced to behave as a passive Brønsted base, reacting with H_2S and **158** to neutralize the acidic protons. However, when other similarly strong bases, such as NaH or CaH_2 were used, the activity is much lower than with KH (Table **5.1**). This suggested that KH behaves as more than just an innocent base, functioning more or less as a "promoter" for HDS, thus worthy of investigation more carefully.

Table **5.1**: Conversion of **109** to **110** and **158** with different scavengers.

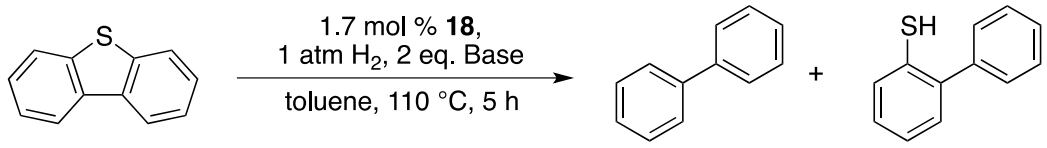

109 **110** **158**

Entry	Base	% Conversion	
		110	**158**
1	CaH_2	1	0
2	NaH	13	0
3	KH	28	18

In early control experiments using purified (K^0-free) KH in both toluene and THF, dramatically improved conversion rates were obtained in THF. Initially, it was proposed that the improvement was due to the improved solubility of the intermediate thiolate in the polar solvent, after breaking only the first C–S bond. However, control experiments suggested an alternative explanation (Table **5.2**): KH itself can accomplish HDS at elevated

temperatures (≥110 ºC), regardless of the presence of hydrogen (Entry 1, 3). In THF, moderate conversion of 34% was obtained for **158** without hydrogen (Entry 1), and a slightly lower conversion of 28% for **158** was obtained when hydrogen was present (Entry 2). In contrast, much lower conversions (1% and 2%) were obtained in toluene at the same temperature (Entry 3, 4), presumably due to the lower solubility of KH in the less polar solvent.

Table **5.2**: Control experiment of KH for HDS with/without hydrogen.

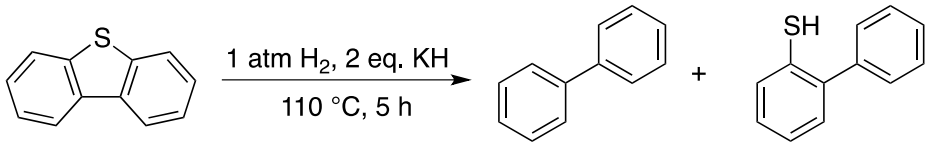

109 **110** **158**

Entry	Control Conditions	Solvent	% Conversion	
			110	**158**
1	KH	THF	1	34
2	KH+H_2	THF	0	28
3	KH	Toluene	0	2
4	KH+H_2	Toluene	0	1

Further isotopic control experiments reveal deuterium scrambling into all of the aromatic hydrogens in DBT under normal HDS conditions (Eqn. **5.3**). Thus we propose that the KH itself deprotonates the aromatic protons, which may lead to C–S bond scission of **109** through a benzyne intermediate. In addition, alkali metals are known to accomplish stoichiometric HDS in the presence of hydrogen.[142,143] Thus bulk KH could also behave as a strong reducing reagent to transfer one electron to DBT, which would also lead to C–S bond scission. In reality, the reason for the HDS activity of KH could be combination of its strong basicity, reducing potential,[65] nucleophilic hydride source itself, and more unusually, the promoter effect of potassium cation.

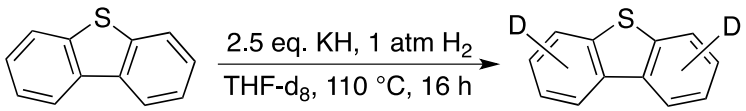

109

Equation **5.3**

In summary, KH should not be used as a base scavenger in THF due to substantial background reaction(s). In toluene, it is tolerable to use KH for preliminary exploration to prove activity, considering that the background conversion is only 2%, at most, to give **158**. However, considering the ambiguous HDS activity in THF and safety constraints for handling the purified, surface-active KH, replacement by an alternative passive hydrogen sulfide scavenger is imperative.

5.2.2 The search for new scavengers for use in catalytic HDS

Before the discussion of the scavenger hunt, the promotional effect of potassium cation needs to be discussed more thoroughly. In the initial scavenger exploration using heterocubane cobalt catalyst **22**, Dr. Houston Brown discovered that higher conversions were observed when the potassium salts of a given base were used, compared the sodium or lithium salts (Table **5.3**). Even through the reactions were run in THF, which could be problematic for KH, the promoting effect of the potassium cation was obvious.

When HDS catalysis using different metal clusters was investigated in our group, similar results were obtained consistently: stoichiometric potassium salts provided higher activities, as demonstrated through the use of KDA versus LDA, KTMP versus LiTMP, and KO^{t}Bu versus NaO^{t}Bu.

The "K^+ effect" is precedented in HDS reactions using a ruthenium catalyst. In 1998, Bianchini et al. reported the HDS of benzothiophene **150** using catalytic [(triphos)RuH(BH_4)] **159** (triphos = MeC(CH_2PPh_2)$_3$). The authors noted that the addition of KO^{t}Bu accelerates the reaction, possibly by promoting the reductive elimination of ethylthiophenol to regenerate the ruthenium hydride **160**[136] (Fig. **5.8**).

Table **5.3**: Catalytic HDS of DBT using **22** with different scavengers.

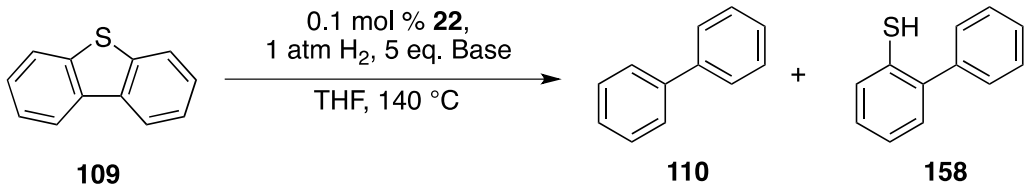

109 **110** **158**

Entry	Scavengers	Time (h)	TOF(h^{-1})[a]
1	NaO^{t}Bu	16	0
2	KO^{t}Bu	16	0
3	LDA	16	0.71
4	KDA	16	32.73
5	LiTMP	16	0.55
6	KTMP	16	75.5
7	NaH	16	0
8	KH	0.4	310[b]

[a] C–S bond cleavages per mol of cluster per hour over the 16 h reaction period, as determined from product distributions by GC-MS. Single point TOF determination.
[b] Rxn proceed to completion, calculated TOF is considered a minimum.

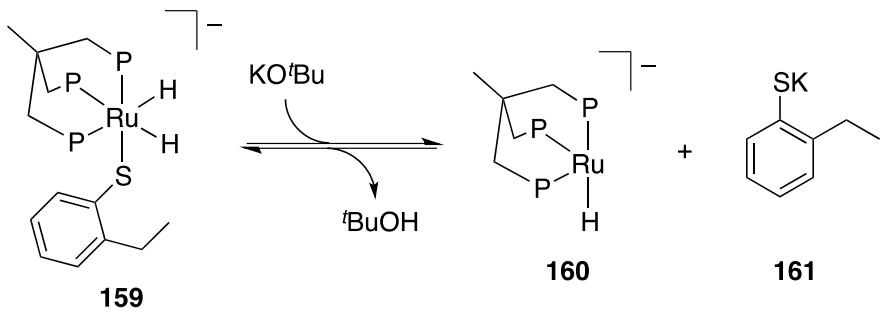

159 **160** **161**

Figure **5.8**: Proposed reductive elimination of **159** accelerated by KO^{t}Bu.

In addition, there have been several studies regarding the coordination of alkali metal cations to metal sulfide systems by dative bond formation and the effects of metal additives on activity.[144-148] Thus we propose that the potassium cation, *perhaps uniquely*, can coordinate to the metal sulfide intermediates, and this coordination may accelerate the hydrogenative sulphur extrusion and regeneration of the metal hydride (Fig. **5.9**). The

reason why potassium is special is not yet clear, but the heavier element might provide a better orbital match with the lone pair on sulphur. To assess this assumption, several members of the group have recently been engaged in synthesizing discrete metal sulfide clusters containing phosphoranimide ligands. As possible HDS intermediates, these sulfide-containing clusters could provide an understanding of the sulphur extrusion step, facilitating the development of catalytic potassium promoter for HDS.

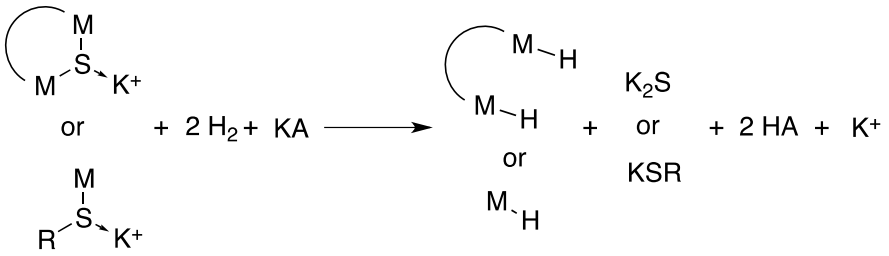

Figure **5.9**: Proposed mechanism for "K^+ effect".

In the following investigation, selected strong potassium bases other than KH were assessed as scavengers for HDS. The results of control experiments, run in the absence of catalyst, are listed in Table **5.4**. From entries 1-4, it is obvious that KTMP can itself mediate HDS in the presence of hydrogen. Substantial conversion was observed even under one atmosphere of hydrogen at 110 ºC (Entry 2). Conversions were higher at increased temperature (Entry 3 versus Entry 2) and higher hydrogen pressure (Entry 4 versus Entry 3). Even in a less polar solvent, cyclooctane, significant conversion was observed (Entry 1). The cases of KNH_2 is similar, with substantial conversion to **110** and **158** (Entry 5). When KHMDS is used as scavenger, no background activity was observed under one atmosphere of hydrogen at 150 ºC (Entry 6), however under higher pressure 59% conversion to **158** was observed (Entry 7). Thus the nitrogen-based scavengers should be avoided in all further HDS study. From Entries 7-9, it is clear that the less basic KO^{t}Bu and K_2S scavengers provided no conversions, even under high pressure of hydrogen (500 psi). The other insight we obtained from the control experiments is that the basicity of the scavenger is a more important factor to the HDS activity, compared with the nucleophilic hydride and reducing potential.

Table **5.4**: Control experiment using different potassium scavengers for HDS.

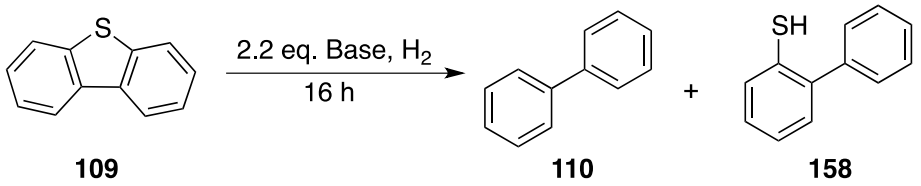

109 **110** **158**

Entry	Base	Solvent	Temperature (ºC)	H_2 (atm)[a]	Conversions (%)	
					110	**158**
1	KTMP	Cyclooctane	175	34	36	42
2	KTMP	Toluene	110	1	1	8
3	KTMP	Toluene	150	1	8	68
4	KTMP	Toluene	150	10	11	72
5	KNH_2	Toluene	150	1	44	27
6	KHMDS	Toluene	150	1	0	0
7	KHMDS	Toluene	150	34	1	59
8	KO^{t}Bu	Toluene	150	34	0	0
9	KO^{t}Bu	Cyclooctane	175	34	0	0
10	K_2S	Toluene	175	34	0	0

[a] The hydrogen pressure is the pressure under room temperature. The pressure was higher after heating.

In summary, the use of strongly basic scavengers (KTMP, KNH_2, KHMDS, and KH) must be avoided when evaluating HDS catalysts. Instead, the less basic, commercially available, and easy-to-handle solid bases KO^{t}Bu and K_2S are appropriate for use as passive scavengers, provided the catalysts are reactive enough.

5.2.3 HDS activity of [Ni(NP^{t}Bu$_3$)]$_4$ 18

The HDS activity of the neutral cluster [Ni(NP^{t}Bu$_3$)]$_4$ **18** has been investigated using the new scavengers. The cationic cluster [Ni$_4$(NP^{t}Bu$_3$)$_4$]BPh$_4$ **23** was not investigated due to the limitations in solubility. Cationic **23** is only soluble in polar solvents, such as THF, and insoluble in toluene. Furthermore, when **23** was exposed to KO^{t}Bu, an immediate color

change from blue to green was observed, suggesting the facile reduction to neutral **18** by the base.

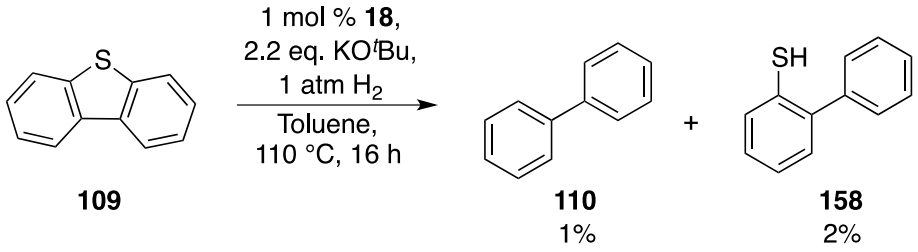

Equation **5.4**

Using the neutral catalyst **18** and KO^{t}Bu as scavenger, only low conversion was observed under the mildest HDS conditions (110 ºC, 1 atm H_2) (Eqn. **5.4**). This is probably due to the greatly reduced basicity of KO^{t}Bu compared with KH and KTMP.

Separately, another group member, Orain Brown, develop a new reaction conditions for heterogeneous HDS using weaker base scavengers (KO^{t}Bu or K_2S). The overall optimized conditions were 175 ºC, 34 atm H_2, and high surface area γ-alumina. Alumina functions as a support for heterogeneous phosphoranimide catalysts, by one of two mechanisms: (1) by coordination of the nitrogen lone pair of the doubly bridging phosphoranimide to a Lewis acidic site on the alumina surface or (2) by protonolysis of a terminal phosphoranimide ligand, to graft the cluster to a weakly acidic $(–O)_3AlOH$ residue. By grafting the metal clusters on the alumina surface, the chance of catalyst decomposition/agglomeration is reduced substantially.

HDS using neutral cluster **18** was investigated under the newly optimized conditions. Conversions were improved dramatically, and up to 93% conversion to biphenyl **110** was observed (Fig. **5.5**). Even through these reaction conditions are more intensive than the general conditions previously used, the temperature and pressure are still lower than current industrial methods.

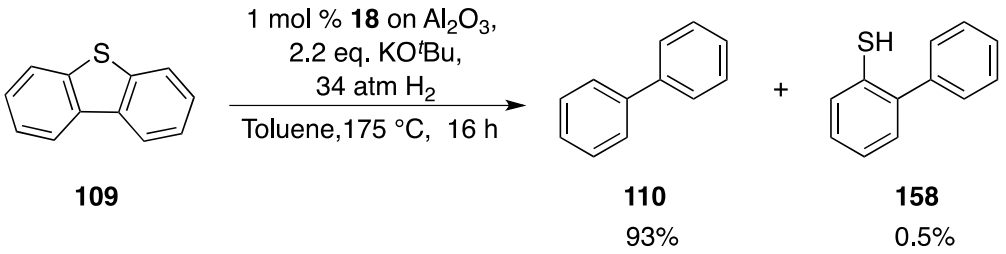

109 **110** 93% **158** 0.5%

Equation **5.5**

Importantly, HDS conditions using the insoluble, weakly basic K_2S as a scavenger were also investigated using alumina-supported catalysts. Selected results are presented in Table **5.5**, showing temperature and pressure effects on the HDS of **109**. Based on the results, it is clear that the activity is more affected by temperature (Entry 2 versus Entry 3) than hydrogen pressure (Entry 1 versus Entry 3). Excellent conversion to **110** was obtained when the temperature was raised to 200 ºC. The "K^+ effect" is still an important factor, as there was barely any conversion when Na_2S (Entry 4) or Li_2S (Entry 5) were used. Finally, much lower conversions were observed when **18** was replaced by other Ni compounds.

Table **5.5**: HDS results using **18**, when M_2S was used as scavenger.

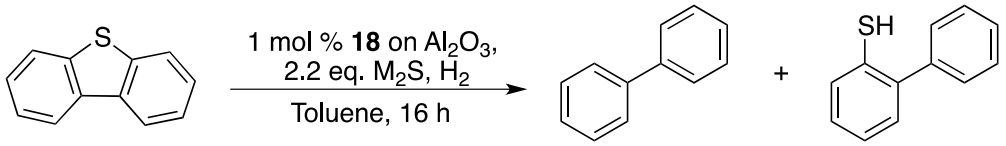

109 **110** **158**

Entry	Catalyst	M_2S	Temperature (ºC)	H_2 (atm)[a]	Conversions (%)	
					110	**158**
1	**18**	K_2S	175	14	42	1
2	**18**	K_2S	175	34	42	1
3	**18**	K_2S	200	34	83	0.5
4	**18**	Na_2S	175	34	1	1
5	**18**	Li_2S	175	34	1	0
6	$Ni(COD)_2$	K_2S	175	34	3	0
7	NiS	K_2S	175	34	0	0

[a] The hydrogen pressure is the pressure under room temperature. The pressure was higher after heating.

In conclusion, under new reaction conditions and immobilized one a support, high HDS activity was observed for neutral precatalyst **18**. As scavengers, both KO^{t}Bu and K_2S are much more commercially affordable and easy to handle, and the insolubility of K_2S and K_2S_2 make them ideal laboratory scavengers for catalyst investigation. As these preliminary results show, the concept of using structurally engineered first-row transition metal clusters for HDS treatment makes it possible to consider further development and ultimately, industrial applications.

5.2.4 HDS activity of M[Ni$_4$(NP^{t}Bu$_3$)$_4$] (M = Na, K)

The HDS activity of anionic cluster **31** was also investigated since the γ-alumina supporting could reduce the chance of decomposition substantially. The anionic cluster **31** was prepared *in situ* and mixed with γ-alumina. The color of the alumina changed from white to grey within 5 minutes and the solution turned colorless. The potassium analog of the anionic cluster K[Ni$_4$(NP^{t}Bu$_3$)$_4$] **162** was also investigated by reduction with KC_8 and grafting on γ-alumina. The HDS was run under the optimized condition and the results are shown below in Table 5.6.

Table **5.6**: HDS results using **31** or **162**, when MO^{t}Bu was used as scavenger.

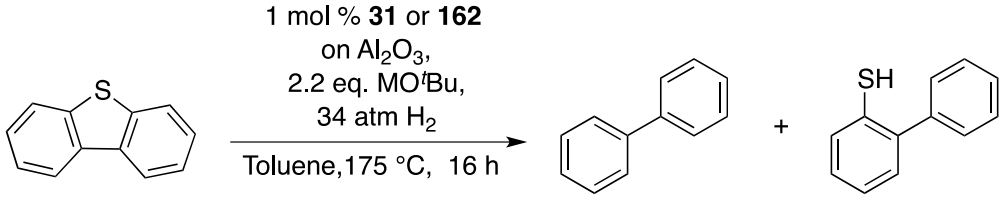

109 **110** **158**

Entry	Catalyst	Base	Conversions (%)	
			110	**158**
1	**31**	NaO^{t}Bu	12	0
2	**31**	KO^{t}Bu	98	0
3	**162**	NaO^{t}Bu	9	0
4	**162**	KO^{t}Bu	89	1

Based on the results, close to quantitative conversion (98%) was obtained for **31** under optimum conditions (Entry 2), although the accurate reaction rate was not known since the reaction could be completed before 16 hours. A relatively close conversion, 89%, was observed for anionic cluster **162**, suggesting similar HDS activity for anionic cluster. The comparison between Entry 1 versus 2, and Entry 3 versus 4 eatablished that the promoting effect is substantial, and there is close to 10 times difference between NaO^{t}Bu and KO^{t}Bu as scavengers. Moreover, a stoichiometric amount of K^+ cation is necessary, comparing to the catalytic amount present in Entry 3.

The anionic cluster **31** is the most active catalyst among all the phosphoranimide-bridged first-row transition metal clusters. Besides the 98% conversion under optimum condition, it is the only catalyst that turns over at all when NaO^{t}Bu is used as the scavengers. Further study is continuing in the group.

5.2.5 Preliminary hydrogenation and HDS study of [Ni(η^3-allyl)(NPEt$_3$)]$_2$ 114

The allyl-capped nickel dimer [Ni(η^3-allyl)(NPEt$_3$)]$_2$ **114** was designed as a second-generation nickel phosphoranimide precatalyst for HDS. For hydrogen to react with the cluster, the allyl group must undergo η^3–η^1 isomerization, dissociating to provide a vacant coordination site. Thus NMR spectroscopy under elevated temperatures was studied in deuterated toluene (C_7D_8). Both ^{1}H-NMR and ^{31}P-NMR spectra at various temperatures were obtained. The two sets of allyl group signals become broadened at 80°C and eventually coalesced into one set of signals at higher temperatures. Thus, the rate of allyl isomerization becomes fast on the NMR time scale above 80 °C. In addition, a slight color change from red to orange was also observed when the precatalyst was heated in the presence of hydrogen. Since this temperature is still lower than the reaction temperatures required for HDS, precatalyst activation should not be a limitation for **114** and other similar allyl-capped nickel phosphoranimide clusters.

As a prerequisite for HDS, catalytic hydrogenation using [Ni(η^3-allyl)(NPEt$_3$)]$_2$ **114** was investigated to establish the activity of the cluster. The reaction temperature was set at 100

°C to promote allyl activation and a 5% loading of catalyst was used. Full conversion of **20** to **42** was observed, although the long reaction time probably masks the actual reaction rate (Eqn. **5.6**). In addition, the hydrogenation activity of the trimetallic cation $[Ni_3(\eta^3\text{-allyl})_3(\mu^3\text{-NPEt}_3)_2]PF_6$ **124** was also demonstrated. Quantitative conversion of **20** to **42** was also observed, with the same catalyst loading and conditions (Eqn. **5.6**). No conversions were obtained using dimeric **114 or 124** at room temperature, suggesting that elevated temperature is necessary for precatalyst activation.

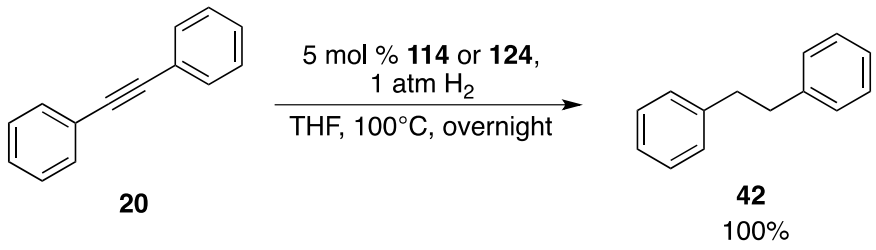

Equation **5.6**

Thus, both $[Ni(\eta^3\text{-allyl})(NPEt_3)]_2$ **114** and $[Ni_3(\eta^3\text{-allyl})_3(\mu^3\text{-NPEt}_3)_2]PF_6$ **124** are catalysts for the hydrogenation of **20**. Elevated temperature is necessary for the reaction to proceed. The results, however, proves that nickel hydrides are likely produced during hydrogenation and, potentially, for other hydrotreatment process such as HDS.

A thorough HDS investigation of allyl-capped dimer **114** has also been accomplished. Surprisingly, KO^{t}Bu is effective as the scavenger for both supported and unsupported versions of the catalyst. The results are presented in Table **5.7**, showing that only stoichiometric conversion was observed at low hydrogen pressure (1 atm) (Entries 1,2). This is consistent with the HDS results using **18** in supported form: when KO^{t}Bu is used as scavenger, higher hydrogen pressure is necessary to turn the catalyst over. When the hydrogen pressure was increased to 34 atm, the conversions obtained are dependent on the polarity of the solvent. In THF (Entry 3), only stoichiometric conversion was obtained, while a significant increase in conversion was observed using the less polar solvents toluene (Entry 4) and cyclooctane (Entry 5). Slightly higher conversion was obtained in the less polar of the two solvents, cyclooctane. The exact reason for the difference is still

unknown, but we propose that the dimeric nickel cluster intermediate may be more prone to aggregation/decomposition in polar solvents. Upon supporting the precatalyst on γ-alumina, the conversions were only slightly improved (Entries 6,7) in both toluene and cyclooctane, which is very different from the dramatic improvement obtained using the supported version of **18** as the catalyst, as observed by Orain Brown during his optimization. We proposed, tentatively, that the reason could be that [$NPEt_3^-$] ligand is not as electron-donating as [$NP^tBu_3^-$], so the coordination of precatalyst to the Lewis acidic surface is more effective in stabilizing the latter catalyst.

Table **5.7**: HDS results using **114**, with KO^tBu as scavenger.

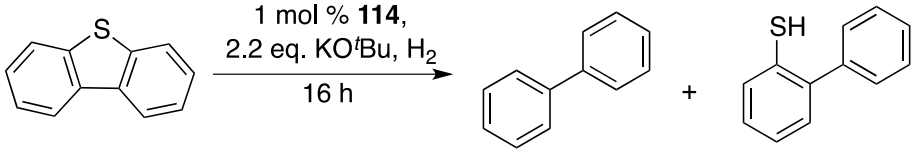

109 **110** **158**

Entry	Support	Solvent	Temperature (ºC)	H_2 (atm)[a]	Conversions (%)	
					110	**158**
1	–	THF	150	1	0	1
2	–	Toluene	150	1	0	1
3	–	THF	150	34	0	2
4	–	Toluene	150	34	7	71
5	–	Cyclooctane	150	34	13	63
6	Al_2O_3	Toluene	150	34	30	43

[a] The hydrogen pressure is the pressure under room temperature. The pressure was higher after heating.

In conclusion, allyl-capped dimer [Ni(η^3-allyl)($NPEt_3$)]$_2$ **114** is an active hydrogenation and HDS catalyst. This preliminary study proved that using allyl groups to occupy two coordination sites is an effective method for building robust phosphoranimide-bridged nickel precatalysts for HDS. Further study, using isostructural allyl-capped nickel dimer such as [Ni(η^3-allyl)($NPPh_3$)]$_2$ **122** and other later first-row transition metals (Co, Fe) is continuing by other group members.

In addition, grafting the nickel dimer **114** on a purely Lewis acidic heterogeneous support was also studied to explore applications where water-sensitivity is not an issue. As mentioned in the previous chapter, the $[Ni(\eta^3\text{-allyl})(NPEt_3)]_2$ **114** coordinates Lewis acids to form heterotrimetallic clusters. Anhydrous magnesium chloride **163** was used for reaction to prevent contamination from reaction with acidic protons. Hexane was selected as the solvent because of the insolubility of magnesium chloride. Upon mixing 100 equivalents of **163** with red solution of **114**, the stirred suspension became paler as the loading proceeded, eventually turning the solution colorless. Meanwhile the $MgCl_2$ powder turned from white to light orange. ^{1}H-NMR and ^{31}P-NMR spectroscopies confirmed that no starting material remained in the solvent. We propose, that the nitrogen in dimer **114** coordinates to the magnesium cations on the surface (Eqn. **5.7**).

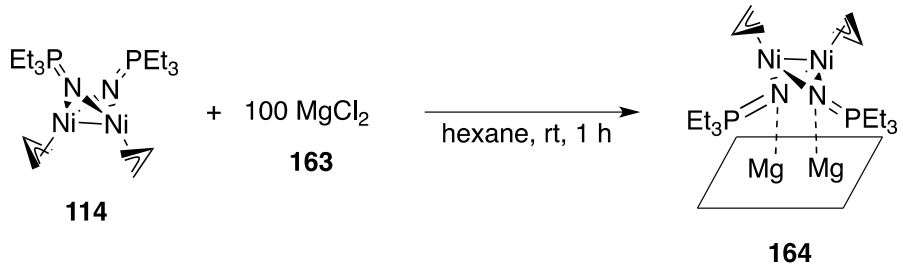

Equation **5.7**

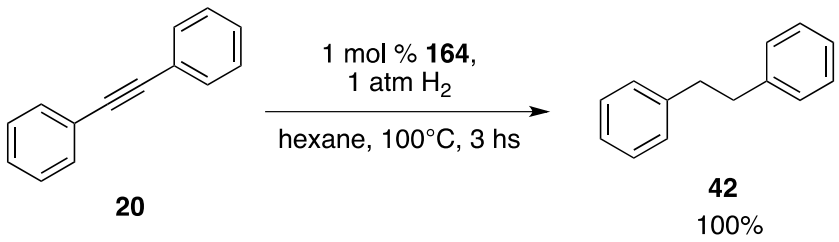

Equation **5.8**

The hydrogenation activity of this otherwise uncharacterized heterogeneous catalyst **164** was briefly investigated. Hexane was again used as the solvent. The reaction mixture was charged with one atmosphere of hydrogen and heated to 100 °C for 3 hours. Quantitative conversion of **20** to **42** was observed by GC and ^{1}H-NMR spectroscopy (Eqn. **5.8**). The

homogeneity of the catalyst is to be investigated in future. Further development of heterogeneous catalysts is ongoing by other group members.

5.3 Conclusion

In this chapter, the non-innocent role of KH in preliminary HDS was determined, establishing that even in non-polar solvents, KH use should be limited to preliminary results. Strong nitrogen bases are also non-innocent and should not be used. KO^{t}Bu and K_2S, however, produce no background reaction and are appropriate scavengers for further HDS study. Instead, more intense reaction conditions are necessary under this scenario: 150 °C, 34 atm of hydrogen pressure, and alumina as support for the metal clusters. More mechanistic study about the weak base scavenger is necessary to understand the role of scavenger, including D-labeling control experiment.

The neutral cluster **18** and nickel dimer **114** were proved active HDS catalysts, and anionic cluster **31** is by far the most efficient catalyst under the new optimum conditions. These results validate the proposal that structural engineered first-row transition metal compounds are capable of catalytic HDS.

Future improvement of the HDS catalysis could derive from understanding the effect of oxidation state on activity (**18** versus **31**), and better design of heteropolymetallic clusters to provide more efficient catalytic system. Incorporation of the K^+ promoter into the cluster design can avoid the addition of stoichiometric amount of potassium salt. In addition, easier extrusion of sulfide and replacement of basic scavenger to passive scavengers (ZnO or Fe_2O_3) can also be achieved possibly by rational design of the catalyst and appropriate support.

Chapter 6. Experimental

6.1 General procedures (partially adapted from previous Stryker group theses)

6.1.1 General experimental procedures

All manipulations were performed using standard Schlenk techniques on a vacuum/N_2 (or Ar) double manifold or using a Labmaster sp MBraun glovebox under a N_2 atmosphere. Glovebox experiments were performed when the O_2 level was <5 ppm as measured by a Pb-based fuel cell Teledyne O_2 sensor. Solvents were either distilled from Na (toluene), Na/benzophenone (THF, benzene), K/benzophenone (hexane, pentane, ether, dioxane) under nitrogen when dark blue or purple, from CaH_2 (MeCN, CH_2Cl_2) under nitrogen or collected from Pure Process Technology free standing solvent purification system (SPS). Glovebox solvents were tested with a Na/benzophenone solution in THF to ensure they were dry and degassed. Liquid reagents were either distilled under N_2 (or Ar) and stored in a glass "bomb" (a medium walled glass tube with a 14/20 sidearm that seals with a Teflon high vacuum valve) or passed through Activity I neutral alumina into a bomb and subsequently freeze-pump-thaw degassed three times. Hygroscopic solids were dried overnight in a vacuum oven to remove water before bringing them into the glovebox while hot. Non-hygroscopic solids were brought into the glovebox in vials covered with a Kimwipes. Volatile solids were pumped into the glovebox inside of argon-filled Schlenk flasks. All glassware was flame-dried or dried for at least 3 hours in a 150°C oven before use. Low temperature crystallizations were done at -35 °C in the glovebox freezer. Sample preparation for air sensitive IR spectroscopy was done in the glovebox. Solution IR cells were sealed with Teflon stoppers and parafilm prior to data collection. Solid sample was prepared in a special cell with KBr salt plate on top and bottom and a rubber ring between covered with silica grease. For elemental analysis of air sensitive compounds, the samples were prepared in the glovebox using two preweighed tin boats. Approximately 1.6 mg of sample was placed in one boat and folded into a cube and then inserted into the second boat, which was also folded into a cube. The cube was then sealed in a one-dram vial and immediately submitted for analysis. Duplicate samples were run whenever possible. NMR

spectroscopy was done in standard NMR tubes sealed with either plastic caps or NMR-tube sized septa. Magnetic susceptibility measurements were obtained via the Evans' method[58] in standard NMR tubes. For controlled heating of reaction mixtures, Ika stir plates with digital temperature control were used along with heavy mineral oil (<110°C) or silicone oil (>110°C) baths. For reactions requiring sustained low temperature, an immersion cooler (Neslab Cryotrol cc-100) equipped with a temperature controller was used. A high vacuum line, equipped with a three-stage diffusion pump, was used to dry materials for elemental analysis ($<10^{-5}$ Torr).

6.1.2 Method for determining magnetic susceptibility (partially adapted from previous Stryker group theses)[149]

The Evans' method[58] was used to determine magnetic susceptibilities, deriving the room temperature magnetic moment and an estimate of the number of unpaired electrons for $[Ni_4(NP^tBu_3)_4]BPh_4$. A reference solution of 95/5 v/v THF-d_8/cyclohexane was prepared. The solid sample (~5 mg) was dissolved in 2 mL of the reference solution. For each determination, measurements of three separate sample solutions were made. The sample solution was placed in a melting point capillary tube using a syringe with a 10 cm long 22-gauge needle. This capillary was then placed into a standard NMR tube containing the reference solution and the tube was capped. The ^{1}H-NMR spectrum was then obtained at room temperature for each sample.

6.1.3 Instrumentation (partially adapted from previous Stryker group theses)

X-ray crystallography was performed using either a Bruker DB diffractometer or a Bruker PLATFORM diffractometer, both equipped with a SMART APEX II CCD area detectors. Diffraction data collection and crystal structures determinations were done by Dr. Robert McDonald and Dr. Michael Ferguson of the University of Alberta Department of Chemistry X-ray Crystallography Laboratory. CHNS elemental analyses were performed on a Carlo Erba EA1108 Elemental Analyzer. Gas chromatography-mass spectrometry was performed using a Hewlett Packard GCD series G1800A GC-MS. The mass detectors used

were either HP 5870 or 5971 MSD. The column used was an Agilent DB-5 MS 25m x 0.25 mm x 0.25-micron film thickness. The MS library was the NIST/EPA/NIH 2011 Mass Spectral Library and Software package was NIST11. IR spectroscopic analyses were performed using a Nicolet Magna 750 FT-IR Spectrometer, or a Nicolet 8700 FT-IR Spectrometer operating by OMNIC Spectra Software. All elemental analyses, GC-MS and FT-IR data were obtained by staff at the University of Alberta Department of Chemistry Analytical and Instrumentation Laboratory. ^{1}H and ^{31}P NMR spectra were obtained using eitheran Agilent/Varian Inova 300 MHz spectrometer or an Agilent/Varian Inova 400 MHz spectrometer at 27 °C unless otherwise mentioned. Chemical shifts for ^{1}H NMR spectra are reported in ppm and referenced against the residual proton signals of the NMR solvent. ^{31}P NMR chemical shifts are reported in ppm, referenced to 85% phosphoric acid which is assigned a value of 0 ppm.

6.1.4 Chemical materials (adapted from previous Stryker group theses)

All commercial reagents were purchased from Strem or Sigma-Aldrich chemical companies were used as received. Where necessary, reagent purifications were accomplished using standard methods. Potassium hydride[150] required rigorous purification to remove traces of potassium metal and was thus heated overnight at reflux in THF containing 20 mol% naphthalene, then washed three times with anhydrous THF, three times with dried hexanes and dried under vacuum before use. Materials prepared by literature methods or modifications of such methods are noted in the appropriate experimental sections.

6.1.5 Cyclic Voltammetry

Cyclic voltammetry was carried out using a WaveNow USB potentiostat from Pine Industry Instrumentation and Aftermath operating software. Ceramic patterned platinum electrodes with silver pseudo-reference (for non-aqueous solutions) were used as working and counter electrodes. *n*-Bu_4NPF_6 was used as electrolyte with 0.1 mol/L concentration. The analyte solution was prepared in the glovebox by dissolving the analyte in *n*-Bu_4NPF_6

solution to make 0.01mol/L solution of analyte. The additive such as $NaPF_6$ or KPF_6 was added based on specific requirement. The solution was then transferred to the instrument and then transferred out of the glovebox with proper sealing. The cyclic voltammetry was obtained after the instrument was connected to the WaveNow USB potentiostat, which was connected to a computer with Aftermath software. The general scan rate was 0.1V/s unless otherwise noticed.

6.1.6 UV-Vis spectroscopy

The solution was prepared in the glovebox and transferred into a 0.1mL UV cell and pumped out of the glovebox. The top of the cell was wrapped with parafilm immediately when it was out of the glovebox. The UV-Vis spectroscopy was done on Agilent/HP 8453 UV-Vis spectroscopy system. The software being used was version B.04.01 of UV-Vis ChemStation.

6.2 Experimental procedures for chapter 1

6.2.1 Synthesis of $[Ni_4(NP^tBu_3)_4]BPh_4$ 23

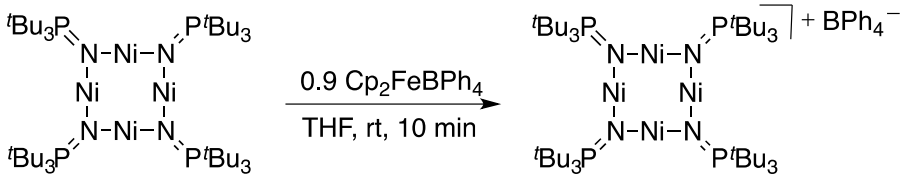

18 **23** 83%

$[NiNP^tBu_3]_4BPh_4$ **23**: In the glovebox, $[Ni(NP^tBu_3)]_4$ (110.0 mg, 0.1000 mmol) was dissolved in 10 mL of THF. A slurry of 0.9 equivalent of Cp_2FeBPh_4 (45.5 mg, 0.0900 mmole) in 2 mL THF was added into the solution dropwise by pipette. As the addition of Cp_2FeBPh_4 proceeded, the color of the solution changed from green to blue. The solution was stirred for 30 minutes and then the solvent was removed under vacuum. The residue was washed with pentane to remove the extra $[Ni(NP^tBu_3)]_4$ **18** and ferrocene. Then the

solid was extracted with 2 mL of THF for three times, giving dark blue solution. The combined solution was filtrated through Celite and the solvent was removed. 106.2mg of product $[Ni(NP^tBu_3)]_4BPh_4$ **23**, was collected and the yield was 83%. Single crystals of **23** were grown by cooling saturated THF solution. IR: ν/cm^{-1} in solid state= 1017 s, 1042 s, 1357 m, 1365 m, 1389 m, 1402 m, 1424 m, 1445 m, 1471m, 1482 m, 2900 s, 3056 m; Elemental analysis: C: 60.75 (60.93) H: 9.17 (9.09) N: 3.94 (3.95).

6.2.2 Synthesis for $[Ni_4(NP^tBu_3)_4]BPh_4$ 23 from $NiBr_2$·DME

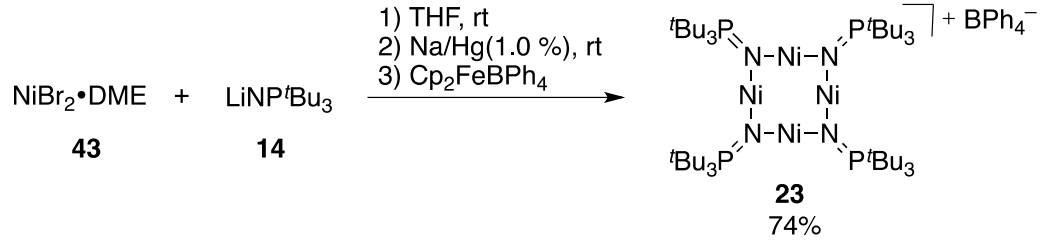

$[Ni_4(NP^tBu_3)_4]BPh_4$ **23**: In the glove box, $LiNP^tBu_3$ **14** (344 mg, 1.54 mmol) and $NiBr_2$·DME **43** (569 mg, 1.84 mmol) were mixed in a 5-dram vial and dissolved in 5 mL THF at room temperature. The solution turned green immediately. After stirring for half an hour, the mixture was settled with some yellow powder on the bottom of the vial. The green solution was then decanted to another vial before excess Na/Hg (1.0%) (13.5 g, 6.12 mmol) was added. The solution was stirred for 2 hours during which the color changed gradually from dark green to light green. The solvent was then removed under vacuum. Three times 5 mL of pentane was used to extract the residue. After filtration and evaporation of pentane, Crude $[Ni(NP^tBu_3)]_4$ **18** (370 mg, 0.336 mmol) was obtained as green powderand used directly in the next step. Crude $[Ni(NP^tBu_3)]_4$ **18** was dissolved in 2 mL THF and Cp_2FeBPh_4 (170 mg, 0.336 mmol) was added slowly as solid. As the addition of Cp_2FeBPh_4 proceeded, the color of the solution changed from green to blue. After stirring for 30 minutes, 10 mL hexane was added to the solution to precipitate the blue product. The mixture was filtrated and the product was washed with hexane thrice and dried on high vacuum line. 405mg of the product, $[Ni_4(NP^tBu_3)_4]BPh_4$ **23**, was obtained as a blue powder, giving 74% yield (94% for the first step). IR: ν/cm^{-1} in solid state= 1017 s,

1042 s, 1357 m, 1365 m, 1389 m, 1402 m, 1424 m, 1445 m, 1471m, 1482 m, 2900 s, 3056 m; Elemental analysis: C: 60.75 (60.93) H: 9.17 (9.09) N: 3.94 (3.95).

6.2.3 Synthesis of $[Ni_4(NP^tBu_3)]PF_6$ 30

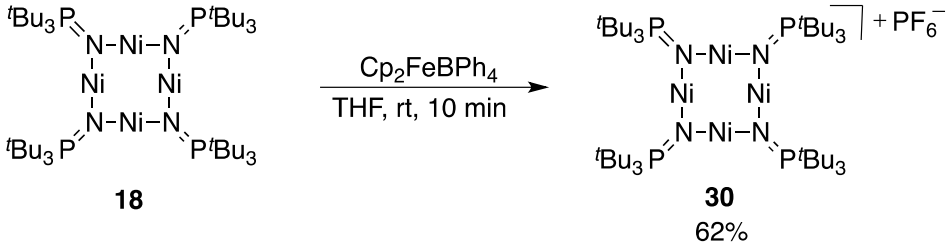

18 → **30**, 62%

$[Ni_4(NP^tBu_3)_4]PF_6$ **30** was synthesized by the same preparation of $[Ni_4(NP^tBu_3)_4]BPh_4$ **23**, the only difference was that Cp_2FePF_6 was used as oxidant. The product is blue in solution. After drying on the high vacuum line overnight, a green powder was obtained, with 62% crude yield. The product was used without further purification. Single crystals were grown by cooling saturated THF solution.

6.2.4 Synthesis of $[Ni(NP^tBu_3)]_4$ 18 by reduction of $[Ni_4(NP^tBu_3)_4]BPh_4$ 23

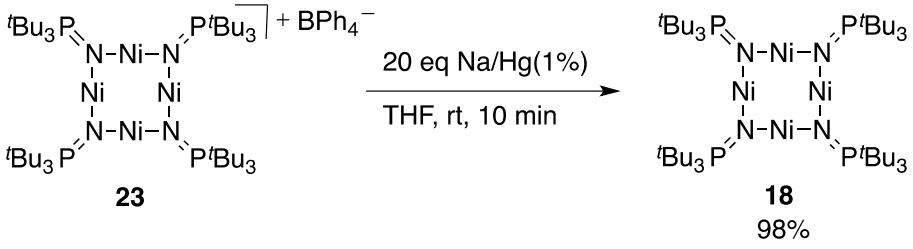

23 → **18**, 98%

$[Ni(NP^tBu_3)]_4$ **18**: In the glovebox, $[Ni_4(NP^tBu_3)_4]BPh_4$ **23** (30.3 mg, 0.021 mmol) was dissolved in 2 mL THF in a 5-dram vial. Excess 1% Na/Hg (975.2 mg, 0.424 mmol) was added to the solution under stirring. The solution turned from blue to green within minutes upon addition of the amalgam. After stirring for 10 min at room temperature, the solvent was removed under vacuum. The product was extracted by 2 mL pentane thrice and filtered

through Celite. After evaporation of pentane under vacuum, [Ni(NP^{t}Bu$_3$)]$_4$ **18** (23.0 mg) was obtained in a yield of 98%.

6.2.5 Reduction of [Ni(NP^{t}Bu$_3$)]$_4$ 18

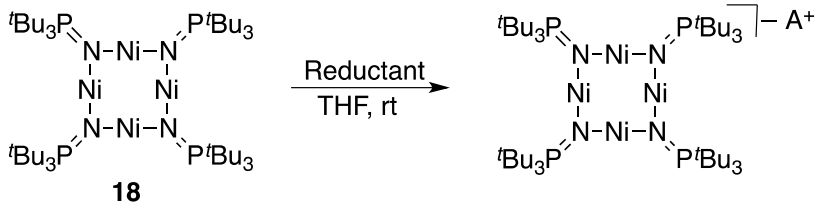

18

[Ni(NP^{t}Bu$_3$)]$_4$ **18** used in these reactions was prepared freshly from NiBr$_2$·DME **43** and used within two days or prepared by reduction of [Ni$_4$(NP^{t}Bu$_3$)$_4$]BPh$_4$ **23** immediately before use by 1% Na/Hg. [Ni(NP^{t}Bu$_3$)]$_4$ **18** (40.0mg, 0.0364mmol) was dissolved in 3 mL of THF. The reductant (Na/Hg, KC$_8$, Li and so on) was added in excess to the solution under stirring. After certain amount of time (noted in the content), the solvent was removed under vacuum. The product was extracted by 2 mL of pentane thrice and filtered through a plug of Celite. After evaporation of pentane under vacuum, the product was dissolved in various solvents for recrystallization.

6.2.6 Ionic exchange of Na[Ni$_4$(NP^{t}Bu$_3$)$_4$] 31 and ^{n}Bu$_4$NBr

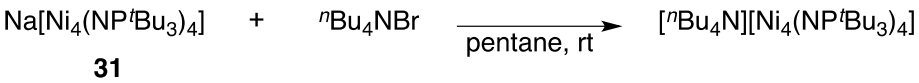

31

[Ni(NP^{t}Bu$_3$)]$_4$ **18** (50 mg, 0.045 mmol) was dissolved in 5 mL of THF and excess 40% Na/Hg was added in the solution under stirring. After 30 minutes the solvent was evaporated under vacuum. The product was extracted by 2 mL of pentane thrice and filtered through Celite, giving a brown solution. Then ^{n}Bu$_4$NBr (14.6 mg, 0.045 mmol) was added to the solution. After stirring for another 30 minutes, the solvent was removed under vacuum, leaving black residue. The black powder was extracted with 3 mL of pentane,

ether and THF consecutively. The product was then set up for recrystallization separately. No single crystals were obtained.

6.2.7 Comproportionation of $[Ni_4(NP^tBu_3)_4]BPh_4$ 23 and $Na[Ni_4(NP^tBu_3)_4]$ 31

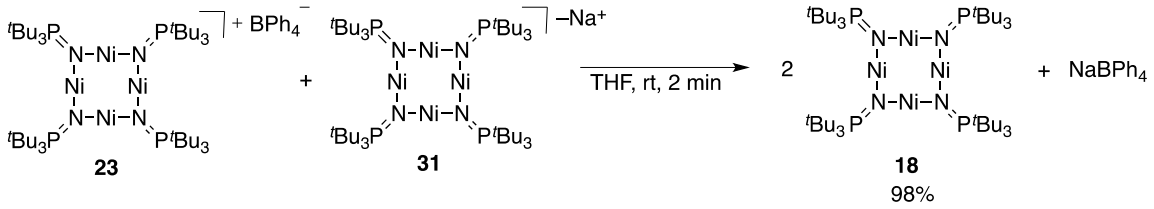

$[Ni(NP^tBu_3)]_4$ **18** (14.8 mg, 0.0135 mmol) was dissolved in 2 mL of THF and charged with excess Na/Hg (40%). The solution was stirred at room temperature for 15 min, giving a brown solution. The dark brown solution was then transferred into another vial and mixed with a blue solution of $[Ni_4(NP^tBu_3)_4]BPh_4$ **23** (19.1 mg, 0.0135 mmol). Immediately color change was observed from blue to green. The solvent was removed under vacuum. The residue was extracted with 2 mL of pentane thrice. The combined pentane solution was filtrated through Celite and concentrated to give $[Ni(NP^tBu_3)]_4$ **18** with 98% crude yield.

6.2.8 Consistent procedure for $Na[Ni_4(NP^tBu_3)_4]$

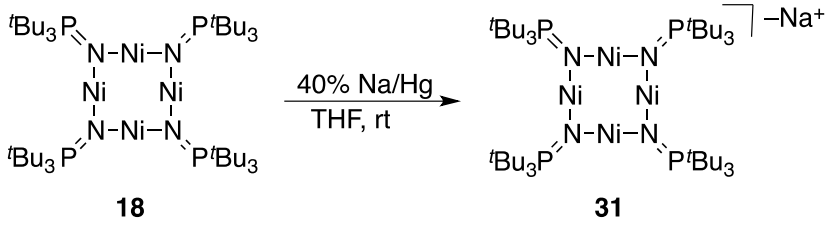

The $[Ni(NP^tBu_3)]_4$ **18** used in these reactions are prepared either freshly from $NiBr_2$·DME within three days or reduced from $[Ni_4(NP^tBu_3)_4]BPh_4$ immediately before use by 1% Na/Hg. $[Ni(NP^tBu_3)]_4$ **18** (40.0 mg, 0.0364 mmol) was dissolved in 3 mL of THF. Excess 40% Na/Hg was added to the solution. After stirring for 15 min, the solution was passed throught Celite and the putative product $Na[Ni_4(NP^tBu_3)_4]$ **31** was used immediately for

catalysis. When the following catalytic reaction was carried out in a solvent other than THF, the THF was removed first under vacuum. The residue was then extracted by 2 mL of specific solvent as noted. Passing the solution through Celite resulted in the solution of $Na[Ni_4(NP^tBu_3)_4]$ **31**, which was also used immediately.

6.3 Experimental procedures for Chapter 2

6.3.1 Calibration of GC for diphenylacetylene 20, dibenzyl 42, *cis*-stilbene 46 and *trans*-stilbene 47.

To characterize all four compounds of hydrogenation of **20** quantitatively, GC analysis was carried out using dodecane as internal standard. A new method was created to get the improved separation of all four compounds by GC. In the method, the oven was first held at 100°C for 2 min. Then the temperature was increased at 4 °C/min until it reached 156°C, after which a rate of 20 °C/min was applied until 300 °C. For each compound, 10 samples of various known ratio of dodecane to analyte were separated and detected by GC. From the resulting linear correlation was found between the ratio of signal integration and ratio of concentration for each compound. All the indexes for this linear correlation were obtained, which eventually allowing the quantitative characterization of all four compounds by GC. The calibration data are listed below for all four compounds.

Calibration of diphenylacetylene **20**:

m(PhCCPh)/mg	V(dodecane)/ µL	total solvent(mL)	[M](PhCCPh)/ [M](dodecane)	Area(PhCCPh)/ Area (dodecane)
5.7	20	10	0.349169443	0.285
9.03	20	10	0.553157907	0.4515
11.75	20	10	0.719779115	0.5875
17.26	20	10	1.057309577	0.863
22.09	20	10	1.353184737	1.1045
31.54	20	10	1.932070918	1.577
43.14	20	10	2.642661364	2.157
50.38	20	10	3.086167815	2.519
64.98	20	10	3.980531651	3.249
103.8	20	10	6.358559332	5.19

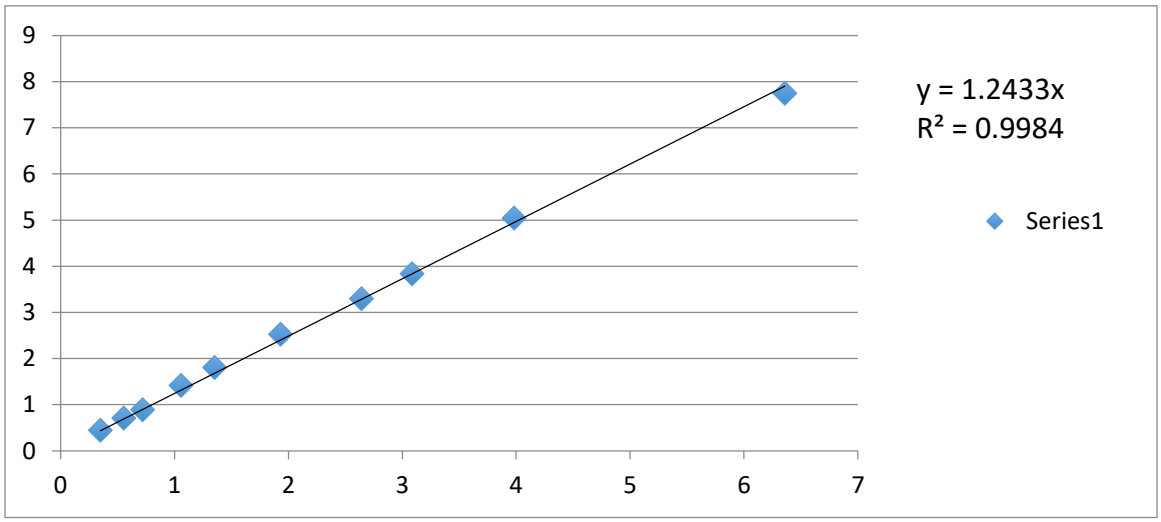

Calibration of *cis*-stilbene **46**:

m(*cis*-stilbene)/mg	V(dodecane)/ µL	total solvent(mL)	[M](*cis*-stilbene)/ [M](dodecane)	Area(*cis*-stilbene)/ Area (dodecane)
6	20	10	0.363448202	0.425090137
8.4	20	10	0.508827483	0.59611824
15.4	20	10	0.932850386	1.173724024
18.8	20	10	1.138804367	1.371522755
26.5	20	10	1.60522956	1.960682141
32.2	20	10	1.950505352	2.323473695
36.8	20	10	2.229148974	2.605162593
52.2	20	10	3.16199936	3.80815463
65.8	20	10	3.985815285	4.724426126
89.8	20	10	5.439608094	6.61730652

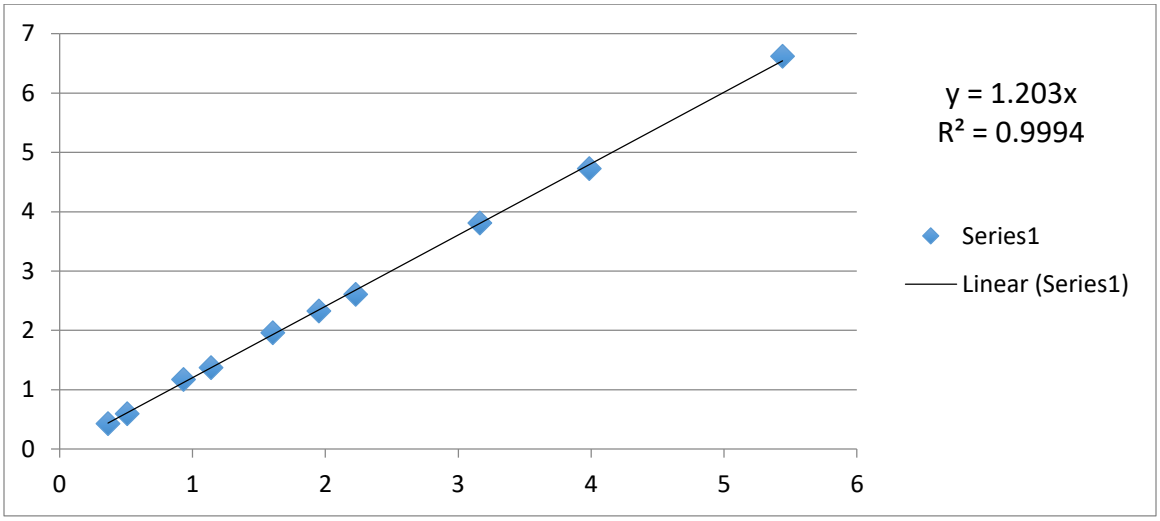

Calibration of *trans*-stilbene **47**:

m(*trans*-stilbene)/mg	V(dodecane)/ µL	total solvent(mL)	[M](*trans*-stilbene)/ [M](dodecane)	Area(*trans* -stilbene)/ Area (dodecane)
5.7	20	10	0.345275792	0.446801123
10.26	20	10	0.621496426	0.785044894
15.89	20	10	0.962531989	1.220643098
20.11	20	10	1.218157225	1.561147394
31.09	20	10	1.883267435	2.346496218
43.34	20	10	2.625307514	3.200445247
50.04	20	10	3.031158007	3.650730165
59.99	20	10	3.633876276	4.48275673
82.61	20	10	5.004075998	5.710508657
103.41	20	10	6.264029766	7.700191404

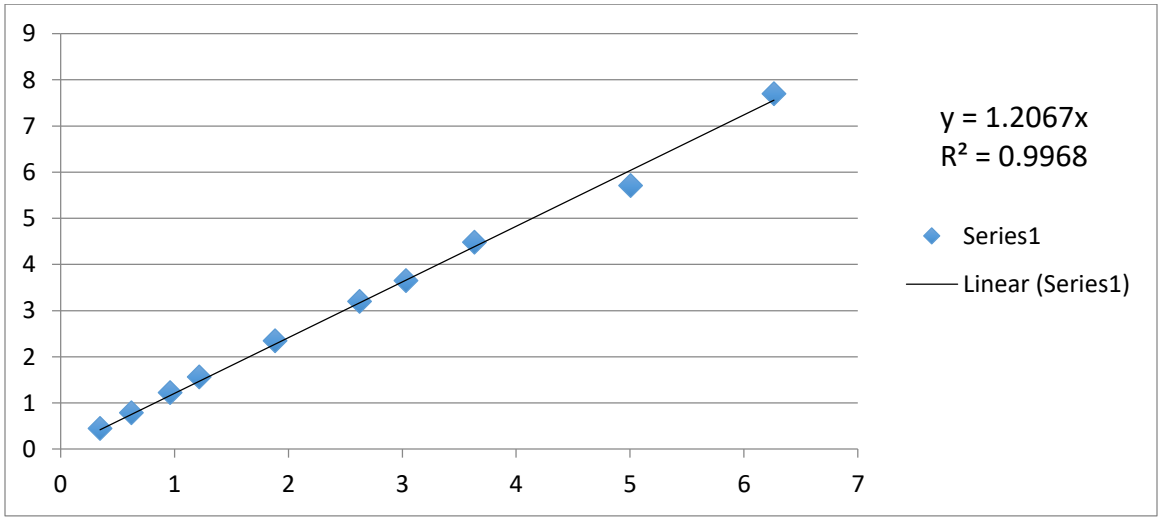

Calibration of bibenzyl **42**:

m(*trans*-stilbene)/mg	V(dodecane)/ µL	total solvent(mL)	[M](*trans*-stilbene)/ [M](dodecane)	Area(*trans* -stilbene)/ Area (dodecane)
5.86	20	10	0.351053088	0.496311592
11.17	20	10	0.669157508	0.920307249
16.7	20	10	1.000441395	1.335193704
20.94	20	10	1.254445678	1.64956812
35.47	20	10	2.124889598	2.698088088
43.76	20	10	2.621515896	3.322828859
46.82	20	10	2.804830307	3.588208305
64.21	20	10	3.846607305	4.987665409
77.88	20	10	4.665531489	5.813845735
98.29	20	10	5.888226632	7.702462797

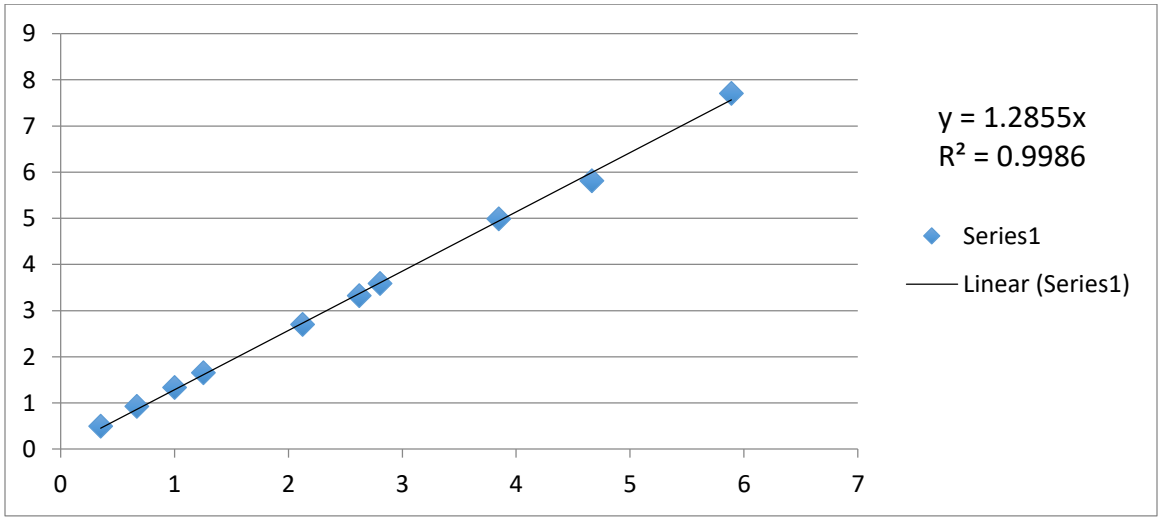

6.3.2 General procedure for hydrogenation with [Ni(NP^{t}Bu$_3$)]$_4$ 18 in THF

The [Ni(NP^{t}Bu$_3$)]$_4$ **18** used in the hydrogenation was prepared immediately before use by the reduction of [Ni$_4$(NP^{t}Bu$_3$)$_4$]BPh$_4$ **23** (7.7 mg, 0.0055 mmol). The substrate (0.55 mmol),

catalyst (5.9mg, 0.00055mmol), 5 mL THF and a glass-encased stir bar were mixed in a medium-walled glass reactor with Teflon screwed stopper. The glass reactor was transferred out of the glovebox and connected to a hydrogen-filled schlenk line. The solution was degassed by standard freeze-pump-thaw thrice. The reactor was then sealed and stirred at room temperature for 6 hours unless otherwise noted. After one hour, the reactor was open to air. Within a few minutes the nickel catalyst precipitated out. The solution was then passed through Celite and mixed with 10 μL of dodecane before submission for GC or GC-MS analysis. If a ^{1}H-NMR spectrum was needed, the solvent was removed and the solid was dissolved in $CDCl_3$ for ^{1}H-NMR, using 2mg of C_6Me_6 as internal standard.

6.3.2.1 Hydrogenation of diphenylacetylene 20 with [Ni(NP^{t}Bu$_3$)]$_4$ 18

The general procedure was applied to [Ni(NP^{t}Bu$_3$)]$_4$ **18** (6.0 mg, 0.0055 mmol) and diphenylacetylene **20** (100.0 mg, 0.55 mmol). The product was characterized quantitatively by GC. The only product is *cis*-stilbene **46**, obtained in 2% yield. The remaining material balance consisted of starting compound.

6.3.2.2 Hydrogenation of *cis*-stilbene 46 with [Ni(NP^{t}Bu$_3$)]$_4$ 18

The general procedure was applied to [Ni(NP^{t}Bu$_3$)]$_4$ **18** (6.0 mg, 0.0055 mmol) and *cis*-stilbene **46** (102.0 mg, 0.55 mmol). The product was characterized quantitatively by GC. The yield for *trans*-stilbene **47** was 20% and the yield for bibenzyl **42** was 5%. The remaining material balance consisted of starting compound.

6.3.2.3 Hydrogenation of *trans*-stilbene 47 with [Ni(NP^{t}Bu$_3$)]$_4$ 18

The general procedure was applied to [Ni(NP^{t}Bu$_3$)]$_4$ **18** (6.0 mg, 0.0055 mmol) and *trans*-stilbene **47** (102.0 mg, 0.55 mmol). The product was characterized quantitatively by GC. The only product was bibenzyl **42** in 23% yield. The remaining material balance consisted of starting compound.

6.3.2.4 Hydrogenation of allylbenzene 40 with [Ni(NP^{t}Bu$_3$)]$_4$ 18

The general procedure was applied to [Ni(NP^{t}Bu$_3$)]$_4$ **18** (6.0 mg, 0.0055 mmol) and allylbenzene **40** (57.0 mg, 0.55 mmol). The product was characterized by GC-MS and ^{1}H-NMR. The yield of 1-phenylpropane **41** was 95%. The remaining material balance consisted of starting compound.

6.3.2.5 Hydrogenation of styrene 48 with [Ni(NP^{t}Bu$_3$)]$_4$ 18

The general procedure was applied to [Ni(NP^{t}Bu$_3$)]$_4$ **18** (6.0 mg, 0.0055 mmol) and styrene **48** (65.0 mg, 0.55 mmol). The product was characterized by GC-MS and ^{1}H-NMR. The yield of ethylbenzene was 100%.

6.3.2.6 Hydrogenation of tetraphenylethylene 49 with [Ni(NP^{t}Bu$_3$)]$_4$ 18

The general procedure was applied to [Ni(NP^{t}Bu$_3$)]$_4$ **18** (6.0 mg, 0.0055 mmol) and tetraphenylethylene **49** (182.0 mg, 0.55 mmol). The product was characterized by GC-MS and ^{1}H-NMR. The starting material was the only compound recovered.

6.3.2.7 Hydrogenation of diphenylacetylene 20 with [Ni(NP^{t}Bu$_3$)]$_4$ 18 at 40 °C

The general procedure was applied to [Ni(NP^{t}Bu$_3$)]$_4$ **18** (6.0 mg, 0.0055 mmol) and diphenylacetylene **20** (100.0 mg, 0.55 mmol). The glass reactor was immersed in 40 °C mineral oil bath after the addition of H_2. The products were characterized quantitatively by GC. The yield was 1% for bibenzyl **42**, 9% for *cis*-stilbene **46** and 1% for *trans*-stilbene **47**. The remaining material balance consisted of starting compound.

6.3.2.8 Hydrogenation of diphenylacetylene 20 with [Ni(NP^{t}Bu$_3$)]$_4$ 18 at 60 °C

The general procedure was applied to [Ni(NP^{t}Bu$_3$)]$_4$ **18** (6.0 mg, 0.0055 mmol) and

diphenylacetylene **20** (100.0 mg, 0.55 mmol). The glass reactor was immersed in 60 °C mineral oil bath after the addition of H_2. The products were characterized quantitatively by GC. The yield was 85% for bibenzyl **42**, 6% for *cis*-stilbene **46**, and 9% for *trans*-stilbene **47**.

6.3.2.9 Mercury test of hydrogenation of diphenylacetylene 20 with [Ni(NP^{t}Bu$_3$)]$_4$ 18 at 60 °C

The general procedure was applied to [Ni(NP^{t}Bu$_3$)]$_4$ **18** (6.0 mg, 0.0055 mmol) diphenylacetylene **20** (100.0 mg, 0.55 mmol). Excess mercury (5.5 mmol, 1.102 g) was also added in the glass reactor. The glass reactor was immersed in 60 °C mineral oil bath after the addition of H_2. The products were characterized quantitatively by GC. The conversions were 73% for bibenzyl **42**, 15% for *cis*-stilbene **46** and 13% for *trans*-stilbene **47**.

6.3.2.10 Mercury test of hydrogenation of diphenylacetylene 20 with [Ni(NP^{t}Bu$_3$)]$_4$ 18 at 80 °C

The general procedure was applied to [Ni(NP^{t}Bu$_3$)]$_4$ **18** (6.0 mg, 0.0055 mmol) diphenylacetylene **20** (100.0 mg, 0.55 mmol). Excess mercury (5.5 mmol, 1.102 g) was also added in the glass reactor. The glass reactor was immersed in 80 °C mineral oil bath after the addition of H_2. The products were characterized quantitatively by GC. The conversions were 5% for bibenzyl **42**, 52% for *cis*-stilbene **46**, and 2% for *trans*-stilbene **47**.

6.3.3 General procedure for hydrogenation with Na[Ni$_4$(NP^{t}Bu$_3$)$_4$] 31 in THF

The [Ni(NP^{t}Bu$_3$)]$_4$ **18** used here was prepared immediately prior to use from reduction of [Ni$_4$(NP^{t}Bu$_3$)$_4$]BPh$_4$ 23 by 1% Na/Hg. The green solid [Ni(NP^{t}Bu$_3$)]$_4$ **18** (5.9 mg, 0.00055 mmol) was dissolved in 1 mL of THF. After the solid was dissolved, one drop of 40% Na/Hg was added to the solution and stirred for 15 min. The color changed from green to

brown gradually. The solution was then passed through Celite, giving a brown solution of $Na[Ni_4(NP^tBu_3)_4]$ **31**. Then the substrate (0.055 mol), solution of $Na[Ni_4(NP^tBu_3)_4]$ **31**, another 4 mL THF and a glass-encased stir bar were mixed in a medium-walled glass reactor fitted with a Teflon high-vacuum valve. The glass reactor was transferred out of the glovebox and connected to a hydrogen-filled Schlenk line. The solution was degassed by standard freeze-pump-thaw thrice, after which the reactor was filled with 1 atm H_2 as the solution warmed to room temperature. The reactor was then sealed and stirred at room temperature for 6 hours unless otherwise noted. After 6 hours, the reactor was open to air. Within a few min the nickel catalyst precipitated out. The solution was then passed through Celite and mixed with 10 μL of dodecane before submission for analysis by GC or GC-MS. If ^{1}H-NMR was needed, the solvent was removed, and the solid was dissolved in $CDCl_3$ for ^{1}H-NMR with 2 mg of C_6Me_6 as internal standard.

6.3.3.1 Hydrogenation of diphenylacetylene 20 with $Na[Ni_4(NP^tBu_3)_4]$ 31

The general procedure was applied to $[Ni(NP^tBu_3)]_4$ **18** (6.0 mg, 0.0055 mmol) and diphenylacetylene **20** (100.0 mg, 0.55 mmol). The product was characterized quantitatively by GC. The only product was bibenzyl **42** in 100% yield.

6.3.3.2 Hydrogenation of *cis*-stilbene 46 with $Na[Ni_4(NP^tBu_3)_4]$ 31

The general procedure was applied to $[Ni(NP^tBu_3)]_4$ **18** (6.0 mg, 0.0055 mmol) and *cis*-stilbene **46** (102.0 mg, 0.55 mmol). The product was characterized quantitatively by GC. The yields were 85% for bibenzyl **42** and 15% for *trans*-stilbene **47**.

6.3.3.3 Hydrogenation of *trans*-stilbene 47 with $Na[Ni_4(NP^tBu_3)_4]$ 31

The general procedure was applied to $[Ni(NP^tBu_3)]_4$ **18** (6.0 mg, 0.0055 mmol) and *trans*-stilbene **47** (102.0 mg, 0.55 mmol). The product was characterized quantitatively by GC. The only product was bibenzyl in 45% yield. The remaining material balance consisted of starting compound.

6.3.3.4 Hydrogenation of allylbenzene 40 with $Na[Ni_4(NP^tBu_3)_4]$ 31

The general procedure was applied to $[Ni(NP^tBu_3)]_4$ **18** (6.0 mg, 0.0055 mmol) and allylbenzene **40** (57.0 mg, 0.55 mmol). The product was characterized by GC-MS and ^{1}H-NMR. The yield of 1-phenylpropane **41** was 100%.

6.3.3.5 Hydrogenation of styrene 48 with $Na[Ni_4(NP^tBu_3)_4]$ 31

The general procedure was applied to $[Ni(NP^tBu_3)]_4$ **18** (6.0 mg, 0.0055 mmol) and styrene **48** (65.0 mg, 0.55 mmol). The product was characterized by GC-MS and ^{1}H-NMR. The product was a mixture of polystyrene.

6.3.3.6 Hydrogenation of tetraphenylethylene 49 with $Na[Ni_4(NP^tBu_3)_4]$ 31

The general procedure was applied to $[Ni(NP^tBu_3)]_4$ **18** (6.0 mg, 0.0055 mmol) and tetraphenylethylene **49** (182.0 mg, 0.55 mmol). The product was characterized by GC-MS and ^{1}H-NMR. The starting material was the only compound recovered.

6.3.3.7 Hydrogenation of diphenylacetylene 20 with $Na[Ni_4(NP^tBu_3)_4]$ 31 at 0 °C

The general procedure was applied to $[Ni(NP^tBu_3)]_4$ 18 (6.0 mg, 0.0055 mmol) and diphenylacetylene **20** (100.0 mg, 0.55 mmol). The glass reactor was immersed in ice bath after the addition of H_2. The products were characterized quantitatively by GC. The conversions were 8% for bibenzyl **42**, 66% for *cis*-stilbene **46**, and 1% for *trans*-stilbene **47**. The remaining material balance consisted of starting compound.

6.3.3.8 Mercury test for hydrogenation of diphenylacetylene 20 with $Na[Ni_4(NP^tBu_3)_4]$ 31 at 0 °C

The general procedure was applied to $[Ni(NP^tBu_3)]_4$ **18** (6.0 mg, 0.0055 mmol) and diphenylacetylene **20** (100.0 mg, 0.55 mmol). Excess mercury (5.5 mmol, 1.102 g) was also added in the glass reactor. The glass reactor was immersed in ice bath after the addition of H_2. The products were characterized quantitatively by GC. The conversions were 22% for bibenzyl **42**, 54% for *cis*-stilbene **46**, and 4% for *trans*-stilbene **47**. The remaining material balance consisted of starting compound.

6.3.3.9 Mercury test for hydrogenation of diphenylacetylene 20 with $Na[Ni_4(NP^tBu_3)_4]$ 31 at room temperature

The general procedure was applied to $[Ni(NP^tBu_3)]_4$ **18** (6.0 mg, 0.0055 mmol) and diphenylacetylene **20** (100.0 mg, 0.55 mmol). Excess mercury (5.5 mmol, 1.102 g) was also added in the glass reactor. The products were characterized quantitatively by GC. The conversions were 8% for bibenzyl **42**, 39% for *cis*-stilbene **46**, and 4% for *trans*-stilbene **47**.

6.3.3.10 Mercury test for hydrogenation of diphenylacetylene 20 with $Na[Ni_4(NP^tBu_3)_4]$ 31 at 80°C

The general procedure was applied to $[Ni(NP^tBu_3)]_4$ **18** (6.0 mg, 0.0055 mmol) and diphenylacetylene **20** (100.0 mg, 0.55 mmol). Excess mercury (5.5 mmol, 1.102 g) was also added in the glass reactor. The glass reactor was immersed in 80 °C mineral oil bath after the addition of H_2. The products were characterized quantitatively by GC. The conversions were 4% for bibenzyl **42**, 56% for *cis*-stilbene **46**, and 2% for *trans*-stilbene **47**.

6.3.4 General procedure for hydrogenation with $Na[Ni_4(NP^tBu_3)_4]$ 31 in different solvents

The $[Ni(NP^tBu_3)]_4$ **18** used here was prepared immediately from reduction of $[Ni_4(NP^tBu_3)_4]BPh_4$ **23** by 1% Na/Hg. The green solid $[Ni(NP^tBu_3)]_4$ **18** (5.9 mg, 0.00055

mmol) was dissolved in 1 mL of THF. After the solid dissolved, one drop of 40% Na/Hg was added. The solution was stirred 15 minutes during which the color changed from green to brown gradually. After 15 min, the solvent was removed under vacuum. The residue was extracted with 1 mL of the specific solvent, taking hexane for example, giving the solution of $Na[Ni_4(NP^tBu_3)_4]$ **31**. Then the substrate (0.055 mol), solution of $Na[Ni_4(NP^tBu_3)_4]$ **31**, another 4 mL of hexane and a glass-encased stir bar were mixed in a medium-walled glass reactor fitted with a Teflon high-vacuum valve. The glass reactor was transferred out of the glovebox and connected to a hydrogen-filled Schlenk line. The solution was degassed by standard freeze-pump-thaw thrice, after which the glass reactor was filled with 1 atmosphere of H_2 as the solution warmed to room temperature. The reactor was then sealed and stirred at room temperature for one hour unless otherwise noted. After one hour, the reactor was opened to air. Within a few minutes the nickel catalyst precipitated out. The solution was then passed through Celite and mixed with 10 μL of dodecane before submission for GC or GC-MS. If ^{1}H-NMR spectroscopy was needed, the solvent was removed, and the solid was dissolved in $CDCl_3$ for ^{1}H-NMR spectroscopy with 2 mg of C_6Me_6 as internal standard.

6.3.4.1 Hydrogenation of diphenylacetylene 20 with $Na[Ni_4(NP^tBu_3)_4]$ 31 in hexane

The general procedure was applied to $[Ni(NP^tBu_3)]_4$ **18** (6.0 mg, 0.0055 mmol) and diphenylacetylene **20** (100.0 mg, 0.55 mmol). Hexane was used as the solvent. The products were characterized quantitatively by GC. The yields were 21% for bibenzyl **42**, 62% for *cis*-stilbene **46**, and 7% for *trans*-stilbene **47**. The remaining material balance consisted of starting compound.

6.3.4.2 Hydrogenation of diphenylacetylene 20 with $Na[Ni_4(NP^tBu_3)_4]$ 31 in toluene

The general procedure was applied to $[Ni(NP^tBu_3)]_4$ **18** (6.0 mg, 0.0055 mmol) and diphenylacetylene **20** (100.0 mg, 0.55 mmol). Toluene was used as the solvent. The products were characterized quantitatively by GC. The yields were 6% for bibenzyl **42**,

46% for *cis*-stilbene **46**, and 7% for *trans*-stilbene **47**. The remaining material balance consisted of starting compound.

6.3.4.3 Hydrogenation of diphenylacetylene 20 with $Na[Ni_4(NP^tBu_3)_4]$ 31 in benzene

The general procedure was applied to $[Ni(NP^tBu_3)]_4$ **18** (6.0 mg, 0.0055 mmol) and diphenylacetylene **20** (100.0 mg, 0.55 mmol). Benzene was used as the solvent. The products were characterized quantitatively by GC. The yields was 1% for *cis*-stilbene **46** and 1% for *trans*-stilbene **47**. The remaining material balance consisted of starting compound.

6.3.4.4 Hydrogenation of diphenylacetylene 20 with $Na[Ni_4(NP^tBu_3)_4]$ 31 in pentane

The general procedure was applied to $[Ni(NP^tBu_3)]_4$ **18** (6.0 mg, 0.0055 mmol) and diphenylacetylene **20** (100.0 mg, 0.55 mmol). Pentane was used as the solvent. The products were characterized quantitatively by GC. The yields were 23% for bibenzyl **42**, 74% for *cis*-stilbene **46**, and 3% for *trans*-stilbene **47**.

6.3.4.5 Hydrogenation of diphenylacetylene 20 with $Na[Ni_4(NP^tBu_3)_4]$ 31 in DME

The general procedure was applied to $[Ni(NP^tBu_3)]_4$ 18 (6.0 mg, 0.0055 mmol) and diphenylacetylene 20 (100.0 mg, 0.55 mmol). DME was used as the solvent. The products were characterized quantitatively by GC. The yields were 0.6% for bibenzyl **42** and 0.3% for *trans*-stilbene **47**. The remaining material balance consisted of starting compound.

6.3.4.6 Hydrogenation of diphenylacetylene 20 with $Na[Ni_4(NP^tBu_3)_4]$ 31 in Et_2O

The general procedure was applied to $[Ni(NP^tBu_3)]_4$ **18** (6.0 mg, 0.0055 mmol) and diphenylacetylene **20** (100.0 mg, 0.55 mmol). Et_2O was used as the solvent. The products were characterized quantitatively by GC. The yields were 9% for bibenzyl **42**, 34% for *cis*-stilbene **46**, and 10% for *trans*-stilbene **47**.

6.3.5 General procedure for hydrogenation with $[Ni_4(NP^tBu_3)_4]BPh_4$ 23

The substrate (0.055 mol), $[Ni_4(NP^tBu_3)_4]BPh_4$ **23** (7.9 mg, 0.00055 mmol), 5 mL THF and a glass-encased stir bar were mixed in a medium-walled glass reactor fitted with a Teflon high-vacuum valve. The glass reactor was transferred out of the glovebox and connected to a hydrogen-filled Schlenk line. The solution was degassed by standard freeze-pump-thaw thrice, after which the bomb was filled with 1 atm H_2 as the solution warmed to room temperature. The reactor was then sealed and stirred at room temperature for 6 hours unless otherwise noted. After 6 hours, the reactor was opened to air. Within a few min the nickel catalyst precipitated out. The solution was then passed through Celite and mixed with 10 μL of dodecane before submission for GC or GC-MS. If ^{1}H-NMR was needed, the solvent was removed, and the solid was dissolved in $CDCl_3$ for ^{1}H-NMR with 2 mg of C_6Me_6 as internal standard.

6.3.5.1 Hydrogenation of diphenylacetylene 20 with $[Ni_4(NP^tBu_3)_4]BPh_4$ 23

The general procedure was applied to $[Ni_4(NP^tBu_3)_4]BPh_4$ **23** (7.9 mg, 0.00055 mmol) and diphenylacetylene **20** (100.0 mg, 0.55 mmol). The yield was 0%, and only starting material was recovered.

6.3.5.2 Hydrogenation of *cis*-stilbene 46 with $[Ni_4(NP^tBu_3)_4]BPh_4$ 23

The general procedure was applied to $[Ni_4(NP^tBu_3)_4]BPh_4$ **23** (7.9 mg, 0.00055 mmol) and *cis*-stilbene **46** (102.0 mg, 0.55 mmol). The product was characterized quantitatively by GC. The yield was 2% for *trans*-stilbene **47**. The remaining material balance consisted of starting compound.

6.3.5.3 Hydrogenation of *trans*-stilbene 47 with $[Ni_4(NP^tBu_3)_4]BPh_4$ 23

The general procedure was applied to $[Ni_4(NP^tBu_3)_4]BPh_4$ **23** (7.9 mg, 0.00055 mmol) and *trans*-stilbene **47** (102.0 mg, 0.55 mmol). The product was characterized quantitatively by GC. The only product was bibenzyl **42** in 1% yield. The remaining material balance consisted of starting compound.

6.3.5.4 Hydrogenation of allylbenzene 40 with $[Ni_4(NP^tBu_3)_4]BPh_4$ 23

The general procedure was applied to $[Ni_4(NP^tBu_3)_4]BPh_4$ **23** (7.9 mg, 0.00055 mmol) and allylbenzene **40** (57.0 mg, 0.55 mmol). The product was characterized by GC-MS and ^{1}H-NMR. The yield of 1-phenylpropane **41** was 95%. The remaining material balance consisted of starting compound.

6.3.5.5 Hydrogenation of styrene 48 with $[Ni_4(NP^tBu_3)_4]BPh_4$ 23

The general procedure was applied to $[Ni_4(NP^tBu_3)_4]BPh_4$ **23** (7.9 mg, 0.00055 mmol) and styrene **48** (65.0 mg, 0.55 mmol). The product was characterized by GC-MS and ^{1}H-NMR. The product was ethylbenzene in 100% yield.

6.3.5.6 Hydrogenation of tetraphenylethylene 49 with $[Ni_4(NP^tBu_3)_4]BPh_4$ 23

The general procedure was applied to $[Ni_4(NP^tBu_3)_4]BPh_4$ **23** (7.9 mg, 0.00055 mmol) and tetraphenylethylene **49** (182.0 mg, 0.55 mmol). The product was characterized by GC-MS and ^{1}H-NMR. The starting material was the only compound recovered.

6.3.5.7 Hydrogenation of diphenylacetylene 20 with $[Ni_4(NP^tBu_3)_4]BPh_4$ 23 at 40 °C

The general procedure was applied to $[Ni_4(NP^tBu_3)_4]BPh_4$ **23** (7.9 mg, 0.00055 mmol) and diphenylacetylene **20** (100.0 mg, 0.55 mmol). The glass reactor was immersed in 40 °C mineral oil bath after the addition of H_2. The product was characterized quantitatively by GC. The yield was 9% for *cis*-stilbene. The starting material was the only compound recovered.

6.3.5.8 Hydrogenation of diphenylacetylene 20 with $[Ni_4(NP^tBu_3)_4]BPh_4$ 23 at 60 °C

The general procedure was applied to $[Ni_4(NP^tBu_3)_4]BPh_4$ **23** (7.9 mg, 0.00055 mmol) and diphenylacetylene **20** (100.0 mg, 0.55 mmol). The glass reactor was immersed in 60 °C mineral oil bath after the addition of H_2. The products were characterized quantitatively by GC. The yields were 41% for bibenzyl **42**, 50% for *cis*-stilbene **46**, and 9% for *trans*-stilbene **47**.

6.3.5.9 Hydrogenation of diphenylacetylene 20 with $[Ni_4(NP^tBu_3)_4]BPh_4$ 23 at 80 °C

The general procedure was applied to $[Ni_4(NP^tBu_3)_4]BPh_4$ **23** (7.9 mg, 0.00055 mmol) and diphenylacetylene **20** (100.0 mg, 0.55 mmol). The glass reactor was immersed in 80 °C mineral oil bath after the addition of H_2. The product was characterized quantitatively by GC. The yield was 100% for bibenzyl **42**.

6.3.5.10 Mercury test for hydrogenation of diphenylacetylene 20 with $[Ni_4(NP^tBu_3)_4]BPh_4$ 23 at 80°C

The general procedure was applied to $[Ni_4(NP^tBu_3)_4]BPh_4$ **23** (7.9 mg, 0.00055 mmol) and diphenylacetylene **20** (100.0 mg, 0.55 mmol). Excess mercury (5.5 mmol, 1.102 g) was also added in the glass reactor. The glass reactor was immersed in 80 °C mineral oil bath after the addition of H_2. The products were characterized quantitatively by GC. The conversions were 1% for bibenzyl **42**, 28% for *cis*-stilbene **46**, and 1% for *trans*-stilbene **47**.

6.4 Experimental procedures for Chapter 3

6.4.1 General procedure for hydrosilylation with $[Ni(NP^tBu_3)]_4$ 18 in THF

The $[Ni(NP^tBu_3)]_4$ **18** used in the hydrosilylation was prepared immediately from the reduction of $[Ni_4(NP^tBu_3)_4]BPh_4$ **23** (3.9 mg, 0.0025 mmol) by 1% Na/Hg. 0.5 mol% of

catalyst (3.0 mg, 0.0027 mmol), 1.2 eq. of Ph_2SiH_2 (0.0654 mmol, 120.0 mg), 0.5 mL THF and a glass-encased stir bar were mixed in a 5-dram vial and let stir for 5 min in the glovebox. Then a solution of the substrate (0.5 mmol) and 0.5 mL THF was added to the vial. The solution was then set under stirring at room temperature for 1 hour or 16 hours. Certain amount of C_6Me_6 was then added to the solution. A small portion of the solution (normally 1/5) was then transferred to another vial and dried under vacuum. The residue was then dissolved in C_6D_6 for ^{1}H-NMR. The product was identified by comparing with known compound in literature, and the yield was determined by comparing the integration of the C_6Me_6 and specific peaks of the products.[70,80]

6.4.1.1 Hydrosilylation of isovaleraldehyde 64 with 18

The general procedure was applied to 43.0 mg isovaleraldehyde **64**, 133.2 mg Ph_2SiH_2, and 3.0 mg **18**. 64% yield was obtained for (isovaleroxy)diphenylsilane.

6.4.1.2 Hydrosilylation of *n*-heptaldehyde 65 with 18

The general procedure was applied to 62.9 mg *n*-heptaldehyde **65**, 120.9 mg Ph_2SiH_2, and 3.0 mg **18**. 68% yield was obtained for (*n*-heptoxy)diphenylsilane.

6.4.1.3 Hydrosilylation of 1,2,3,6-tetrahydrobenzaldehyde 66 with 18

The general procedure was applied to 59.0 mg 1,2,3,6-tetrahydrobenzaldehyde **66**, 131.2 mg Ph_2SiH_2, and 3.0 mg **18**. 91% yield was obtained for (1,2,3,6-tetrahydrobenzoxy)diphenylsilane.

6.4.1.4 Hydrosilylation of benzaldehyde 67 with 18

The general procedure was applied to 57.0 mg benzaldehyde, 120.4 mg Ph_2SiH_2, and 3.0 mg **18**. 63% yield was obtained for (benzoxy)diphenylsilane, and 18% yield was obtained for bis(benzoxy)diphenylsilane.

6.4.1.5 Hydrosilylation of 4-(dimethylamino)benzaldehyde 68 with 18

The general procedure was applied to 80.6 mg 4-(dimethylamino)benzaldehyde **68**, 122.0 mg Ph_2SiH_2, and 3.0 mg **18**. 99% yield was obtained for 4-(dimethylamino)benzoxydiphenylsilane.

6.4.1.6 Hydrosilylation of *p*-anisaldehyde 69 with 18

The general procedure was applied to 80.6 mg 4-(dimethylamino)benzaldehyde **69**, 122.0 mg Ph_2SiH_2, and 3.0 mg **18**. 99% yield was obtained for 4-(dimethylamino)benzoxydiphenylsilane.

6.4.1.7 Hydrosilylation of biphenyl-4-carboxaldehyde 70 with 18

The general procedure was applied to 101.4 mg biphenyl-4-carboxaldehyde **70**, 120.0 mg Ph_2SiH_2, and 3.0 mg **18**. 62% yield was obtained for biphenyl-4-carboxydiphenylsilane, and 29% yield was obtained for bis(biphenyl-4-carboxy)diphenylsilane.

6.4.1.8 Hydrosilylation of *p*-(methlythio)benzaldehyde 71 with 18

The general procedure was applied to 80 mg *p*-(methlythio)benzaldehyde **71**, 120.0 mg Ph_2SiH_2, and 3.0 mg **18**. 60% yield was obtained for *p*-(methlythio)benzoxydiphenylsilane.

6.4.1.9 Hydrosilylation of cyclohexanone 61 with 18

The general procedure was applied to 49.6 mg cyclohexanone **61**, 132.0 mg Ph_2SiH_2, and 3.0 mg **18**. 83% yield was obtained for (cyclohexoxy)diphenylsilane.

6.4.1.10 Hydrosilylation of cycloheptanone 72 with 18

The general procedure was applied to 59.2 mg cycloheptanone **72**, 112.9 mg Ph_2SiH_2, and 3.0 mg **18**. 99% yield was obtained for (cycloheptoxy)diphenylsilane.

6.4.1.10 Hydrosilylation of 3-pentanone 73 with 18

The general procedure was applied to 48.0 mg 3-pentanone **73**, 135.0 mg Ph_2SiH_2, and 3.0 mg **18**. 11% yield was obtained for (3-pentoxy)diphenylsilane.

6.4.1.11 Hydrosilylation of acetophenone 74 with 18

The general procedure was applied to 65.0 mg acetophenone **74**, 120.0 mg Ph_2SiH_2, and 3.0 mg **18**. 61% yield was obtained for (1-phenylethoxy)diphenylsilane.

6.4.1.12 Hydrosilylation of 4'-ethylacetophenone 75 with 18

The general procedure was applied to 83.0 mg acetophenone **75**, 123.8 mg Ph_2SiH_2, and 3.0 mg **18**. 99% yield was obtained for 1-(4'-ethylphenyl)ethoxydiphenylsilane.

6.4.1.13 Hydrosilylation of 4'-methoxyacetophenone 76 with 18

The general procedure was applied to 82.0 mg 4'-methoxyacetophenone **76**, 120.0 mg Ph_2SiH_2, and 3.0 mg **18**. 50% yield was obtained for 1-(4'-methoxyphenyl)ethoxydiphenylsilane.

6.4.1.14 Hydrosilylation of 4'-chloroacetophenone 77 with 18

The general procedure was applied to 84.0 mg 4'-chloroacetophenone **77**, 120.0 mg Ph_2SiH_2, and 3.0 mg **18**. 98% yield was obtained for 1-(4'-chloroyphenyl)ethoxydiphenylsilane.

6.4.1.15 Hydrosilylation of 4'-fluoroacetophenone 78 with 18

The general procedure was applied to 78.0 mg 4'-fluoroacetophenone **78**, 120.0 mg Ph_2SiH_2, and 3.0 mg **18**. 91% yield was obtained for 1-(4'-fluoroyphenyl)ethoxydiphenylsilane.

6.4.2 General procedure for hydrosilylation with Na[Ni(NP^{t}Bu$_3$)]$_4$ 31 in THF

In the glovebox, [Ni$_4$(NP^{t}Bu$_3$)$_4$]BPh$_4$ **23** (3.9 mg, 0.0027 mmol) was dissolved in 0.5 mL THF and 1 drop (excess) of 40% Na/Hg was added into the solution under stirring. The color changed from blue to green upon adding, and changed to brown gradually in 15 min. The solution was then filtered through Celite and mixed with 1.2 eq. of Ph_2SiH_2 (110.4 mg) and a glass-encased stir bar in another a 5-dram vial. After 5 min of stirring, a solution of the substrate (0.54 mmol) and 0.5 mL THF was added to the vial. The solution was then set under stirring at room temperature for 1 hour or 16 hours. Certain amount of C_6Me_6 was then added to the solution. A small portion of the solution (normally 1/5) was then transferred to another vial and dried under vacuum. The residue was dissolved in C_6D_6 for ^{1}H-NMR. The product was identified by comparing with known compound in literature, and the yields were determined by comparing the integration of the C_6Me_6 and specific peaks of the products.[70,80]

6.4.2.1 Hydrosilylation of isovaleraldehyde 64 with 31

The general procedure was applied to 48.3 mg isovaleraldehyde **64**, 133.0 mg Ph_2SiH_2, and 3.0 mg **31**. 68% yield was obtained for (isovaleroxy)diphenylsilane.

6.4.2.2 Hydrosilylation of *n*-heptaldehyde 65 with 31

The general procedure was applied to 60.4 mg *n*-heptaldehyde **65**, 130.0 mg Ph_2SiH_2, and 3.0 mg **31**. 71% yield was obtained for (*n*-heptoxy)diphenylsilane.

6.4.2.3 Hydrosilylation of 1,2,3,6-tetrahydrobenzaldehyde 66 with 31

The general procedure was applied to 61.0 mg 1,2,3,6-tetrahydrobenzaldehyde **66**, 127.0 mg Ph_2SiH_2, and 3.0 mg **31**. 38% yield was obtained for (1,2,3,6-tetrahydrobenzoxy)diphenylsilane, and 41% yield was obtained for bis-(1,2,3,6-tetrahydrobenzoxy)diphenylsilane.

6.4.2.4 Hydrosilylation of cyclohexanone 61 with 31

The general procedure was applied to 49.9 mg cyclohexanone **61**, 119.0 mg Ph_2SiH_2, and 3.0 mg **31**. 65% yield was obtained for (cyclohexoxy)diphenylsilane.

6.4.2.5 Hydrosilylation of cycloheptanone 72 with 31

The general procedure was applied to 62.7 mg cycloheptanone **72**, 129.0 mg Ph_2SiH_2, and 3.0 mg **31**. 90% yield was obtained for (cycloheptoxy)diphenylsilane.

6.4.2.6 Hydrosilylation of 4'-ethylacetophenone 75 with 31

The general procedure was applied to 81.7 mg acetophenone **75**, 134.4 mg Ph_2SiH_2, and 3.0 mg **31**. 85% yield was obtained for 1-(4'-ethylphenyl)ethoxydiphenylsilane.

6.4.3 General procedure for hydrosilylation with $[Ni_4(NP^tBu_3)_4]BPh_4$ 23 in THF

The $[Ni_4(NP^tBu_3)_4]BPh_4$ **31** (3.9 mg, 0.0027 mmol), 1.2 eq. of Ph_2SiH_2 (0.0654 mmol, 120.0 mg), 0.5 mL THF and a glass-encased stir bar were mixed in a 5-dram vial and let stir for 5 min in the glovebox. Then a solution of the substrate (0.5 mmol) and 0.5 mL THF was added to the vial. The solution was then stirred at room temperature for 1 hour or 16 hours. Certain amount of C_6Me_6 was then added to the solution. A small portion of the solution (normally 1/5) was then transferred to another vial and dried under vacuum. The residue was then dissolved in C_6D_6 for ^{1}H-NMR. The product was identified by comparing with known compound in literature, and the yields were determined by comparing the

integration of the C_6Me_6 and specific peaks of the products.[70,80]

6.4.3.1 Hydrosilylation of isovaleraldehyde 64 with 23

The general procedure was applied to 41.9 mg isovaleraldehyde **64**, 131.0 mg Ph_2SiH_2, and 3.9 mg **23**. 62% yield was obtained for (isovaleroxy)diphenylsilane.

6.4.3.2 Hydrosilylation of 1,2,3,6-tetrahydrobenzaldehyde 66 with 23

The general procedure was applied to 55.5 mg 1,2,3,6-tetrahydrobenzaldehyde **66**, 122.5 mg Ph_2SiH_2, and 3.6 mg **23**. 69% yield was obtained for (1,2,3,6-tetrahydrobenzoxy)diphenylsilane.

6.4.3.3 Hydrosilylation of *p*-(methlythio)benzaldehyde 71 with 23

The general procedure was applied to 75.7 mg *p*-(methlythio)benzaldehyde **71**, 132.0 mg Ph_2SiH_2, and 3.5 mg **23**. 36% yield was obtained for *p*-(methlythio)benzoxydiphenylsilane.

6.4.3.4 Hydrosilylation of cyclohexanone 61 with 23

The general procedure was applied to 43.6 mg cyclohexanone 61, 108.7 mg Ph_2SiH_2, and 3.4 mg **23**. 99% yield was obtained for (cyclohexoxy)diphenylsilane.

6.4.3.5 Hydrosilylation of 4'-ethylacetophenone 75 with 23

The general procedure was applied to 75.0 mg acetophenone **75**, 125.0 mg Ph_2SiH_2, and 3.6 mg **23**. 98% yield was obtained for 1-(4'-ethylphenyl)ethoxydiphenylsilane.

6.4.3.6 Hydrosilylation of 4'-fluoroacetophenone 78 with 23

The general procedure was applied to 63.4 mg 4'-fluoroacetophenone **78**, 98.6 mg Ph_2SiH_2, and 3.1 mg **23**. 78% yield was obtained for 1-(4'-fluoroyphenyl)ethoxydiphenylsilane.

6.4.4 General procedure for deoxygenation with $[Ni(NP^tBu_3)]_4$ 18 in THF

The $[Ni(NP^tBu_3)]_4$ **18,** substrate, 2 eq. of $PhSiH_3$, 1 mL THF and a glass-encased stir bar are mixed in a medium-walled glass reactor in the glovebox. Then the reactor was transferred out of the glovebox and heated in silicone oil at elevated temperature for 16 hours. After heating, the reactor was opened to air and passed through neutral type I alumina. The solution was submitted to GC-MS directly. The conversions obtained were based on GC so it might not be as accurate as those based on NMR.

6.4.4.1 Deoxygenation of 4-(dimethylamino)benzaldehyde 68 with 18

The general procedure was applied to 5 mg of **18**, 150 mg 4-(dimethylamino)benzaldehyde **68**, and 160.0 mg $PhSiH_3$. The temperature was set at 80 °C. The conversions from GC-MS were 37% for N,N,4-trimethylaniline, 29% for 4-dimethylaminobenzyl alcohol, 27% for 4,4'-Ethane-1,2-diylbis(N,N-dimethylaniline), 2% for 4,4'-Methylenebis(N,N-dimethylaniline), 5% for 4-Benzyl-N,N-dimethylaniline, and 1% for 4-dimethylaminobenzyl alcohol.

6.4.4.2 Deoxygenation of *p*-anisaldehyde 69 with 18

The general procedure was applied to 5 mg of **18**, 112 mg *p*-anisaldehyde **69**, and 166.0 mg $PhSiH_3$. The temperature was set at 80 °C. The conversions from GC-MS were 10% for 4-Methylanisole, 67% for p-anisyl alcohol, and 22% for 4,4'-dimethoxybibenzyl.

6.4.4.3 Deoxygenation of *p*-(methylthio)benzaldehyde 71 with 18

The general procedure was applied to 5 mg of **18**, 108 mg *p*-(methylthio)benzaldehyde **71**, and 162.0 mg $PhSiH_3$. The temperature was set at 80 °C. The conversions from GC-MS

were 4% for 4-methylthioanisole, 87% for 4-(methylthio)phenylmethanol, and 9% for 4,4'-bis(methylthio)bibenzyl.

6.4.4.4 Deoxygenation of 4'-ethylacetophenone 75 with 18

The general procedure was applied to 4 mg of **18**, 108 mg 4'-ethylacetophenone **75**, and 160.0 mg $PhSiH_3$. The temperature was set at 80 °C. The conversions from GC-MS were 3% for 1,4-diethylbenzene, 31% for 1-(4-ethylphenyl)ethanol, 1% for 4-ethylstyrene.

6.4.4.5 Deoxygenation of 4'-methoxyacetophenone 76 with 18

The general procedure was applied to 4 mg of **18**, 106.1 mg 4'-methoxyacetophenone **76**, and 181.0 mg $PhSiH_3$. The temperature was set at 80 °C. The conversions from GC-MS were 2% for 1-ethyl-4-methoxybenzene, 25% for 1-(4-methoxyphenyl)ethanol, 2% for 4-methoxystyrene, and 3% for 1,1'-(2,3-butanediyl)bis(4-methoxybenzene).

6.4.4.6 Deoxygenation of (±)-carvone 99 with 18

The general procedure was applied to 4 mg of **18**, 105.3 mg (±)-carvone **99**, and 132.0 mg $PhSiH_3$. The temperature was set at 60 °C. The conversion from GC-MS was 1% for (±)-limonene.

6.4.4.7 Deoxygenation of 3,4-diphenyl-2-cyclopenten-1-one 102 with 18

The general procedure was applied to 4 mg of **18**, 155.0 mg 3,4-diphenyl-2-cyclopenten-1-one **102**, and 200.3 mg $PhSiH_3$. The temperature was set at 60 °C. The conversion from GC-MS was 2% for 1,1'-(2-cyclopentene-1,2-diyl)dibenzene.

6.4.4.8 Deoxygenation of 2-cyclohexen-1-one 104 with 18

The general procedure was applied to 5 mg of **18**, 87.0 mg 2-cyclohexen-1-one **104**, and 196.2 mg $PhSiH_3$. The temperature was set at 80 °C. The conversions from GC-MS were 5% for cyclohexane, 6% for cyclohexene, and 28% for 1,1'-bi(2-cyclohexen-1-yl).

6.4.4.9 Deoxygenation of 2-cyclohexen-1-one 104 with 18 at 160 °C

The general procedure was applied to 5 mg of **18**, 97.9 mg 2-cyclohexen-1-one **104**, and 198.4 mg $PhSiH_3$. The temperature was set at 160 °C for 5 days. The conversions from GC-MS were 21% for cyclohexane, 12% for cyclohexene, 6% for 1,4-cyclohexadiene, and 51% for 1,1'-bi(2-cyclohexen-1-yl).

6.5 Experimental procedures for Chapter 4

The synthesis of $[Ni(\eta^3\text{-allyl})(NP^tBu_3)]_2$ **46** and allyl-capped cobalt clusters were accomplished by Fiona Nkala, so the experimental details will be included in her Master's Thesis.

6.5.1 Synthesis of Et_3PBr_2

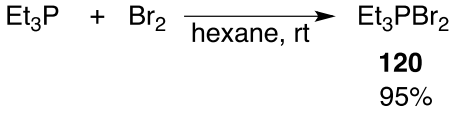

To a solution of PEt_3 (1.21 g, 0.0102 moles) in hexane (40 mL) at room temperature was added by syringe Br_2 (1.64 g, 0.0102 moles). The mixture was stirred for a further 16 h after the addition was complete, after which the solvent was removed under vacuum. Extraction of residual PEt_3 with 3 × 15 mL portions of hexane afforded Et_3PBr_2 **120** (2.69 g, 94.8 %) as a white solid. ^{31}P-NMR (202 MHz, CD_2Cl_2): δ 103.423, 87.616.[151]

6.5.2 Synthesis of $KNPEt_3$ 115

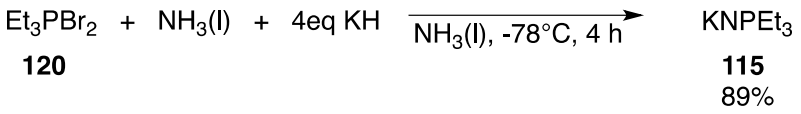

50 mL of ammonia was condensed and kept under -78 °C using a dry ice bath in a three-neck flask on the Schlenk line. KH (3.894 g, 0.09735 mol) was added to the flask using a solid addition funnel. The solution changed to blue as the addition proceeded. PEt_3Br_2 **120** (6.765 g, 0.02433 mol) was then added by portion through the side neck under positive nitrogen pressure. After the addition was finished, the reaction was allowed to warm-up overnight as the ammonia evaporated. The flask was then transferred into the glovebox. The residual solid was extract with hexane (3 × 20 mL) and filtrated through Celite. After evaporation of hexane under vacuum, 2.684 g of $KNPEt_3$ **115** was obtained as yellow powder with 89% yield. ^{1}H-NMR (500 MHz, C_6D_6): δ 1.312(br, 6H), 1.068(br, 9H); ^{31}P-NMR: (500MHz): δ -15.067(br).

6.5.3 Synthesis of $[Ni(\eta^3\text{-allyl})(NPEt_3)]_2$ 114

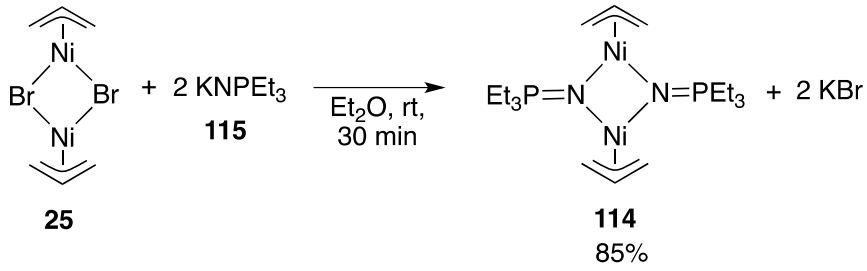

$[Ni(\eta^3\text{-allyl})Br]_2$ **25** (360mg, 1.00mmol) and $KNPEt_3$ **115** (342mg, 2.00mmol) were each dissolved in 10 mL Et_2O in the glovebox. The $KNPEt_3$ **115** was added to $[Ni(\eta^3\text{-allyl})Br]_2$ **25** solution dropwise with stirring at room temperature. Black solids precipitated immediately upon adding. The solution stayed red during the process. After stirring for 15 min, the solvent was removed under vacuum. The solid was triturated with 3 × 5 mL Et_2O. After removing the solvent, 0.464 g of spectroscopically pure red solid was obtained in 85% yield. The stoichiometry of the starting material must be accurate at 1:2, otherwise the product will be obtained as a red oil. Single crystals were obtained by cooling a

saturated Et_2O solution of crude product. ^{1}H-NMR (400MHz, C_6D_6): δ 5.293 (tt, *J* = 10, 7 Hz, 1H), 5.229 (tt, *J* = 10, 7 Hz, 1H), 2.189 (d, *J* = 7 Hz, 2H), 2.152(d, *J* = 7 Hz, 2H), 1.475 (d, *J* = 10.5 Hz, 2H), 1.450 (d, *J* = 10 Hz, 2H), 1.376 (m, 6H), 1.339 (m, 6H), 1.158 (td, *J* = 8, 7.5 Hz, 9H), 1.127 (td, *J* = 8, 7.5Hz, 9H). ^{31}P-NMR (400MHz, C_6D_6): δ 34.61 (s), 34.12 (s). ^{13}C-NMR: δ 99.221, 99.000, 43.741, 43.561, 22.810, 22.797, 22.211, 22.198. Elemental analysis: C: 46.58 (46.55) H: 8.76 (8.62) N: 5.73 (6.03).

6.5.4 Synthesis of {[Ni(η^3-allyl)(NPEt$_3$)]$_2$}$_2$[LiBr]$_2$ 116

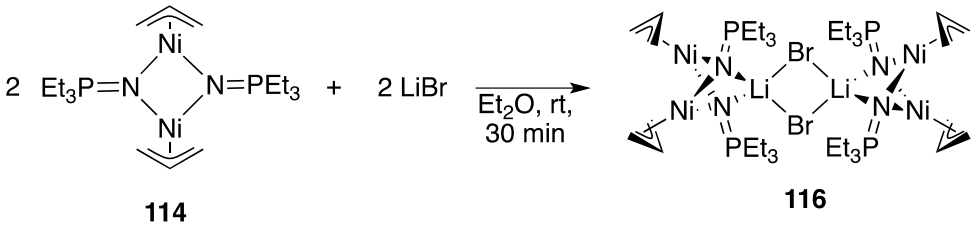

114 **116**

To a 5 mL THF solution of [Ni(η^3-allyl)(NPEt$_3$)]$_2$ **114** (40.5 mg, 0.0873 mmol), anhydrous LiBr (7.6 mg, 0.0874 mmol) was added. The solution was stirred for 2 hours, during which the color changed gradually from red to reddish-orange. The solvent was then removed under vacuum. The product was then recrystallized by cooling a saturated mixed solution of DME and hexane. The structure was determined by X-ray crystallography, but the yield was not determined.

6.5.5 Synthesis of [Ni(η^3-allyl)(NPPh$_3$)]$_2$ 122

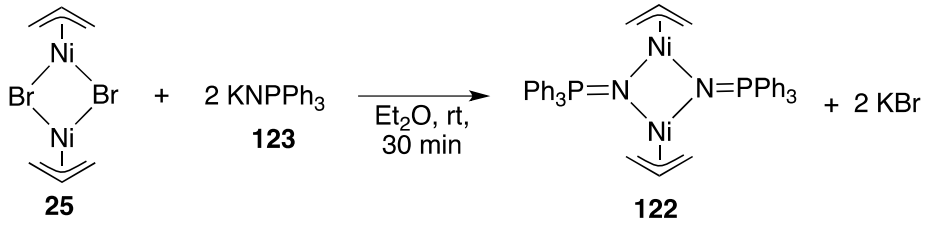

25 **122**

[Ni(η^3-allyl)Br]$_2$ **25** (75.7 mg, 0.210 mmol) and KNPPh$_3$ **123** (119.2 mg, 0.378 mmol) were each dissolved in 10 mL Et_2O in the glovebox. The KNPPh$_3$ **123** was added to [Ni(η^3-

allyl)Br]$_2$ **25** dropwise with stirring at room temperature. Black powder precipitates immediately upon addition and the solution stayed red during the process. After stirring for 15 min, the solvent was removed under vacuum. The solid was extracted with 3 × 5 mL Et_2O. The extracts were combined, and Et_2O was removed under vacuum. 0.1066 g red solid was obtained in 75% yield. Single crystals were obtained by cooling the saturated mixed solution of THF and hexane of the product. ^{1}H-NMR (500MHz, C_6D_6): δ 8.286 – 8.202 (m, 12H), 7.169 – 7.112 (m, 18H), 5.108 (tt, *J* = 10, 7 Hz, 1H), 4.843 (tt, *J* = 10, 7 Hz, 1H), 1.770 (d, *J* = 7 Hz, 2H), 1.728 (d, *J* = 7 Hz, 2H), 1.625 (d, *J* = 10.5 Hz, 2H), 1.174 (d, *J* = 10 Hz, 2H). ^{31}P-NMR (202 MHz, C_6D_6): δ 24.783 (s), 24.008 (s).

6.5.6 Synthesis of $[Ni_3(\eta^3\text{-Allyl})_3(\mu^3\text{-NPEt}_3)_2]PF_6$ 124

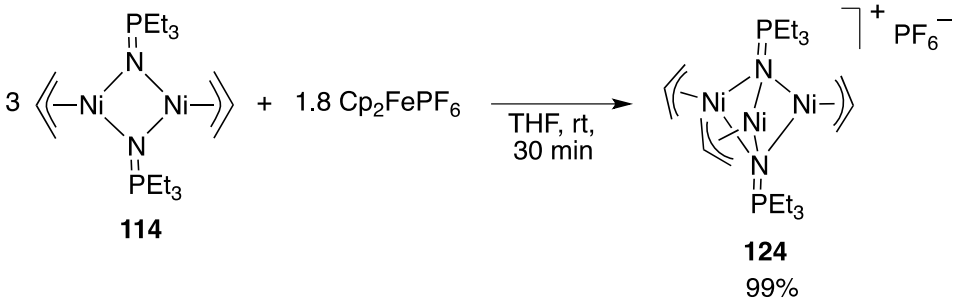

114 **124**
99%

$[Ni(\eta^3\text{-allyl})NPEt_3]_2$ **114** (126.3mg, 0.2722mmol) was dissolved in 10 mL THF and Cp_2FePF_6 (54.0mg, 0.163mmol) was added to the solution slowly at room temperature with stirring. 1.8 eq. of Cp_2FePF_6 was added to ease further purification. After stirring for 30 min, the solvent was removed, leaving behind a red solid. 3 × 5mL pentane was used to wash away the extra staring material, ferrocene and other organic product. Then 3 × 2mL dimethoxyethane(DME) was used to extract the product. The solutions were filtrated and combined, then the solvent was removed under vacuum. 108.4mg of $[Ni_3(\eta^3\text{-Allyl})_3(\mu^3\text{-NPEt}_3)_2]PF_6$ **124** was isolated in 99% yield. Single crystals were obtained by cooling a saturated DME solution of the product to -35 °C. **124** is paramagnetic so NMR spectra are not provided.

6.5.7 Synthesis of $[(\eta^3\text{-allyl})Ni]_2CoCl_2(\mu^3\text{-}NPEt_3)_2$ 126

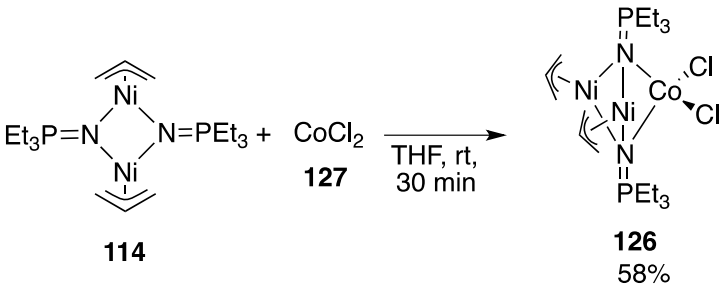

114 **126**
58%

To a 5 mL THF solution of $[Ni(\eta^3\text{-allyl})(NPEt_3)]_2$ **114** (61.0 mg, 0.131 mmol), anhydrous $CoCl_2$ (17.6 mg, 0.131 mmol) was added. The solution was stirred for 30 min, during which the color changed gradually from red to green. The solvent was then removed under vacuum leaving 45.6 mg of crude product as a green solid, in 58% yield. Single crystals were obtained by cooling a saturated mixed solution of THF and hexane.

6.5.8 Methylation of $[(\eta^3\text{-allyl})Ni]_2CoCl_2(\mu^3\text{-}NPEt_3)_2$ 126

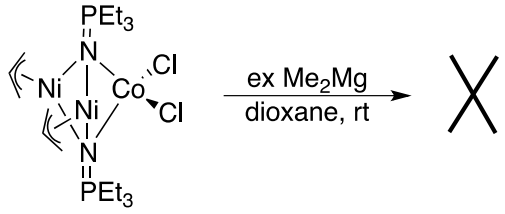

126

To the 1 mL dioxane solution of $[(\eta^3\text{-allyl})Ni]_2CoCl_2(\mu^3\text{-}NPEt_3)_2$ **126** (10.0 mg, 0.0168 mmol), 1 mL dioxane solution of Me_2Mg (1.0 mg, 0.0185 mmol) was added at room temperature. Immediately a color change was observed from green to dark brown. The solvent was removed under vacuum. A blue compound was obtained by extraction with THF, however, with low yield of less than 1 mg. Recrystallization of the blue compound was unsuccessful, resulting only in the formation of an insoluble precipitate.

6.6 Experimental procedures for Chapter 5

The control experiments of KTMP and HDS study of [Ni(η^3-allyl)(NPEt$_3$)]$_2$ **114** were accomplished by Fiona Nkala. The experimental procedures details will be included in her Master's thesis.

The control experiment of KO^{t}Bu, K_2S and HDS study of [Ni(NP^{t}Bu$_3$)]$_4$ **18** were accomplished by Orain Brown. The experimental procedures will be included in his PhD thesis.

6.6.1 Control experiment of KH for HDS, with/without hydrogen.

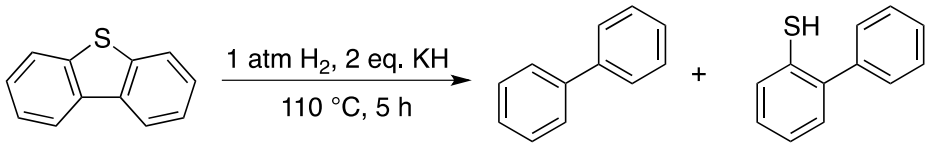

109 **110** **158**

Entry	Control Conditions	Solvent	% Conversion	
			110	**158**
1	KH	THF	1	34
2	KH+H_2	THF	0	28
3	KH	Toluene	0	2
4	KH+H_2	Toluene	0	1

Dibenzothiophene **109** (92.0 mg, 0.500 mmol), KH (40.0 mg, 1.00 mmol), 10 mL of solvent (THF or toluene), and a glass-encased stir bar were mixed in a medium-walled glass reactor in the glovebox. The glass reactor was then transferred out of the glovebox and connected to a hydrogen-filled Schlenk line (if hydrogen was need). The solution was degassed by applying standard freeze-pump-thaw thrice. The glass reactor was then heated in a mineral oil bath at 110 °C. After 16 hours, the reactor was opened to air and acidic workup (dilute HCl) was used to quench the left base. The organic layer was then filtrated, dried over $MgSO_4$, and submitted for GC analysis. The yields shown here were determined by GC.

6.6.2 D-scrambling control experiment using KH and H_2 in THF-d_8 for HDS of DBT

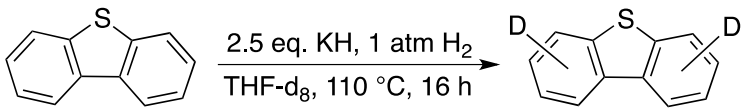

109

Dibenzothiophene (DBT) **109** (92.0 mg, 0.500 mmol), KH (40.0 mg, 1.00 mmol), 10 mL of THF-d_8, and a glass-encased stir bar were mixed in a thick-wall glass reactor in the glovebox. The glass reactor was then transferred out of the glovebox and connected to a hydrogen-filled Schlenk line. The solution was degassed by applying standard freeze-pump-thaw thrice. The glass reactor was then heated in a mineral oil bath at 110 °C. After 16 hours, the reactor was opened to air and acidic workup (dilute HCl) was used to quench the left base. The organic layer was then filtrated and dried. The solvent was removed under vacuum. The solid was dissolved in THF-d_8 and THF for D-NMR. D-NMR (400 MHz): δ 7.600, 7.432, 7.229.

6.6.3 NMR spectroscopy study of $[Ni(\eta^3\text{-allyl})(NPEt_3)]_2$ 114 under various temperature

5 mg of $[Ni(\eta^3\text{-allyl})(NPEt_3)]_2$ **114** was dissolved in 0.7 mL of deuterated toluene (C_7D_8) and submitted to Dr. Mark Miskolzie for NMR-spectroscopy under various temperatures. The results are shown in the appendix.

6.6.4 Hydrogenation of diphenylacetylene using $[Ni(\eta^3\text{-allyl})(NPEt_3)]_2$ 114 and $[Ni_3(\eta^3\text{-Allyl})_3(\mu^3\text{-NPEt}_3)_2]PF_6$ 124

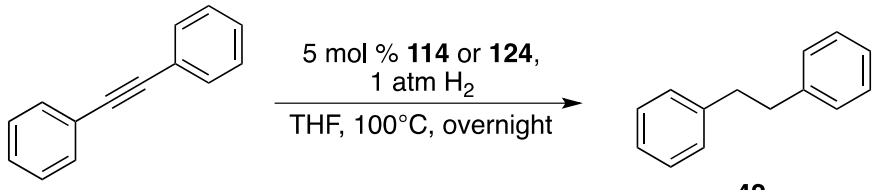

20

42
100%

The standard procedure from **6.3.1** was applied to **114** and **124**. GC was used to characterize the conversion of the product. 100% conversion to bibenzyl **42** was observed for both cases.

6.6.5 Synthesis of $MgCl_2$ supported $[Ni(\eta^3\text{-allyl})(NPEt_3)]_2$ 114

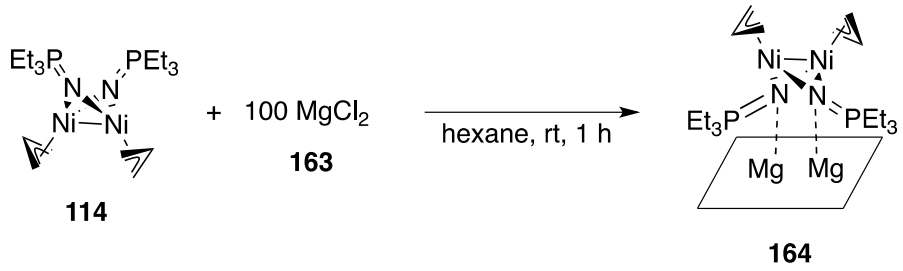

114 **164**

$[Ni(\eta^3\text{-allyl})(NPEt_3)]_2$ **114** (13.3 mg, 0.0287 mmol) was dissolved in 6 mL hexane and stirred with 100 equivalent of $MgCl_2$ **163** (272 mg, 2.86 mmol) suspended in the solution. The red solution decolorized gradually, and at the same time, the $MgCl_2$ powder turned to yellow. After stirring for 3 hours, the solid was filtrated, dried under vacuum, and stored for future use. Absorption was assumed to be quantitative.

6.6.6 Hydrogenation of diphenylacetylene with $MgCl_2$ supported $[Ni(\eta^3\text{-allyl})(NPEt_3)]_2$ 164

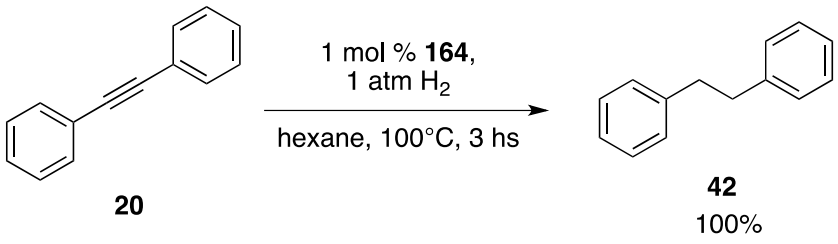

20 **42**
100%

Diphenylacetylene **20** (102 mg, 0.573 mmol) was dissolved in 3 mL hexane and 36 mg of $MgCl_2$ supported $[Ni(\eta^3\text{-allyl})NPEt_3]_2$ **164** was added in the solution and transferred into a glass reactor. The glass reactor was transferred out of the glovebox and charged with 1 atm H_2 on a hydrogen-filled Schlenk line. The suspension was heated to 100°C for 3 hours. The reactor was exposed to air and filtrate through Celite and submitted for GC-MS. 100%

conversion to dibenzyl **42** was obtained for this hydrogenation without further purifications.

6.6.6 HDS of DBT with M[Ni$_4$(NP^{t}Bu$_3$)$_4$] (M = Na, K) 31, 162

[Ni(NP^{t}Bu$_3$)]$_4$ **18** (5.5 mg, 0.005 mmol) was dissolved in 1 mL THF and the excess reductant (40% Na/Hg or KC_8) was added under stirring. After 15 min, the solution was filtered through Celite and mixed with neutral type I γ-alumina (137.5 mg) under stirring. The solution decolorized gradually and the alumina turned to grey. After decanting the solvent, the alumina with grafted catalysts was mixed with dibenzothiophene **109** (92.0 mg, 0.500 mmol), MO^{t}Bu (M = K, Na) (1.1 mmol), 7 mL of THF, and a glass-encased stir bar in a medium-walled glass vessel. The vessel was then transferred into a steel high pressure reactor. The reactor was then transferred out of the glovebox and charged with 500 psi (34 atm) H_2. The reactor was then heated in a silicone oil bath at 175 °C. After 16 hours, the reactor was opened to air and acidic workup (dilute HCl) was used to quench the left base. The organic layer was then filtrated, dried over $MgSO_4$, and submitted for GC analysis. The yields shown here were determined by GC.

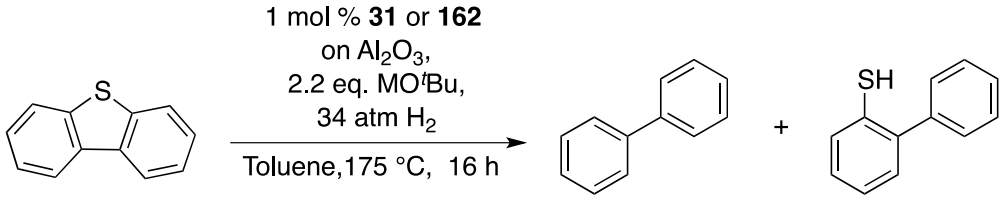

109 **110** **158**

Entry	Catalyst	Base	Conversions (%)	
			110	**158**
1	**31**	NaO^{t}Bu	12	0
2	**31**	KO^{t}Bu	98	0
3	**162**	NaO^{t}Bu	9	0
4	**162**	KO^{t}Bu	89	1

Bibliography

(1) Ault, A. *J. Chem. Educ.* **2002**, *79*, 572.

(2) Casey, C. P. *J. Chem. Educ.* **2006**, *83*, 192.

(3) Johansson Seechurn, C. C.; Kitching, M. O.; Colacot, T. J.; Snieckus, V. *Angew. Chem. Int. Ed.* **2012**, *51*, 5062-5085.

(4) Chirik, P.; Morris, R. *Acc. Chem. Res.* **2015**, *48*, 2495-2495.

(5) Gandeepan, P.; Cheng, C.-H. *Acc. Chem. Res.* **2015**, *48*, 1194-1206.

(6) Jackson, E. P.; Malik, H. A.; Sormunen, G. J.; Baxter, R. D.; Liu, P.; Wang, H.; Shareef, A.-R.; Montgomery, J. *Acc. Chem. Res.* **2015**, *48*, 1736-1745.

(7) Liu, C.; Liu, D.; Lei, A. *Acc. Chem. Res.* **2014**, *47*, 3459-3470.

(8) Standley, E. A.; Tasker, S. Z.; Jensen, K. L.; Jamison, T. F. *Acc. Chem. Res.* **2015**, *48*, 1503-1514.

(9) Thakur, A.; Louie, J. *Acc. Chem. Res.* **2015**, *48*, 2354-2365.

(10) Tobisu, M.; Chatani, N. *Acc. Chem. Res.* **2015**, *48*, 1717-1726.

(11) Tollefson, E. J.; Hanna, L. E.; Jarvo, E. R. *Acc. Chem. Res.* **2015**, *48*, 2344-2353.

(12) Miao, J.; Ge, H. *Eur. J. Org. Chem.* **2015**, *2015*, 7859-7868.

(13) Ryken, S. A.; Schafer, L. L. *Acc. Chem. Res.* **2015**, *48*, 2576-2586.

(14) Chakraborty, S.; Bhattacharya, P.; Dai, H.; Guan, H. *Acc. Chem. Res.* **2015**, *48*, 1995-2003.

(15) Chirik, P. J. *Acc. Chem. Res.* **2015**, *48*, 1687-1695.

(16) Li, Y.-Y.; Yu, S.-L.; Shen, W.-Y.; Gao, J.-X. *Acc. Chem. Res.* **2015**, *48*, 2587-2598.

(17) Morris, R. H. *Acc. Chem. Res.* **2015**, *48*, 1494-1502.

(18) McCann, S. D.; Stahl, S. S. *Acc. Chem. Res.* **2015**, *48*, 1756-1766.

(19) Liu, W.; Groves, J. T. *Acc. Chem. Res.* **2015**, *48*, 1727-1735.

(20) Su, B.; Cao, Z.-C.; Shi, Z.-J. *Acc. Chem. Res.* **2015**, *48*, 886-896.

(21) Klosin, J.; Fontaine, P. P.; Figueroa, R. *Acc. Chem. Res.* **2015**, *48*, 2004-2016.

(22) Small, B. L. *Acc. Chem. Res.* **2015**, *48*, 2599-2611.

(23) Staudinger, H.; Meyer, J. *Helv. Chim. Acta* **1919**, *2*, 635-646.

(24) Schmidbaur, H.; Jonas, G. *Chem. Ber.* **1968**, *101*, 1271-1285.

(25) Schmidbour, H.; Wolfsberger, W. *Chem. Ber.* **1967**, *100*, 1000-1015.

(26) Dehnicke, K.; Krieger, M.; Massa, W. *Coord. Chem. Rev.* **1999**, *182*, 19-65.

(27) Dehnicke, K.; Strähle, J. *Polyhedron* **1989**, *8*, 707-726.

(28) Dehnicke, K.; Weller, F. *Coord. Chem. Rev.* **1997**, *158*, 103-169.

(29) Stephan, D. W. *Organometallics* **2005**, *24*, 2548-2560.

(30) Stephan, D. W. *Adv. Organomet. Chem.* **2006**, *54*, 267-291.

(31) LePichon, L.; Stephan, D. W.; Gao, X.; Wang, Q. *Organometallics* **2002**, *21*, 1362-1366.

(32) Wolczanski, P. T. *Polyhedron* **1995**, *14*, 3335-3362.

(33) Batsanov, A.; Davidson, M.; Howard, J. K.; Price, R. *Chem. Commun.* **1997**, 1211-1212.

(34) Anfang, S.; Seybert, G.; Harms, K.; Geiseler, G.; Massa, W.; Dehnicke, K. *Z. Anorg. Allg. Chem.* **1998**, *624*, 1187-1192.

(35) Chitsaz, S.; Neumüller, B.; Dehnicke, K. *Z. Anorg. Allg. Chem.* **1999**, *625*, 9-10.

(36) Courtenay, S.; Wei, P.; Stephan, D. W. *Can. J. Chem.* **2003**, *81*, 1471-1476.

(37) Gröb, T.; Harms, K.; Dehnicke, K. *Z. Anorg. Allg. Chem.* **2000**, *626*, 1065-1072.

(38) Gröb, T.; Müller, C.; Massa, W.; Miekisch, T.; Seybert, G.; Harms, K.; Dehnicke, K. *Z. Anorg. Allg. Chem.* **2001**, *627*, 2191-2197.

(39) Sundermann, A.; Schoeller, W. W. *J. Am. Chem. Soc.* **2000**, *122*, 4729-4734.

(40) Schlecht, S.; Deubel, D. V.; Frenking, G.; Geiseler, G.; Harms, K.; Magull, J.; Dehnicke, K. *Z. Anorg. Allg. Chem.* **1999**, *625*, 887-891.

(41) Nußhär, D.; Weller, F.; Dehnicke, K. *Z. Anorg. Allg. Chem.* **1993**, *619*, 507-512.

(42) Honeyman, C. H.; Lough, A. J.; Manners, I. *Inorg. Chem.* **1994**, *33*, 2988-2993.

(43) Klein, H. F.; Haller, S.; Koenig, H.; Dartiguenave, M.; Dartiguenave, Y.; Menu, M. J. *J. Am. Chem. Soc.* **1991**, *113*, 4673-4675.

(44) Abram, S.; Abram, U.; zu Köcker, R. M.; Dehnicke, K. *Z. Anorg. Allg. Chem.* **1996**, *622*, 867-872.

(45) Camacho-Bunquin, J.; Ferguson, M. J.; Stryker, J. M. *J. Am. Chem. Soc.* **2013**, *135*, 5537-5540.

(46) Hollink, E.; Wei, P.; Stephan, D. W. *Can. J. Chem.* **2005**, *83*, 430-434.

(47) Stephan, D. W. In *Macromolecular Symposia*; Wiley Online Library: 2001; Vol. 173, p 105-116.

(48) Stephan, D. W.; Stewart, J. C.; Guérin, F.; Spence, R. E. v. H.; Xu, W.; Harrison, D. G. *Organometallics* **1999**, *18*, 1116-1118.

(49) Tolman, C. A. *J. Am. Chem. Soc.* **1970**, *92*, 2956-2965.

(50) Dehnicke, K.; Greiner, A. *Angew. Chem. Int. Ed.* **2003**, *42*, 1340-1354.

(51) Zimmer, H.; Jayawant, M.; Gutsch, P. *J. Org. Chem.* **1970**, *35*, 2826-2828.

(52) Berhault, G.; Maugé, F.; Lavalley, J.-C.; Lacroix, M.; Breysse, M. *J. Catal.* **2000**, *189*, 431-437.

(53) Chianelli, R.; Berhault, G.; Raybaud, P.; Kasztelan, S.; Hafner, J.; Toulhoat, H. *Appl. Catal., A* **2002**, *227*, 83-96.

(54) Harris, S.; Chianelli, R. *J. Catal.* **1984**, *86*, 400-412.

(55) Ho, T. C. *Catal. Today* **2004**, *98*, 3-18.

(56) Pecoraro, T.; Chianelli, R. *J. Catal.* **1981**, *67*, 430-445.

(57) Prins, R.; De Beer, V.; Somorjai, G. *Catal. Rev. Sci. Eng.* **1989**, *31*, 1-41.

(58) Evans, D. *J. Chem. Soc.* **1959**, 2003-2005.

(59) Zhao, T.; Hamilton, R.; Han, C.; Bai, T. Unpublished results. **2014**.

(60) Brown, H. Doctorate, University of Alberta, 2013.

(61) Richardson, D. E.; Taube, H. *Coord. Chem. Rev.* **1984**, *60*, 107-129.

(62) Faust, M.; Bryan, A. M.; Mansikkamäki, A.; Vasko, P.; Olmstead, M. M.; Tuononen, H. M.; Grandjean, F.; Long, G. J.; Power, P. P. *Angew. Chem. Int. Ed.* **2015**, *54*, 12914-12917.

(63) Mingos, D. M. P. *Essential trends in inorganic chemistry*; Oxford University Press Oxford, 1998.

(64) Neumann, F.; Hampel, F.; Schleyer, P. v. R. *Inorg. Chem.* **1995**, *34*, 6553-6555.

(65) Connelly, N. G.; Geiger, W. E. *Chem. Rev.* **1996**, *96*, 877-910.

(66) Brown, O.; Zhao, T.; Nkala, F. Unpublished results. 2015.

(67) Merrill, B. A. In *Encyclopedia of Reagents for Organic Synthesis*; John Wiley & Sons, Ltd: 2001.

(68) Molander, G. A.; Harris, C. R. In *Encyclopedia of Reagents for Organic Synthesis*; John Wiley & Sons, Ltd: 2001.

(69) Pfirrmann, S.; Limberg, C.; Herwig, C.; Stößer, R.; Ziemer, B. *Angew. Chem. Int. Ed.* **2009**, *48*, 3357-3361.

(70) Bunquin, J. Unpublished results.

(71) Bergman, R. G.; Danheiser, R. L. *Angew. Chem. Int. Ed.* **2016**, *55*, 12548-12549.

(72) Whitesides, G. M.; Hackett, M.; Brainard, R. L.; Lavalleye, J. P. P.; Sowinski, A. F.; Izumi, A. N.; Moore, S. S.; Brown, D. W.; Staudt, E. M. *Organometallics* **1985**, *4*, 1819-1830.

(73) Widegren, J. A.; Finke, R. G. *J. Mol. Catal. A: Chem.* **2003**, *198*, 317-341.

(74) Clarson, S. J. *Silicon* **2009**, *1*, 57-58.

(75) MacMillan, S. N.; Harman, W. H.; Peters, J. C. *Chem. Sci.* **2014**, *5*, 590-597.

(76) Morris, R. H. *Chem. Soc. Rev.* **2009**, *38*, 2282-2291.

(77) Ruddy, A. J.; Kelly, C. M.; Crawford, S. M.; Wheaton, C. A.; Sydora, O. L.; Small, B. L.; Stradiotto, M.; Turculet, L. *Organometallics* **2013**, *32*, 5581-5588.

(78) Tondreau, A. M.; Darmon, J. M.; Wile, B. M.; Floyd, S. K.; Lobkovsky, E.; Chirik, P. J. *Organometallics* **2009**, *28*, 3928-3940.

(79) Trovitch, R. J. *Synlett* **2014**, *25*, 1638-1642.

(80) Yang, J.; Tilley, T. D. *Angew. Chem. Int. Ed.* **2010**, *49*, 10186-10188.

(81) Frogneux, X.; Jacquet, O.; Cantat, T. *Catal. Sci. Tech.* **2014**, *4*, 1529-1533.

(82) Iglesias, M.; Fernández-Alvarez, F. J.; Oro, L. A. *ChemCatChem* **2014**, *6*, 2486-2489.

(83) Jaseer, E.; Akhtar, M. N.; Osman, M.; Al-Shammari, A.; Oladipo, H. B.; Garcés, K.; Fernández-Alvarez, F. J.; Al-Khattaf, S.; Oro, L. A. *Catal. Sci. Tech.* **2015**, *5*, 274-279.

(84) Riener, K.; Högerl, M. P.; Gigler, P.; Kühn, F. E. *ACS Catal.* **2012**, *2*, 613-621.

(85) Scheuermann, M. L.; Semproni, S. P.; Pappas, I.; Chirik, P. J. *Inorg. Chem.* **2014**, *53*, 9463-9465.

(86) Schneider, J.; Jia, H.; Muckerman, J. T.; Fujita, E. *Chem. Soc. Rev.* **2012**, *41*, 2036-2051.

(87) Windle, C. D.; Perutz, R. N. *Coord. Chem. Rev.* **2012**, *256*, 2562-2570.

(88) Shaikh, N. S.; Junge, K.; Beller, M. *Org. Lett.* **2007**, *9*, 5429-5432.

(89) Shaikh, N. S.; Enthaler, S.; Junge, K.; Beller, M. *Angew. Chem. Int. Ed.* **2008**, *47*, 2497-2501.

(90) Nishiyama, H.; Furuta, A. *Chem. Commun.* **2007**, 760-762.

(91) Furuta, A.; Nishiyama, H. *Tetrahedron Lett.* **2008**, *49*, 110-113.

(92) Tondreau, A. M.; Lobkovsky, E.; Chirik, P. J. *Org. Lett.* **2008**, *10*, 2789-2792.

(93) Nesbit, M. A.; Suess, D. L.; Peters, J. C. *Organometallics* **2015**, *34*, 4741-4752.

(94) Bleith, T.; Wadepohl, H.; Gade, L. H. *J. Am. Chem. Soc.* **2015**, *137*, 2456-2459.

(95) Junge, K.; Schröder, K.; Beller, M. *Chem. Commun.* **2011**, *47*, 4849-4859.

(96) Zhang, M.; Zhang, A. *Appl. Organomet. Chem.* **2010**, *24*, 751-757.

(97) Zuo, Z.; Sun, H.; Wang, L.; Li, X. *Dalton Trans.* **2014**, *43*, 11716-11722.

(98) Zuo, Z.; Zhang, L.; Leng, X.; Huang, Z. *Chem. Commun.* **2015**, *51*, 5073-5076.

(99) Zhou, H.; Sun, H.; Zhang, S.; Li, X. *Organometallics* **2015**, *34*, 1479-1486.

(100) Sauer, D. s. e. C.; Wadepohl, H.; Gade, L. H. *Inorg. Chem.* **2012**, *51*, 12948-12958.

(101) Chakraborty, S.; Krause, J. A.; Guan, H. *Organometallics* **2008**, *28*, 582-586.

(102) Kundu, S.; Brennessel, W. W.; Jones, W. D. *Inorg. Chem.* **2011**, *50*, 9443-9453.

(103) Tran, B. L.; Pink, M.; Mindiola, D. J. *Organometallics* **2009**, *28*, 2234-2243.

(104) Díez-González, S.; Nolan, S. P. *Acc. Chem. Res.* **2008**, *41*, 349-358.

(105) Lipshutz, B. H. *Synlett* **2009**, *2009*, 509-524.

(106) Rendler, S.; Oestreich, M. *Angew. Chem. Int. Ed.* **2007**, *46*, 498-504.

(107) Bandini, M.; Bernardi, F.; Bottoni, A.; Cozzi, P. G.; Miscione, G. P.; Umani-Ronchi, A. *Eur. J. Org. Chem.* **2003**, *2003*, 2972-2984.

(108) Ramón, D. J.; Yus, M. *Chem. Rev.* **2006**, *106*, 2126-2208.

(109) Alonso, D. M.; Bond, J. Q.; Dumesic, J. A. *Green Chem.* **2010**, *12*, 1493-1513.

(110) Gallezot, P. *Chem. Soc. Rev.* **2012**, *41*, 1538-1558.

(111) Huber, G. W.; Corma, A. *Angew. Chem.* **2007**, *119*, 7320-7338.

(112) Marshall, A. L.; Alaimo, P. J. *Chem. Eur. J.* **2010**, *16*, 4970-4980.

(113) Naik, S. N.; Goud, V. V.; Rout, P. K.; Dalai, A. K. *IRESR* **2010**, *14*, 578-597.

(114) Serrano-Ruiz, J. C.; Luque, R.; Sepulveda-Escribano, A. *Chem. Soc. Rev.* **2011**, *40*, 5266-5281.

(115) Zhang, X.; Tu, M.; Paice, M. G. *Bioenergy Res* **2011**, *4*, 246-257.

(116) Farrar, W. *J. Appl. Chem.* **1964**, *14*, 389-399.

(117) Laskowski, C. A.; Bungum, D. J.; Baldwin, S. M.; Del Ciello, S. A.; Iluc, V. M.; Hillhouse, G. L. *J. Am. Chem. Soc.* **2013**, *135*, 18272-18275.

(118) Fontanille, M.; Guyot, A. *Recent advances in mechanistic and synthetic aspects of polymerization*; Springer Science & Business Media, 2012; Vol. 215.

(119) Kurosawa, H. *J. Organomet. Chem.* **1987**, *334*, 243-253.

(120) Takagi, K.; Tomita, I.; Endo, T. *Macromolecules* **1997**, *30*, 7386-7390.

(121) Henc, B.; Jolly, P.; Salz, R.; Stobbe, S.; Wilke, G.; Benn, R.; Mynott, R.; Seevogel, K.; Goddard, R.; Krüger, C. *J. Organomet. Chem.* **1980**, *191*, 449-475.

(122) Birkenstock, U.; Bönnemann, H.; Bogdanovic, B.; Walter, D.; Wilke, G. *Adv. Chem. Ser.* **1968**, *70*, 250-265.

(123) Lee, C. E.; Tiege, P. B.; Xing, Y.; Nagendran, J.; Bergens, S. H. *J. Am. Chem. Soc.* **1997**, *119*, 3543-3549.

(124) Smith, C. R.; Zhang, A.; Mans, D. J.; RajanBabu, T. *Org. Synth.* **2008**, 248-266.

(125) Kölmel, C.; Ochsenfeld, C.; Ahlrichs, R. *Theor. Chem. Acc.* **1992**, *82*, 271-284.

(126) Bridgeman, A. J. *Dalton Trans.* **2008**, 1989-1992.

(127) Brück, A.; Englert, U.; Kuchen, W.; Peters, W. *Chem. Ber.* **1996**, *129*, 551-555.

(128) Frömmel, T.; Peters, W.; Wunderlich, H.; Kuchen, W. *Angew. Chem. Int. Ed.* **1992**, *31*, 612-613.

(129) Frömmel, T.; Peters, W.; Wunderlich, H.; Kuchen, W. *Angew. Chem. Int. Ed.* **1993**, *32*, 907-909.

(130) Sánchez-Delgado, R. A. *Organometallic modeling of the hydrodesulfurization and hydrodenitrogenation reactions*; Springer Science & Business Media, 2002; Vol. 24.

(131) Sánchez-Delgado, R. A. *J. Mol. Catal.* **1994**, *86*, 287-307.

(132) Eliel, E. L.; Krishnamurthy, S. *J. Org. Chem.* **1965**, *30*, 848-854.

(133) Hauptmann, H.; Walter, W. F. *Chem. Rev.* **1962**, *62*, 347-404.

(134) Nagai, M.; Urimoto, H.; Uetake, K.; Sakikawa, N.; Gonzalez, R. D. *Bull. Chem. Soc. Jpn.* **1989**, *62*, 557-562.

(135) Arévalo, A.; Bernès, S.; García, J. J.; Maitlis, P. M. *Organometallics* **1999**, *18*, 1680-1685.

(136) Bianchini, C.; Meli, A.; Moneti, S.; Vizza, F. *Organometallics* **1998**, *17*, 2636-2645.

(137) Hernández, M.; Miralrio, G.; Arévalo, A.; Bernès, S.; García, J. J.; López, C.; Maitlis, P. M.; del Rio, F. *Organometallics* **2001**, *20*, 4061-4071.

(138) Jones, W. D.; Chin, R. M. *J. Organomet. Chem.* **1994**, *472*, 311-316.

(139) Matsubara, K.; Okamura, R.; Tanaka, M.; Suzuki, H. *J. Am. Chem. Soc.* **1998**, *120*, 1108-1109.

(140) Torres-Nieto, J.; Arévalo, A.; García, J. J. *Organometallics* **2007**, *26*, 2228-2233.

(141) Riaz, U.; Curnow, O.; Curtis, M. D. *J. Am. Chem. Soc.* **1991**, *113*, 1416-1417.

(142) Baird Jr, W. C.; Bearden Jr, R.; Google Patents: 1977.

(143) Bearden, R.; Fink, T.; Google Patents: 1974.

(144) Duhme, A. K.; Strasdeit, H. *Eur. J. Inorg. Chem.* **1998**, *1998*, 657-662.

(145) Esmieu, C. n.; Orio, M.; Le Pape, L.; Lebrun, C.; Pécaut, J.; Ménage, S. p.; Torelli, S. p. *Inorg. Chem.* **2016**.

(146) Kan, Y.; Tso, K. C.-H.; Chan, S. L.-F.; Guan, X.; Che, C.-M. *New J. Chem.* **2013**, *37*, 1811-1816.

(147) Smiles, D. E.; Wu, G.; Hayton, T. W. *New J. Chem.* **2015**, *39*, 7563-7566.

(148) Takemura, H.; Nakashima, S.; Kon, N.; Inazu, T. *Tetrahedron Lett.* **2000**, *41*, 6105-6109.

(149) Chan, B. C. K.

(150) Gawley, R. E.; Zhang, X.; Wang, Q. In *Encyclopedia of Reagents for Organic Synthesis*; John Wiley & Sons, Ltd: 2001.

(151) Godfrey, S.; McAuliffe, C.; Pritchard, R.; Sheffield, J. *Dalton Trans.* **1998**, 3815-3818.

Appendix 1 Selected X-Ray Crystallography Data

A1.1 $[Ni_4(NP^tBu_3)_4][Li_3Br_4(Et_2O)_3]$

STRUCTURE REPORT

XCL Code: JMS1329 **Date:** 25 November 2015

Compound: $[Ni_4(NP^tBu_3)_4][Li_3(OEt_2)_3Br_4]$

Formula: $C_{60}H_{138}Br_4Li_3N_4Ni_4O_3P_4$

Supervisor: J. M. Stryker **Crystallographer:** M. J. Ferguson

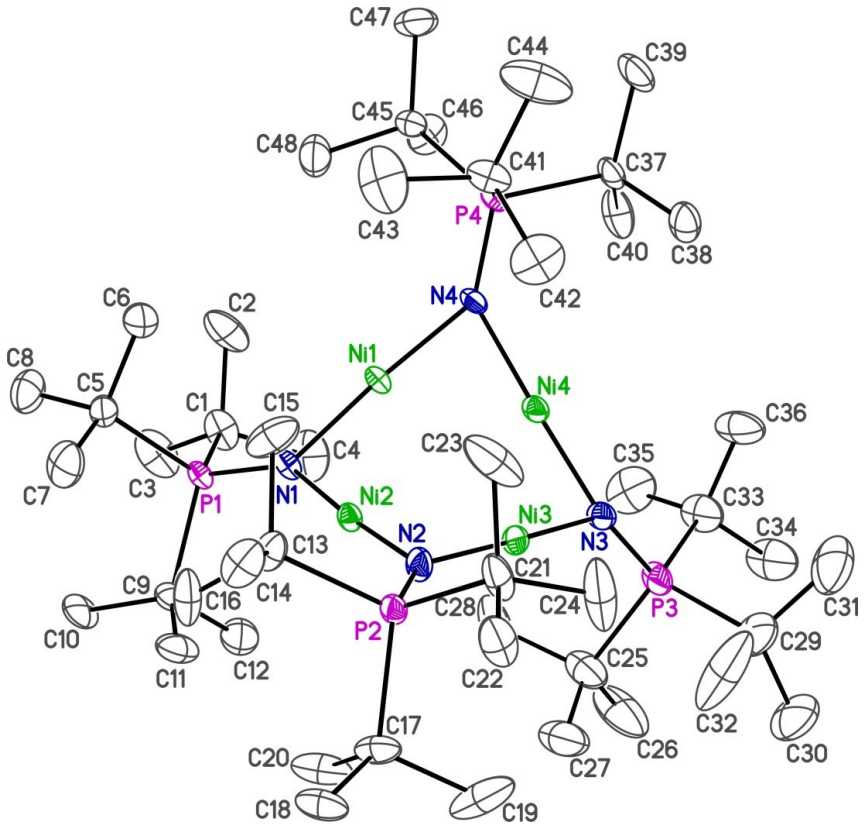

Figure Legends

Figure 1. Perspective view of the $[Ni_4(NP^tBu_3)_4]^+$ cation showing the atom labelling scheme. Non-hydrogen atoms are represented by Gaussian ellipsoids at the 30% probability level. Hydrogen atoms are not shown.

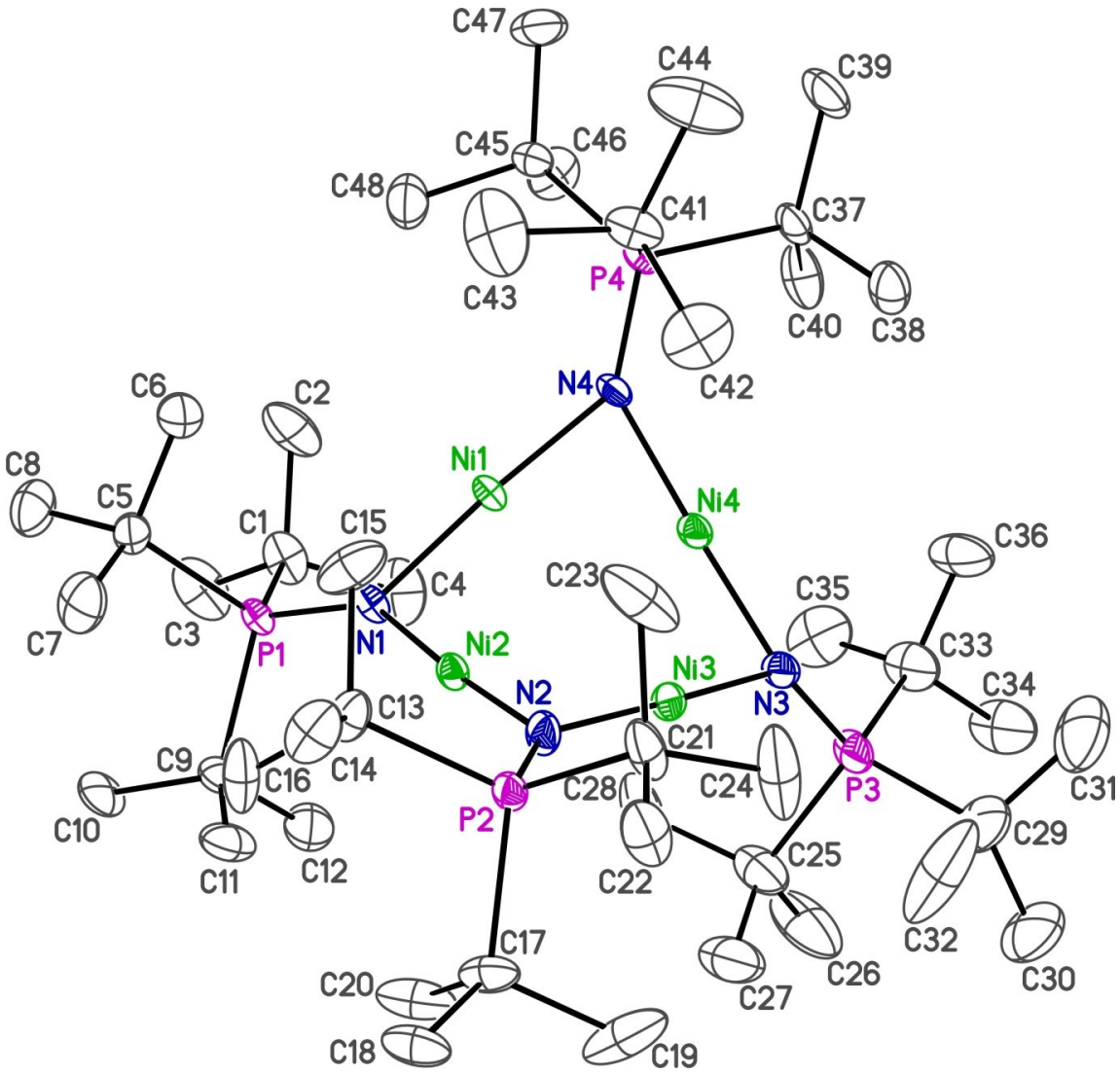

Table 1. Crystallographic Experimental Details

A. Crystal Data	
formula	$C_{60}H_{138}Br_4Li_3N_4Ni_4O_3P_4$
formula weight	1662.92
crystal dimensions (mm)	0.27 × 0.23 × 0.10
crystal system	orthorhombic
space group	$Pca2_1$ (No. 29)
unit cell parameters[a]	
a (Å)	28.5709 (12)
b (Å)	12.9283 (5)
c (Å)	22.1639 (9)
V (Å^3)	8186.8 (6)
Z	4
ρ_{calcd} (g cm^{-3})	1.349
μ (mm^{-1})	2.975
B. Data Collection and Refinement Conditions	
diffractometer	Bruker D8/APEX II CCD[b]
radiation (λ [Å])	graphite-monochromated Mo Kα (0.71073)
temperature (°C)	–100
scan type	ω scans (0.3°) (20 s exposures)
data collection 2θ limit (deg)	54.97
total data collected	70962 (-37<=h<=37, -16<=k<=16, -28<=l<=28)
independent reflections	18748 (R_{int} = 0.0520)
number of observed reflections (*NO*)	15188 [$F_o^2 \geq 2\sigma(F_o^2)$]
structure solution method	intrinsic phasing (*SHELXT-2014*[c])
refinement method	full-matrix least-squares on F^2 (*SHELXL–2014*[d])
absorption correction method	Gaussian integration (face-indexed)
range of transmission factors	0.7771–0.5067
data/restraints/parameters	18748 / 87[e] / 770
Flack absolute structure parameter[f]	0.408(9)
goodness-of-fit (*S*)[g] [all data]	1.023
final *R* indices[h]	
R_1 [$F_o^2 \geq 2\sigma(F_o^2)$]	0.0442
wR_2 [all data]	0.1103
largest difference peak and hole	1.121 and –0.812 e Å^{-3}

[a]Obtained from least-squares refinement of 9956 reflections with 4.62° < 2θ < 52.24°.

[b]Programs for diffractometer operation, data collection, data reduction and absorption

correction were those supplied by Bruker.

[c]Sheldrick, G. M. *Acta Crystallogr.* **2015**, *A71*, 3–8. (*SHELXT-2014*)

[d]Sheldrick, G. M. *Acta Crystallogr.* **2015**, *C71*, 3–8. (*SHELXL-2014*)

[e]The following distance restraints were applied to the diethylether molecules of the $[Li_3(OEt_2)_3Br_4]^-$ anion: O–C, 1.430(4) Å; C–C, 1.530(4) Å; O···C, 2.420(6) Å; C···C, 2.340(6) Å. Additionally, the anisotropic displacement parameters for atoms O2, C55, C56, C57 and C58 were restrained using RIGU and ISOR.

[f]Flack, H. D. *Acta Crystallogr.* **1983**, *A39*, 876–881; Flack, H. D.; Bernardinelli, G. *Acta Crystallogr.* **1999**, *A55*, 908–915; Flack, H. D.; Bernardinelli, G. *J. Appl. Cryst.* **2000**, *33*, 1143–1148. The Flack parameter will refine to a value near zero if the structure is in the correct configuration and will refine to a value near one for the inverted configuration. The value observed herein is indicative of racemic twinning, and was accomodated during the refinement (using the *SHELXL-2014* TWIN instruction [see reference *d*]).

[g]$S = [\Sigma w(F_o^2 - F_c^2)^2/(n-p)]^{1/2}$ (n = number of data; p = number of parameters varied; $w = [\sigma^2(F_o^2) + (0.0605P)^2 + 4.5531P]^{-1}$ where $P = [\mathrm{Max}(F_o^2, 0) + 2F_c^2]/3$).

[h]$R_1 = \Sigma||F_o| - |F_c||/\Sigma|F_o|$; $wR_2 = [\Sigma w(F_o^2 - F_c^2)^2/\Sigma w(F_o^4)]^{1/2}$.

A 1.2 $[Ni_4(NP^tBu_3)_4][BPh_4]$

STRUCTURE REPORT

XCL Code: JMS1333 **Date:** 26 September 2013

Compound: $[Ni_4(NP^tBu_3)_4][BPh_4]$

Formula: $C_{72}H_{128}BN_4Ni_4P_4$

Supervisor: J. M. Stryker **Crystallographer:** M. J. Ferguson

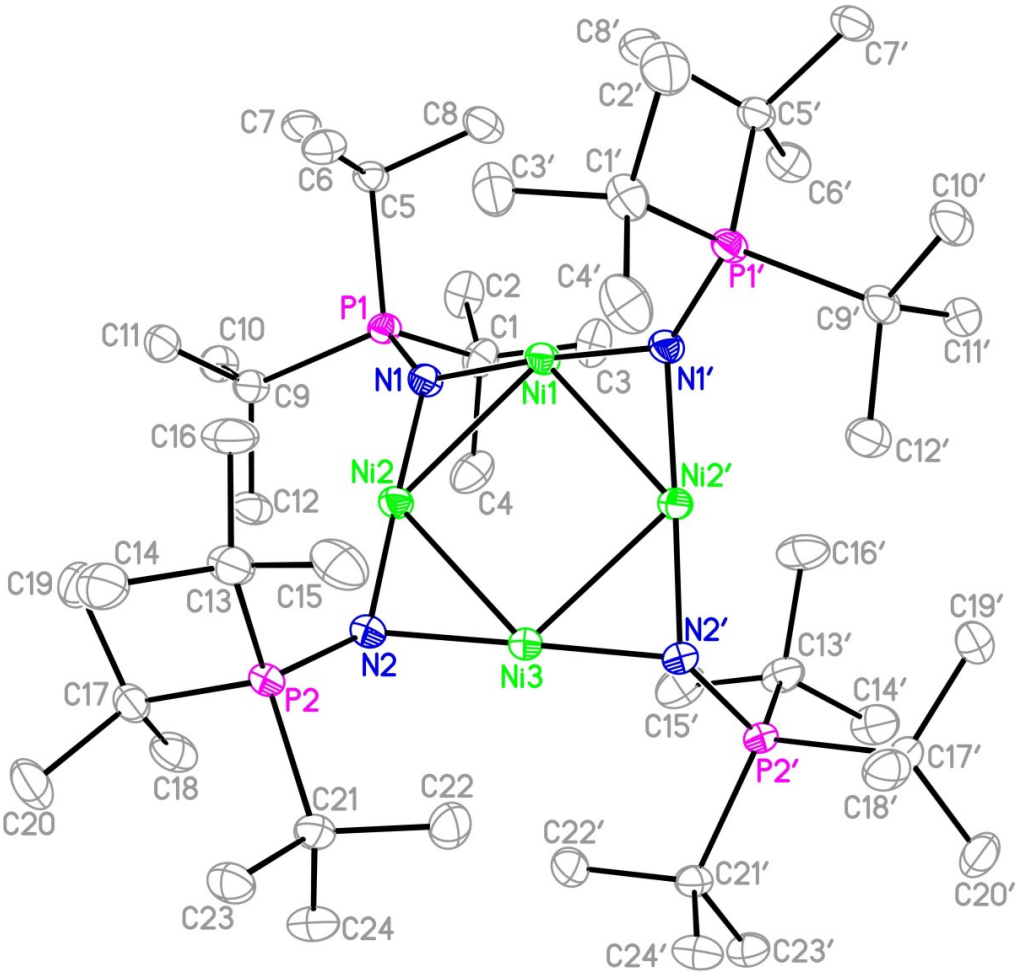

Figure Legends

Figure 1. Perspective view of the $[Ni_4(NP^tBu_3)_4]^+$ cation showing the atom labelling scheme. Primed atoms are related to unprimed ones by the 2-fold rotation axis at (0.75, *y*, 0). Non-hydrogen atoms are represented by Gaussian ellipsoids at the 20% probability level. Hydrogen atoms are not shown.

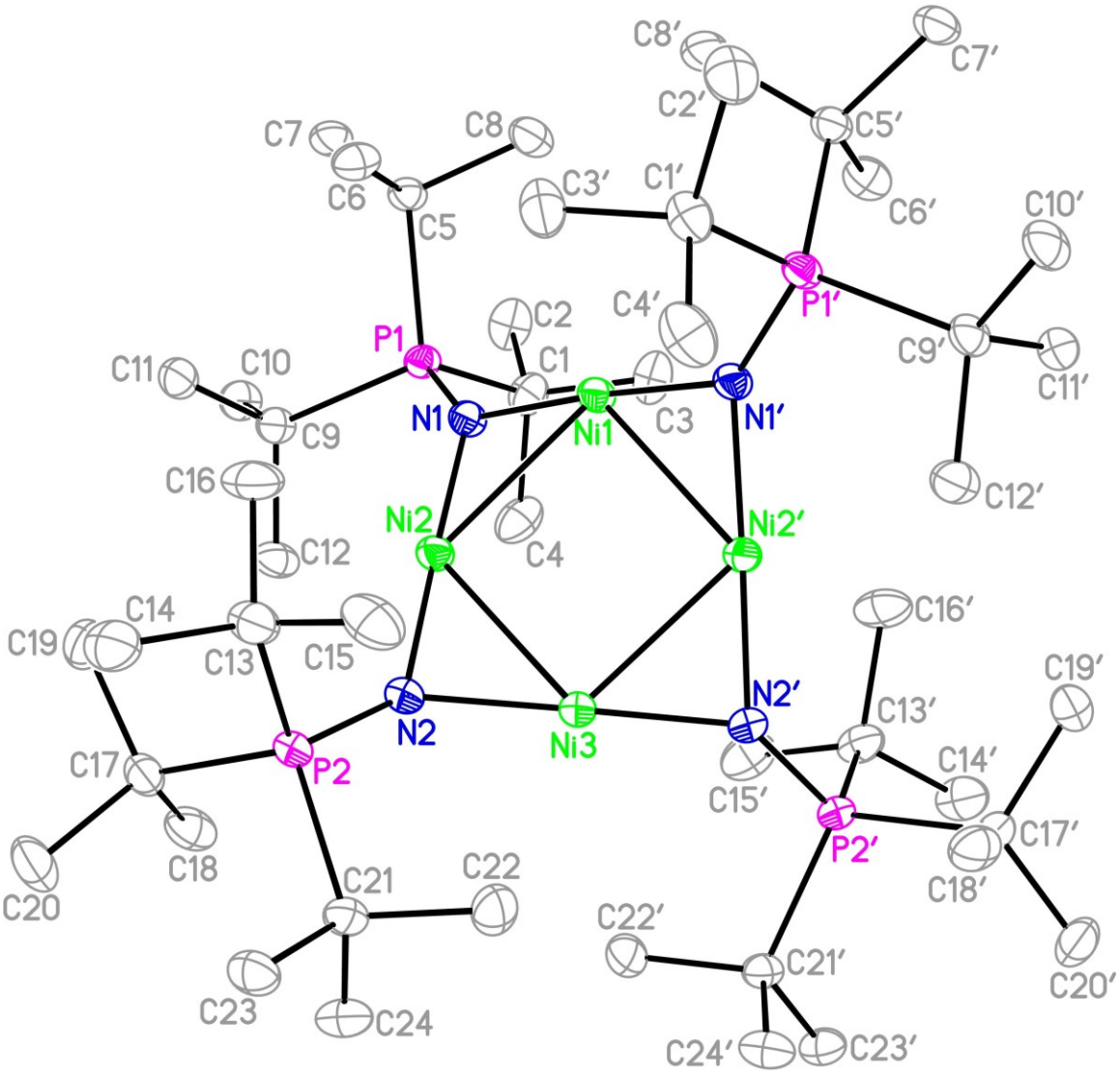

Table 1. Crystallographic Experimental Details

A. Crystal Data	
formula	$C_{72}H_{128}BN_4Ni_4P_4$
formula weight	1419.31
crystal dimensions (mm)	$0.12 \times 0.11 \times 0.11$
crystal system	monoclinic
space group	*I*2/*a* (an alternate setting of *C*2/*c* [No. 15])
unit cell parameters[a]	
a (Å)	17.5253 (9)
b (Å)	23.5825 (11)
c (Å)	18.2279 (9)
β (deg)	93.124 (3)
V (Å^3)	7522.2 (6)
Z	4
ρ_{calcd} (g cm^{-3})	1.253
μ (mm^{-1})	2.225
B. Data Collection and Refinement Conditions	
diffractometer	Bruker D8/APEX II CCD[b]
radiation (λ [Å])	Cu Kα (1.54178) (microfocus source)
temperature (°C)	–100
scan type	ω and ϕ scans (1°) (5 s exposures)
data collection 2θ limit (deg)	141.59
total data collected	24167 ($-21 \le h \le 21$, $-28 \le k \le 28$, $-21 \le l \le 22$)
independent reflections	7193 (R_{int} = 0.0450)
number of observed reflections (*NO*)	5478 [$F_o^2 \ge 2\sigma(F_o^2)$]
structure solution method	intrinsic phasing (*SHELXT*[c])
refinement method	full-matrix least-squares on F^2 (*SHELXL–97*[c])
absorption correction method	Gaussian integration (face-indexed)
range of transmission factors	0.8709–0.7359
data/restraints/parameters	7193 / 0 / 404
extinction coefficient (*x*)[d]	0.00018(3)
goodness-of-fit (*S*)[e] [all data]	1.102
final *R* indices[f]	
R_1 [$F_o^2 \ge 2\sigma(F_o^2)$]	0.0507
wR_2 [all data]	0.1538
largest difference peak and hole	0.493 and –0.866 e Å^{-3}

[a]Obtained from least-squares refinement of 9930 reflections with 6.14° < 2θ < 139.78°.

[b]Programs for diffractometer operation, data collection, data reduction and absorption

correction were those supplied by Bruker.

[c]Sheldrick, G. M. *Acta Crystallogr.* **2008**, *A64*, 112–122.

[d]$F_c^* = kF_c[1 + x\{0.001F_c^2\lambda^3/\sin(2\theta)\}]^{-1/4}$ where k is the overall scale factor.

[e]$S = [\Sigma w(F_o^2 - F_c^2)^2/(n - p)]^{1/2}$ (n = number of data; p = number of parameters varied; $w = [\sigma^2(F_o^2) + (0.0939P)^2]^{-1}$ where $P = [\text{Max}(F_o^2, 0) + 2F_c^2]/3$).

[f]$R_1 = \Sigma||F_o| - |F_c||/\Sigma|F_o|$; $wR_2 = [\Sigma w(F_o^2 - F_c^2)^2/\Sigma w(F_o^4)]^{1/2}$.

A 1.3 $[Ni_4(\mu–NP^tBu_3)_4][PF_6]•C_4H_8O$

STRUCTURE REPORT

XCL Code: JMS1510 **Date:** 16 October 2015

Compound: $[Ni_4(\mu–NP^tBu_3)_4][PF_6]•C_4H_8O$

Formula: $C_{52}H_{116}F_6N_4Ni_4OP_5$ ($C_{48}H_{108}N_4Ni_4P_4•C_4H_8O$)

Supervisor: J. M. Stryker **Crystallographer:** R. McDonald

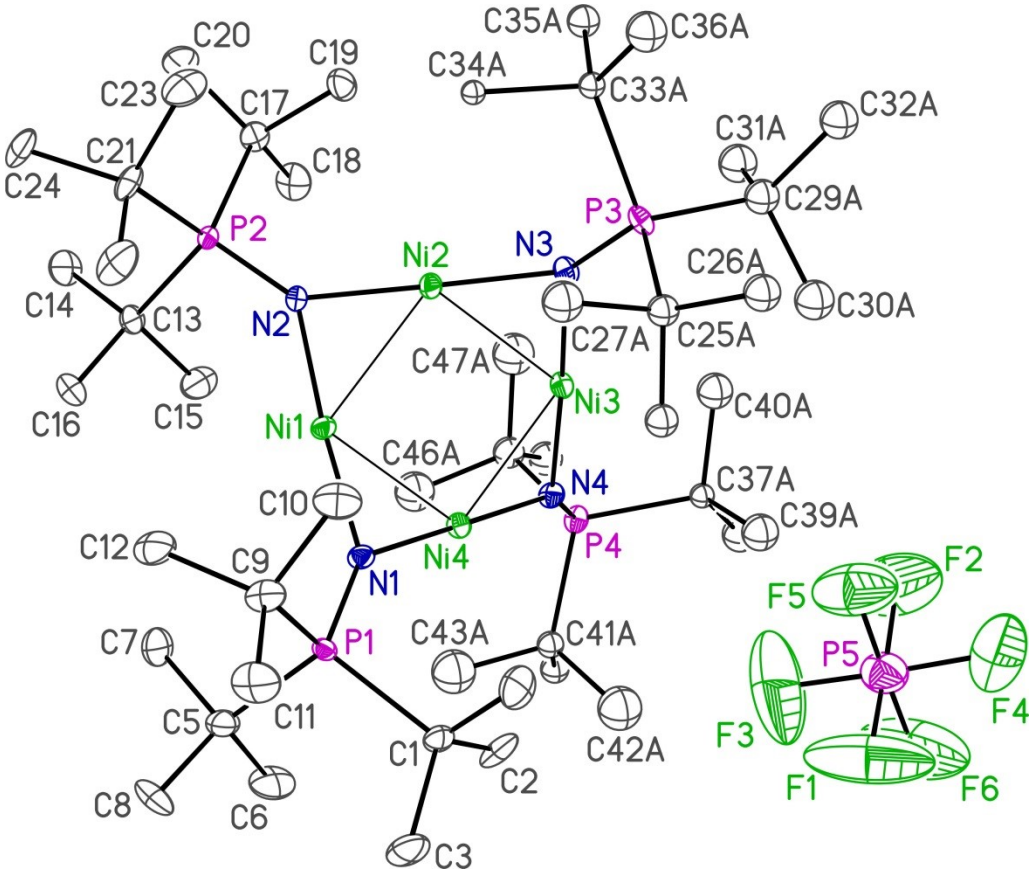

Figure Legends

Figure 1. Perspective view of the $[Ni_4(\mu\text{–}NP^tBu_3)_4]^+$ ion and the associated hexafluorophosphate ion showing the atom labelling scheme. Non-hydrogen atoms are represented by Gaussian ellipsoids at the 30% probability level. Hydrogen atoms are not shown.

Figure 2. Alternate view of the $[Ni_4(\mu\text{–}NP^tBu_3)_4]^+$ ion.

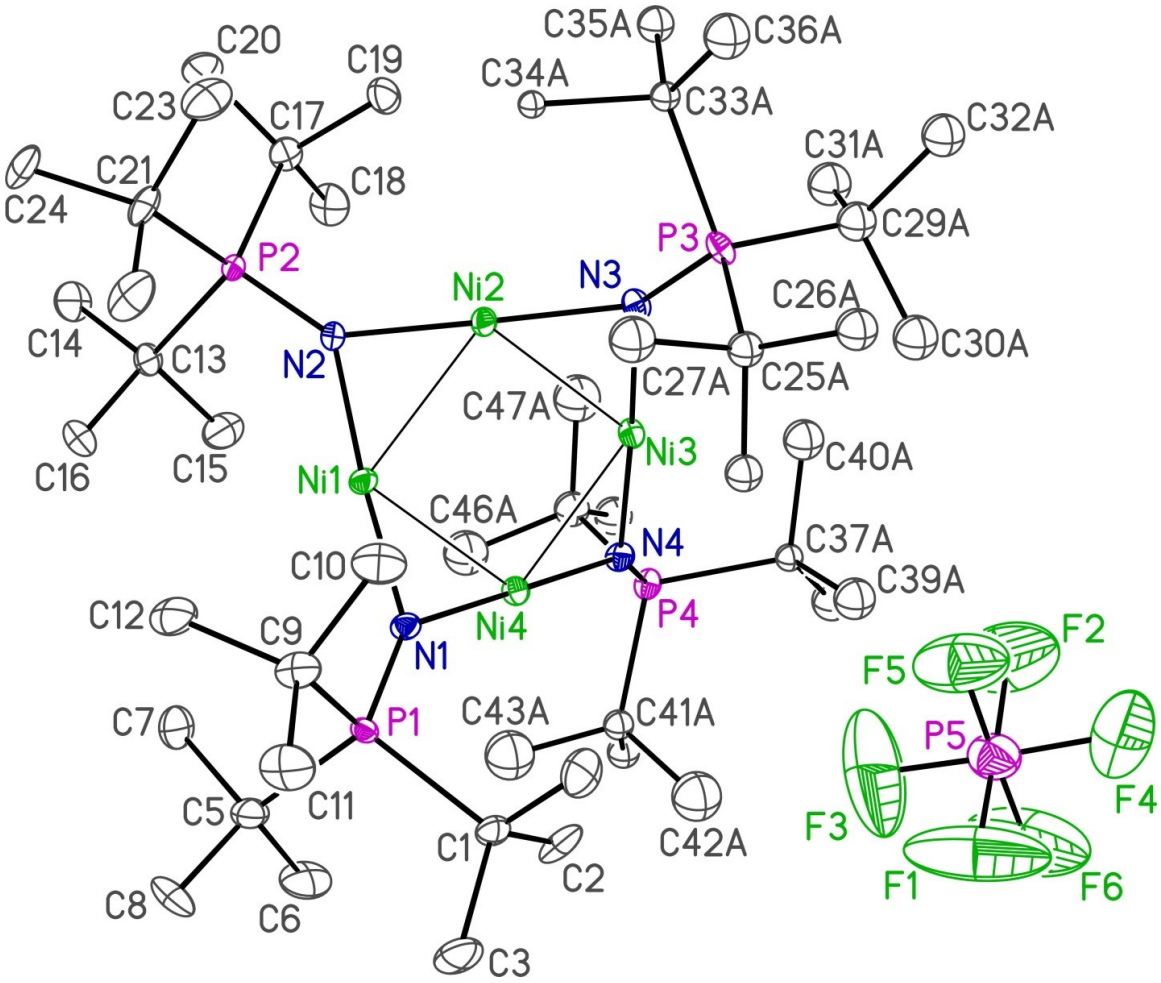

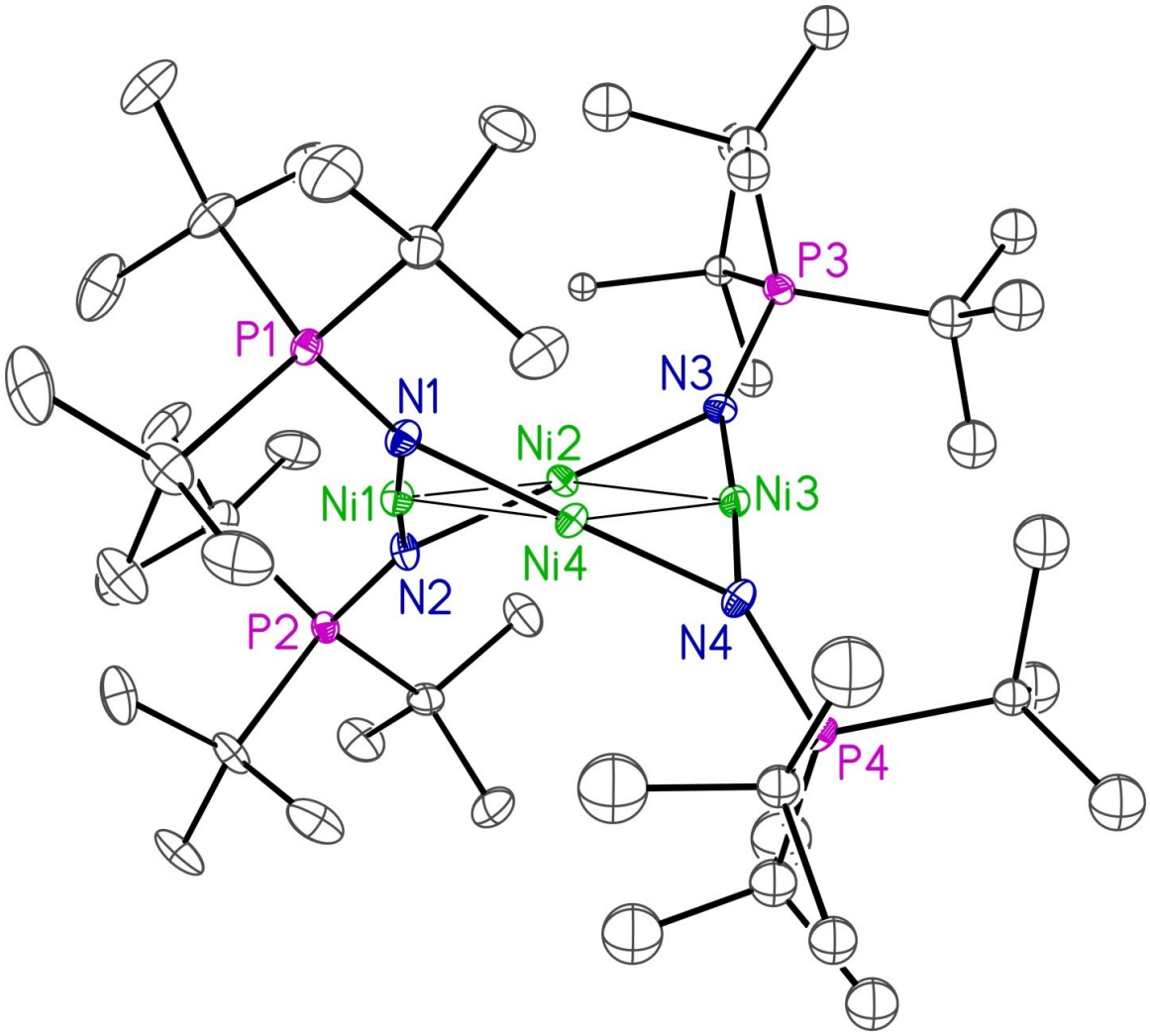
P1
N1
N3
P3
Ni2
Ni1
Ni3
Ni4
N2
P2
N4
P4

Table 1. Crystallographic Experimental Details

A. Crystal Data	
formula	$C_{52}H_{116}F_6N_4Ni_4OP_5$
formula weight	1317.17
crystal dimensions (mm)	$0.43 \times 0.28 \times 0.18$
crystal system	monoclinic
space group	*Cc* (No. 9)
unit cell parameters[a]	
a (Å)	23.1890 (9)
b (Å)	12.9545 (5)
c (Å)	23.7093 (9)
β (deg)	114.6748 (13)
V (Å^3)	6472.0 (4)
Z	4
ρ_{calcd} (g cm^{-3})	1.352
μ (mm^{-1})	2.916
B. Data Collection and Refinement Conditions	
diffractometer	Bruker D8/APEX II CCD[b]
radiation (λ [Å])	Cu Kα (1.54178) (microfocus source)
temperature (°C)	–100
scan type	ω and ϕ scans (1.0°) (5 s exposures)
data collection 2θ limit (deg)	148.16
total data collected	112770 ($-28 \le h \le 28$, $-15 \le k \le 15$, $-29 \le l \le 29$)
independent reflections	12792 (R_{int} = 0.0397)
number of observed reflections (*NO*)	12663 [$F_o^2 \ge 2\sigma(F_o^2)$]
structure solution method	Patterson/structure expansion (*DIRDIF–2008*[c])
refinement method	full-matrix least-squares on F^2 (*SHELXL–2014*[d])
absorption correction method	multi-scan (*TWINABS*)
range of transmission factors	0.6970–0.4742
data/restraints/parameters	12792 / 17[e] / 628
Flack absolute structure parameter[f]	0.008(12)
goodness-of-fit (*S*)[g] [all data]	1.033
final *R* indices[h]	
R_1 [$F_o^2 \ge 2\sigma(F_o^2)$]	0.0433
wR_2 [all data]	0.1147
largest difference peak and hole	0.473 and –0.409 e Å^{-3}

[a]Obtained from least-squares refinement of 9963 reflections with $7.64° < 2\theta < 147.74°$.

[b]Programs for diffractometer operation, data collection, data reduction and absorption correction were those supplied by Bruker. The crystal used for data collection was found to display non-merohedral twinning. Both components of the twin were indexed with the program *CELL_NOW* (Bruker AXS Inc., Madison, WI, 2004). The second twin component can be related to the first component by 180º rotation about the [0.4 0 1] axis in real space and about the [0 0 1] axis in reciprocal space. Integrated intensities for the reflections from the two components were written into a *SHELXL-2014* HKLF 5 reflection file with the data integration program *SAINT* (version 8.34A), using all reflection data (exactly overlapped, partially overlapped and non-overlapped).

[c]Beurskens, P. T.; Beurskens, G.; de Gelder, R.; Smits, J. M. M.; Garcia-Granda, S.; Gould, R. O. (2008). The *DIRDIF-2008* program system. Crystallography Laboratory, Radboud University Nijmegen, The Netherlands.

[d]Sheldrick, G. M. *Acta Crystallogr.* **2015**, *C71*, 3–8.

[e](a) The following P–C distances were constrained to be equal (within 0.03 Å) to a common refined value during refinement: d(P3–C33A), d(P3–C33B), d(P4–C41A), d(P4–C45A), d(P4–C41B), d(P4–C45B). (b) The following C–C distances were constrained to be equal (within 0.03 Å) to a common refined value during refinement: d(C41A–C42A), d(C41A–C43A), d(C41A–C44A), d(C45A–C46A), d(C45A–C47A), d(C45A–C48A), d(C45B–C46B), d(C45B–C47B), d(C45B–C48B).

[f]Flack, H. D. *Acta Crystallogr.* **1983**, *A39*, 876–881; Flack, H. D.; Bernardinelli, G. *Acta Crystallogr.* **1999**, *A55*, 908–915; Flack, H. D.; Bernardinelli, G. *J. Appl. Cryst.* **2000**, *33*, 1143–1148. The Flack parameter will refine to a value near zero if the structure is in the correct configuration and will refine to a value near one for the inverted configuration.

[g]$S = [\Sigma w(F_o^2 - F_c^2)^2/(n-p)]^{1/2}$ (n = number of data; p = number of parameters varied; $w = [\sigma^2(F_o^2) + (0.0579P)^2 + 20.0995P]^{-1}$ where $P = [\mathrm{Max}(F_o^2, 0) + 2F_c^2]/3$).

[h]$R_1 = \Sigma||F_o| - |F_c||/\Sigma|F_o|$; $wR_2 = [\Sigma w(F_o^2 - F_c^2)^2/\Sigma w(F_o^4)]^{1/2}$.

A 1.4 $[Co_2(NP^tBu_3)_4][PF_6]$

STRUCTURE REPORT

XCL Code: JMS1343 **Date:** 29 November 2013

Compound: $[Co_2(NP^tBu_3)_4][PF_6]$

Formula: $C_{48}H_{108}Co_2F_6N_4P_5$

Supervisor: J. M. Stryker **Crystallographer:** M. J. Ferguson

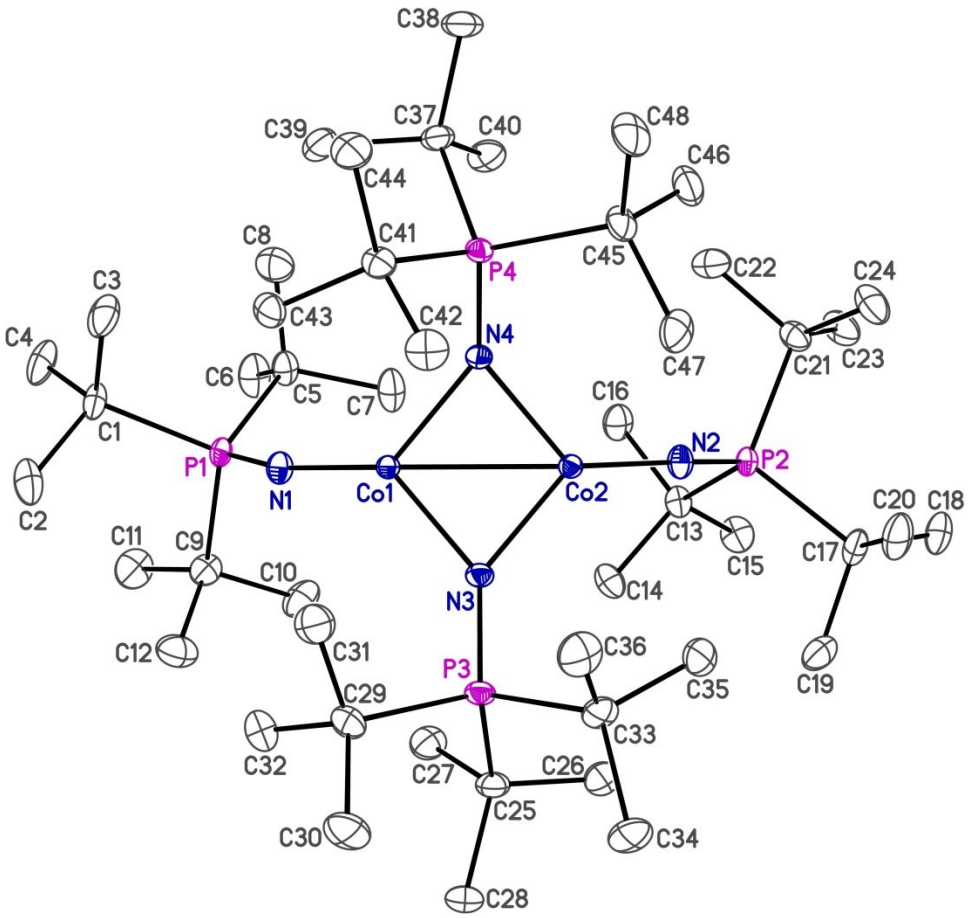

Figure Legends

Figure 1. Perspective view of the $[Co_2(NP^tBu_3)_4]^+$ ion showing the atom labelling scheme. Non-hydrogen atoms are represented by Gaussian ellipsoids at the 30% probability level. Hydrogen atoms are not shown.

Figure 2. Alternate view of the cation.

Figure 3. Same view of the cation, with the phosphorus hexafluoride anion included. *Note:* P10 is located on an inversion centre and P20 is disordered across a 2-fold rotation axis, resulting in the cation:anion ratio of 1:1.

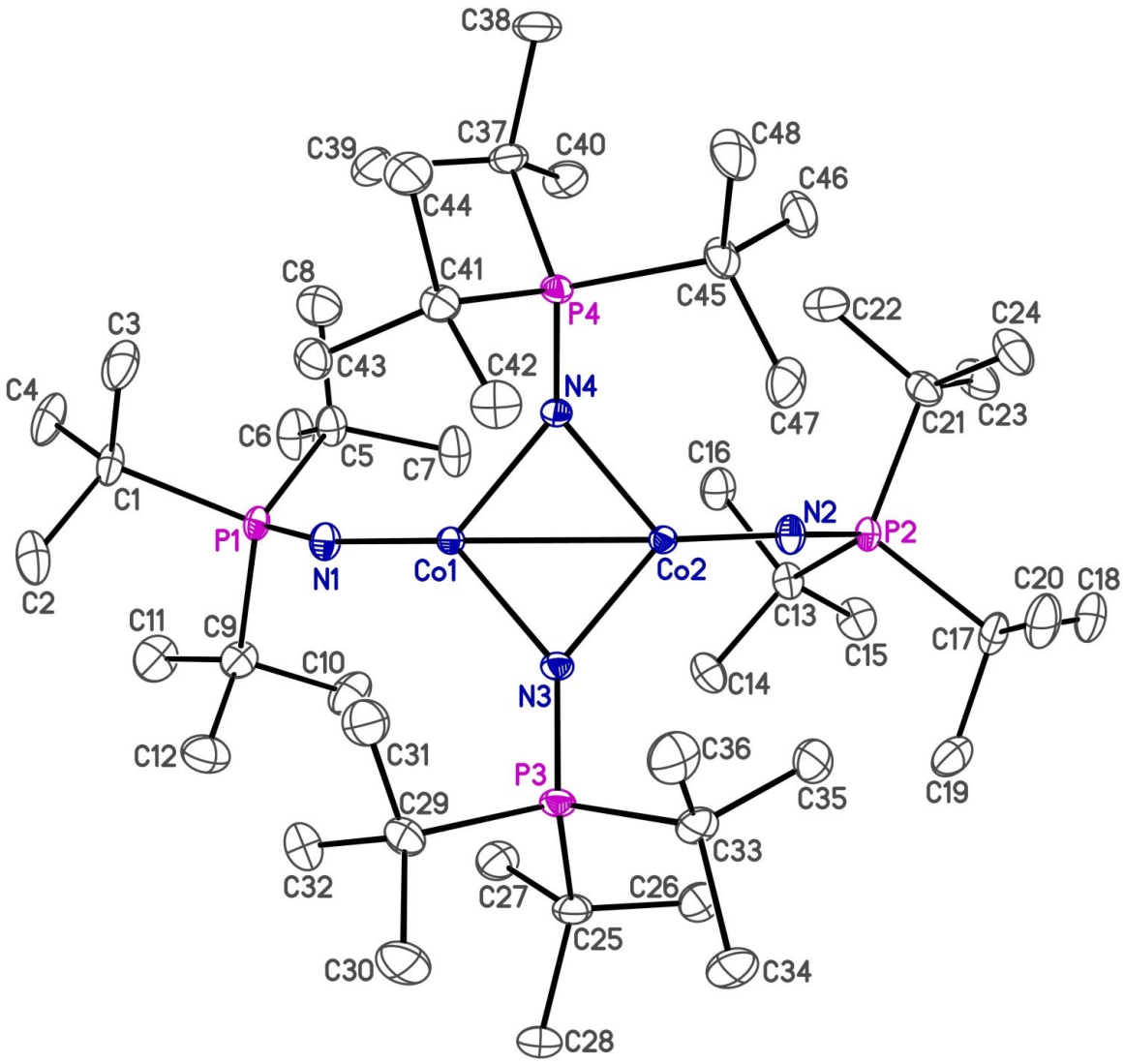

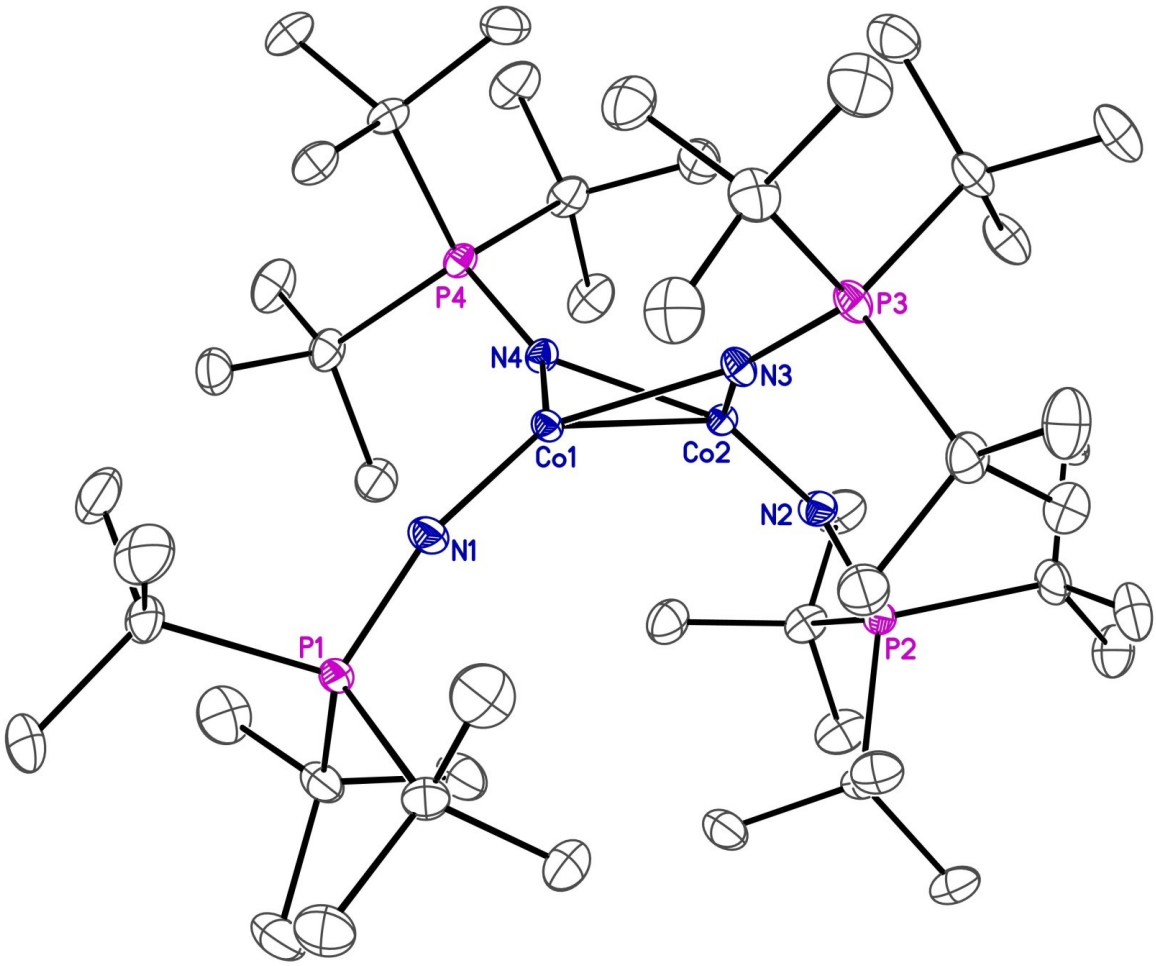
P4
P3
N4
N3
Co1
Co2
N2
N1
P1
P2

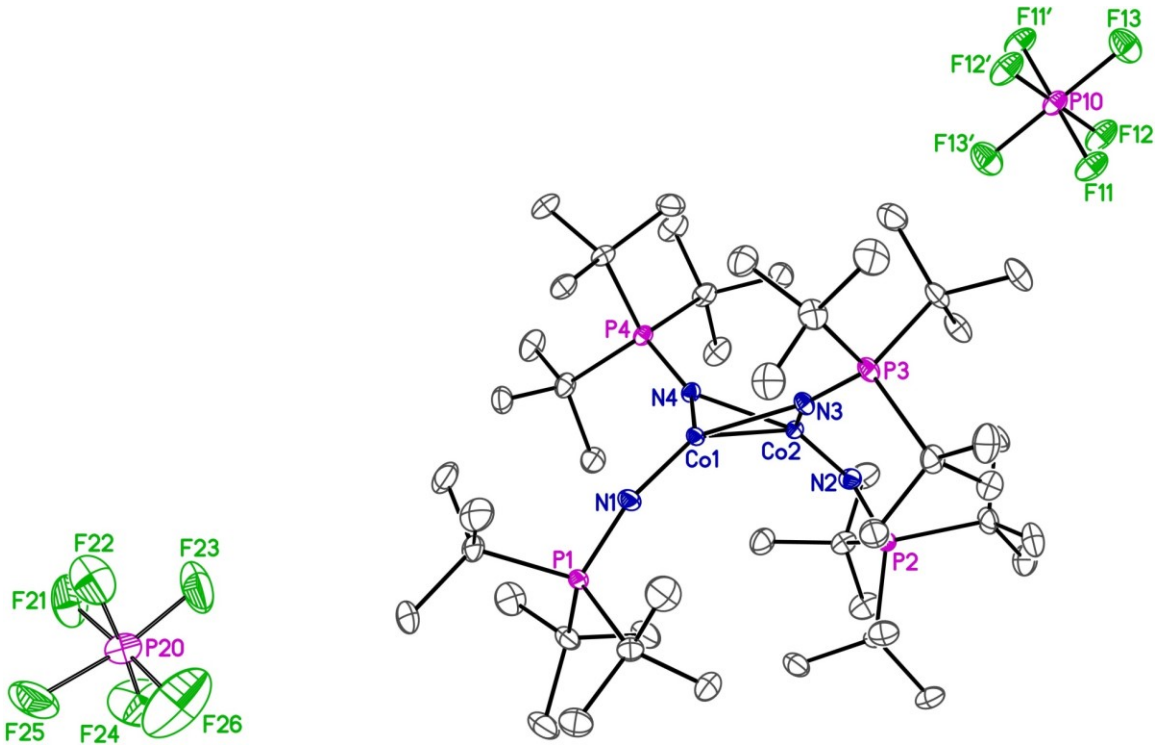
F11′
F13
F12′
P10
F12
F13′
F11
P4
P3
N4
N3
Co1
Co2
N2
N1
P1
P2
F22
F23
F21
P20
F25
F24
F26

Table 1. Crystallographic Experimental Details

A. Crystal Data	
formula	$C_{48}H_{108}Co_2F_6N_4P_5$
formula weight	1128.09
crystal dimensions (mm)	0.44 × 0.42 × 0.32
crystal system	monoclinic
space group	*C*2/*c* (No. 15)
unit cell parameters[a]	
a (Å)	43.6858 (19)
b (Å)	12.8855 (6)
c (Å)	22.7021 (10)
β (deg)	110.9702 (5)
V (Å^3)	11932.9 (9)
Z	8
ρ_{calcd} (g cm^{-3})	1.256
μ (mm^{-1})	0.743
B. Data Collection and Refinement Conditions	
diffractometer	Bruker D8/APEX II CCD[b]
radiation (λ [Å])	graphite-monochromated Mo Kα (0.71073)
temperature (°C)	–100
scan type	ω scans (0.3°) (20 s exposures)
data collection 2θ limit (deg)	54.99
total data collected	52271 (-56 ≤ *h* ≤ 56, -16 ≤ *k* ≤ 16, -29 ≤ *l* ≤ 29)
independent reflections	13704 (R_{int} = 0.0147)
number of observed reflections (*NO*)	12477 [$F_o^2 \geq 2\sigma(F_o^2)$]
structure solution method	intrinsic phasing (*SHELXT*[c])
refinement method	full-matrix least-squares on F^2 (*SHELXL–2013*[c])
absorption correction method	Gaussian integration (face-indexed)
range of transmission factors	0.8711–0.7837
data/restraints/parameters	13704 / 6[d] / 656
goodness-of-fit (*S*)[e] [all data]	1.040
final *R* indices[f]	
R_1 [$F_o^2 \geq 2\sigma(F_o^2)$]	0.0287
wR_2 [all data]	0.0801
largest difference peak and hole	0.989 and –0.309 e Å^{-3}

[a]Obtained from least-squares refinement of 9603 reflections with 4.36° < 2θ < 54.98°.

[b]Programs for diffractometer operation, data collection, data reduction and absorption

correction were those supplied by Bruker.

[c]Sheldrick, G. M. *Acta Crystallogr.* **2008**, *A64*, 112–122.

[d]The P–F distances within the disordered PF_6 anion were restrained to be approximately the same.

[e]$S = [\Sigma w(F_o^2 - F_c^2)^2/(n - p)]^{1/2}$ (n = number of data; p = number of parameters varied; $w = [\sigma^2(F_o^2) + (0.0420P)^2 + 13.5584P]^{-1}$ where $P = [\text{Max}(F_o^2, 0) + 2F_c^2]/3$).

[f]$R_1 = \Sigma||F_o| - |F_c||/\Sigma|F_o|$; $wR_2 = [\Sigma w(F_o^2 - F_c^2)^2/\Sigma w(F_o^4)]^{1/2}$.

A 1.5 [$Na_4(NP^tBu_3)_4$]•*n*-pentane

STRUCTURE REPORT

XCL Code: JMS1475 **Date:** 4 December 2015

Compound: [$Na_4(NP^tBu_3)_4$]•*n*-pentane

Formula: $C_{53}H_{120}N_4Na_4P_4$ ($C_{48}H_{108}N_4Na_4P_4$•C_5H_{12})

Supervisor: J. M. Stryker **Crystallographer:** R. McDonald

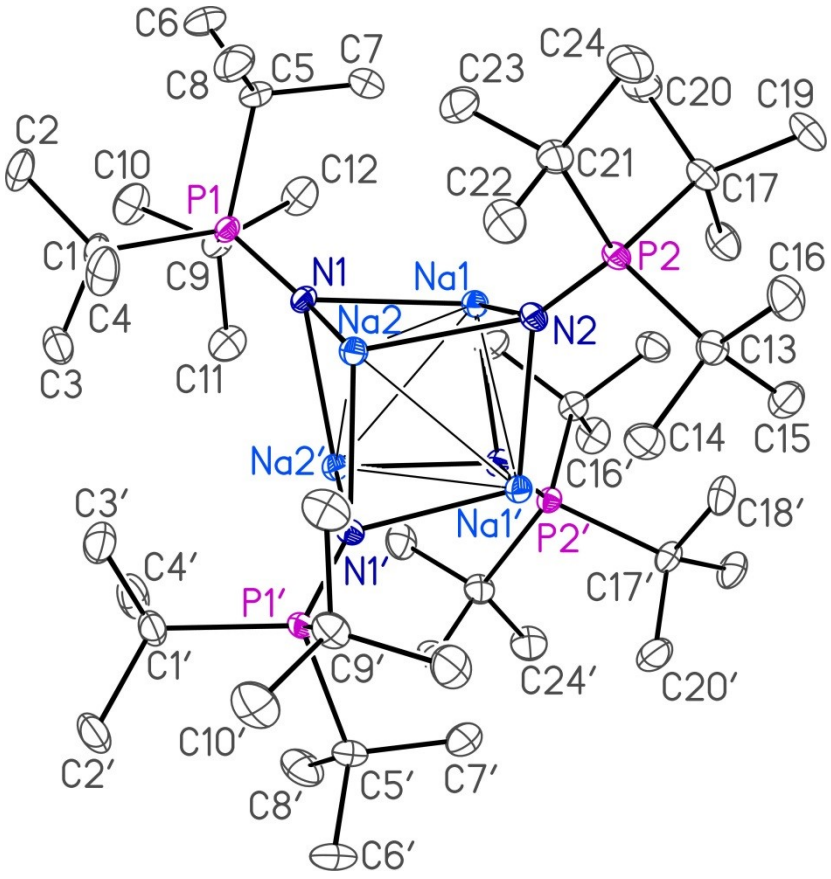

Figure Legends

Figure 1. Perspective view of the $[Na_4(NP^tBu_3)_4]$ molecule showing the atom labelling scheme. Non-hydrogen atoms are represented by Gaussian ellipsoids at the 30% probability level. Hydrogen atoms are not shown. Primed atoms are related to unprimed ones via the crystallographic twofold rotational axis (0, *y*, $^1/_4$).

Figure 2. Illustration of the $Na_4(NP)_4$ core of the molecule.

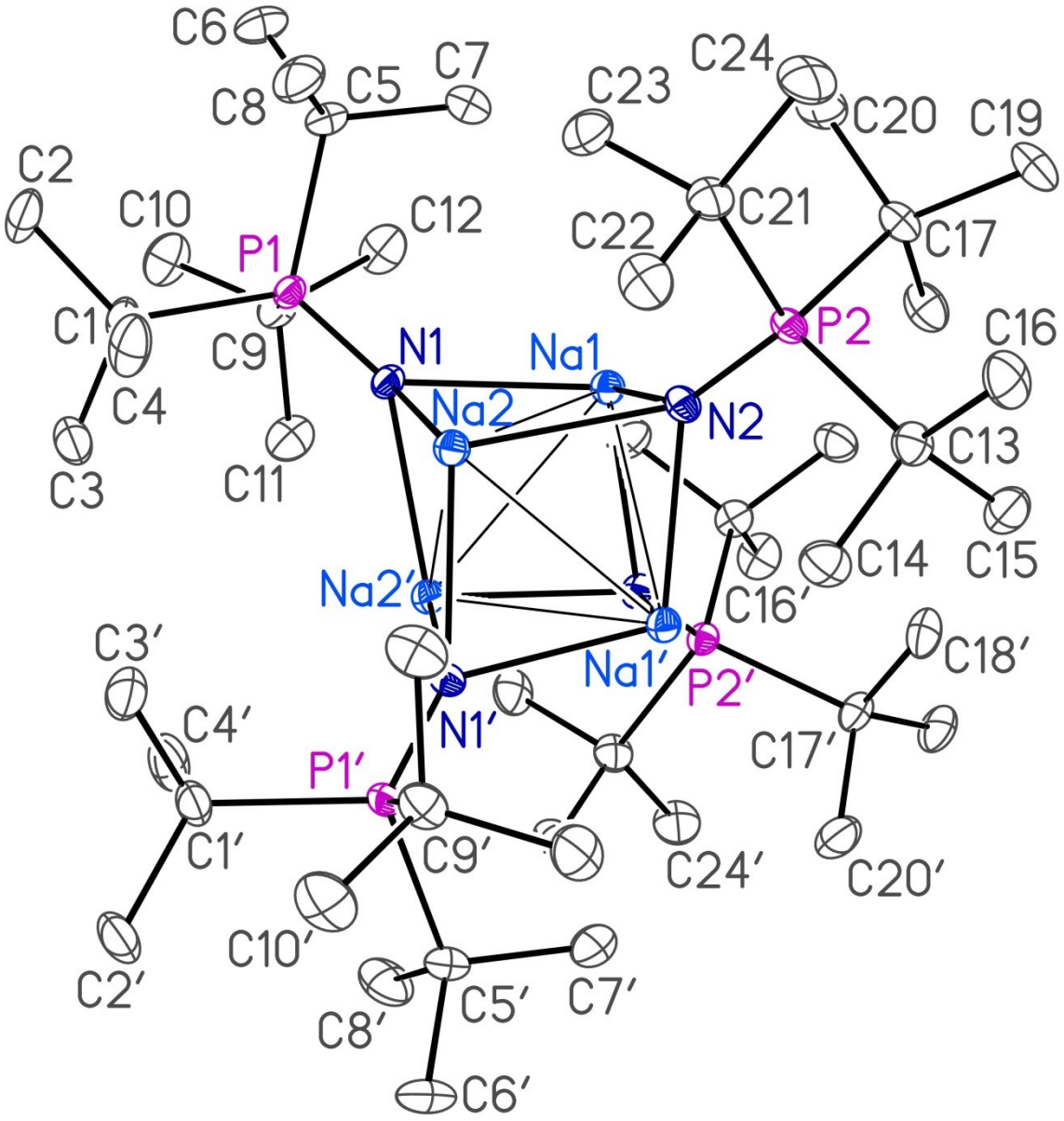

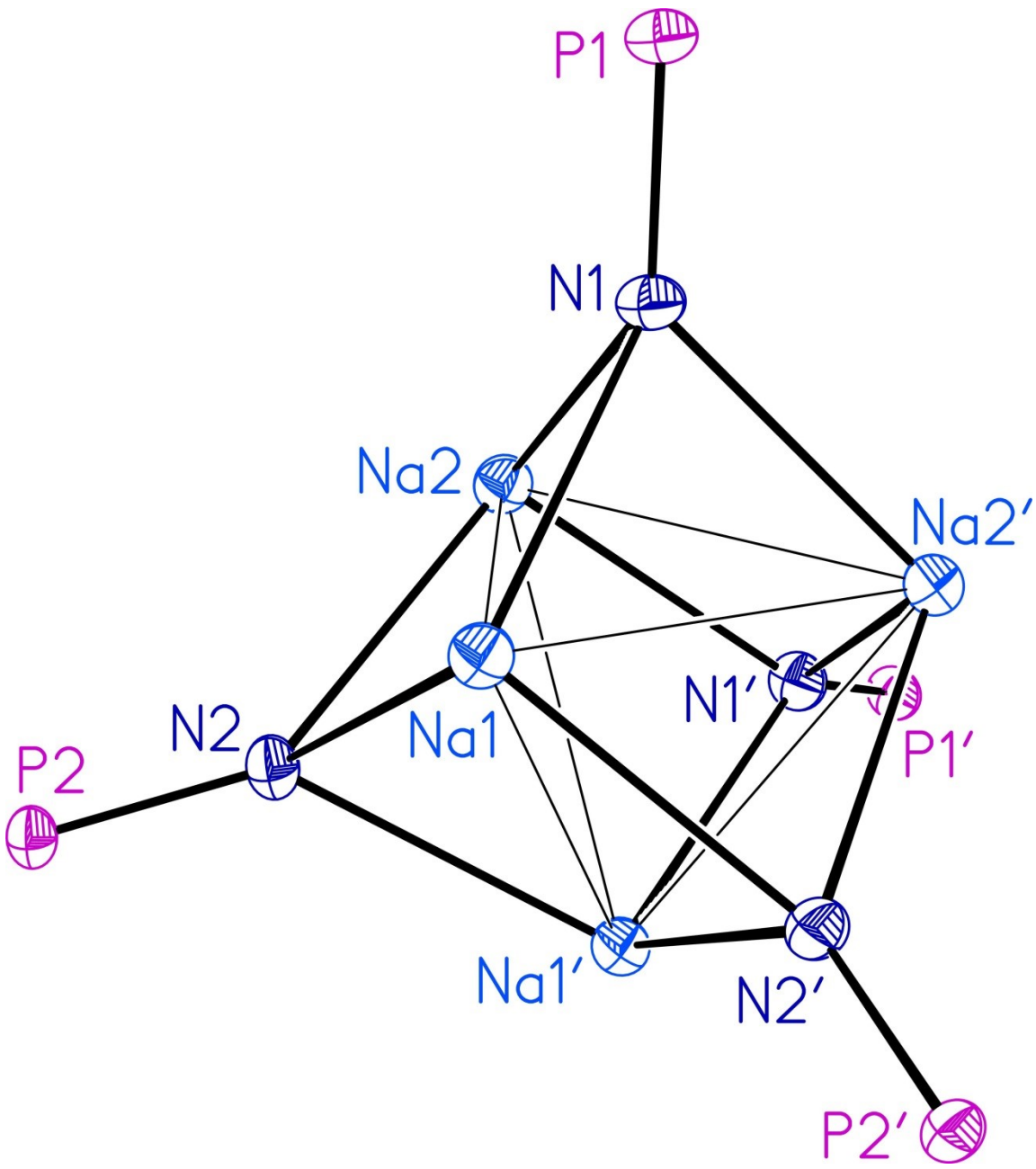
P1
N1
Na2
Na2′
N1′
P1′
N2
Na1
P2
Na1′
N2′
P2′

Table 1. Crystallographic Experimental Details

A. Crystal Data	
formula	$C_{53}H_{120}N_4Na_4P_4$
formula weight	1029.36
crystal dimensions (mm)	0.62 × 0.60 × 0.47
crystal system	monoclinic
space group	*C*2/*c* (No. 15)
unit cell parameters[a]	
a (Å)	23.2447 (5)
b (Å)	12.4816 (3)
c (Å)	24.4865 (6)
β (deg)	115.6395 (6)
V (Å^3)	6404.8 (3)
Z	4
ρ_{calcd} (g cm^{-3})	1.068
μ (mm^{-1})	1.600
B. Data Collection and Refinement Conditions	
diffractometer	Bruker D8/APEX II CCD[b]
radiation (λ [Å])	Cu Kα (1.54178) (microfocus source)
temperature (°C)	–100
scan type	ω and ϕ scans (1.0°) (5 s exposures)
data collection 2θ limit (deg)	145.45
total data collected	21765 (-28 ≤ *h* ≤ 28, -15 ≤ *k* ≤ 15, -29 ≤ *l* ≤ 30)
independent reflections	6373 (R_{int} = 0.0220)
number of observed reflections (*NO*)	6262 [$F_o^2 \geq 2\sigma(F_o^2)$]
structure solution method	intrinsic phasing (*SHELXT-2014*[c])
refinement method	full-matrix least-squares on F^2 (*SHELXL–2014*[d])
absorption correction method	Gaussian integration (face-indexed)
range of transmission factors	0.6301–0.4973
data/restraints/parameters	6373 / 0 / 316
goodness-of-fit (*S*)[e] [all data]	1.058
final *R* indices[f]	
R_1 [$F_o^2 \geq 2\sigma(F_o^2)$]	0.0318
wR_2 [all data]	0.0883
largest difference peak and hole	0.307 and –0.300 e Å^{-3}

[a]Obtained from least-squares refinement of 9728 reflections with 8.24° < 2θ < 144.64°.

[b]Programs for diffractometer operation, data collection, data reduction and absorption correction were those supplied by Bruker.

[c]Sheldrick, G. M. *Acta Crystallogr.* **2015**, *A71*, 3–8.

[d]Sheldrick, G. M. *Acta Crystallogr.* **2015**, *C71*, 3–8.

[e]$S = [\Sigma w(F_o^2 - F_c^2)^2/(n - p)]^{1/2}$ (n = number of data; p = number of parameters varied; $w = [\sigma^2(F_o^2) + (0.0476P)^2 + 4.4198P]^{-1}$ where $P = [\text{Max}(F_o^2, 0) + 2F_c^2]/3$).

[f]$R_1 = \Sigma||F_o| - |F_c||/\Sigma|F_o|$; $wR_2 = [\Sigma w(F_o^2 - F_c^2)^2/\Sigma w(F_o^4)]^{1/2}$.

A 1.6 $[Ni_2(allyl)_2(NPEt_3)_2]$

STRUCTURE REPORT

XCL Code: JMS1332 **Date:** 11 October 2013

Compound: $[Ni_2(allyl)_2(NPEt_3)_2]$

Formula: $C_{18}H_{40}N_2Ni_2P_2$

Supervisor: J. M. Stryker **Crystallographer:** M. J. Ferguson

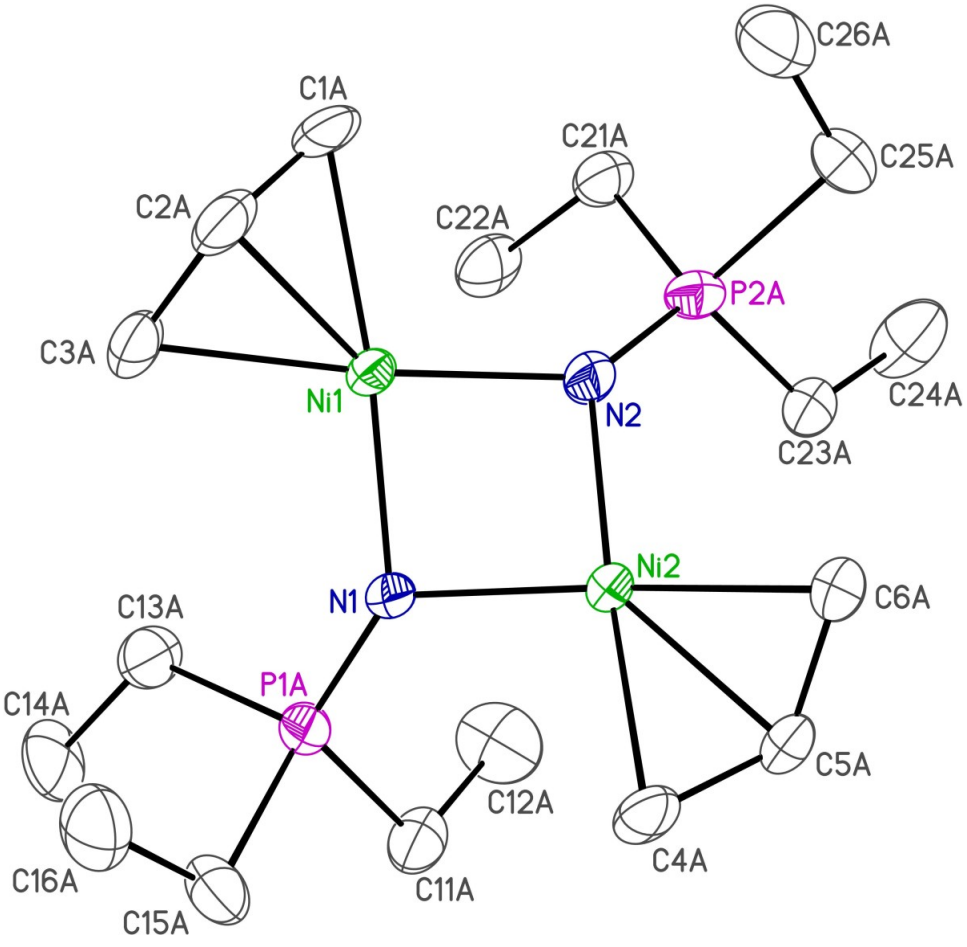

Figure Legends

Figure 1. Perspective view of the $[Ni_2(allyl)_2(NPEt_3)_2]$ molecule showing the atom labelling scheme. Only one orientation of the disordered groups is shown. Non-hydrogen atoms are represented by Gaussian ellipsoids at the 30% probability level. Hydrogen atoms are not shown.

Figure 2. Same view of the molecule showing the relative orientation of the disordered allyl and phosphoranamido groups.

Figure 3. Alternate view of the molecule.

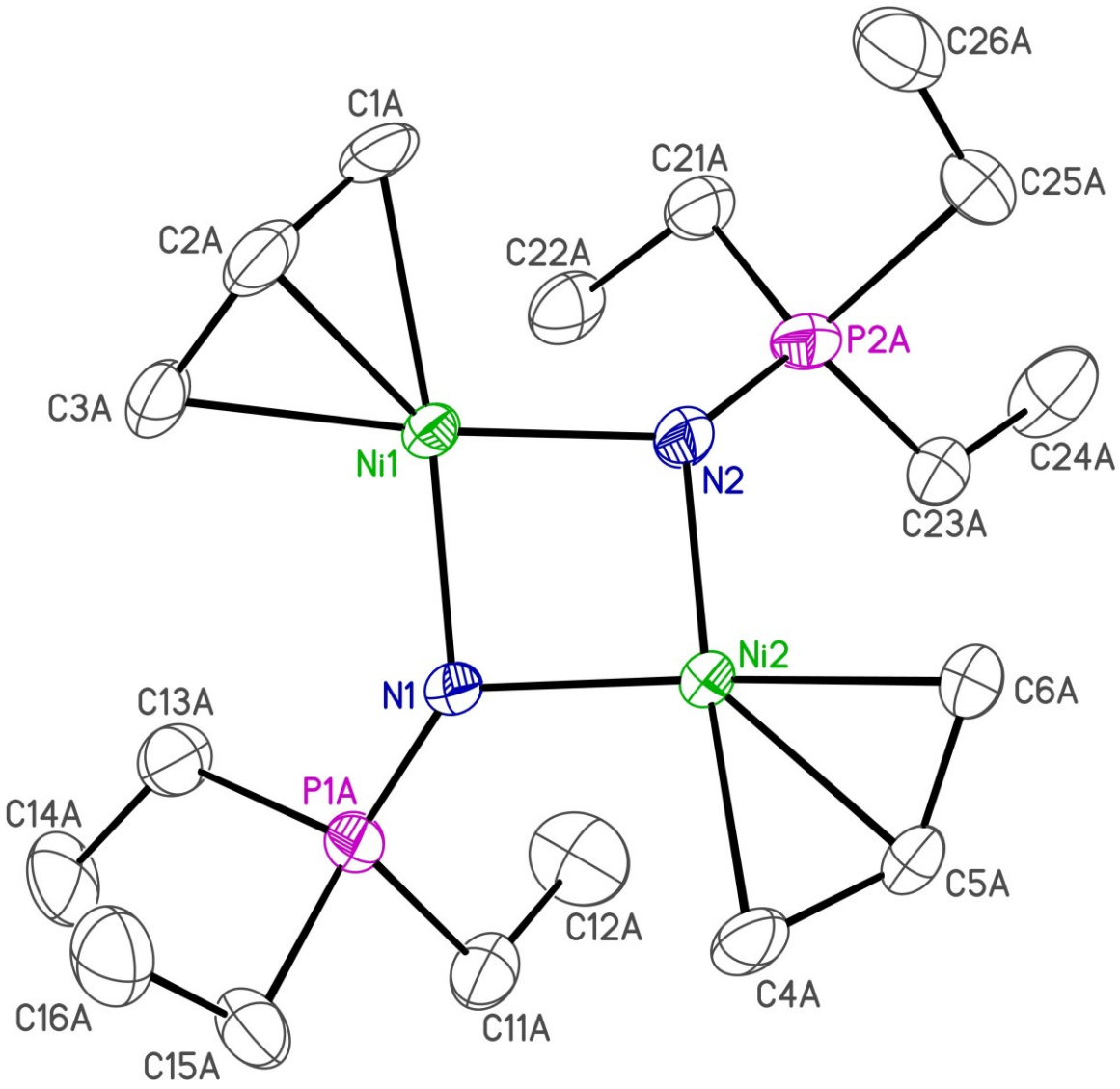
C26A
C1A
C21A
C25A
C2A
C22A
P2A
C3A
Ni1
N2
C24A
C23A
Ni2
N1
C6A
C13A
P1A
C14A
C5A
C12A
C4A
C16A
C11A
C15A

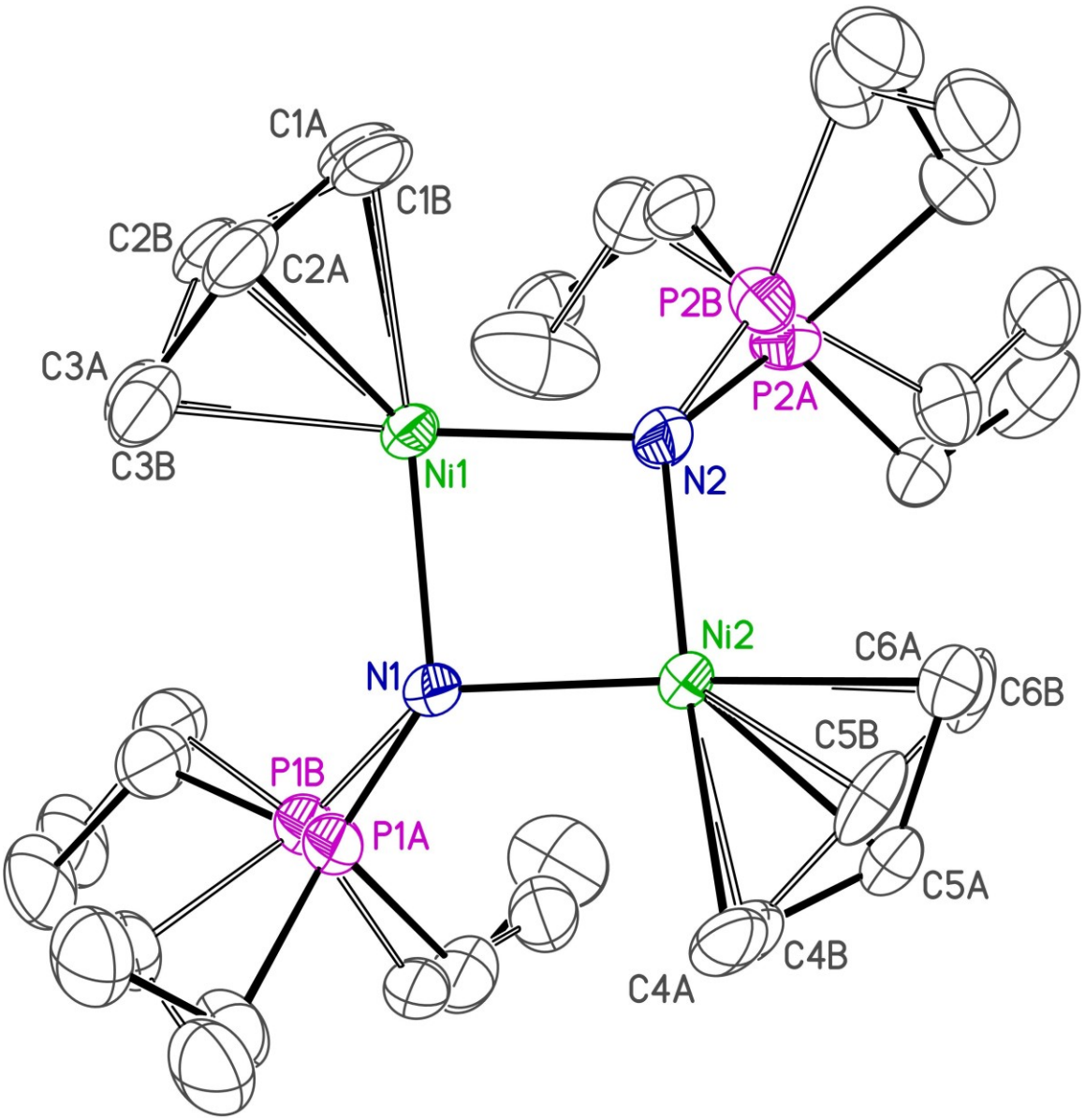
C1A
C1B
C2B
C2A
C3A
C3B
Ni1
N2
P2B
P2A
N1
Ni2
C6A
C6B
C5B
P1B
P1A
C5A
C4B
C4A

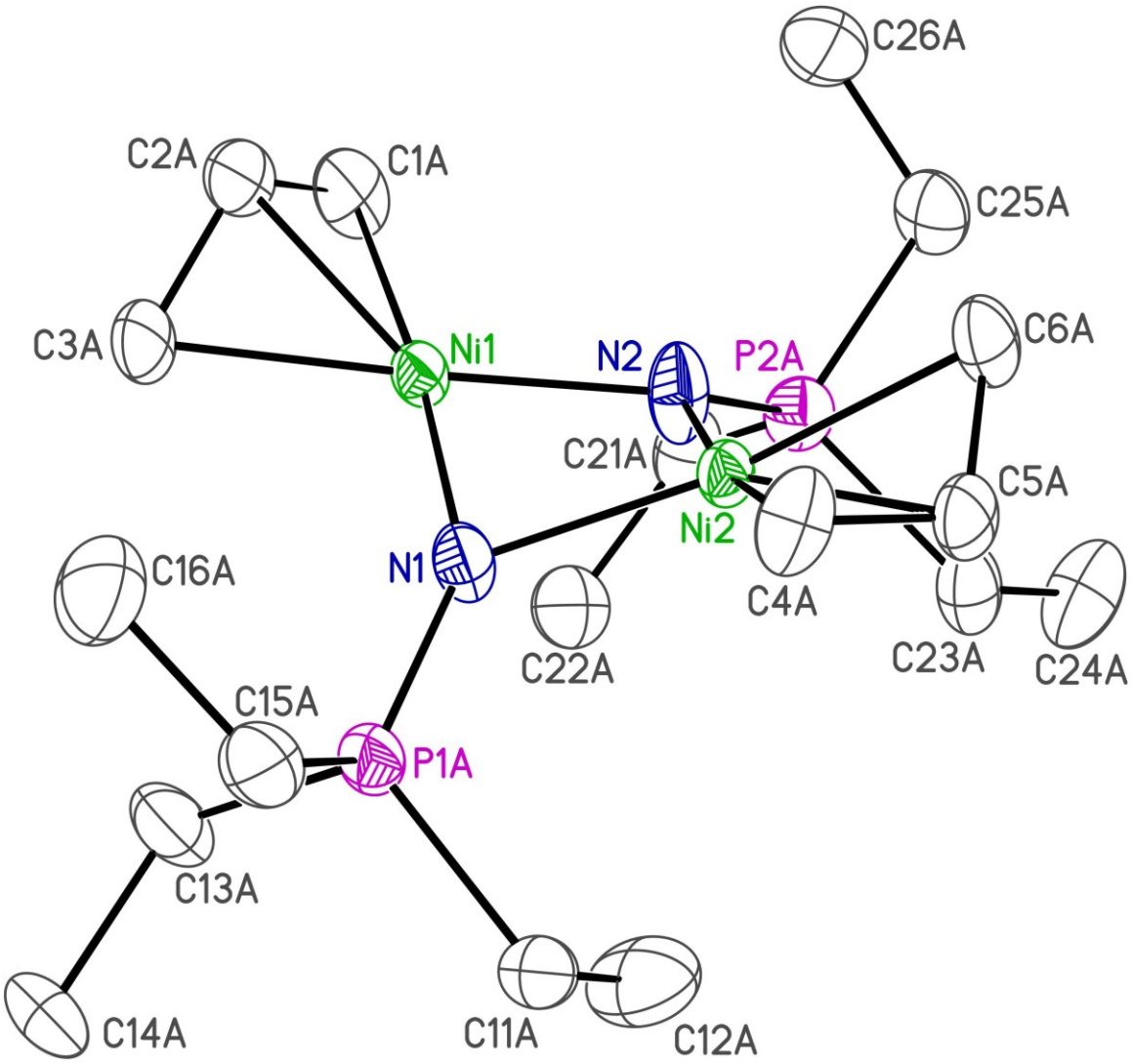
C26A
C2A
C1A
C25A
C3A
Ni1
N2
P2A
C6A
C21A
C5A
Ni2
N1
C16A
C4A
C22A
C23A
C24A
C15A
P1A
C13A
C14A
C11A
C12A

Table 1. Crystallographic Experimental Details

A. Crystal Data	
formula	$C_{18}H_{40}N_2Ni_2P_2$
formula weight	463.88
crystal dimensions (mm)	0.44 × 0.33 × 0.30
crystal system	monoclinic
space group	$P2_1/n$ (an alternate setting of $P2_1/c$ [No. 14])
unit cell parameters[a]	
a (Å)	14.4679 (16)
b (Å)	9.4003 (10)
c (Å)	18.067 (2)
β (deg)	106.5993 (14)
V (Å^3)	2354.7 (4)
Z	4
ρ_{calcd} (g cm^{-3})	1.309
μ (mm^{-1})	1.738
B. Data Collection and Refinement Conditions	
diffractometer	Bruker D8/APEX II CCD[b]
radiation (λ [Å])	graphite-monochromated Mo Kα (0.71073)
temperature (°C)	–100
scan type	ω scans (0.3°) (20 s exposures)
data collection 2θ limit (deg)	56.76
total data collected	5850 (-19 ≤ *h* ≤ 18, 0 ≤ *k* ≤ 12, 0 ≤ *l* ≤ 24)
independent reflections	5850 (R_{int} = 0.0213)
number of observed reflections (*NO*)	4837 [$F_o^2 \geq 2\sigma(F_o^2)$]
structure solution method	intrinsic phasing (*SHELXT*[c])
refinement method	full-matrix least-squares on F^2 (*SHELXL–97*[c])
absorption correction method	multi-scan (*TWINABS*)
range of transmission factors	0.7456–0.5748
data/restraints/parameters	5850 / 43[d] / 370
goodness-of-fit (*S*)[e] [all data]	1.057
final *R* indices[f]	
R_1 [$F_o^2 \geq 2\sigma(F_o^2)$]	0.0367
wR_2 [all data]	0.1093
largest difference peak and hole	0.760 and –0.451 e Å^{-3}

[a]Obtained from least-squares refinement of 9933 reflections with 4.70° < 2θ < 56.70°.

[b]Programs for diffractometer operation, data collection, data reduction and absorption correction were those supplied by Bruker. The crystal used for data collection was

found to display non-merohedral twinning. Both components of the twin were indexed with the program *CELL_NOW* (Bruker AXS Inc., Madison, WI, 2004). The second twin component can be related to the first component by 180º rotation about the [0 0 1] axis in real space and about the [–0.23 0 1] axis in reciprocal space. Integrated intensities for the reflections from the two components were written into a *SHELXL* HKLF 5 reflection file with the data integration program *SAINT* (version 8.32B) and the scaling program *TWINABS* (version 2012/1), using all reflection data involving domain 1. The refined value of the twin fraction (*SHELXL* BASF parameter) was 0.0530(5).

[c]Sheldrick, G. M. *Acta Crystallogr.* **2008**, *A64*, 112–122.

[d]The C–C distances within the disordered allyl groups were restrained to be the same by use the *SHELXL* **SADI** instruction. Likewise, a **SADI** restraint was used on the C11A–C12A/C11B–C12B distances. The P–N and the P–C distances within the disordered phosphoranamido ligand were restrained by use of a **DFIX** instruction; the target value for the P–N bond distance refined to 1.550(11) while that for the P–C bond distance refined to 1.832(6) Å. Finally, a rigid-bond restraint was applied to the anisotropic displacement parameters for P2A, C23A, C11A, C12A, and all atoms of the disordered allyl groups, by use of the **DELU** instruction.

[e]$S = [\Sigma w(F_o^2 - F_c^2)^2/(n - p)]^{1/2}$ (n = number of data; p = number of parameters varied; $w = [\sigma^2(F_o^2) + (0.0724P)^2 + 0.3778P]^{-1}$ where $P = [\mathrm{Max}(F_o^2, 0) + 2F_c^2]/3$).

[f]$R_1 = \Sigma||F_o| - |F_c||/\Sigma|F_o|$; $wR_2 = [\Sigma w(F_o^2 - F_c^2)^2/\Sigma w(F_o^4)]^{1/2}$.

A 1.7 $[Ni_3(\eta^3\text{–allyl})_3(\mu^3\text{–NPEt}_3)_2][PF_6]$

STRUCTURE REPORT

XCL Code: JMS1331 **Date:** 8 October 2013

Compound: $[Ni_3(\eta^3\text{–allyl})_3(\mu^3\text{–NPEt}_3)_2][PF_6]$

Formula: $C_{21}H_{45}F_6N_2Ni_3P_3$

Supervisor: J. M. Stryker **Crystallographer:** R. McDonald

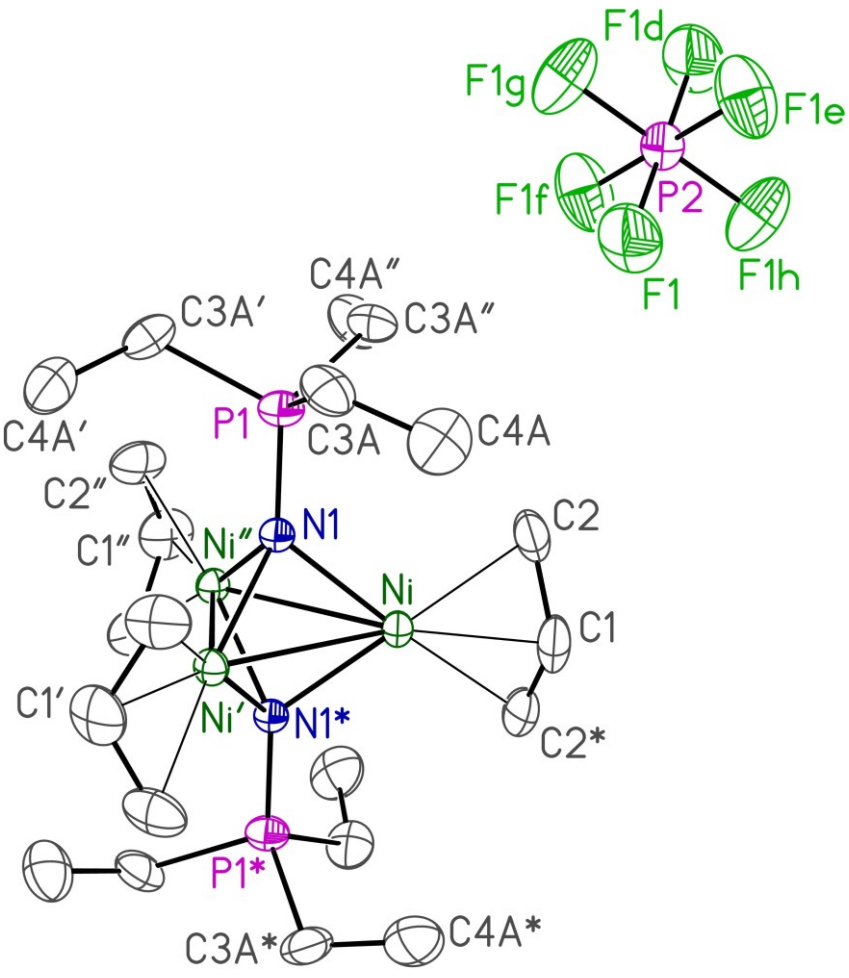

Figure Legends

Figure 1. Perspective view of the $[Ni_3(\eta^3\text{–allyl})_3(\mu^3\text{–NPEt}_3)_2]^+$ ion and the associated hexafluorophosphate ion showing the atom labelling scheme. Non-hydrogen atoms are represented by Gaussian ellipsoids at the 30% probability level. Hydrogen atoms are not shown. Primed atoms are related to unprimed ones via the crystallographic symmetry operation (1–*y*, 1+*x*–*y*, *z*) (120º rotation about the threefold axis ($^1/_3$, $^2/_3$, *z*)). Double-primed atoms are related to unprimed ones via the crystallographic symmetry operation (*y*–*x*, 1–*x*, *z*) (the opposite-handed 120º rotation about the threefold axis ($^1/_3$, $^2/_3$, *z*)). Starred atoms are related to unprimed ones via the crystallographic symmetry operation (*x*, *y*, $^1/_2$–*z*) (reflection across the mirror plane (*x*, *y*, $^1/_4$) upon which the nickel atoms are located). The hexafluorophosphate ion is located on a $\bar{3}$ center of symmetry (combined inversion and threefold rotational symmetry); the symmetry operations relating the fluorine atoms are given in the footnotes to Tables 2 and 3.

Figure 2. Alternate view of the cation-anion pair highlighting the threefold rotational syymetry of both ions. The view direction is approximately parallel to the crystal unit cell's *z* axis.

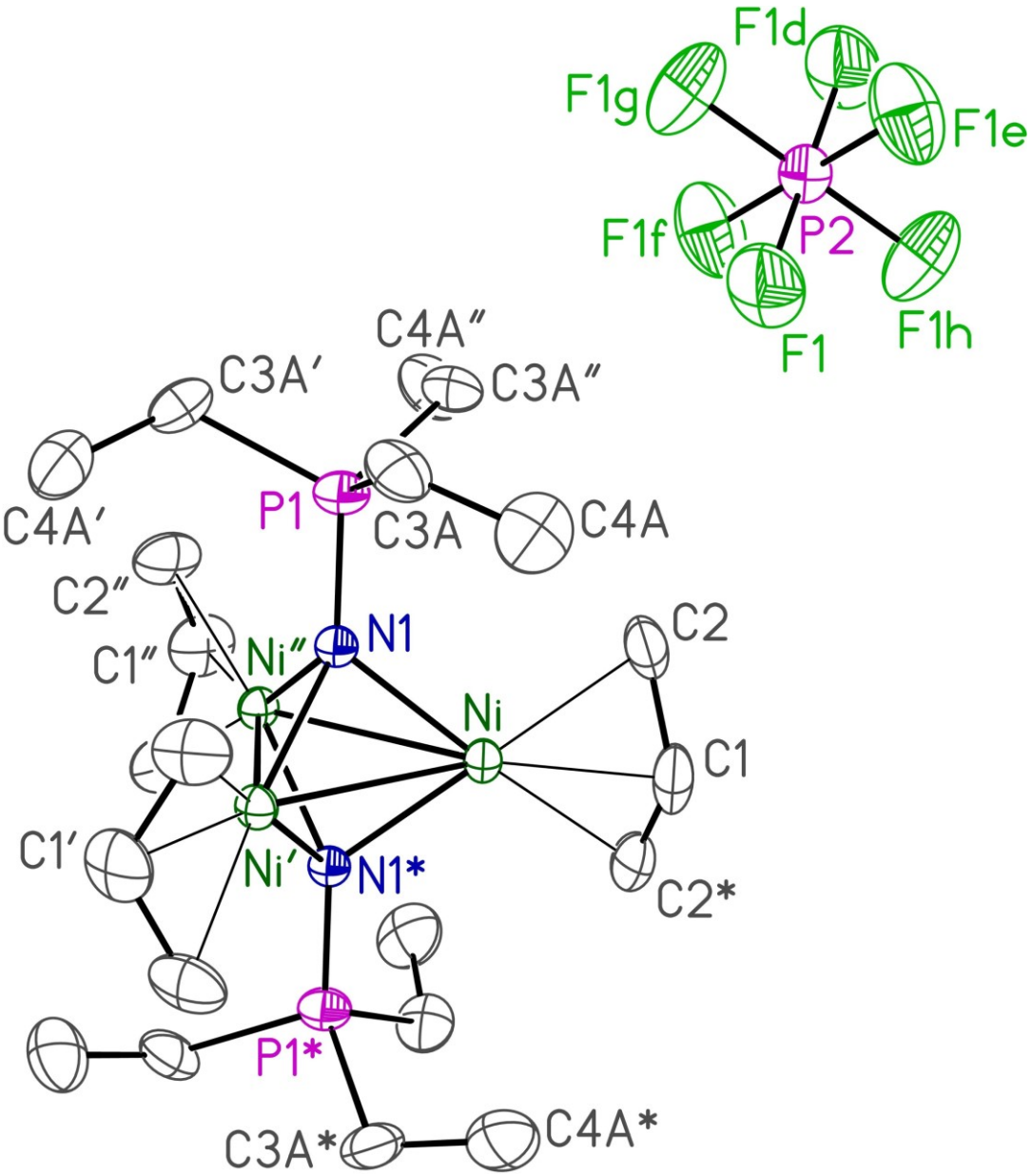
F1d
F1g
F1e
F1f
P2
F1
F1h
C4A″
C3A′
C3A″
C4A′
P1
C3A
C4A
C2″
C1″
Ni″
N1
C2
Ni
C1
C1′
Ni′
N1*
C2*
P1*
C3A*
C4A*

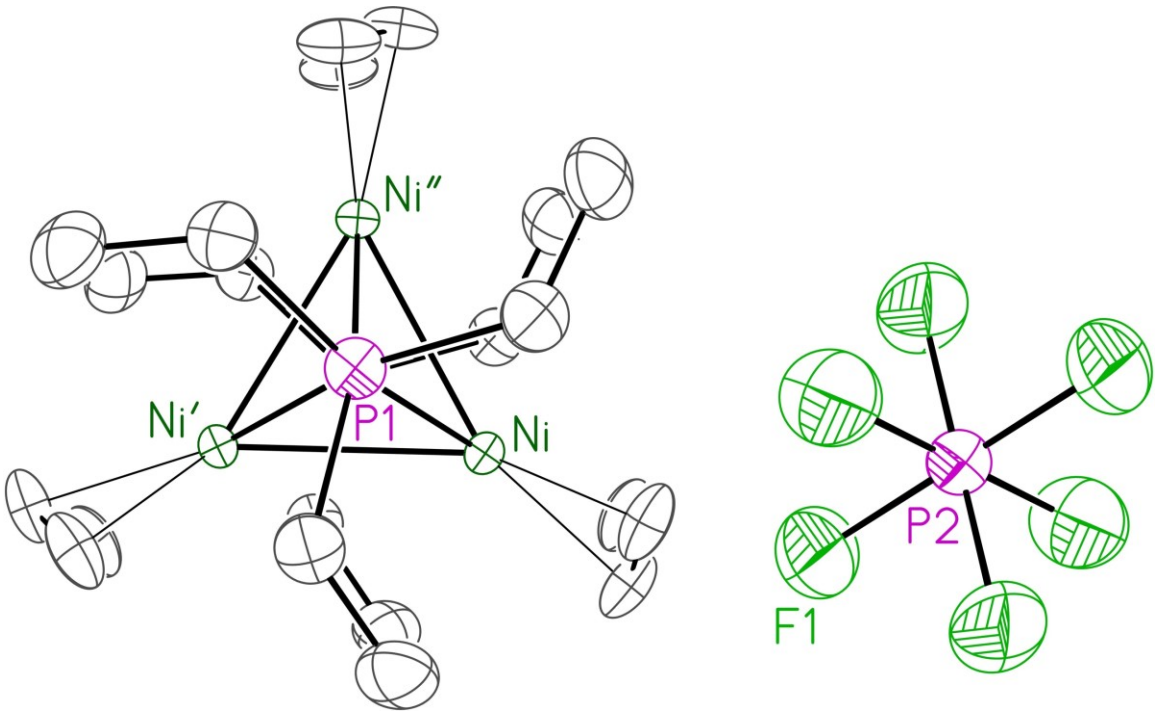
Ni″
Ni′
P1
Ni
P2
F1

Table 1. Crystallographic Experimental Details

A. Crystal Data	
formula	$C_{21}H_{45}F_6N_2Ni_3P_3$
formula weight	708.63
crystal dimensions (mm)	0.39 × 0.20 × 0.07
crystal system	hexagonal
space group	$P6_3/m$ (No. 176)
unit cell parameters[a]	
a (Å)	8.7149 (3)
c (Å)	22.9737 (8)
V (Å^3)	1511.08 (12)
Z	2
ρ_{calcd} (g cm^{-3})	1.557
μ (mm^{-1})	2.059
B. Data Collection and Refinement Conditions	
diffractometer	Bruker D8/APEX II CCD[b]
radiation (λ [Å])	graphite-monochromated Mo Kα (0.71073)
temperature (°C)	–100
scan type	ω scans (0.3°) (20 s exposures)
data collection 2θ limit (deg)	55.14
total data collected	13595 (-11 ≤ h ≤ 11, -11 ≤ k ≤ 11, -29 ≤ l ≤ 29)
independent reflections	1206 (R_{int} = 0.0174)
number of observed reflections (*NO*)	1148 [$F_o^2 \geq 2\sigma(F_o^2)$]
structure solution method	intrinsic phasing (*SHELXT*[c])
refinement method	full-matrix least-squares on F^2 (*SHELXL–2013*[c])
absorption correction method	Gaussian integration (face-indexed)
range of transmission factors	0.8956–0.5778
data/restraints/parameters	1206 / 2[d] / 76
goodness-of-fit (S)[e] [all data]	1.080
final R indices[f]	
R_1 [$F_o^2 \geq 2\sigma(F_o^2)$]	0.0354
wR_2 [all data]	0.0963
largest difference peak and hole	0.690 and –0.377 e Å^{-3}

[a]Obtained from least-squares refinement of 9957 reflections with 5.40° < 2θ < 54.56°.

[b]Programs for diffractometer operation, data collection, data reduction and absorption correction were those supplied by Bruker.

[c]Sheldrick, G. M. *Acta Crystallogr.* **2008**, *A64*, 112–122.

[d]Distances involving the carbons of the $NPEt_3$ ligand's disordered ethyl group were constrained to be equal (within 0.03 Å) during refinement: d(P1–C3A) = d(P1–C3B); d(C3A–C4A) = d(C3B–C4B).

[e]$S = [\Sigma w(F_o^2 - F_c^2)^2/(n - p)]^{1/2}$ (n = number of data; p = number of parameters varied; $w = [\sigma^2(F_o^2) + (0.0465P)^2 + 1.9173P]^{-1}$ where $P = [\mathrm{Max}(F_o^2, 0) + 2F_c^2]/3$).

[f]$R_1 = \Sigma||F_o| - |F_c||/\Sigma|F_o|$; $wR_2 = [\Sigma w(F_o^2 - F_c^2)^2/\Sigma w(F_o^4)]^{1/2}$.

A 1.8 [{(η^3–allyl)Ni}$_2$CoCl$_2$(μ-^{3}–NPEt$_3$)$_2$]

STRUCTURE REPORT

XCL Code: JMS1402 **Date:** 27 May 2014

Compound: [{(η^3–allyl)Ni}$_2$CoCl$_2$(κ^3–NPEt$_3$)$_2$]

Formula: $C_{18}H_{40}Cl_2CoN_2Ni_2P_2$

Supervisor: J. M. Stryker **Crystallographer:** R. McDonald

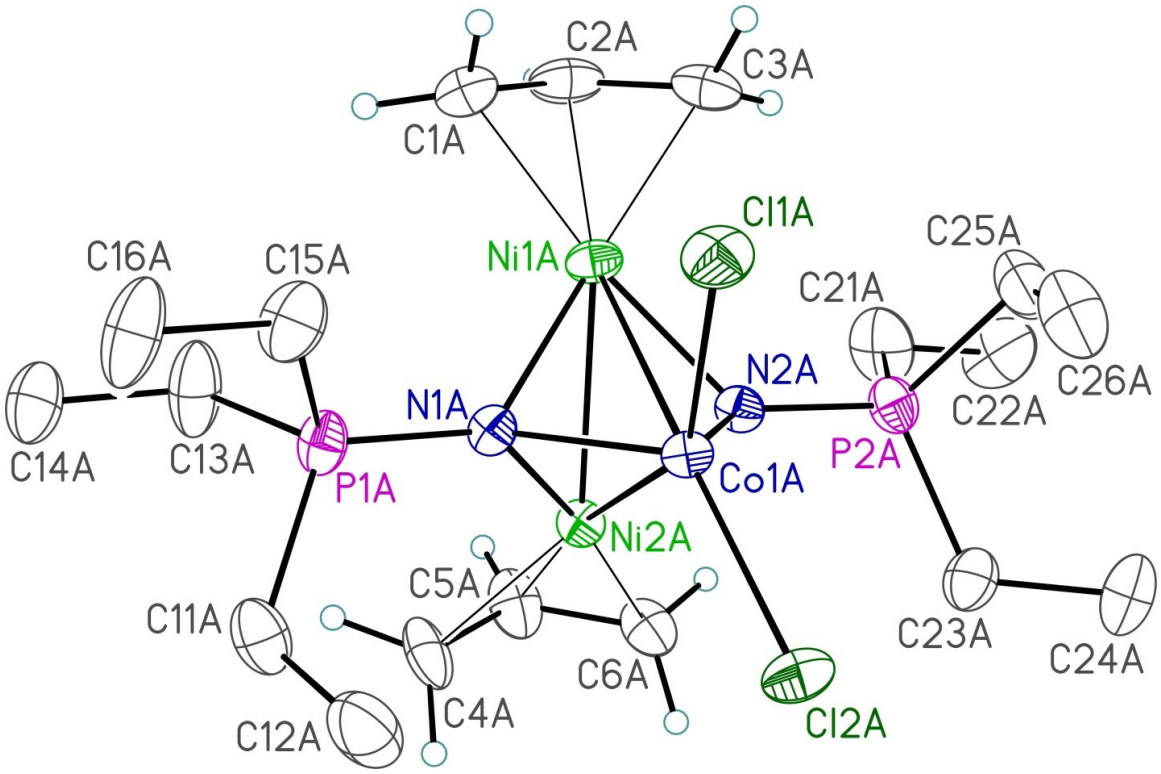

Figure Legends

Figure 1. Perspective view of one of the two crystallographically-independent molecules of [{(η^3–allyl)Ni}$_2$CoCl$_2$(κ^3–NPEt$_3$)$_2$] (molecule A) showing the atom labelling scheme. Non-hydrogen atoms are represented by Gaussian ellipsoids at the 30% probability level. Ally-group hydrogen atoms are shown with arbitrarily small thermal parameters; hydrogens of the NPEt$_3$ groups are not shown.

Figure 2. View of the second crystallographically-independent molecule of [{(η^3–allyl)Ni}$_2$CoCl$_2$(κ^3–NPEt$_3$)$_2$] (molecule B).

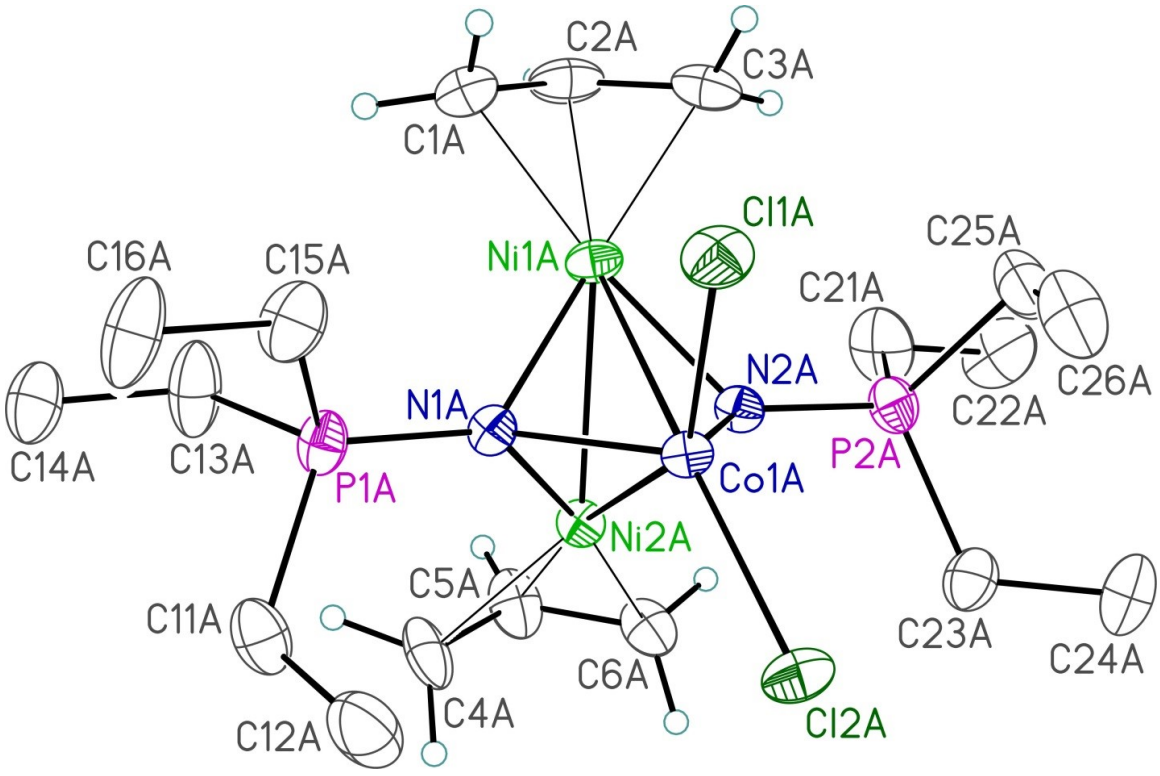

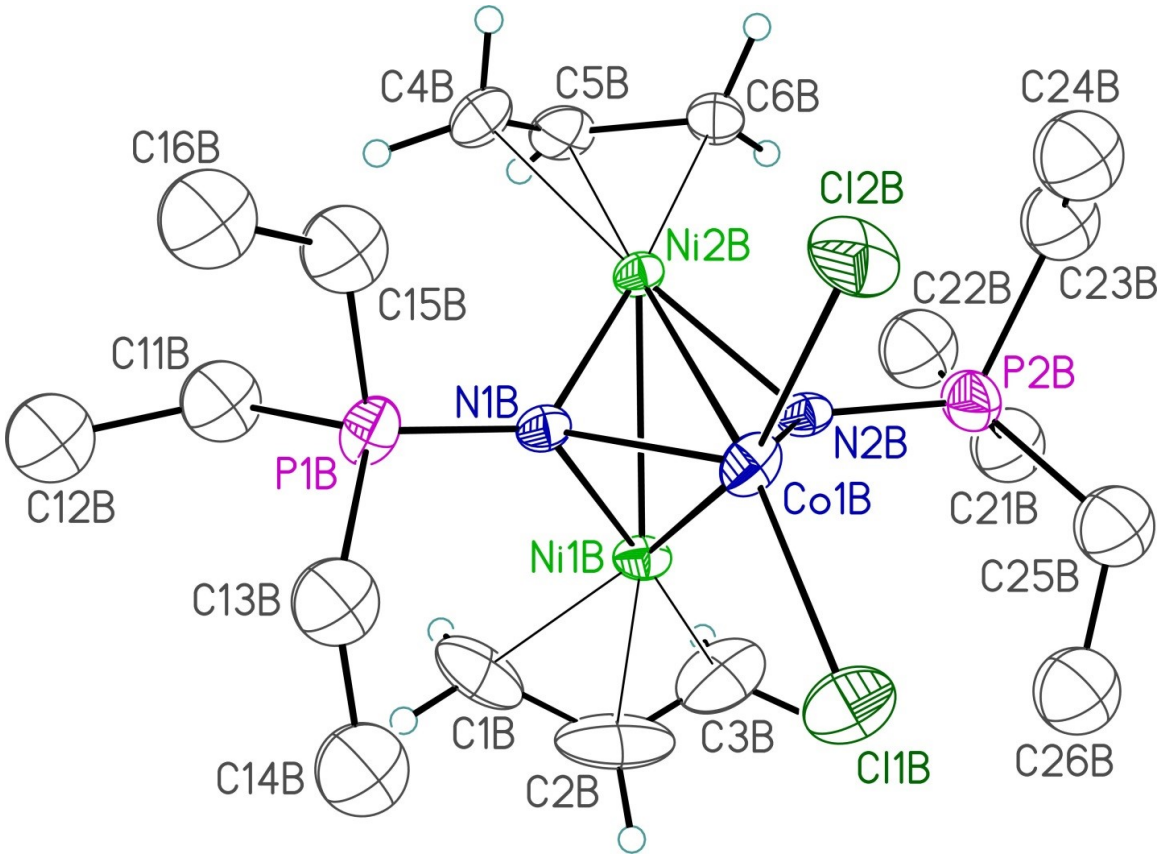
C4B
C5B
C6B
C24B
C16B
Cl2B
Ni2B
C22B
C23B
C15B
C11B
P2B
N1B
N2B
P1B
Co1B
C12B
C21B
Ni1B
C25B
C13B
C1B
C3B
Cl1B
C26B
C14B
C2B

Table 1. Crystallographic Experimental Details

A. Crystal Data	
formula	$C_{18}H_{40}Cl_2CoN_2Ni_2P_2$
formula weight	593.71
crystal dimensions (mm)	0.50 × 0.40 × 0.31
crystal system	orthorhombic
space group	*Pccn* (No. 56)
unit cell parameters[a]	
a (Å)	16.1176 (11)
b (Å)	30.824 (2)
c (Å)	15.8524 (11)
V (Å^3)	7875.6 (10)
Z	12
ρ_{calcd} (g cm^{-3})	1.502
μ (mm^{-1})	2.377
B. Data Collection and Refinement Conditions	
diffractometer	Bruker D8/APEX II CCD[b]
radiation (λ [Å])	graphite-monochromated Mo Kα (0.71073)
temperature (°C)	–100
scan type	ω scans (0.3°) (15 s exposures)
data collection 2θ limit (deg)	56.69
total data collected	70531 (-21 ≤ *h* ≤ 20, -41 ≤ *k* ≤ 41, -21 ≤ *l* ≤ 21)
independent reflections	9784 (R_{int} = 0.0219)
number of observed reflections (*NO*)	8639 [$F_o^2 \geq 2\sigma(F_o^2)$]
structure solution method	ntrinsic phasing (*SHELXT*[c])
refinement method	full-matrix least-squares on F^2 (*SHELXL–2013*[c])
absorption correction method	Gaussian integration (face-indexed)
range of transmission factors	0.6333–0.4776
data/restraints/parameters	9784 / 12[d] / 467
goodness-of-fit (*S*)[e] [all data]	1.053
final *R* indices[f]	
R_1 [$F_o^2 \geq 2\sigma(F_o^2)$]	0.0390
wR_2 [all data]	0.1144
largest difference peak and hole	0.971 and –0.797 e Å^{-3}

[a]Obtained from least-squares refinement of 9336 reflections with 4.46° < 2θ < 45.84°.

[b]Programs for diffractometer operation, data collection, data reduction and absorption correction were those supplied by Bruker.

[c]Sheldrick, G. M. *Acta Crystallogr.* **2008**, *A64*, 112–122.

[d]P–C and C–C distances within the disordered NPEt3 group of molecule B were restrained as follows: d(P1B–C11B) = d(P1B–C13B) = d(P1B–C15B) = d(P2B–C21B) = d(P2B–C23B) = d(P2B–C25B) = 1.82(1) Å; d(C11B–C12B) = d(C13B–C14B) = d(C15B–C16B) = d(C21B–C22B) = d(C23B–C24B) = d(C25B–C26B) = 1.52(1) Å.

[e]$S = [\Sigma w(F_o^2 - F_c^2)^2/(n - p)]^{1/2}$ (n = number of data; p = number of parameters varied; $w = [\sigma^2(F_o^2) + (0.0595P)^2 + 10.5592P]^{-1}$ where $P = [\mathrm{Max}(F_o^2, 0) + 2F_c^2]/3$).

[f]$R_1 = \Sigma||F_o| - |F_c||/\Sigma|F_o|$; $wR_2 = [\Sigma w(F_o^2 - F_c^2)^2/\Sigma w(F_o^4)]^{1/2}$.

A 1.9 ^{1}H-NMR spectra of 114 at various temperature.

Room temperature:

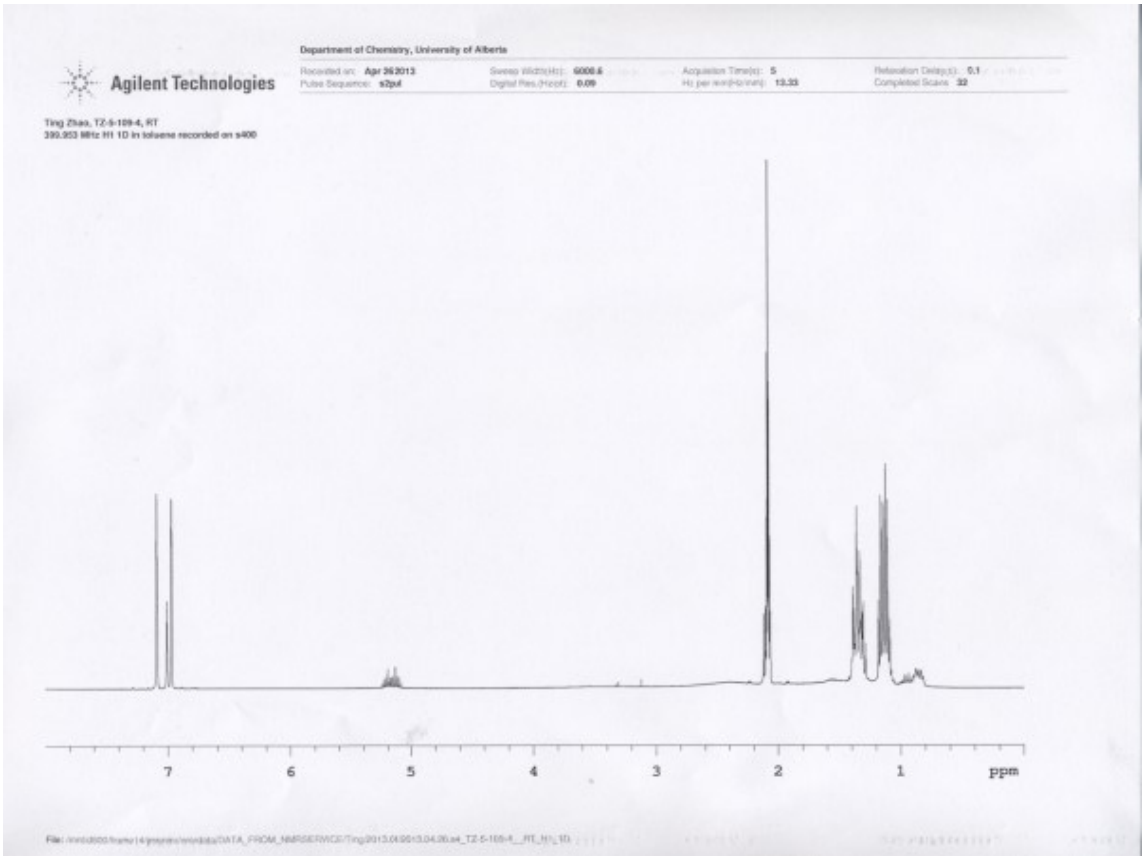

60 °C:

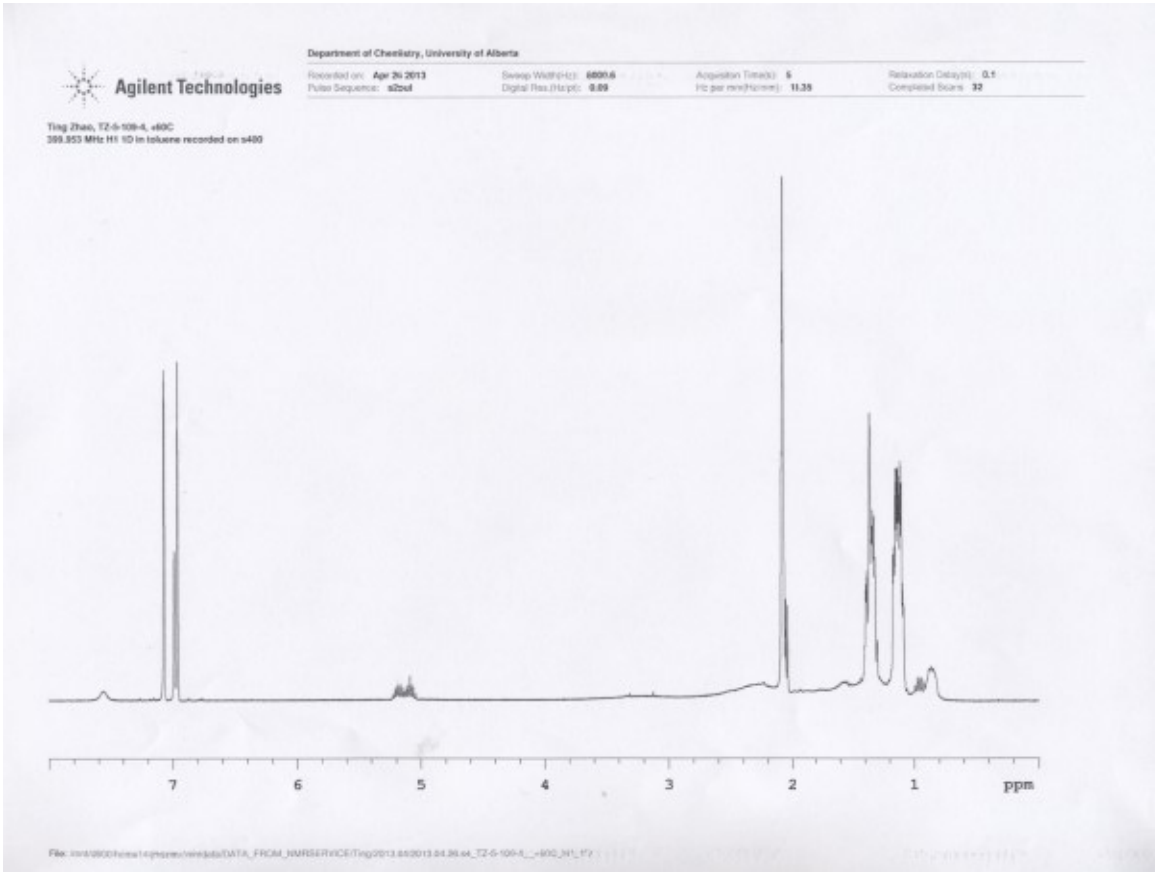
Department of Chemistry, University of Alberta
Agilent Technologies
Ting Zhao, TZ-5-109-4, x60C
399.953 MHz H1 1D in toluene recorded on s400
7
6
5
4
3
2
1
ppm

80 °C:

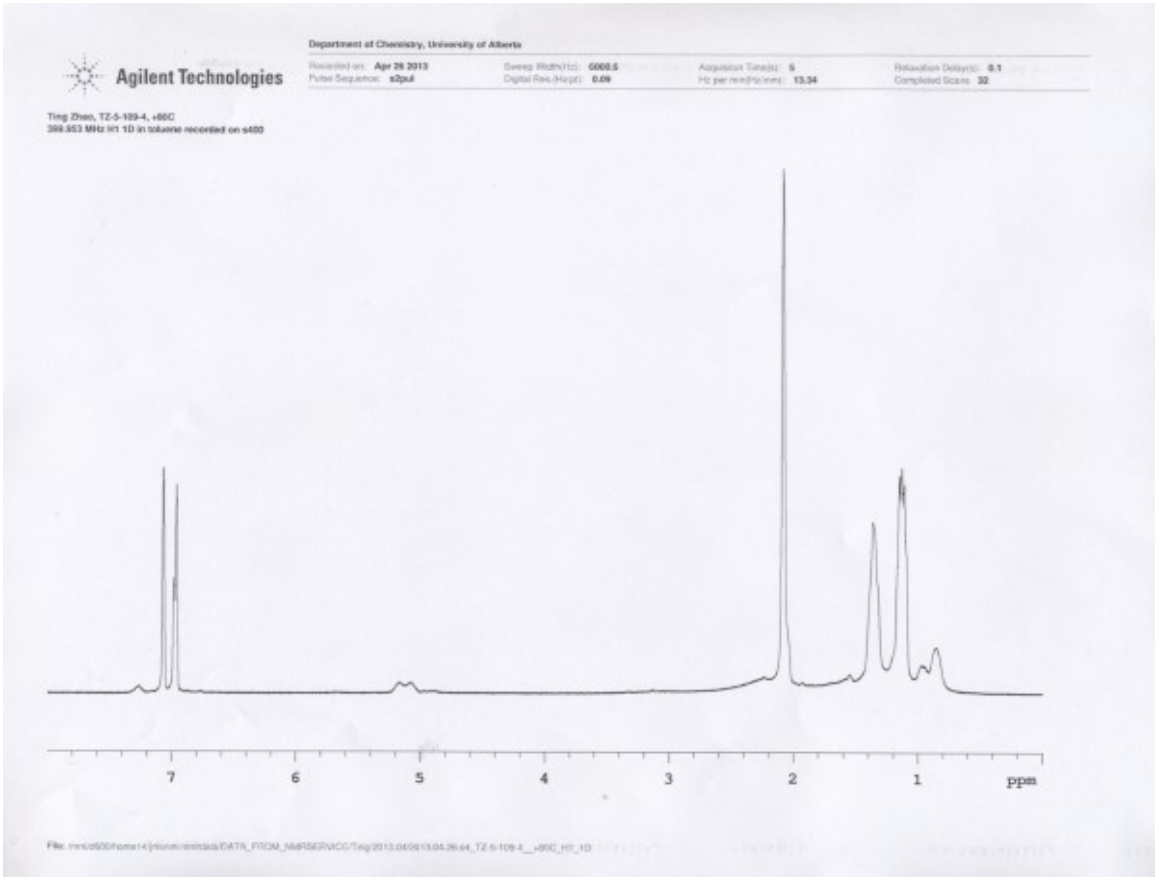
Department of Chemistry, University of Alberta
Agilent Technologies
Ting Zhao, TZ-5-109-4, +80C
399.953 MHz H1 1D in toluene recorded on s400
7
6
5
4
3
2
1
ppm

100 °C:

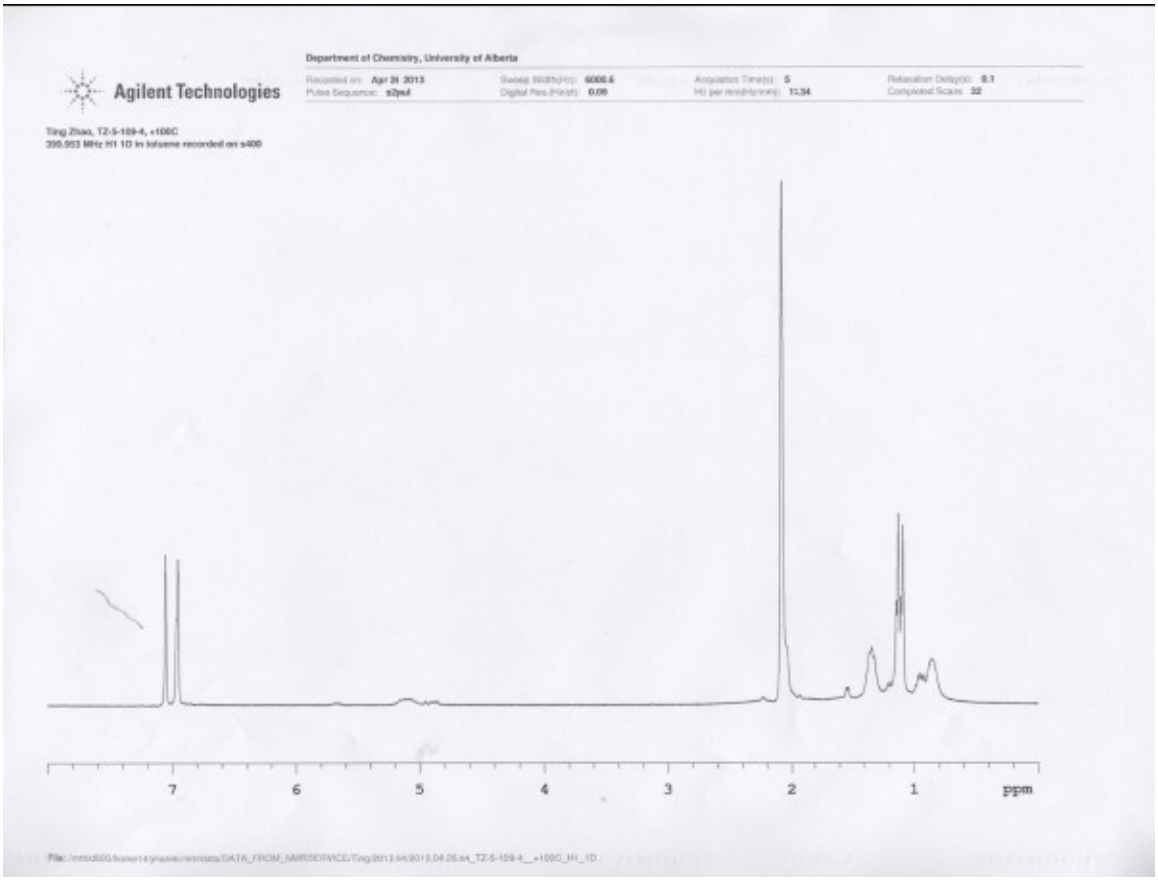
Department of Chemistry, University of Alberta
Agilent Technologies
Ting Zhao, TZ-5-109-4, +100C
399.953 MHz H1 1D in toluene recorded on s400
7
6
5
4
3
2
1
ppm